UNIVERSITY OF LIVERPOOL

Triboelectric Energy Harvesting and Non-smooth Systems

Thesis submitted in accordance with the requirements of the University of Liverpool for the degree of Doctor in Philosophy

By

Yiqiang Fu

August 2019

Abstract

Vibration energy harvesting techniques, which can convert the mechanical energy of ambient vibration into electricity, have drawn great attention in recent years owing to the development of the Internet of Things, industry 4.0 and smart cities and the advancement of sensor technologies that allow them to work with quite low power consumption. The number of the sensors connected to these networks can be enormous, and powering all of them with batteries or from the mains power source is infeasible considering the onerous as well as costly monitoring, replacement and recycling work incurred, especially for those embedded in structures or employed in remote or hazardous places. Therefore, vibration energy harvesters are introduced as an alternative means of power supplement. In addition to working as a powering unit, vibration energy harvesters can also be used for sensing, in which case they become self-powered sensors and are quite competitive over the conventional sensors. Apart from the utilization of the direct effect of an electrification mechanism in vibration energy harvesters, the study of the involved electromechanical coupling mechanisms can facilitate the development of relevant actuators which are based on the corresponding converse effect.

Triboelectric energy harvesting is one of the common vibration energy harvesting techniques and is fairly new compared to electromagnetic and piezoelectric energy harvestings. Triboelectric energy harvesters (TEHs) are dependent on the repeated impact or relative sliding between materials of opposite tribopolarities. Relevant studies of TEHs from the perspectives of structural dynamics are very rare in the literature yet they play an important role in optimization. Therefore, this thesis focuses on studying TEHs of different working modes and improving the understanding of their working mechanisms through theoretical modelling, numerical simulation, and experimental investigation and validation.

TEHs are usually non-smooth in terms of their mechanical behaviours, and vibro-impact and friction can be involved in TEHs of different working modes. Analysing the vibro-impact dynamics of TEHs, which are based on repeated contact and separation, is essential to optimization, and this constitutes the first part of this research. The complex vibro-impact dynamics of a three-degree-of-freedom vibro-impact oscillator, which corresponds

to the mechanical system of a contact freestanding triboelectric-layer mode TEH, is unveiled, especially the effects of mass ratios and spacings investigated. The resulted electrical responses are obtained via a developed circuit simulator in Simulink and are compared in terms of efficient energy conversion for different types of vibrations.

The second major part of this research deals with more advanced modelling and numerical methods and with experimental validations for a TEH of the same working mode with that presented in the first part but based on the vibro-impact of three cantilevered beams. A relationship between the just-before-impact velocity and the coefficient of restitution is experimentally identified and is used in the mechanical modelling. The theoretical model of the electrical system is established rather than using the previously developed circuit simulator. A numerical scheme, which is based on the TR-BDF2 (the trapezoidal rule and the second order backward differentiation formula) method, is proposed to integrate the non-smooth mechanical system and the stiff electrical system. Experimental validations of the proposed modelling and numerical methods and studies of the effects of key parameters are carried out in the end.

A sliding mode TEH, which incorporates friction and magnetic multistability, is proposed and studied in the third main part of this research. The non-smoothness incurred by friction is considered in the modelling. The magnetic multistability is employed to broaden the energy harvesting frequency band. An algorithm that categorizes different types of stability of a multistable non-conservative system is developed and the influence of friction on the system multistability investigated. Comparisons among three types of stability indicate the superiority of bistability. The effects of excitation level and friction on the responses of the system are studied. Giving the fact that a multistable as well as non-smooth system is sensitive to initial conditions, an analysis of the basins of attraction is conducted.

Having carried out analyses based on the “direct electromechanical coupling” in the previous three main parts, the effects of the electrical properties including the tribo-charge surface density and the load resistance on the behaviours of the mechanical systems in TEHs are studied in the final part, which is based on the “reverse electromechanical coupling”. This part of study unveils the electromechanical coupling mechanisms and sheds some light on tuning the harvester from the electrical aspects.

Acknowledgements

I am grateful to my supervisors, Professor Huajiang Ouyang (University of Liverpool) and Professor R. Benjamin Davis (University of Georgia), for their superb guidance and supervision throughout my PhD research. The suggestions and support that they have generously provided are really indispensable during my four years of study.

I also appreciate the joint scholarship programme provided by the Chinese Scholarship Council and the University of Liverpool for covering my tuition fees, study costs and living expenses. Their financial support has been critical for me to finish my PhD research.

I would also like to thank everyone in the Dynamics and Control Lab and the System Identification Lab at the University of Liverpool for the useful discussions as well as the joyful moments that we have made and experienced. Many thanks to Prof Ivan Au, Dr Sebastiano Fichera, Mr Derek Neary for the generosity of providing their measurement devices and help.

Finally, I would like to express my sincere gratitude to my parents and sisters. Their love and care have always been with me and encouraged me to go through all of the ups and downs in these years.

Table of Contents

List of Figures

List of Tables

Chapter 1

Introduction

1.1. Motivation

Energy has been playing an indispensable and irreplaceable role in the evolution of human civilization. It can be said that the evolution of human civilization is exactly an evolution of energy consumption. From drilling wood for fire to exploiting atomic energy, human beings have been consuming energy all the time, which has kept and developed the civilization. However, the large scale consumption of fossil fuels over the past centuries has been undermining the environment disastrously. It is not until the recent decades that harvesting clean as well as renewable energies has been widely exploited and spread.

Following a period of hot research on large-scale energy harvestings, such as wind turbines, solar energy stations and tidal power plants, small-scale energy harvestings, ranging from nanowatts to milliwatts, have received much attention. A main factor that has contributed to this is the dramatic increase in the use of sensors, especially in the development of the Internet of Things (IoT) [1, 2], industry 4.0 [3] (or smart factories in which machines are enhanced with wireless connectivity and sensors and are connected to a system that can monitor and guide the manufacturing) and smart cities [4], in which energy harvesters can be used to scavenge energy from the surrounding environment and power the designated sensors and enable the sensor network to be wireless as well as self-powered. Secondly, it is owing to the advancement of sensor technologies which enable them to work with ultra-low power consumption [5, 6], for example ultra-low power devices for monitoring the physical activity and respiratory frequency of fishes [7] and ultra-low power MEMS shock sensors for acceleration monitoring [8].

Sensors have reached every corner of our life and have became indispensable, and their applications include medical and structural health monitoring, industrial manufacturing

monitoring, ambient condition monitoring, etc. A conventional means of powering sensors is using batteries; however, batteries need to be monitored, replaced and recycled when necessary due to their limited lifetime. This monitoring, replacement and recycling work can be onerous and expensive when the sensors are in remote and/or hazardous places or embedded in structures. Besides, battery cannot be a solution for powering all the sensors connected to IoT because the amount of sensors employed in a network of IoT can be vast and the maintenance task will be huge and even impossible. Thus, most of the IoT cannot be realized without making the connected devices self-powered [9, 10], and ideal power units should have the characteristics of mobility, availability, and sustainability [9].

An energy harvester that converts the ambient energy, such as sound, light, thermal, wind, wave, and mechanical energies, into electricity becomes a competent candidate for the ideal power units. Therefore, the study of the energy harvester for making it a good companion with the sensors deployed in various networks becomes the main motivation of this research.

In addition to scavenging energy from the surrounding environment and powering designated sensors, an energy harvester itself can also work as a self-powered sensor, such as simultaneous acoustic energy harvesting and active acoustic sensing [11], thermal energy harvesting and temperature sensing [12], knee joint force detection and centre of pressure tracking and mechanical energy harvesting [13], etc. Such a capability makes an energy harvester really promising in the development of IoT and forms the second motivation of this thesis.

Furthermore, both energy harvesters and sensors utilize the direct effect of a physical phenomenon, such as the direct piezoelectric effect that converts mechanical motion into electricity [14] and the direct thermoelectric effect that turns temperature differences into electric voltage [15], while an actuator uses its converse effect. Therefore, contributions can also be made by studying the coupling effect between two systems that the physical phenomenon involves, such as the electromechanical coupling [16] between the mechanical and electrical systems caused by piezoelectric effect in piezoelectric energy harvesters, sensors and actuators. The relevant studies will benefit the development of actuators, such as the piezoelectric precision positioning actuator and vibration suppressor, which forms the third motivation.

1.2. Aim and Objectives

The aim of this research is to study and optimize triboelectric energy harvesters of different working modes from the perspectives of nonlinear vibration and non-smooth dynamics and to improve the understanding of their working mechanisms, such as the electromechanical coupling effect, to assist and spur studies from the perspectives of electronics. The objectives are as follows:

(1) To establish the model of a triboelectric energy harvester of contact freestanding triboelectric-layer mode, which is based on a three-degree-of-freedom vibro-impact oscillator, and study the vibro-impact dynamics of the mechanical system and investigate its effect on the electrical system.

(2) To develop more advanced models and methods of a triboelectric energy harvester which is based on a three-cantilever-beam-system and study and validate them via experiments.

(3) To build up the model of a sliding mode triboelectric energy harvester involving friction and incorporating magnetic multistability to study the nonlinear dynamics of the system and achieve broadband energy harvesting.

(4) To systematically investigate the effects of electrical properties on the behaviours of the mechanical systems due to electromechanical coupling in triboelectric energy harvesters of both vertical contact-separation mode and sliding mode.

1.3. Outline of Chapters

This thesis summarises the research status of the vibration energy harvesting, especially triboelectric energy harvesting, and presents the progress that has been made by the author. It is expected that, by reading this thesis, not only the research status is known and the research achievements acknowledged, but also new research ideas spurred.

Chapter 2 - Literature Review

This chapter presents the research status of vibration energy harvesting, especially triboelectric energy harvesting. The basic working mechanisms of three common vibration energy harvestings, namely electromagnetic, piezoelectric and triboelectric energy harvestings, are introduced. The common techniques used in improving the harvesting

performance, such as frequency up-conversion and broadband energy harvesting, are discussed. Particular attention has been paid to the involvements of vibro-impact, multistability and friction in vibration energy harvesting. Research gaps and issues in triboelectric energy harvesting are described, and the following chapters will try to address them.

Chapter 3 - Fundamentals of Triboelectric Energy Harvesters

Some fundamental knowledge about triboelectric energy harvesters is given in this chapter for providing a better understanding of triboelectric energy harvesting and the work presented in the following chapters. Triboelectrification is first explained, which is followed by the introduction of the basic working modes of triboelectric energy harvesters. The fundamental theories related to the electrical systems of triboelectric energy harvesters are then presented.

Chapter 4 - Nonlinear Dynamics and Triboelectric Energy Harvesting from a Three-Degree-of-Freedom Vibro-Impact Oscillator

A triboelectric energy harvester based on a three-degree-of-freedom vibro-impact oscillator is presented. Both the dynamic model of the oscillator and the theoretical model of the oscillator-based triboelectric energy harvester are established. The dynamic response and its effect on the electrical output are considered for various mass ratios and spacings. Different types of motions are compared for their capability in terms of energy conversion.

Chapter 5 - Triboelectric Energy Harvesting from the Vibro-Impact of Three Cantilevered Beams

A new system that harvests vibration energy through triboelectric and electrostatic effects from the vibro-impact of three parallel cantilevered beams is theoretically studied and experimentally validated. Two modelling methods of the mechanical vibration, which differ in the consideration of the eccentricity of the tip mass, are presented and compared with the experimental results for validation. An experimentally identified and numerically fitted relationship between the just-before-impact velocity and the coefficient of restitution is used to model the impact. The electrical model of the triboelectric energy harvester is then established. Two schemes, which are based on the TR (the trapezoidal rule) and TR-BDF2 (the composite of the trapezoidal rule and the second order backward differentiation formula) methods, are proposed to solve the non-smooth mechanical system and the stiff electrical system. Experimental studies and validations are carried out in the end.

Chapter 6 - Nonlinear Structural Dynamics of a Triboelectric Energy Harvester in Sliding Mode with Multistability

A new sliding mode triboelectric energy harvester in the form of a cantilever beam with a tip mass that is acted upon by both magnetic and friction forces is modelled and simulated. The numerical scheme proposed in Chapter 5 is used to solve the combined non-smooth mechanical and stiff electrical system. This is the first study of the structural dynamics of the sliding mode triboelectric energy harvester; additionally, a magnetic field that induces multistability is present to achieve broadband energy harvesting. A comparison between the coupled and uncoupled electro-mechanical models is made to find out the effect of the electrostatic force between electrodes. The influence of the non-conservative force (the friction force) on the multistability of the system is investigated. Comparisons among three types of stability are made. The effects of excitation level and friction on the responses of the system are studied. Finally, an analysis of the basins of attraction is carried out.

Chapter 7 - Effects of Electrical Properties on Vibration via Electromechanical Coupling in Triboelectric Energy Harvesting

Through the electromechanical coupling, not only the mechanical properties can affect the performance of the electrical system, but also the electrical properties can influence the behaviours of the mechanical system. The effects of electrical properties, including tribo-charge surface density and load resistance, on the vibrational behaviours of triboelectric energy harvesters of both vertical contact-separation and lateral sliding modes are investigated. Guidance on controlling the harvester from the electrical aspects is given.

Chapter 8 - Conclusions and Future Work

The main conclusions of this research are drawn. Recommendations for future work are given.

Chapter 2

Literature Review

2.1. Common Vibration Energy Harvesting Techniques

Common vibration energy harvesting techniques include electromagnetic, magnetoelectric, piezoelectric, triboelectric, and electrostatic energy harvestings. In the current study of the magnetoelectric energy harvesting, the magnetoelectric coupling in composites is mediated mainly through strain, and the composites usually consist of a magnetic layer and a piezoelectric layer [17]. The operating principle is usually that the vibration first causes a change of the magnetic field by moving magnets, which then leads to the deformation of the magnetostrictive layers and then the attached piezoelectric layers [18]. Hence, electricity is actually generated through piezoelectric effect in magnetoelectric energy harvesting. Besides, the architectures of magnetoelectric energy harvesters are usually similar to those of electromagnetic energy harvesters. A similar situation appears in triboelectric and electrostatic energy harvestings. Therefore, studies mainly about electromagnetic, piezoelectric and triboelectric energy harvestings will only be reviewed in detail in the following sections.

2.1.1. Electromagnetic Energy Harvesting

The study of the electromagnetic energy harvesters (EEHs) starts in 1990s [19-21], and various models have been developed by many research institutions during these decades. Commercialization of the EEHs [22] has been going on in the meantime, and successful products, such as the PMG7 series from the Perpetuum Ltd, are pouring into the markets and being used in engineering practice, which, in turn, stimulate the relevant research.

2.1.1.1. Main Architectures

Numerous architectures of EEHs have been prototyped and tested. Generally, they can be classified into two groups, namely "Magnet in-line coil" and "Magnet across coil" architectures, and their corresponding typical schematic diagrams are shown in Figure 2.1 for a better understanding. A further classification can consider whether back iron components are included or not in the architecture [19]. Despite the various architectures, a main purpose is to facilitate the oscillation of the magnet relative to the coil (or vice versa) so that the kinetic energy can be turned into electricity to respect Faraday's laws of electromagnetic induction.

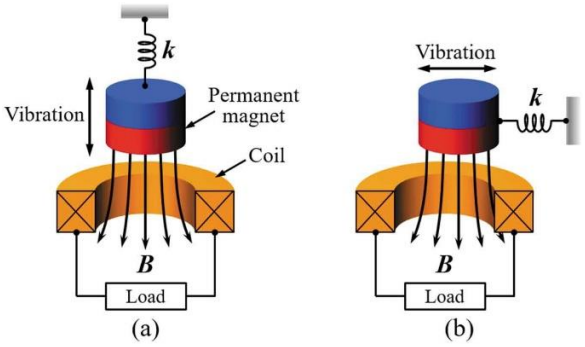

Figure 2.1 Schematic diagrams of (a) a typical "Magnet in-line coil" EEH and (b) a typical "Magnet across coil" EEH proposed by Toshiyoshi et al. [23].

The design of EEH arrays has also drawn some attention since they can achieve broadband energy harvestings. Foisal et al. [24] designed and tested two EEH arrays aiming at extracting vibration energy from ambient vibrations of different frequencies and showed their efficiency at a low-frequency range of 7-10 Hz. Alavikia et al. [25] demonstrated the viability of a wideband Ground-backed Complementary Split-Ring Resonator (WG-CSRR) arrays whose efficiency on power conversion was superior to the G-CSRR arrays.

2.1.1.2. Nonlinearities

The investigation and employment of nonlinearities may help improve the harvesting efficiency, such as broadening the energy harvesting bandwidth. Besides, many vibration energy harvesters are nonlinear due to their intrinsic characteristics, for example, the magnetic force involved in vibration energy harvesters is nonlinear. Therefore, many studies have been carried out to investigate the effects of nonlinearities in vibration energy harvesters. Soares dos Santos et al. [26] developed a semi-analytical, nonlinear model that enabled

efficient and accurate analysis of the energy transduction and had the model verified by experiments. Foong et al. [27] proposed a novel method for effective EEH through the anti-phase resonance of the motion between the coil and magnets, and significant power increase was achieved. Dai et al. [28] investigated a galloping-based EEH and found that the coupled damping and the onset speed of galloping can be strongly dependent on the electrical load resistance but not in the case of large load resistance. Besides, a good correlation between the normal form solutions and numerical simulation was obtained near Hopf bifurcation. Belhaq and Hamdi [29] investigated harvesting energy from quasi-periodic vibrations, in which the harvester was incorporated with a delayed van der Pol oscillator and the double-step perturbation method was used to approximate the amplitude of the quasi-periodic vibrations of the oscillator. It was revealed that, under certain parametric conditions, quasi-periodic vibrations can be more efficient in both power extraction and broadening effective harvesting band. Magnetically and mechanically coupled pendulum systems can have rich nonlinear behaviours. By employing such systems, enhancements on both the power amplitude and the frequency band has been observed in experiments in Ref. [30]. Besides, it has been found that the surrounding temperature and its variation can influence the performance of an EEH [31]. An increment of the temperature can result in lower magnetic flux density, resonant frequency, relative velocity, and open circuit output voltage and higher damping ratio. Therefore, the influence of temperature is better to be considered in both design and application.

In addition, the effects of Duffing-type nonlinearity and the hardening and softening phenomena on the performance of EEHs have been investigated. Green et al. [32] studied a single-degree-of-freedom EEH subject to a broadband white noise base excitation. They presented a successful miniaturization of EEHs using Duffing-type nonlinearities via the FPK (Fokker-Planck-Kolmogorov) equation and found that the optimal load resistance of the harvester was different from the one determined by the principle of impedance matching. However, it was found that the nonlinear stiffness term involved had no influence on the output performance of the presented EEH. Palagummi and Yuan [33] discussed the methods to mitigating the eddy current damping and the geometry of a coil and conducted experiments on the system of optimized parameters, in which a hardening type nonlinearity was found. Fan et al. [34] developed a monostable EEH featuring typical softening response and the shift of frequency band towards left and conducted experiments with the EEH attached on legs in

both walking and running conditions using a treadmill, approximately 0.5 mW and 0.7 mW of power were extracted, respectively.

2.1.1.3. Electromechanical Coupling

The electromechanical coupling in EEHs raises issues of simultaneous optimizations between the mechanical and electrical systems since electrical properties of the outside circuit can also affect the mechanical behaviours of the harvester. Cannarella et al. [35] discussed the use of the common defined electromechanical coupling factor in two cases. They presented that the factor worked well in the case of a coil oscillating vertically to the surface of the magnet but broke down when the coil oscillating parallel to the magnet surface, and it was suggested to use the commercial electromagnetic field simulators to do the optimization in the latter case. Loong et al. [36] investigated the effect of the nonlinear circuit on the behaviour of the harvester-structure coupled system under sinusoidal excitation using a first-order harmonic balance method and suggested a better design of the circuit to achieve high harvesting efficiency. Zhang et al. [37] studied the effects of electrical loads containing non-resistive components, such as rectifiers and capacitors, on the performance of an EEH. Three types of electrical loads were evaluated. The results suggested that the device performance under pure-resistive loads cannot be generalized to devices incorporating rectifier and/or capacitor loads and the harvester's characteristics and performance can be tuned and improved using an adjustable regulating capacitor and a larger storing capacitor, respectively.

2.1.1.4. Ferrofluids

Most of the EEHs employ solid magnets for magnetic induction. However, ferrofluids have been found to have better performance than solid magnets under certain circumstances. Bibo et al. [38] proposed the use of ferrofluids rather than solid magnets in EEHs and demonstrated that the ferrofluid-based EEH can work at even very small excitation levels owing to the fluidity of ferrofluids. Kim [39] compared the working efficiency between two ferrofluid-based EEHs, respectively, equipped with back-iron and air yokes and verified the superiority of the former with tests. Despite the advantages, predicting the performance and maintaining a steady output of a ferrofluid-based EEH might rise challenges because of the fluid-structure interaction issues.

2.1.1.5. Energy Sources and Excitation Forms

Various energy sources and excitation forms have been exploited and studied. The energy sources include human motion [40], railroad [41], bridge [42], vehicle [43], etc. The excitation forms involve sinusoidal excitation [44], impulsive excitation [45], random excitation [46], etc. Energy harvesting from flow-induced vibrations is relatively vibrant in EEHs and is more challenging, especially in terms of simulations. Wang et al. [47] proposed an EEH which harvested energy from the vibration induced by Kármán vortex street and developed the corresponding analytical method to serve the design, and a prototype was fabricated and tested in a small simple water tunnel. Park et al. [48] studied the fluid-structure interaction between a T-shaped cantilever EEH and the wind flow both numerically and experimentally and employed the vortex particle method to determine the aerodynamic damping and analyse the stability of the harvester section. The estimated parameters were used to find the critical wind speed of flutter onset and the optimal load resistance. Wind tunnel tests were carried out to do the validation. Caruso et al. [49] studied a bridge-EEH coupled model, in which the bridge vibration was reduced through a modal analysis, and a simplified tuning procedure was established for a real-time harvester.

2.1.1.6. Applications

Applications of EEHs can be seen in numerous aspects. Jung et al. [50] used an EEH harvesting energy from the wind-induced vibration of a stay cable to power a wireless sensor node on the cable. Padasdao et al. [51] explored simultaneous sensing and harvesting of respiratory rate and motion. A prototype was tested on both a mechanical chest simulator and 20 human subjects, and comparisons were made between them for improvement. Joyce et al. [52] proposed the use of an EEH inside the wind turbine blades for powering the attached structural health monitoring (SHM) systems. Guo et al. [53] both numerically and experimentally investigated a hydraulic electromagnetic energy-harvesting shock absorbers (HESAs) which can reduce the vibration of vehicle suspensions as well as extract vibration energy. The designed and optimized HESAs can serve typical heavy-duty trucks and railway freight vehicles. Karageorgos et al. [54] investigated extracting energy from the motions of the cardiovascular system to enable the realization of a self-powered implantable cardiovascular monitor which was expected to avoid costly and complex battery replacements. Afsharfard [55] introduced the coupling between an EEH and a nonlinear magnetic vibro-impact vibration suppressor. The resultant system can waste energy during

the inelastic contacts and extract energy through the electromagnetic induction, which resulted in the attenuation of undesired vibrations and energy conversion.

2.1.2. Piezoelectric Energy Harvesting

Among the common vibrational energy harvesting mechanisms, piezoelectric energy harvesting (PEH, which also represents piezoelectric energy harvester in the context) has received the greatest attention in the past decade, which can be directly concluded from the huge number of related publications that have appeared in the literature and is owing to the advantages of piezoelectric materials, i.e., large power densities and ease of application [16].

Piezoelectric materials have the abilities [56] to convert electrical energy into mechanical strain energy, which is called the converse piezoelectric effect and is often used in vibration control including attenuation [57], actuation [58] and precision positioning [59], and transform mechanical strain energy into electrical energy, which is regarded as the direct piezoelectric effect and often functions as sensors, especially in vibration energy harvesting.

2.1.2.1. Main Architectures

A typical cantilever-based bimorph PEH proposed by Fu et al. [60] is shown in Figure 2.2, in which a beam (the substrate) has its one end clamped onto a beam holder or a base and the other end attached with an inertial mass and both sides are attached with piezoelectric layers and electrodes. The excitation can be applied at either the free end or the clamped end, though it is often the case of the latter since vibration energy harvesters are mostly base-excited. The deformation of the piezoelectric layers will accompany that of the substrate and convert part of the mechanical energy into electricity owing to the direct piezoelectric effect.

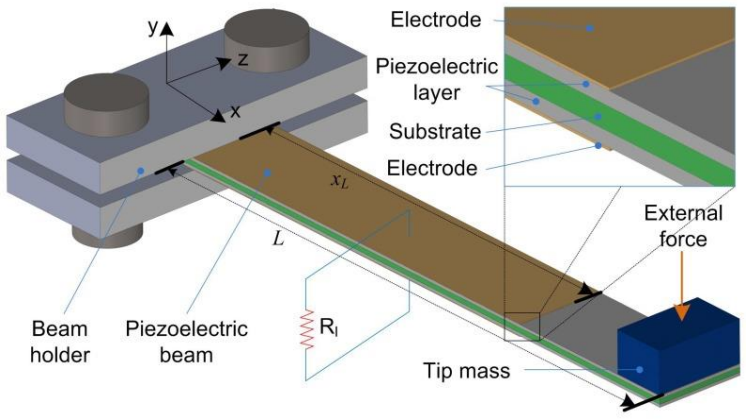

Figure 2.2 Schematic diagram of a typical cantilever-based bimorph PEH proposed by Fu et al. [60].

2.1.2.2. Plucking

Beam plucking can be seen in the cases in which the excitation is applied at the free end of a piezoelectric beam, and it can be achieved via non-contact magnetic interaction between a tip magnet and a moving magnet or via geometric contact between the tips of a piezoelectric beam and an interactive beam or a plectrum [61, 62]. The configuration of a typical magnetic beam plucking PEH [63] is shown in Figure 2.3 as an example. The driving or moving magnet can be mounted on moving belts and rotating discs. The plucking of the piezoelectric beams can help realize frequency up-conversion. Dauksevicius et al. [64] reported a numerical-experimental analysis of a PEH which was based on magnetic plucking for contactless mechanical frequency up-conversion. A phenomenon of transient resonance, which delivered peak power and energy outputs, was demonstrated. Kathpalia et al. [65] presented a geometrically nonlinear plucking-based configuration for frequency up-conversion of a PEH. Von Kármán type geometrically nonlinear deformation of the plectrum cantilever was used, which resulted in the coupling between the plectrum and the piezoelectric cantilevers. The effects of the parameters, such as the overlap length between these two cantilevers, were analysed.

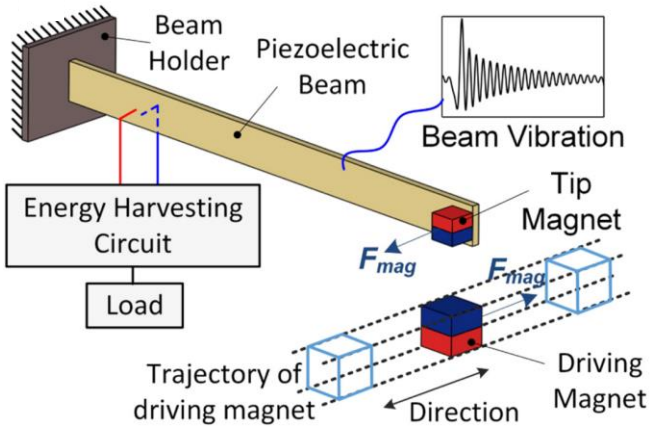

Figure 2.3 Schematic diagram of a typical magnetic beam plucking PEH proposed by Fu et al. [63]. Reproduced with kind permission of IOP Publishing.

2.1.2.3. Nonlinearities

Nonlinearities have been exploited to improve harvesting performance in PEH as well. Firoozy et al. [66] considered the nonlinearities caused by the curvature and inertia terms due to large amplitude vibrations of the piezoelectric cantilever beam. It was shown that the addition of a sufficient large tip mass could result in significant increases in the electrical

outputs. Besides, two frequencies of the system were excited in the presence of the tip mass compared to the case without a tip mass, and the second frequency was three times of the first one. Garg and Dwivedy [67] studied the response and stability of a parametrically excited PEH with 1:3 internal resonance under principal parametric resonance conditions. Bifurcations including turning point, pitch-fork and Hopf were observed. Broadband energy harvesting was achieved by tuning the attached mass to an optimal value, but it should be noted that it would be difficult to achieve such tuning in real applications. Yang and Towfighian [68] addressed the two shortcomings of parametric resonance harvesters, i.e., high threshold excitation and narrow bandwidth, by involving magnetic nonlinearity to the system. The threshold excitation level for parametric resonance was controlled by adjusting the properties of the magnetic field. Frequency bandwidth was enlarged by the softening and hardening behaviours.

In addition to the nonlinearities in the mechanical systems, the effect of the piezoelectric nonlinearities on both electrical and mechanical responses have also been investigated. Stanton et al. [69] highlighted the necessity of modelling inherent piezoelectric nonlinearities including higher order elastic effects and nonlinear coupling to an outside circuit. They identified nonlinear coefficients using a nonlinear least-squares optimization algorithm which used an approximate analytic solution derived by the harmonic balance method. Abdelkefi et al. [70] considered geometric, inertia, and piezoelectric nonlinearities into modelling and used the method of multiple scales to determine the analytical solutions for both mechanical and electrical systems. Their results presented that one- or two-mode approximations were not sufficiently accurate for predicting the electrical responses. Zhang et al. [71] studied the fundamental effects of electrical loads involving non-resistive components, e.g. rectifiers and capacitors, on the performance of piezoelectric energy harvesters. It was shown that the performance of a device based on pure resistive loads could not be generalized to applications containing non-resistive components. Besides, it was found that an adjustable regulating capacitor and a proper rectifier could be used to tune the natural frequency of a PEH. Morel et al. [72] studied tuning the properties of highly coupled PEHs using the resistive, capacitive and inductive behaviours of the electrical interface, and experiments were used to support their methods.

2.1.2.4. Optimizations

Optimizations of PEHs have been carried out from various perspectives. Nabavi and Zhang [73] employed the genetic algorithm, which was an evolutionary computation method and made optimizations through mimicking biological evolution, in their study of optimizing a PEH. It was shown that several parameters were optimized leading to considerably enhanced output voltage. Franco and Varoto [74] studied the effects of multi-parameter uncertainties on the performance of a piezoelectric cantilever beam carrying a tip mass. An optimal set of parameters, which resulted in optimal electrical outputs, was first obtained through the sequential quadratic planning optimization. Random perturbations were then introduced, and the Monte Carlo method was used, to study how those uncertainties propagate and influence the electrical outputs. Gedeon and Rupitsch [75] presented an accurate modelling of linear PEHs using the finite element method (FEM). The developed finite element model by a specialized modal truncation method was coupled to electric circuits via Simulink and was validated against analytical models and full finite element models. Li et al. [76] proposed a generalized multimode PEH which consisted of a primary piezoelectric cantilever beam and multiple secondary cantilever beams attached at the free end of the primary cantilever beam. The performance of the multimode PEH can be tuned by varying the characteristics of the secondary cantilever beams.

2.1.2.5. Energy Sources and Excitation Forms

Among the various energy sources for PEHs, harvesting energy from flow-induced vibration has received much attention. Bibo and Daqaq [77] studied a PEH under the combined base and aerodynamic excitations. A 5-DOF lumped-parameter model involving nonlinear quasi-steady aerodynamics was established. Methods of centre manifold reduction and normal form were used. It was found that the resultant effects from these two forms of excitations can be distinct as the wind speed across the flutter speed. Hobeck and Inman [78] presented a theoretical analysis of a PEH exposed to turbulent cross-flow. The distributed parameter model was developed using a combination of both the Rayleigh-Ritz analytical approximation and the statistical techniques to account for the beam vibrations and define the turbulence-induced forcing function, respectively. Zakaria et al. [79] showed that self-excited oscillations resulted by geometric nonlinearities can be used to initiate vibrations of a cantilever beam placed in an air flow and eliminate the need of attaching certain structures onto the beam. It was shown that the system responses were strongly dependent on the air

speed and the angle of attack. Cha et al. [80] explored underwater energy harvesting from the undulations of a biomimetic fish tail. The developed harvester and methods can be used to power fish-tags which were externally or internally implanted on fishes for understanding their migratory patterns and movements. Demori et al. [81] studied the vibrations of a piezoelectric flexure beam which was excited by von Kármán vortices detached form a bluff body placed upstream. The relationship between the vortex shedding frequency and the flow velocity was assessed by computational fluid dynamics (CFD) simulations. The configuration was then optimized in terms of efficient energy harvesting. The harvested energy was finally used to power two measurement sensors of temperature and flow velocity.

Random vibrations are more practical forms of excitations regarding to their similarities to real ambient vibrations. Quaranta et al. [82] proposed a comprehensive method for the electromechanical probabilistic analysis of PEHs subject to modulated and filtered white Gaussian noise. The mean and standard deviation of the harvested energy can be estimated using the proposed method. Wang et al. [83] utilized a mechanical vibration frequency stabilizer, which consisted of a spiral spring and a series of gear sets, to convert irregular energy, such as impact energy from roads, into more stable electrical outputs.

PEH from other forms of excitations including moving load, rotation, etc. Amini et al. [84] investigated PEH from vibrations induced by multi-moving loads. Effects of piezoelectric bonding location and the properties of the moving loads on the produced power were studied. Cooley and Chai [85] studied energy harvesting from rotating systems of constant speeds. They found that PEHs, depending on their mechanical dampings, could have two local maxima of electrical output which, though, were sensitive to small changes in the excitation frequency but not to small changes in rotation speed. They also compared viscous and structural dampings in a lumped-parameter model of a PEH in another study [86]. Two maxima might also exist, and one of them was not sensitive to the damping model and the other one, however, had meaningful differences between viscous and structural damping models. Besides, the differences between those two models increase along with the increase of electromechanical coupling.

2.1.2.6. Soft Piezoelectric Materials

Studies on the improvement of the material properties of piezoelectric layers or patches can also be found. In addition to the common “hard” piezoelectric beams, Mutsuda et al. [87] proposed a painted highly flexible piezoelectric device which had a laminated structure

composed by a piezoelectric paint and an elastic material. The device can be easily excited due to its high flexibility. Chou et al. [88] fabricated a stretchable PEH which can bear stretched, clustered, folded, and twisted stimulations and work as not only an efficient harvester but also a tension and gesture sensor. The great progress they made may impact the prospects of artificial intelligence and individualized medical care.

2.1.2.7. Applications

All the studies of PEHs should eventually serve the applications, and numerous applications have been exploited. Eshghi et al. [89] proposed a new design of a self-powered tyre pressure monitoring sensor considering the uncertainties in car speed, material properties and dimensional tolerances and compared it with the traditional deterministic design optimization, and a significant increase of reliability from the new design was shown and verified by experiments. Kim et al. [90] presented a PEH-based floor tile for smart home energy management. The harvested energy was used to power a wireless sensor node which can control the power switch of home appliances in real time. Safaei et al. [13] proposed to incorporate piezoelectric transducers into knee implants for both medical sensing, e.g. force detection and centre of pressure tracking, and energy harvesting. The integrated knee implant can be self-powered and can provide the in vivo data from the knee joint to support the establishment of well-quantified alignment methods. Shin et al. [91] developed a piezoelectric polymer-based roadway energy harvesting module which featured the ability of amplifying a 2.5 mm vertical displacement up to 13 mm horizontal deformation of the piezoelectric polymer without affecting the driving experience. The output power was found in a linear relationship with the vehicle speed and weight, which indicated the module's potential of being used as a self-powered vehicle speed measurement sensor.

2.1.3. Triboelectric Energy Harvesting

In comparison, triboelectric energy harvesting (TEH, which also stands for triboelectric energy harvesters in the context) is relatively new and the first report of it appears in 2012 [92]. TEHs are receiving more and more attention owing to their high conversion efficiency, simple fabrication, wide choice of materials, cost-effectiveness, and wide variety of applications [93]. Four fundamental working modes have been identified and they are vertical contact-separation, lateral sliding, single-electrode, and freestanding triboelectric-layer modes [9], and their working mechanisms are detailed in Section 3.3. Basically, they

operate via a combination of triboelectrification or triboelectric effect and electrostatic induction between materials that have the opposite triboelectric polarities [94] and through repeated contact and separation or relative sliding motions between different triboelectric materials. An example of a TEH of contact-separation mode proposed by Saadatnia et al. [95] is shown in Figure 2.4. When the top electrode (copper) is separated with the dielectric (Aerogel), a potential difference can be generated between them by the triboelectric charges induced during contact, which can drive electrons to flow between electrodes, and a reverse current flow is induced as a result, as shown in Figure 2.4(c).

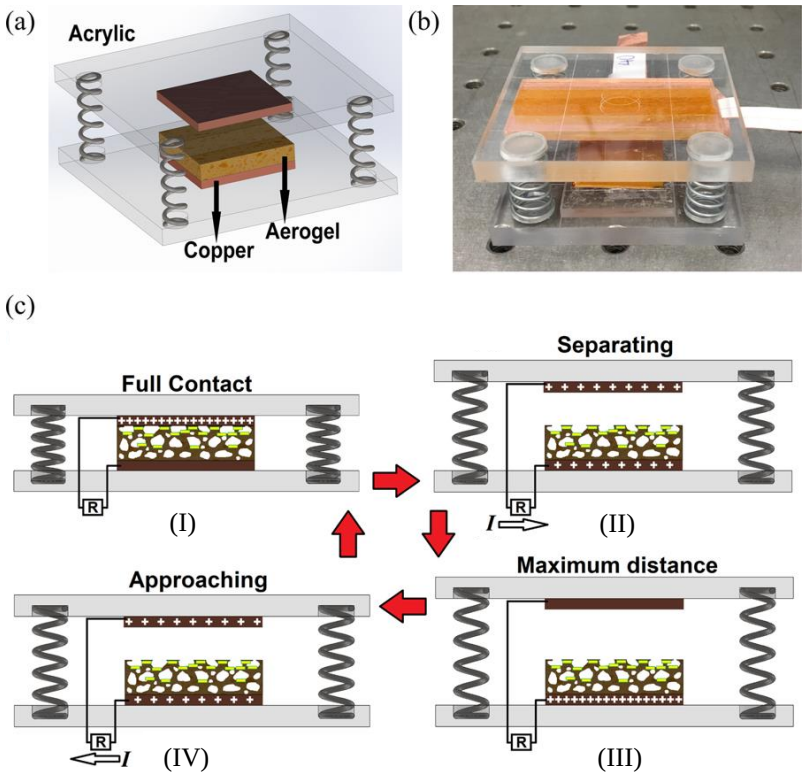

Figure 2.4 Schematic diagrams of a high performance TEH of vertical contact-separation mode proposed by Saadatnia et al. [95]; (a) configuration of the TEH, (b) picture of the prototype and (c) the corresponding working mechanism.

2.1.3.1. Architectures and Fabrications

Studies on the architectures and fabrications of TEHs have been vibrant since beneficial architectures and state-of-the-art fabricating techniques can help improve the harvesting efficiency dramatically. Cui et al. [96] fabricated a wearable TEH which was made of nylon and Dacron fabric and worked via the friction between the two parts located at forearms and human body during arm swings. It can be used to charge portable electronic devices and can

be easily folded, kneaded and washed as a common clothe. Wang et al. [97] proposed a freestanding, fully enclosed TEH that contained a rolling ball inside a rocking spherical shell of a diameter of 6 cm. The TEH featured lightweight, simple structure and capability of harvesting wave energy, and it prompted the development of large-scale blue energy harvesting from oceans and lakes [98]. Chen et al. [99] fabricated a contact-separation mode TEH which utilized magnetic plucking. The unique design was tailored for applications to harvesting energy from rotations. It was shown that the harvester lit up 24 spot lights (0.6 W each) simultaneously at a wind speed of 6.5 m/s or a water flow rate of 5.5 L/min. Shankaregowda et al. [100] developed a graphene-based TEH using chemical vapour deposition which made the TEH highly conductive, transparent, and efficient. Chun et al. [101] reported a TEH consisted of three layers in which there was an electric double layer located between a top Al/polydimethylsiloxane layer and a bottom Al layer and electrically connected to the earth. A performance of 1.22 mA and 46.8 mW/cm^2 under 3 Hz was shown. The harvester was also demonstrated to charge a smart watch and a mobile phone.

Sliding mode is another prevalent basic mode based on which plentiful architectures have been built. Wang et al. [102] demonstrated the first study of a sliding mode TEH. Its power density reached 5.3 W/m^2 and it was used to light up hundreds of LEDs instantaneously. The working mechanism and the influence of sliding motions on the electrical outputs were studied comprehensively. Yang et al. [103] designed a hybrid TEH that worked through a combination of vertical contact-separation and lateral sliding modes. The unique design facilitated multi-direction vibration energy harvesting over a wide bandwidth. The prototype device was tested under different excitations including cable vibration, human walking, and bicycle wheel rotation. Du et al. [104] fabricated a multi-layer sliding mode TEH. Linear relationships between the transferred charges and the sliding displacement and between the short-circuit current and the sliding velocity were obtained through fittings of experimental results, which indicated the potential applications of the harvester as self-powered displacement and velocity sensors. Lin et al. [105] proposed a TEH which relied on the rolling motion of steel rods between the top and bottom FEP layers for inducing potential difference and then electron flows between two electrodes. The rolling motion reduced the energy consumption by friction and improved energy conversion efficiency up to 55% and enhanced the durability of the device. Prototypes based on rolling balls were also developed to meet different kinds of mechanical energy source.

2.1.3.2. Modelling and Analysis of Electrical Systems

Theoretical models that govern the electrical systems of TEHs and studies that focus on the working mechanisms of TEHs have been established and developed. Niu and Wang and other members in Wang's group [106-108] have developed the theoretical models or the first-order lumped-parameter equivalent circuit models, which were also known as the V - Q - x relationships, of TEHs of different working modes. Those theoretical models made the theoretical analysis, especially optimizations from the perspectives of structural dynamics, of TEHs feasible and were milestone works for comprehensive understanding of the working mechanisms of TEHs. A new simulation method for integrated TEH systems that contained TEHs, power management and storage circuits was also developed by Niu et al. [109]. The method integrated the equivalent circuit models of TEHs into SPICE (simulation program with integrated circuit emphasis) software and was validated by analytical solutions. The behaviour of a TEH in charging capacitors was analysed by them [110] as well. Both numerical and analytical analyses were carried out. It was shown that the charging behaviour of a TEH with a bridge rectifier under periodic excitation was similar to that of a DC voltage source in series connection with an internal resistance. An optimum load capacitance, which matched the TEH impedance, could be found and was linearly proportional to the inherent TEH capacitance and the charging cycles. Yang et al. [111] presented a theoretical model for contact-separation mode TEHs using the principles of charge conservation and zero loop-voltage. Experiments were conducted to validate the theoretical model and good agreement was found.

Analyses of the electrical output of TEHs have been carried out from different aspects including studying the effects of temperature, electrical impedance, contact behaviours, etc. Su et al. [112] investigated the dependence of TEHs' output on the ambient temperature ranging from 77 K to 320 K. A tendency of increasing output voltage against decreasing temperature was found when metal and polymer were used since the surface charge density was greatly affected by the thermal diffusion during the cryogenic process. A reverse tendency was observed when semiconductor and polymer were used due to the carrier density and conductivity. Dharmasena et al. [113] revealed the power output characteristics of TEHs by comprehensively analysing their impedance behaviour as a function of the excitation and device parameters. Norton's theorem was extended to model TEHs, which allowed accurate analysis of TEHs' electrical output through impedance plots. Optimization strategies, device limitations, and effects of motion parameters were discussed. Jin et al. [93]

studied the contact behaviour of micro/nano-structured surfaces in contact-separation mode TEHs. In their numerical simulation, the adhesive interactions were denoted by an interaction potential and the deformations of contact surfaces were coupled via half-space Green's functions discretized on the contact surfaces. The simulation verified that the deformation of the interfacial structures directly determined the relationship between the pressure applied and the voltage generated. Park et al. [114] found that the output performance of TEHs can be improved by introducing an electron blocking layer between the electrode and the negative tribo-material layer. This was because a higher tribo-charge surface density on the negative tribo-material was maintained after the introduction of the electron blocking layer which, moreover, enhanced the polarization of the negative tribo-material.

Triboelectric material surface modification plays a significant role in enhancing the performance of TEHs. Nafari et al. [115] studied the effect of micro/nano scale material surface modification on the performance of TEHs, and the models used and the results obtained are shown in Figure 2.5. The importance of using surface morphology was denoted and it was shown that the power output of a TEH was increased by 118% after the involvement of effective surface modification. Various surface patterns have been fabricated, such as pyramid and cubic patterns [116], nanowire array [102], and nanopores [103]. Note that triboelectric energy harvesters with micro/nano scale surface modifications are usually called triboelectric nanogenerators (TENGs), but they will not be distinguished in the context.

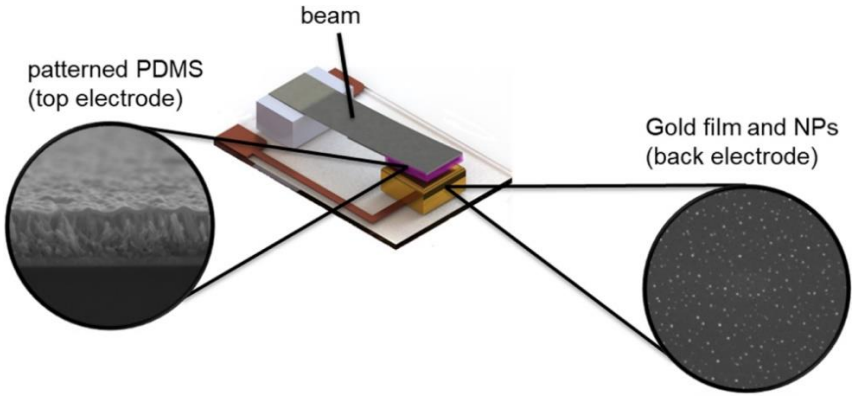

(a)

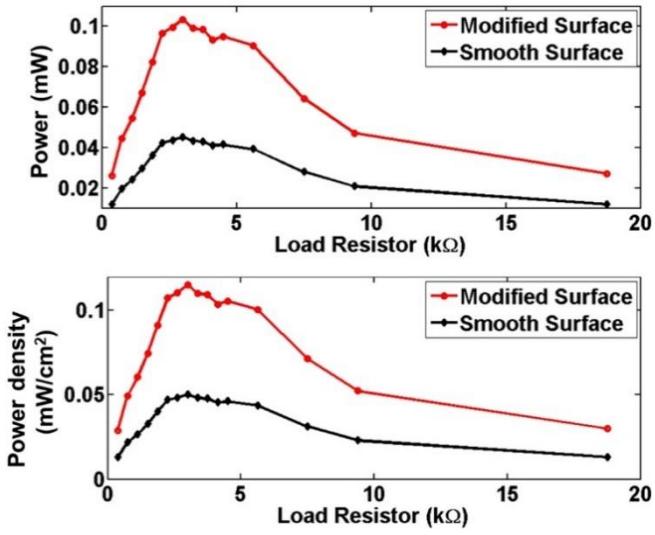

(b)

Figure 2.5 A cantilever-beam-based TEH of contact-separation mode with surface modifications studied by Nafari et al. [115]: (a) schematic diagram with SEM images of surface morphology (where NPs stands for nanoparticles) and (b) the comparisons of power output between modified (patterned) and smooth (unpatterned) surfaces. Reproduced with kind permission of IOP Publishing.

2.1.3.3. Modelling and Analysis of Mechanical Systems

There are only a few reports of the investigations of TEHs from the perspectives of structural dynamics. Dhakar et al. [117] experimentally studied a cantilever-based TEH of the contact-separation mode. The output performance was shown at different excitation levels and proof mass loadings and the design was demonstrated to have wide bandwidth characteristics. Helseth and Guo [118] designed a system which combined triboelectric and electromagnetic effects and used electromagnetic induction for energy harvesting and triboelectric effect for motion sensing. The low friction design eliminated the influence of the triboelectric signal detection on the electromagnetic induction. Ibrahim et al. [119] established a coupled electromechanical model for an impact TEH. Piecewise stiffness was used to model the impact interaction. Close agreement was found between the numerical and experimental results. It was observed that the surface charge density increased with the excitation level, which was regarded as the result of the growing penetration of the contact surfaces. Parametric study revealed that smaller gaps can result in larger bandwidths. They also studied a TEH-based smart knee implant [120]. The fabricated harvester was tested under a 1 Hz sinusoidal excitation which was regarded as an approximation of an axial tibiofemoral load profile from normal walking. The developed device can work as both an energy harvester and a load sensor owing to the proportional relationship between its RMS voltage and the applied load. Their analysis showed the feasibility of sensing the load several times a day using only the harvested power.

2.1.3.4. Applications

Broad applications of TEHs have been made owing to their competitive advantages. Some examples are given as follows. Wen et al. [121] fabricated a blow-driven TEH which worked as an active alcohol breath analyser. Its voltage output was proportional to the alcohol concentration regardless the blow speed. Good selectivity and anti-interference were also displayed by the fabricated device. Yeh et al. [122] presented a self-powered electrochemical recovery system which can collect Cu ions in wastewater to avoid pollutions. Taking advantage of the kinetic energy of water flows, a collection efficiency up to 80% was reached. The study indicated promising applications of TEHs in self-powered electrochemical systems. Uddin et al. [123] developed a self-powered active gas sensor which was used to detect acetylene via evaluating its output voltage. The sensor relied on a surface reaction between

acetylene and one of the triboelectric layers which also exhibited good hydrophobicity reducing the influence of humidity on sensing performance.

2.2. Vibro-Impact Systems in Energy Harvesting

Vibro-impact systems are usually characterized by repeated vibration and impact between the components in the systems. Vibro-impact appears in many engineering applications, such as hand-held percussion machines, pile-driving machines, periodic rubbing between the rotor blades and the stators in turbomachinery, braking systems in automobiles and cutting and grinding machines [124-127]. Vibro-impact systems have been studied extensively in different contexts. For example, Cao et al. [128] studied the bifurcations and penetrating rate of percussive drilling, while others have focused on suppressing the vibration of civil engineering structures by using SMAs (shape memory alloys) [129, 130]. Other studies have focused on the finite codimension bifurcation and coexisting attractors in forming machines [131, 132], the numerical and experimental bifurcation of a forced impacting beam [133, 134], the dynamic analysis of an impact force generator in a heat exchanger [135], and vibro-impact systems under random excitation [136, 137]. Interestingly, some systems purposely exploit the vibro-impact while others try to avoid it. For example, percussion and pile driving machines employ vibro-impact motion, while turbomachinery and braking system are designed to prevent in vibro-impact conditions. However, examples of vibro-impact systems can be found in almost all types of vibration-based energy harvesters.

2.2.1. Vibro-Impact Systems in Electromagnetic Energy Harvesters

The most common configuration of EEHs uses a tube-structure to house magnets of opposing polarity [138]. In the modelling of such systems, the impact between magnets is usually not considered since it only occurs at quite large base excitations. In a similar configuration, the magnets fixed at the two ends of the tube in a conventional levitation-based EEH [138] were replaced with springs and thus vibro-impact motion can happen, such as in the study presented by Haroun et al. [139] in which a magnet could do free-flight and impact with side springs and undertook the frictional resistance from the frame and effective power extraction at low frequencies was shown.

Nevertheless, some studies [140-144] have employed vibro-impact beam systems to enhance the harvesting efficiency of EEHs using frequency up-conversion and by broadening the

harvesting bandwidth. In these cases, magnets [140, 142] or coils [141, 143, 144] are mounted on the free end of a cantilever beam as well as on a stopper or another beam. The theoretical modelling of such vibro-impact system is mostly done by simplifying the continuous beam system into a corresponding discrete mass-spring-damper system and modelling a non-smooth impact into bilinear stiffness and damping, such as in Refs. [140-142]. Besides, mechanical impact has been used to combine with bistability in EEHs by Podder et al. [145]. Both of these two nonlinearities were shown to be able to broaden the harvesting bandwidth, and such broadening from the impact was even bigger than that from the bistability. The exploitation of bistability in vibration energy harvesting will be discussed in a later section.

2.2.2. Vibro-Impact Systems in Piezoelectric Energy Harvesters

Vibro-impact is often used in PEHs since impact improves harvesting efficiency through frequency up-conversion [146-149], which helps cope with the frequency incompatibility between the ambient vibration and the harvester. Impact is also capable of broadening the frequency span of effective energy harvesting [150, 151], which enables the harvester to work efficiently even when the frequency of the ambient vibration fluctuates in a range.

The vibro-impact in PEHs usually happens between flexible beams and relatively rigid stoppers or teeth. In one of the two scenarios, stoppers or teeth vibrate and trigger the oscillation of the beams [146], which are mostly cantilevers, such as the configuration shown in Figure 2.6 [152, 153], which has been successfully employed in buoy-based wave energy harvesting [146]. Alternatively, the beams oscillate and hit the stoppers [149]. Either way, the low-frequency ambient vibration can be up-converted to the higher frequency vibration of the beams, which then improves harvesting efficiency.

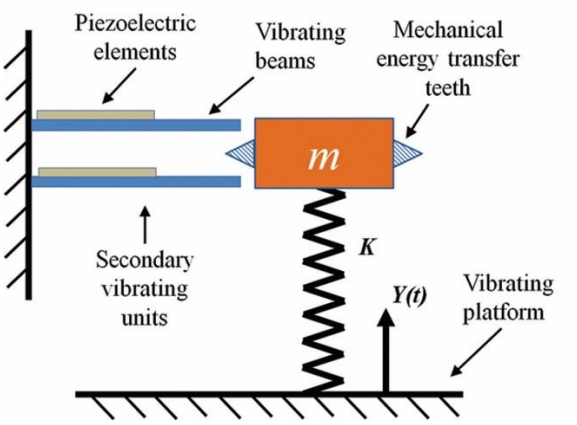

Figure 2.6 Schematic diagram of a two-stage frequency up-conversion configuration proposed by Rastegar et al. [152, 153]. Reproduced with kind permission of AIP Publishing.

In addition to the beam-stopper arrangement, vibro-impact between beams that have different natural frequencies and interacting mode shapes has been exploited as well. Dauksevicius et al. [154] reported a nonlinear frequency up-conversion PEH by leveraging vibro-impact interaction between two high-frequency piezoelectric beams and two low-frequency beams with commensurate natural frequencies in the 2:1 ratio. The developed model accommodating multiple mechanical contact pairs which were defined by nonlinear dissipative Hunt-Crossley contact force formulation. Hardening-type responses were shown in their results. Comparisons were made between their model and the conventional counterparts. Vijayan et al. [155] investigated energy harvesting from two coupled impacting beams. It was shown that the harvested power by the proposed system was sensitive to the thickness ratio of the beams and the clearance. Higher power was generated than the linear system, which was dependent on the dissimilarity in the mode shapes of the interacting close modes.

Different models have been used to describe impact motion. The coefficient of restitution [156, 157] is one of the most common models that has been used to describe the impact between concentrated masses, between concentrated mass and rigid walls or stoppers, etc. Piecewise stiffness or restoring force is often seen in modelling the impact between concentrated mass and massless spring-supported stoppers. Ai et al. [150] studied using non-smooth nonlinearities to achieve broadband energy harvesting. A SDOF model with a mechanical end-stop was considered. Impact was shown to be able to strongly modify the mechanical as well as electrical responses. Poincaré maps, bifurcation diagrams and phase spaces were used for analysing. Wu et al. [151] presented a nonlinear energy harvesting

circuit incorporated with synchronous mechanical switches. Two mechanical stoppers were used to confine the tip oscillation of a piezoelectric beam, and the interaction between them was represented by piecewise-linear stiffness. The added mechanical stoppers and the self-synchronized nonlinear energy extraction interface were shown to be able to achieve broadband energy harvesting. Hertz's contact theory and Hunt-Crossley model are both nonlinear models, and the latter can be regarded as an augmentation of the former with a nonlinear damper. They can be used to represent sphere-on-sphere and sphere-on-plane impacts and are formulated under the assumption that the collision is nearly perfectly elastic [158]. Fu and Liao [159] studied the mechanism of impact dissipation in impact-based PEHs. They considered the electromechanical model, Hertzian contact theory, and Hunt-Crossley model of impact dissipation as constitutive mechanisms and analysed the developed model in terms of impact force and energy distribution. Besides, an experimental method was proposed to validate the developed model and good agreement was shown.

2.2.3. Vibro-Impact Systems in Triboelectric Energy Harvesters

Among the four fundamental triboelectric energy harvesting modes, the vertical contact-separation mode and the in-plane contact-sliding mode are the two most commonly used modes. Generally, the vertical contact-separation mode relies on vibro-impact. The TEHs which work on the vertical contact-separation mode take simple structural forms, such as the most common experimental TEH systems [95, 160] which consist of two plates (assumed rigid) connected by springs as shown in Figure 2.4 in Section 2.1.3. A more complicated configuration is the triple-cantilever TEH [161, 162] which may have rich dynamic responses, but the corresponding theoretical model has not yet been studied. The contact-mode freestanding TEH [101, 163] seems to have higher working efficiency, and the relevant research shows some applications, such as quantitative measurements of vibration amplitude [163] and the portable power-supplying system [101].

Few studies can be found in investigating the effects of impact or vibro-impact motion on the performance of TEHs. Wen et al. [164] fabricated a TEH which featured a wavy film sandwiched by two flat plates. The wavy film acted as not only a triboelectric layer but also a spring. This special structure was capable of converting impact deformation of the wavy film into lateral sliding during the contact between the wavy film and the flat plates. The working principle was studied using the capacitor model and finite element simulation. Experiments on harvesting the wave energy were carried out using the fabricated device. Nelson et al.

[165] proposed a tuneable TEH that had a wide bandwidth at low frequencies. By adjusting the axial load, the stiffness of the system could be changed, which could allow vibro-impact motions to happen over wider frequency spans. Ibrahim et al. [119] investigated an impact vibration harvester with triboelectric transduction both experimentally and theoretically, and introduced a piece-wise stiffness to the system to enlarge the frequency bandwidth, and the relationship between the surface charge density and the vibration amplitude was revealed by experiments. In comparison, impact or vibro-impact motion should have a more profound influence on the performance of TEHs than both PEHs and EEHs. Not only both frequency up-conversion and broadband energy harvesting can be achieved, but also the enhancement of triboelectrification or triboelectric effect produced by impact will enable better performance, though the study of the latter is beyond the scope of this research.

2.3. Energy Harvesting with Multistability

Multistability, especially bistability, has been utilized in vibration energy harvesting to broaden the frequency range from which energy can be extracted, and to provide a high-energy orbit over a wide range of frequencies [166] — two features that are highly desirable in energy harvesting applications.

Bistable systems are well known for having a double-well potential energy curve which results in two distinct types of oscillation: low-energy intrawell and high-energy interwell oscillations, the latter of which has been found to be more efficient in energy harvesting applications [167]. Bistability, as a particular case of multistability, has been extensively studied in the context of symmetries, phase transitions, and hysteresis [168]. Numerous attractors can coexist for a fixed set of parameters of a bistable system. For instance, a small change in initial conditions can turn a steady-state intrawell oscillation into an interwell oscillation owing to their coexistence [169]. For such systems, basins of attraction are often investigated, such as in Refs. [170, 171].

Bistable energy harvesters can be categorized into three main different mechanisms according to their manifestations of bistability [167]: magnetic attraction bistability [172-174], magnetic repulsion bistability [175, 176], and mechanical bistability [177-179]. The former two mechanisms rely on a magnetic force while the latter depends on either a mechanical pre-load [177, 178] or material anisotropy [179].

2.3.1. Electromagnetic Energy Harvesting with Multistability

Utilization of multistability can also be found in EEHs, though it is often seen in PEHs. Cottone et al. [180] showed that, at an optimal excitation level, a bistable EEH can outperform its monostable counterpart by a 2.5 times wider bandwidth and higher outputs away from the natural resonance. Chiacchiari et al. [45] experimentally studied a bistable EEH under impulsive base excitation. The bistability was achieved through a buckled beam possessing both cubic nonlinear and negative linear stiffnesses. Effective energy conversion was shown in periodic cross-well oscillations, especially at low-level excitations. Pennisi et al. [181] investigated an EEH which was coupled to a nonlinear energy sink (NES, or a nonlinear vibration absorber). Bistability and tristability could be achieved by adjusting the arrangement of the magnets. The vibration energy was first absorbed by the NES and then converted into electricity by the coupled EEH. The former two studies utilized mechanical bistability while the last used magnetic bistability, and it seems that mechanical bistability is more preferable than magnetic bistability because EEHs depend on magnets due to their nature and the involvement of additional magnets can complicate both the magnetic field and simulation and maybe the performance as well.

2.3.2. Piezoelectric Energy Harvesting with Multistability

PEH is the most successful one that has been integrated with multistability, especially bistability, among these three vibration energy harvesting methodologies. Beams and plates have been used as the host structures and the former is more common. The schematic diagrams of the three main manifestations of bistability in PEHs, i.e., magnetic repulsion, magnetic attraction and mechanical buckling, are shown in Figure 2.7 [167]. Note that the cantilever beam in Figure 2.7(b) is a ferromagnetic elastic beam which can magnetically interact with the two fixed magnets. Alternatively, a third magnet can be attached at the free end of the cantilever beam and aligned to attract the fixed magnets in the magnetic attraction manifestation in Figure 2.7(b). In addition to these three manifestations of bistability, other means of realizing bistability can also be found, for example Litak et al. [182] studied the nonlinear vibrations of a mechanical resonator which had single- or double-well potential depending on the gravity force from the tip mass.

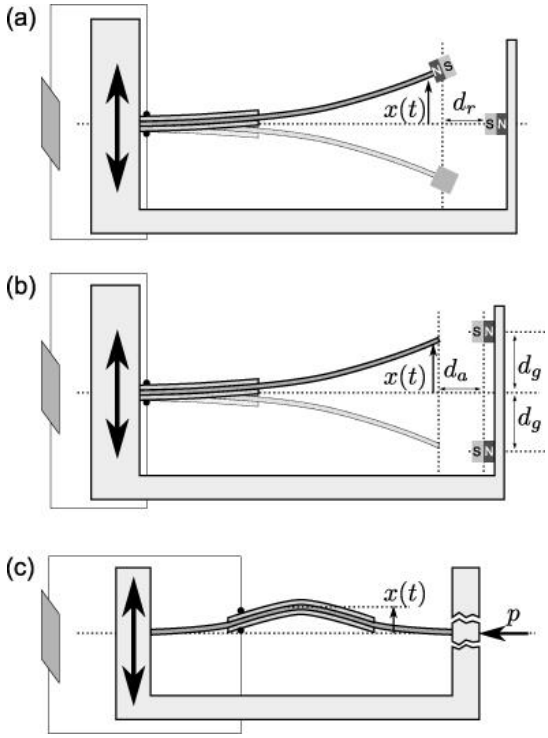

Figure 2.7 Schematic diagram of (a) bistable magnetic repulsion PEH, (b) magnetic attraction PEH and (c) mechanically buckled beam PEH; piezopatches are shown in light grey layers which sandwiches the beams; Parallelograms represent resistors. Produced by Harne et al. [167]. Reproduced with kind permission of IOP Publishing.

Adjustments on the configurations of bistable PEHs have been proposed by a number of researchers to enhance the performance. Leng et al. [183] replaced the stiff support of the fixed magnet in the common two-magnet bistable configuration with an elastic one, which enabled frequent bistable transition oscillations between two wells even when the system was under low-intensity random excitation. Wang and Liao [184] proposed to enhance the performance of a bistable PEH by connecting the harvester to the base via an elastic magnifier which was used to amplify the base vibration level, and their numerical simulations showed that the proposed architecture can outperform that of the configuration without an elastic magnifier. Lan and Qin [185] proposed the use of an additional small magnet in the common three-magnet bistable configuration to reduce the potential barrier between the two wells and facilitate the snap-through at small excitation levels. Wang et al. [186] combined the nonlinearity of cantilever-surface contact and magnetoelasticity and introduced a quadstable PEH. The cantilever-surface contact features advantages including minimal moving parts, high shock resistance and low frictional losses. Good performance of the PEH was shown under low intensity excitations and over a wide bandwidth.

The importance and benefits of studying nonlinear vibrations of multistable PEHs have been raised from many aspects as multistable PEHs are nonlinear systems and have rich nonlinear behaviours. Arrieta et al. [187] investigated a bistable PEH which was based on a composite plate. Rich nonlinear behaviours were found and were compared for their harvesting efficiency. Van Blarigan and Moehlis [188] showed that the presence of a chaotic attractor, which was a product of a period doubling cascade or a boundary crisis, could be a sufficient condition for predicting high power output. Harne and Wang [189] investigated the effects of superharmonic dynamics on bistable energy harvesting. It was shown that superharmonic spectra could yield a superior electrical power compared with the fundamental harmonic. Ibrahim et al. [190] studied the transition regime in bistable PEHs and showed the interesting combined hardening and softening responses that happened before and after the transition, and this transition regime was regarded as an optimal region for efficient conversion in terms of the bandwidth and electrical outputs.

In addition to the numerical and experimental studies, some approximate analytical methods have been used to investigate bistable harvesters, such as harmonic balance method [191], the method of multiple scales [192], and Melnikov's method [193]. By analysing the bifurcation and stability characteristics of the system, design and operation guidance can be provided. For example, the frequency span between a saddle-node and a period-doubling bifurcation might be used to approximate the bandwidth within which the harvester can achieve high-energy orbits and thus produce high energy outputs [194]. Besides, for bistable PEHs under the excitation of an impulse, Harne et al. [195] proposed a new analytical method for estimating both mechanical and electrical outputs, and both direct numerical simulation and experiments were used to validate the proposed method and excellent agreement was obtained. For randomly excited bistable PEHs, Zhang et al. [196] proposed a novel state-probability estimation method based on the theoretically derived probability density function of system energy. The approach was used to statistically classify the stationary probability of stochastic vibrations including interwell and intrawell oscillations. Their theoretical results were validated by both numerical and experimental results.

2.3.3. Triboelectric Energy Harvesting with Multistability

The application and study of bistability or multistability in triboelectric energy harvesting is only very recently reported by Nelson et al. [177], and the schematic diagram of the model that they proposed is given in Figure 2.8 which shows a triboelectric threshold shock sensor

composed by a mechanically buckled beam and a TEH of vertical contact-separation mode. The threshold of the sensor was tuneable via varying the compressive force (represented by P) applied axially on the buckled beam. A mathematical model, which can predict the behaviour of the shock sensor, was established to guide the design.

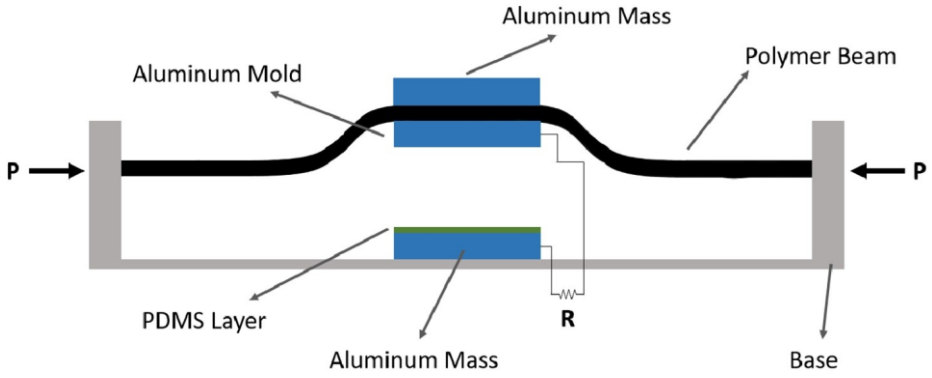

Figure 2.8 Schematic diagram of a bistable triboelectric threshold shock sensor proposed by Nelson et al. [177]. Reproduced with kind permission of Elsevier.

Owing to the special structures of TEHs, it seems that TEHs in vertical contact-separation mode are more suitable to be integrated with mechancial bistability achieved by buckled beams and plates, and though TEHs based on buckled plates have not been reported yet they are really promising. TEHs in sliding mode may be enhanced by magnetic bistability or multistability, which will investigated in a later Charpter.

2.4. Friction in Energy Harvesting

Friction dissipates energy, which is detrimental to vibration energy harvesting; yet friction is everywhere, and it can be found in all three types of vibration energy harvesters. Friction may have negative influence on the performances of both PEHs and EEHs, but is essential in TEHs for triboelectrification, especially TEHs in sliding mode. Nevertheless, few studies of the effect of friction on the performance of harvesters can be found.

In the context of EEH, many models are based on magnetic levitation, and the levitated magnet oscillates inside a tube or along a rod, in which case the oscillating magnet undertakes friction force. Green et al. [197] studied such a model. Three different friction models, namely Coulomb, hyperbolic tangent and LuGre, were used, and Coulomb damping model provided the best agreement with experimental results. It was also found that there was no interaction between the Duffing-type and Coulomb nonlinearities when the system

was under a Gaussian white noise excitation, which allowed the study of the effect of the former on the response of a system involving the latter.

Friction damping at connections or joints, though negligible in most cases, might be the only way that friction can have certain effects on the performance of PEHs when friction is not actively involved. Nevertheless, studies of the effect of friction can be found in applications of PEHs of friction-induced vibration. Helseth [198] explored both PEH and TEH from the stick-slip motion between two strips of the commercial hook-loop system. In the stick stage, there was an accumulation of elastic energy with little associated motion, whereas in the slip stage the accumulated elastic energy was released into kinetic energy. It was found that the stick-slip motion can be classified as a coloured noise excitation scheme. The piezoelectric coupling coefficient was found to have a nearly flat frequency response while that of the triboelectric varied in a non-systematic manner. Wang et al. [199] studied PEH from the friction-induced vibration in a pad-on-disc system. Both the tangential and vertical vibrations were considered for energy harvesting. The effects of the driving speed and the normal load on both the vibration behaviours and the harvesting performance were investigated. Besides, a 2-DOF model was proposed for further qualitative study.

Friction plays completely different roles in TEHs and is important in triboelectrification. However, the effects of friction on TEHs are more complicated. Material surface modifications can enlarge the contact or friction area [200] between triboelectric materials on micro- or nano-scale and enhance the electrical output of TEHs, but whether the friction is increased in macro-scale after the surface modification has not been investigated. Besides, on the one hand, the increase of friction has been found benefiting the performance of TEHs in experiments [201], on the other hand, it has been shown that the durability of the triboelectric materials can be a problem when friction is increased up to certain degrees [202]. In addition, some specific applications of TEHs try to lower friction to some extent to facilitate smooth rotation [203].

2.5. Research Gaps and Issues

In this chapter, a comprehensive review of vibration energy harvesting literature related to this research is presented with particular focus on the involvement and investigation of non-smooth systems comprising vibro-impact and friction, multistable systems (especially bistability), and other nonlinear systems. It provides good knowledge of the vibration energy

harvesting mechanisms, techniques, achievements, and applications. Extensive studies on both EEH and PEH have bridged most research gaps and sorted out most of the corresponding issues. However, in view of the young age of TEH, the following research gaps and issues still exist and need to be addressed.

Investigations of the vibro-impact dynamics of TEHs of both vertical contact-separation and contact freestanding triboelectric-layer modes are necessary to understand and optimize the devices from the perspectives of structural dynamics, which are yet to be reported in literature. Such a study is particularly essential to the TEHs of contact freestanding triboelectric-layer mode because this unique mode consists of three oscillating masses or layers and involves much more complicated vibro-impact dynamics. Rich nonlinear dynamic behaviours may exist and will shape the electrical output performance of the harvesters. This work will try to bridge such research gaps by studying the nonlinear dynamics of a three-degree-of-freedom vibro-impact oscillator which is coupled to a TEH of contact freestanding triboelectric-layer mode.

More advanced modelling of the dynamics of the host structures is important, especially when the mechanical and electrical systems are coupled. In the study of vibro-impact based TEHs, the modelling of impact can be an issue. The use of piecewise stiffness modelling needs to know the impact or contact stiffnesses of the triboelectric layers (such as PTFE and PDMS layers). However, these layers are usually quite thin and the correct measurement or identification of their impact or contact stiffnesses can be really difficult. Good estimation of the contact stiffness is also required in the use of both Hertzian and Hunt-Crossley models which, besides, are established by assuming the impact is nearly perfectly elastic. Therefore, the coefficient of restitution law or Newton's law of restitution might be a better choice. Nevertheless, a fixed coefficient of restitution may not be sufficient to describe impacts. Hence, a more advanced impact model, such as a velocity-dependent coefficient of restitution law, is needed. In addition, more advanced structural modelling, such as continuous beam models, is essential as well when being used to simulate the performance of a prototype. Numerical algorithm used in simulation can be another issue since TEH systems are non-smooth in terms of their mechanical systems and are likely stiff regarding to the ordinary differential equations governing their electrical systems. Thus, more sophisticated algorithms should be developed. Furthermore, experimental studies have been conducted a lot in TEH but almost all of them are done from the perspectives of materials and electronics.

Experimental validations of electromechanical coupled models from the aspects of structural dynamics are really rare and need to be carried out for TEHs of different working modes.

A study of the sliding mode TEH from the prospects of structural dynamics is still missing. Friction should be considered in such a study and its effects investigated. It is known that friction is important in triboelectrification, but how friction affects the behaviour of the host structure and thus the performance of a sliding mode TEH is still an open research topic. Given the beneficial employment of magnetic multistability in both EEHs and PEHs, the involvement of magnetic multistability in sliding mode TEHs is promising. Broadband energy harvesting and frequency up-conversion are expected. However, the multistable system of a sliding mode TEH is also non-conservative owing to the nature of friction, and the analysis of the multistability of a non-conservative system or a system involving non-conservative forces is very rare or yet reported in literature. Therefore, new methods should be developed to tackle relevant problems. In addition, a system involving both non-smoothness and multistability is usually sensitive to initial conditions, which leads to the coexistence of different attractors. Thus, the effect of initial conditions on the performance of TEHs is also worth studying.

The last research gap that this work will try to fill is the investigation of the effects of electrical properties of TEHs on the structural responses. The mechanical and electrical systems of TEHs can be coupled via electrostatic force, though sometimes this coupling can be weak. Owing to the electromechanical coupling, the mechanical system can affect the electrical system (which can be studied using structural dynamics) and vice versa. However, an analysis of the influence of the electrical properties on the behaviour of the mechanical system in TEHs is still absent. The resistive shunt damping effect found in PEHs may also exist in TEHs. By investigating such issues, harvesters can be tuned to enhance the output performance through controlling their electrical properties.

Chapter 3

Fundamentals of Triboelectric Energy Harvesting

3.1. Introduction

By reading Chapter 2, one can get an overall view of the research status of TEHs. However, the fundamental working mechanisms of TEHs are to be unveiled to provide a better understanding of both the literature review and the research work that will be shown in later chapters. In this chapter, the triboelectric effect or triboelectrification is first explained and then the common triboelectric materials are ranked in a triboelectric series in Section 3.2. Then, the four fundamental working modes of TEHs are illustrated in Section 3.3. Finally, the fundamental theories related to TEHs of basic working modes are explained and the TEH of the vertical contact-separation mode is taken as an example in deriving the governing equation of the electrical system or the V-Q-x relationship.

3.2. Triboelectric Effect and Materials

Triboelectric effect has been known for a very long time, and the first report of it seems to be Plato's Timaeus in which the phenomenon that rubbed amber is able to attract particles was reported [204]. However, up till today, the mechanism that triboelectrification is based on is still not fully unveiled. Nevertheless, a general belief is that a kind of chemical bond will be formed between some parts of the surfaces of two different materials after their contact (the process is called adhesion), and a charge exchange will happen due to the electrochemical potential difference between two materials and the exchanged charges can be electrons or probably ions or molecules. Once the contact between two materials is broken, some bonds tend to keep extra electrons while others tend to give them away, possibly remaining triboelectric charges on surfaces [94].

On the one hand, triboelectrification is really useful to some industries. The control of the triboelectrification of small (around 10 μm diameter) polymer toner particles is critical to the electrophotographic copying and printing process [204]. Electrostatic separators depend on triboelectrification to separate minerals and coals [205]. And powder coating with charged paint droplets is another example [206]. On the other hand, triboelectrification can be extremely harmful due to the substantial charge build-up on contact surfaces between materials and the potential static discharge, especially when insulating materials (which have strong capabilities in capturing and maintaining the transferred charges) are involved [94]. The resultant triboelectric effect in rocket launching and aircraft flying owing to the air friction can potentially interfere with the function of sensitive electronic equipment onboard and disrupt the signal for the flight termination system [207]. Besides, electrostatic charges can be a threat to safety since it can cause explosion, such as supertanker and flour mill explosions [204], and ignite flammable vapours [94].

It is not until recent years that triboelectric effect is utilized in converting mechanical energy into electricity as a new fashion of vibration energy harvesting, and a large section of the study of TEHs has been conducted from the perspectives of materials, though almost all materials can have triboelectric effect. Undoubtedly, different materials have different extents of capability of gaining or losing electrons. A triboelectric series is a material list which ranks different materials according to their abilities to gain (negative) or lose (positive) electron, and a triboelectric series ranked for some common materials [208] is given in Table 3.1. The further the two materials sit from each other, the stronger the triboelectrification between them.

In addition to selecting materials from the triboelectric series, material surface morphology is often used to create certain surface patterns to increase the contact area in micro- or nano-scale and to possibly enhance the triboelectrification. Material surface functionalization can be used to change the surface potential and thus to enhance the triboelectric effect [94].

Table 3.1 A triboelectric series for some common materials [208].

Positive (+)	Glass
	Mica
	Nylon
	Rock salt (NaCI)
	Wool
	Fur
	Silica
	Silk
	Aluminium
	Poly (vinyl alcohol) (PVA)
	Poly (vinyl acetate) (PVAc)
	Paper
Neutral	Cotton
	Steel
	Wood
	Amber
	Poly (methyl methacrylate) (PMMA)
	Copper
	Silver
	Gold
	Poly (ethylene terephthalate) (Mylar)
	Epoxy resin
	Natural rubber
	Polyacrylonitrile (PAN)
	Poly (bisphenol A carbonate) (Lexan, PC)
	Poly (vinylidene chloride) (Saran)
	Polystyrene (PS)
	Polyethylene (PE)
	Polypropylene (PP)
	Poly (vinyl chloride) (PVC)
Negative (-)	Polytetrafluoroethylene (Teflon, PTFE)

3.3. Fundamental Working Modes

Four fundamental working modes of TEHs have been identified according to their structural designs of electrodes or moving manners of triboelectric layers [94, 209], and their typical configurations are shown in Figure 3.1 [94].

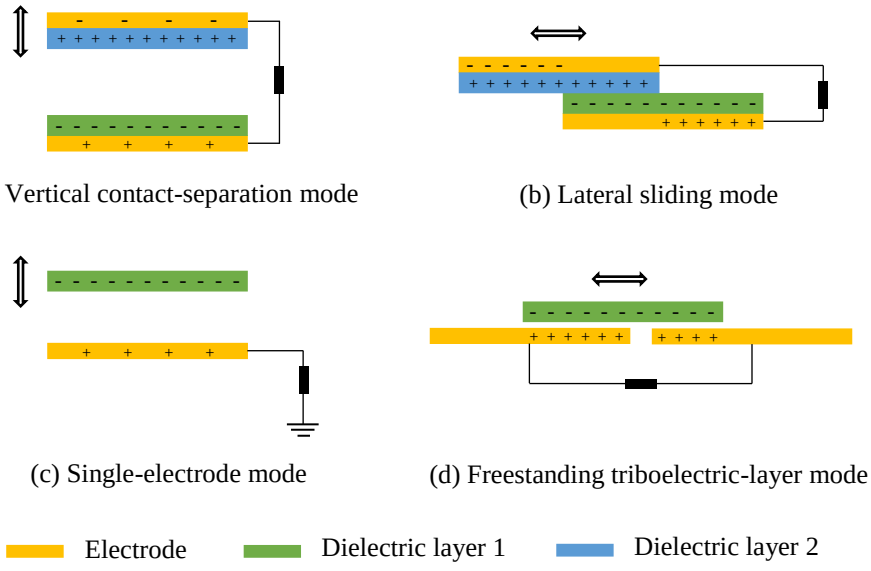

Figure 3.1 Four fundamental working modes of TEHs [94].

The vertical contact-separation mode TEH, shown in Figure 3.1(a), consists of two pairs of the dielectric-electrode combination, and the dielectric layers are of opposite triboelectric polarities. The electrodes are connected via an external load. The top and bottom dielectric layers will get oppositely charged after their contact, and opposite charges against the polarity of the charges on each dielectric layer will be induced on each attached electrode. A mechanical separation between the two pairs will result in a potential difference between two electrodes, and an electron flow will be formed and a reverse current flow induced as the separation distance varies.

The configuration of the sliding mode TEH, shown in Figure 3.1(b), is similar to that of the vertical contact-separation mode TEH given in Figure 3.1(a), and the only difference is that one of the two pairs of the dielectric-electrode combination in the sliding mode TEH laterally slides on the other pair instead of doing repeated contact and separation. With the variation of the overlapped area between the top and bottom dielectric layers, the potential difference

across the two electrodes will change accordingly, which leads to the variation of electron and current flows.

As shown in Figure 3.1(c), the single-electrode mode TEH only has one electrode which is connected to the ground. As a charged dielectric layer moves towards and away from the electrode, the amount of charges induced on the electrode will vary, which leads to the variation of potential difference and electron exchange between the electrode and ground, and an electron flow will be induced to balance the potential difference.

The configuration of the freestanding triboelectric-layer mode TEH is a bit unique as shown in Figure 3.1(d). It is similar to the lateral sliding mode but the arrangement of the two electrodes involved is different. With the movement of the dielectric layer above the two electrodes, different overlapped areas with the dielectric layer are shared by electrodes, which results in different amounts of charges on two electrodes and thus a potential difference that drives electron to exchange between electrodes.

3.4. Fundamental Theories

The equation that governs the electrical system of TEHs is called the V-Q-x relationship [107], where V and Q are the voltage and the amount of transferred charges between electrodes, respectively, and x is the separation distance between triboelectric layers. The V-Q-x relationships of the four fundamental working modes have been established [94, 106-108], and their derivations are similar. Therefore, only the derivation of the V - Q - x relationship of a vertical contact-separation mode TEH will be given here.

The vertical contact-separation mode TEHs can be further categorized into two groups: dielectric-to-dielectric and conductor-to-dielectric types. Their schematic diagrams are shown in Figure 3.2 [106], where σ is the tribo-charge surface density and is a fixed parameter based on the assumption that tribo-charges uniformly distribute on the surfaces of dielectric layers with negligible decay and edge effect [94]; d_1 and d_2 are the thicknesses of the dielectric layers. Note that the amount of transferred charges between electrodes, i.e., Q, equals the instantaneous amount of charges on each electrode. The value of the tribo-charge surface density can be measured by using an atomic force microscope (AFM) in which the AFM tip is coated by Pt and scans over a Parylene surface with a bias, and then the tribo-charge surface density can be characterized by a scanning Kelvin potential microscopy (SKPM) [9].

Please note that, due to the limitation of the experimental conditions and also the knowledge of physics, the tribo-charge surface densities used in this research are either assumed values according to the current available literature (in Chapters 4, 6 and 7) or identified values by using the method of least squares (in Chapter 5).

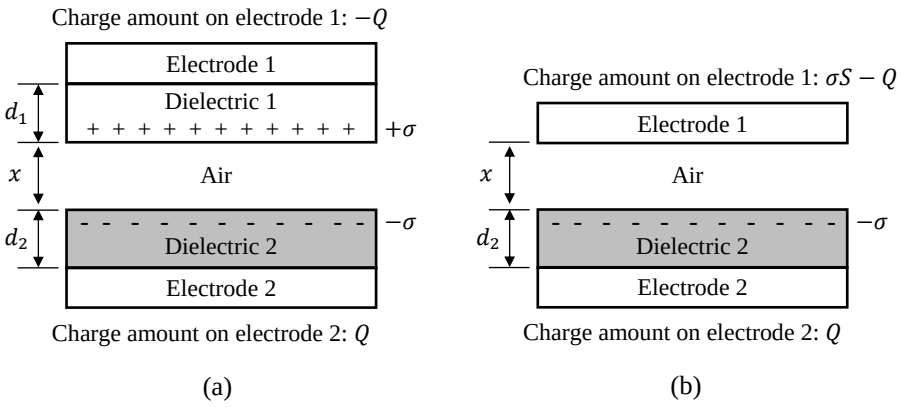

Figure 3.2 Schematic diagrams of vertical contact-separation mode TEHs of (a) dielectric-to-dielectric type and (b) conductor-to-dielectric type [106].

Their V-Q-x relationships can be derived based on electrodynamics. It is assumed that the charges on the metal electrodes uniformly distribute on their inner surfaces (which are surfaces in contact with the dielectric layers) and the edge effect is negligible [94]. According to Gauss's law, the electric fields inside dielectric 1 and 2 and the air gap can be given by [106]

$$E_1 = -\frac{Q}{S\varepsilon_0\varepsilon_{\mathrm{r1}}} \tag{3.1}$$

$$E_2 = -\frac{Q}{S\varepsilon_0\varepsilon_{\mathrm{r2}}} \tag{3.2}$$

$$E_{\mathrm{a}} = \frac{-\frac{Q}{S} + \sigma}{\varepsilon_0} \tag{3.3}$$

where S is the area of the electrode, ε_0 is the vacuum permittivity, $\varepsilon_{\mathrm{r1}}$ and $\varepsilon_{\mathrm{r2}}$ are relative permittivities of the dielectric layers. Thus the voltage between the electrodes can be expressed as [106]

$$V = E_1 d_1 + E_2 d_2 + E_{\mathrm{a}} x \tag{3.4}$$

By combining Eqs. (3.1) to (3.4), one can obtain the V-Q-x relationship of the model of the dielectric-to-dielectric type shown in Figure 3.2(a) as

$$V = -\frac{Q}{S\varepsilon_0}\left(\frac{d_1}{\varepsilon_{\mathrm{r}1}} + \frac{d_2}{\varepsilon_{\mathrm{r}2}} + x\right) + \frac{\sigma x}{\varepsilon_0} \tag{3.5}$$

In the model shown in Figure 3.2(b), the top electrode works as both the top triboelectric layer and electrode. Therefore, two parts of charges, i.e., triboelectric charges (σS) and transferred charges ($-Q$), result in a total amount of charges of ($\sigma S - Q$) on the top electrode. Similarly, the V-Q-x relationship of the model of the conductor-to-dielectric type shown in Figure 3.2(b) can be derived as

$$V = -\frac{Q}{S\varepsilon_0}\left(\frac{d_2}{\varepsilon_{\mathrm{r}2}} + x\right) + \frac{\sigma x}{\varepsilon_0} \tag{3.6}$$

Note that Eq. (3.6) can also be obtained by setting d_1 in Eq. (3.5) to zero. Here, a parameter named the effective thickness constant d_0 can be defined as $d_1/\varepsilon_{\mathrm{r}1}$+$d_2/\varepsilon_{\mathrm{r}2}$ for the dielectric-to-dielectric type and $d_2/\varepsilon_{\mathrm{r}2}$ for the conductor-to-dielectric type. Therefore, the V-Q-x relationships of both types can be given by

$$V = -\frac{Q}{S\varepsilon_0}(d_0 + x) + \frac{\sigma x}{\varepsilon_0} \tag{3.7}$$

When a TEH is connected to an external load resistance R, by using Ohm's law, Eq. (3.7) can be rewritten as

$$R\frac{\mathrm{d}Q}{\mathrm{d}t} = -\frac{Q}{S\varepsilon_0}(d_0 + x) + \frac{\sigma x}{\varepsilon_0} \tag{3.8}$$

The above equation and its variants for governing TEHs of other working modes will be used in the following chapters.

Chapter 4

Nonlinear Dynamics and Triboelectric Energy Harvesting from a Three-Degree-of-Freedom Vibro-Impact Oscillator

4.1. Introduction

Complex vibro-impact dynamics can exist during the function of a TEH of contact freestanding triboelectric-layer mode owing to the unique configuration of this triboelectric working mode, i.e., three masses can be involved in the vibro-impact motion and each mass can impact with its neighbour(s). Since the electrical output is dependent on the mechanical responses of the system, studying the vibro-impact dynamics of the mechanical system plays an important role in obtaining a better understanding of the working mechanisms and optimizing the harvester from the perspectives of structural dynamics, but such a study is still missing in the literature.

In this chapter, a TEH based on a three-degree-of-freedom vibro-impact oscillator is presented. Both the mechanical model of the oscillator and the electrical model of the oscillator-based TEH are established. A circuit simulator, which takes the mechanical responses as inputs and outputs the electrical responses of the harvester, is established using Simulink. The mechanical response and its effect on the electrical output are considered for various mass ratios and mass spacings. The effect of chatter on the output performance of the harvester is exploited.

The rest of this chapter is structured as follows: Section 4.2. presents the mechanical model and formulates the dynamical equations. The conservation of momentum and the coefficient of restitution are used to calculate the just-after-impact velocities. The contact forces during sticking motion are derived and applied to prevent interpenetration and keep the equilibrium of forces. Section 4.3. gives the theoretical electrical model of the oscillator-based triboelectric generator and shows the Simulink simulator. Then, Section 4.4. illustrates the

study of the impact characteristics, the effects of initial mass spacing, mass ratio, and the use of chatter, respectively. Section 4.5 presents the conclusions that can be drawn in this study.

This chapter is based on the following paper published by the author of this thesis and his supervisors:

Y. Fu, H. Ouyang, R.B. Davis, Nonlinear dynamics and triboelectric energy harvesting from a three-degree-of-freedom vibro-impact oscillator, Nonlinear Dynamics 92 (2018) 1985-2004.

4.2. Mechanical Model and Dynamic Equations

The configuration of the three-degree-of-freedom vibro-impact system representing the dynamic elements of a TEH is shown in Figure 4.1. This model could be used to approximate a physical system in which three beams or flat plates are stacked. The three masses are initially separated by two gaps–δ_1 between m_1 and m_2, and δ_2 between m_2 and m_3. The masses are connected to the sinusoidally-driven base via springs and dampers.

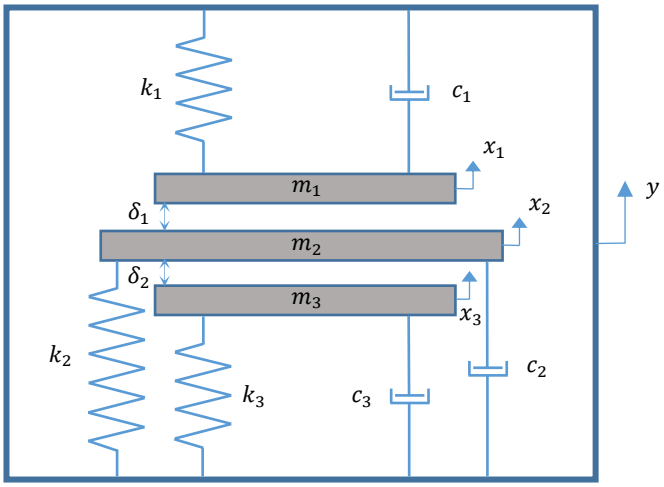

Figure 4.1 The three-degree-of-freedom vibro-impact system.

The equations of motion away from any two consecutive impacts of the system are given as

$$m_i x_i'' + c_i(x_i' - y') + k_i(x_i - y) = 0, (i = 1, 2, 3) \tag{4.1}$$

where $y = A\sin(\omega t)$, and the prime denotes a derivative with respect to time, t. The separation distances, between m_1 and m_2, and between m_2 and m_3 are represented by d_1 and d_2, respectively. These distances are given by

$$d_1 = \delta_1 - (x_2 - x_1),\ d_2 = \delta_2 - (x_3 - x_2) \tag{4.2}$$

Now let $\tau = \frac{t}{t_c}$, $X_1 = \frac{x_1}{x_c}$, $X_2 = \frac{x_2}{x_c}$, $X_3 = \frac{x_3}{x_c}$, $t_c = \sqrt{\frac{m_1}{k_1}}$, and $x_c = \delta_1$. The non-dimensional equations are then

$$\ddot{X}_1 + 2\zeta_1 \dot{X}_1 + X_1 = 2\zeta_1 \frac{A\Omega}{\delta_1}\cos(\Omega\tau) + \frac{A}{\delta_1}\sin(\Omega\tau) \tag{4.3}$$

$$\ddot{X}_2 + 2\zeta_2 \frac{\Omega_2}{\Omega_1}\dot{X}_2 + \frac{\Omega_2^2}{\Omega_1^2}X_2 = 2\zeta_2 \frac{\Omega_2}{\Omega_1}\frac{A\Omega}{\delta_1}\cos(\Omega\tau) + \frac{\Omega_2^2}{\Omega_1^2}\frac{A}{\delta_1}\sin(\Omega\tau) \tag{4.4}$$

$$\ddot{X}_3 + 2\zeta_3 \frac{\Omega_3}{\Omega_1}\dot{X}_3 + \frac{\Omega_3^2}{\Omega_1^2}X_3 = 2\zeta_3 \frac{\Omega_3}{\Omega_1}\frac{A\Omega}{\delta_1}\cos(\Omega\tau) + \frac{\Omega_3^2}{\Omega_1^2}\frac{A}{\delta_1}\sin(\Omega\tau) \tag{4.5}$$

where $\zeta_i = \frac{c_i}{2\sqrt{m_i k_i}}$, $\Omega_i = \sqrt{\frac{k_i}{m_i}}$ $(i = 1, 2, 3)$ and $\Omega = \frac{\omega}{\Omega_1}$. The over-dot denotes a derivative with respect to τ, and the separation distances become

$$D_1 = 1 - (X_2 - X_1),\ D_2 = \frac{\delta_2}{\delta_1} - (X_3 - X_2) \tag{4.6}$$

When impact occurs, i.e. $D_1 = 0$ and/or $D_2 = 0$, by employing the principle of conservation of momentum and the coefficient of restitution, one can get the velocities just after the impact as

$$\dot{X}_{p+} = \frac{m_p - \mu m_q}{m_p + m_q}\dot{X}_{p-} + \frac{m_q(1+\mu)}{m_p + m_q}\dot{X}_{q-} \tag{4.7}$$

$$\dot{X}_{q+} = \frac{m_p(1+\mu)}{m_p + m_q}\dot{X}_{p-} + \frac{m_q - \mu m_p}{m_p + m_q}\dot{X}_{q-} \tag{4.8}$$

where μ is the coefficient of restitution, and the subscript '-' represents the state just before impact while '+' represents the state just after impact. If impact takes place between m_1 and m_2, then $m_p = m_1$, $m_q = m_2$. If it occurs between m_2 and m_3, then $m_p = m_2$, $m_q = m_3$. If m_1 and m_2 are stuck together and impact occurs with m_3, then $m_p = m_1 + m_2$, $m_q = m_3$. Finally, if m_1 impacts with m_2 and m_3 joined together, then $m_p = m_1$, $m_q = m_2 + m_3$.

Sticking motion between any two adjacent masses can happen since the impact is assumed to be partially elastic. During sticking, contact force must maintain the dynamic equilibrium and prevent interpenetration between two sticking masses. Let N_{12} and N_{23} represent the contact

forces, between m_1 and m_2, and between m_2 and m_3, respectively. Then the sticking conditions between m_1 and m_2 are $D_1 = 0, \dot{X}_1 = \dot{X}_2$ and $N_{12} > 0$ while those between m_2 and m_3 are $D_2 = 0, \dot{X}_2 = \dot{X}_3$ and $N_{23} > 0$, and the expressions of the contact forces are given as

$$N_{12} = \frac{1}{2}[2\left(\zeta_2 \frac{\Omega_2}{\Omega_1} - \zeta_1\right)\frac{A\Omega}{\delta_1}\cos(\Omega\tau) + \left(\frac{\Omega_2^2}{\Omega_1^2} - 1\right)\frac{A}{\delta_1}\sin(\Omega\tau) + 2\zeta_1\dot{X}_1 - 2\zeta_2\frac{\Omega_2}{\Omega_1}\dot{X}_2 + X_1 - \frac{\Omega_2^2}{\Omega_1^2}X_2] \tag{4.9}$$

$$N_{23} = \frac{1}{2}[2\left(\zeta_3 \frac{\Omega_3}{\Omega_1} - \zeta_2 \frac{\Omega_2}{\Omega_1}\right)\frac{A\Omega}{\delta_1}\cos(\Omega\tau) + \left(\frac{\Omega_3^2}{\Omega_1^2} - \frac{\Omega_2^2}{\Omega_1^2}\right)\frac{A}{\delta_1}\sin(\Omega\tau) + 2\zeta_2\frac{\Omega_2}{\Omega_1}\dot{X}_2 - 2\zeta_3\frac{\Omega_3}{\Omega_1}\dot{X}_3 + \frac{\Omega_2^2}{\Omega_1^2}X_2 - \frac{\Omega_3^2}{\Omega_1^2}X_3] \tag{4.10}$$

4.3. Theoretical Model of Triboelectric Generator and the Simulink Simulator

4.3.1. Theoretical Model of the Oscillator-Based Triboelectric Generator

To simulate the harvester's electrical output and assess its performance, the theoretical model of the triboelectric energy harvester based on the three-degree-of-freedom vibro-impact oscillator is established. The middle metal layer (aluminium layer) is attached to the middle mass m_2 and is assumed to have negligible mass. This layer is regarded as a freestanding layer [94, 210], which works only as a charge inductor. This kind of triboelectric generator is called the contact-mode freestanding triboelectric generator [9, 94, 210, 211].

The working principle of the vertical contact-separation triboelectric generator involves a combination of contact electrification and electrostatic induction [9, 94, 211]. The charge transfer process is shown in Figure 4.2. When saturation is reached, the amounts of charges on both the dielectric (PTFE films) and freestanding metal layers will become stable and stay unchanged (with negligible decay). When the freestanding metal layer is in contact with the top dielectric, charges are balanced between the freestanding metal layer and the top dielectric and electrode. Meanwhile, a balance is reached between the bottom dielectric and

electrode, as shown in Figure 4.2(a). When the freestanding metal layer moves downwards and is closer to the bottom dielectric, some negative charges are induced on the bottom electrode by the freestanding metal layer, and same amount of positive charges appear on the top electrode. Electrons flow from the top electrode to the bottom electrode, which induces a reverse current flow, as shown in Figure 4.2(b). Then, the freestanding metal layer is in contact with the bottom dielectric as it moves downwards as shown in Figure 4.2(c) in which the situation is similar to Figure 4.2(a). Hereafter, the freestanding metal layer moves upwards and a current, which flows from the top electrode to the bottom electrode, will be induced as shown in Figure 4.2(d). Finally, the middle metal layer comes into contact with the top dielectric again and the cycle begins anew.

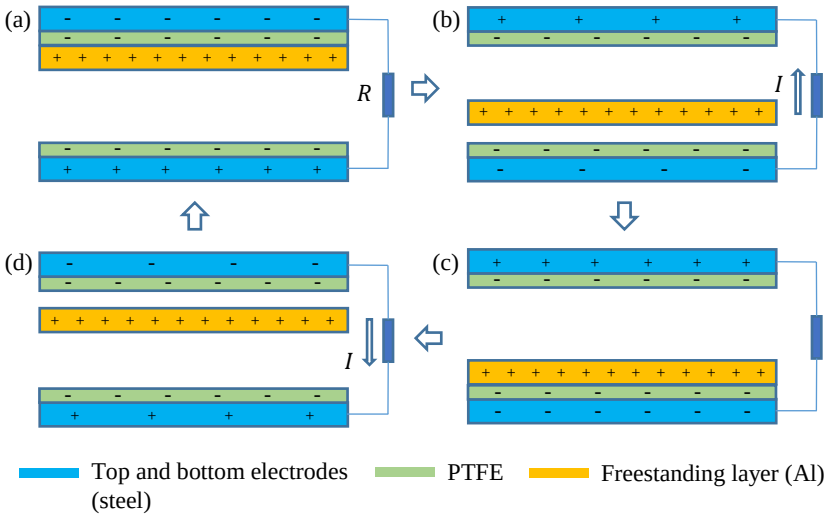

Figure 4.2 The charge transfer process of the oscillator-based triboelectric generator [94].

The model equation of the triboelectric generator [94, 106, 108, 109, 210] can be given as

$$V = -\frac{1}{C}Q + V_{\text{oc}} \tag{4.11}$$

where V is the electric potential difference between electrodes, C is the equivalent capacitance, Q is the amount of transferred charges between electrodes, and V_{oc} is the open-circuit voltage. The equivalent capacitance and the open-circuit voltage are given as [108, 210]

$$C = \frac{\varepsilon_0 S}{d_0 + D_1 + D_2} \tag{4.12}$$

$$V_{oc} = \frac{2\sigma D_2}{\varepsilon_0} \tag{4.13}$$

where ε_0 is the vacuum permittivity, S is the contact area, σ is the tribo-charge surface density; and $d_0 = \frac{d_1}{\varepsilon_{r1}} + \frac{d_2}{\varepsilon_{r2}}$, where d_1 and d_2 are the thicknesses of the top dielectric and the bottom dielectric, respectively, and ε_{r1} and ε_{r2} are relative permittivities of the materials of the top and bottom dielectric layers, respectively (the two dielectric layers are both assumed to be PTFE films with relative permittivities of $\varepsilon_{r1} = \varepsilon_{r2} = 2.0$). D_1 and D_2 are the separation distances between the top dielectric and the middle metal layer, and between the middle metal layer and the bottom dielectric, respectively. Assumed values for the physical parameters are $S = 0.01\ \text{m}^2$, $\sigma = 15\ \mu\text{C/m}^2$ and $d_1 = d_2 = 0.1 \times 10^{-3}\ \text{m}$. By combining Eqs. (4.11) to (4.13), one can obtain a charge transfer equation similar to the one presented as Eq. (9) in Ref. [111]. This expression has been validated by experiment [111], providing a degree of confidence in the present modelling approach.

4.3.2. The Simulink Simulator

The equivalent circuit model [94, 108, 109] for the triboelectric generator can be modelled by using the equivalent capacitance and the open-circuit voltage to represent the electrical properties of the triboelectric generator. Thus, the circuit of a triboelectric generator with a load resistance R is given in Figure 4.3. Note that it would be a short-circuit when the load resistance is zero and an open-circuit when the load resistance is infinite, and there exists an optimum load resistance at where the power output of the harvester reaches its maximum.

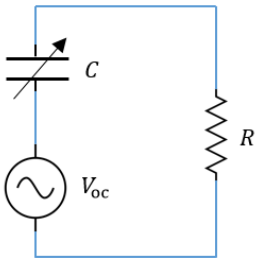

Figure 4.3 The configuration of the equivalent circuit model.

By using Simulink software package, the output performance of the oscillator-based triboelectric generator can be simulated and analysed conveniently. The Simulink model of the equivalent circuit is shown in Figure 4.4, in which the input signals, i.e. the variable

capacitor and the controlled voltage source, are defined by Eqs. (4.12) and (4.13). These are combined with the dynamic responses, i.e. the separations D_1 and D_2, of the three-degree-of-freedom vibro-impact oscillator to calculate the dynamics current and voltage across the resistor.

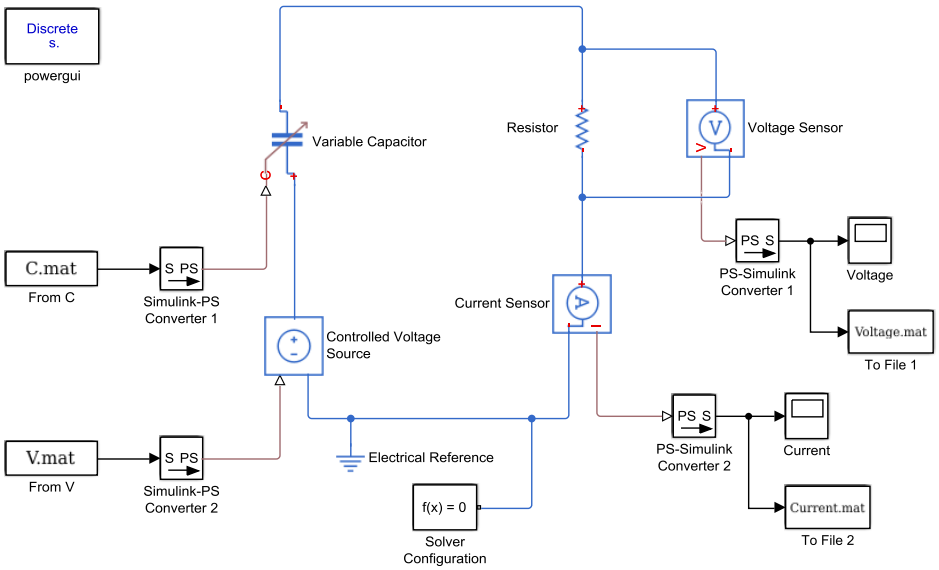

Figure 4.4 The Simulink simulator of the equivalent circuit.

To assess the performance of the oscillator-based triboelectric energy harvester, the average output power per forcing cycle is introduced:

$$P_{\mathrm{a}} = \frac{R \int_0^{N\,T} I^2(t)\,\mathrm{d}t}{N\,T} \tag{4.14}$$

where R is the resistance used in circuit and taken to be $R = 100$ kOhm, T is the dimensional excitation period, N is the number of dimensional excitation periods, and $I(t)$ is the current across the resistor.

4.4. Numerical Simulation

4.4.1. Impact Characteristics

The mass distribution of the three-degree-of-freedom vibro-impact system influences the way in which the three masses interact with each other. To determine designs that work best for energy harvesting, four configurations are considered: two symmetric distributions, (1) $m_1 =$

$m_3 < m_2$ and (2) $m_1 = m_3 > m_2$, and two asymmetric distributions, (3) $m_1 > m_2 > m_3$ and (4) $m_1 < m_2 < m_3$. The values of the parameters used are $k = 120\ \mathrm{N/m}$, $\Omega = 0.70$, $A = 0.08\ \mathrm{m}$, $\mu = 0.60$, $\delta_1 = \delta_2 = 20\ \mathrm{mm}$ and $c_i = 0.02\ \mathrm{N\ s/m}$ ($i = 1, 2, 3$), if not otherwise specified. The fourth-order Runge-Kutta method is used to solve the differential equations. The tolerances used to detect impact or sticking between two masses are both set to 10^{-6}.

4.4.1.1. Different Impact Characteristics

It has been found that different mass distributions can lead to different impact positions. In symmetric case (1), impact only occurs over the static equilibrium of m_1 and below that of m_3 while it exists at the both sides of the static equilibrium position of m_2, as shown in Figure 4.5(a). Interestingly, its opposite is true in symmetric case (2), as shown in Figure 4.5(b). In the third configuration, impact only appears below the static equilibrium of each mass, even for m_2 (see Figure 4.5(c)), and it turns out to be the opposite in case (4), as shown in Figure 4.5(d). From the energy harvesting perspective, it is preferable for m_2 to encounter impact both above and below its static equilibrium position. Therefore, the two symmetric configurations are of greater interest and will be compared in the following study.

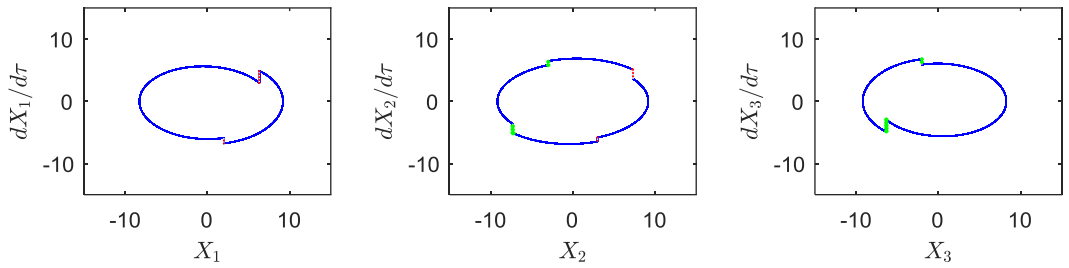

(a)

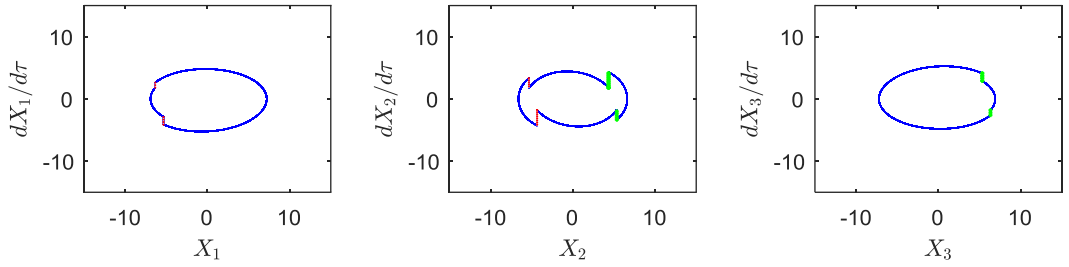

(b)

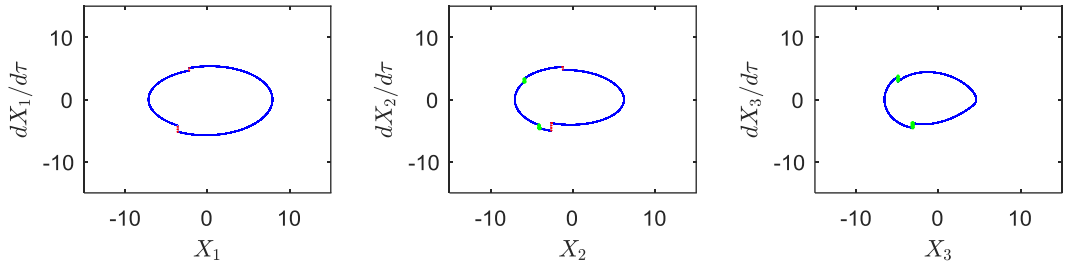

(c)

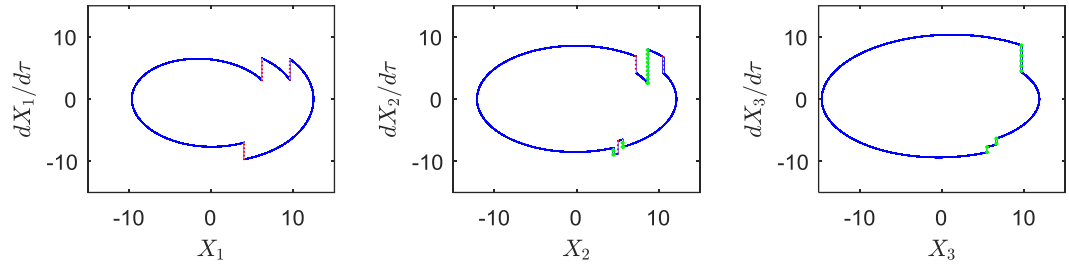

(d)

Figure 4.5 Examples of the phase plots of the three masses in four configurations: (a) Configuration (1), $m_2 = 120 \times 10^{-3}$ kg, $m_1 = m_3 = 0.75\, m_2$; (b) Configuration (2), $m_1 = m_3 = 120 \times 10^{-3}$ kg, $m_2 = 0.50\, m_1$; (c) Configuration (3), $m_1 = 120 \times 10^{-3}$ kg, $m_2 = 0.80\, m_1$, $m_3 = 0.50\, m_1$; (d) Configuration (4), $m_3 = 120 \times 10^{-3}$ kg, $m_2 = 0.80\, m_3$, $m_1 = 0.60\, m_3$; Impacts between m_1 and m_2 are represented by red dotted lines while impacts between m_2 and m_3 are denoted by green '+' dotted lines.

4.4.1.2. Comparison Between the Two Symmetric Configurations

It is not easy to make general observations regarding the two symmetric configurations since altering some of the specified parameters (e.g., the mass ratio or excitation frequency) might lead to different conclusions. In an attempt to make a broad comparison, both low and high mass ratios of each configuration are considered, and the average power output of each configuration at each mass ratio is calculated both at lower and higher excitation frequencies.

In the first symmetric configuration, the mass distribution is configured to $m_2 = 120 \times 10^{-3}$ kg, $m_1 = m_3$, and $R_\mathrm{m} = \frac{m_2}{m_1}$, where $R_\mathrm{m} > 1$, and $R_\mathrm{m} \in [1.5, 2.0, 3.0]$ are taken in the comparison; and that of the second configuration is $m_1 = 120 \times 10^{-3}$ kg, $m_1 = m_3$, and $R_\mathrm{m} = \frac{m_2}{m_1}$, where $0 < R_\mathrm{m} < 1$, and $R_\mathrm{m} \in [0.3, 0.5, 0.7]$ are taken in the comparison.

The average power P_a versus the number of excitation periods N_p is calculated for different excitation frequencies and mass ratios for both configurations. The results are shown in Figure 4.6. It can be seen that the first symmetric configuration has overall better electrical output performance than the second. Therefore, the first symmetric configuration will be studied further.

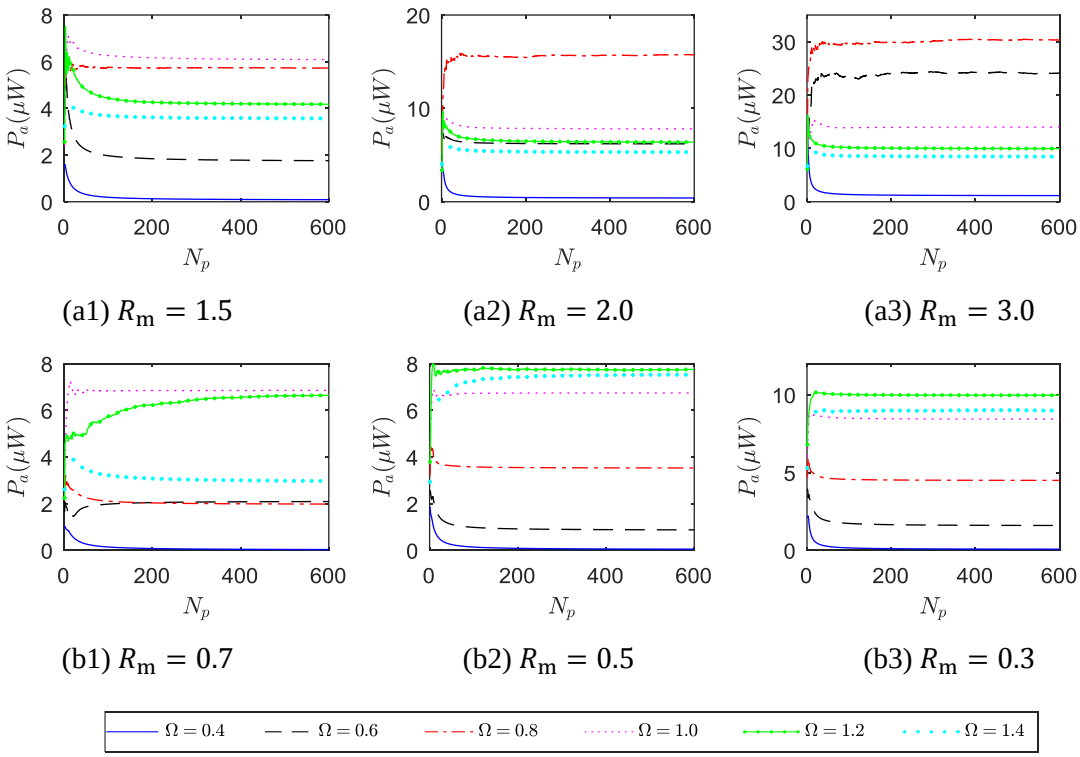

Figure 4.6 The average power output at different excitation frequencies of the two symmetric configurations in different mass ratios: (a) the first configuration and (b) the second configuration.

4.4.2. The Effect of Mass Spacing

The initial mass spacing, δ_1 and δ_2, could be symmetric or asymmetric, and the choice will influence the dynamics of the system deeply because the spacing determines the impact criteria. Additionally, the mass spacing affect the equivalent capacitance and voltage directly, which then results in the change of electrical output.

4.4.2.1. Asymmetric Mass Spacing

Let $R_\delta = \frac{\delta_2}{\delta_1}$ be the mass spacing ratio in the asymmetric spacing case. The bifurcation diagram of X_2 versus R_δ and its local enlargement are calculated and shown in Figure 4.7(a) and (b), respectively, while Figure 4.7(c) and (d) show the corresponding 'bifurcation diagrams of the velocities just prior to impact', in which the values of the quantities concerned, for example, relative velocities between m_1 and m_2, (i.e. V_{12}), and between m_2 and m_3, (i.e. V_{23}), only at impact events within each forcing cycle are sampled. This is one way of displaying the dynamic behaviour of vibro-impact and the present bifurcation idea is similar to that in Ref. [212], which is quite different from the conventional bifurcation concept. Therefore, the countable dots at each value of R_δ represent the number of impacts, rather than the order of periodicity, in one vibration period of periodic motions while the uncountable dots indicate the impacts of non-periodic vibrations. The parameter values used in simulation are $\delta_1 = 20$ mm, $\Omega = 0.70$, $m_1 = m_3 = 90 \times 10^{-3}$ kg and $m_2 = 120 \times 10^{-3}$ kg.

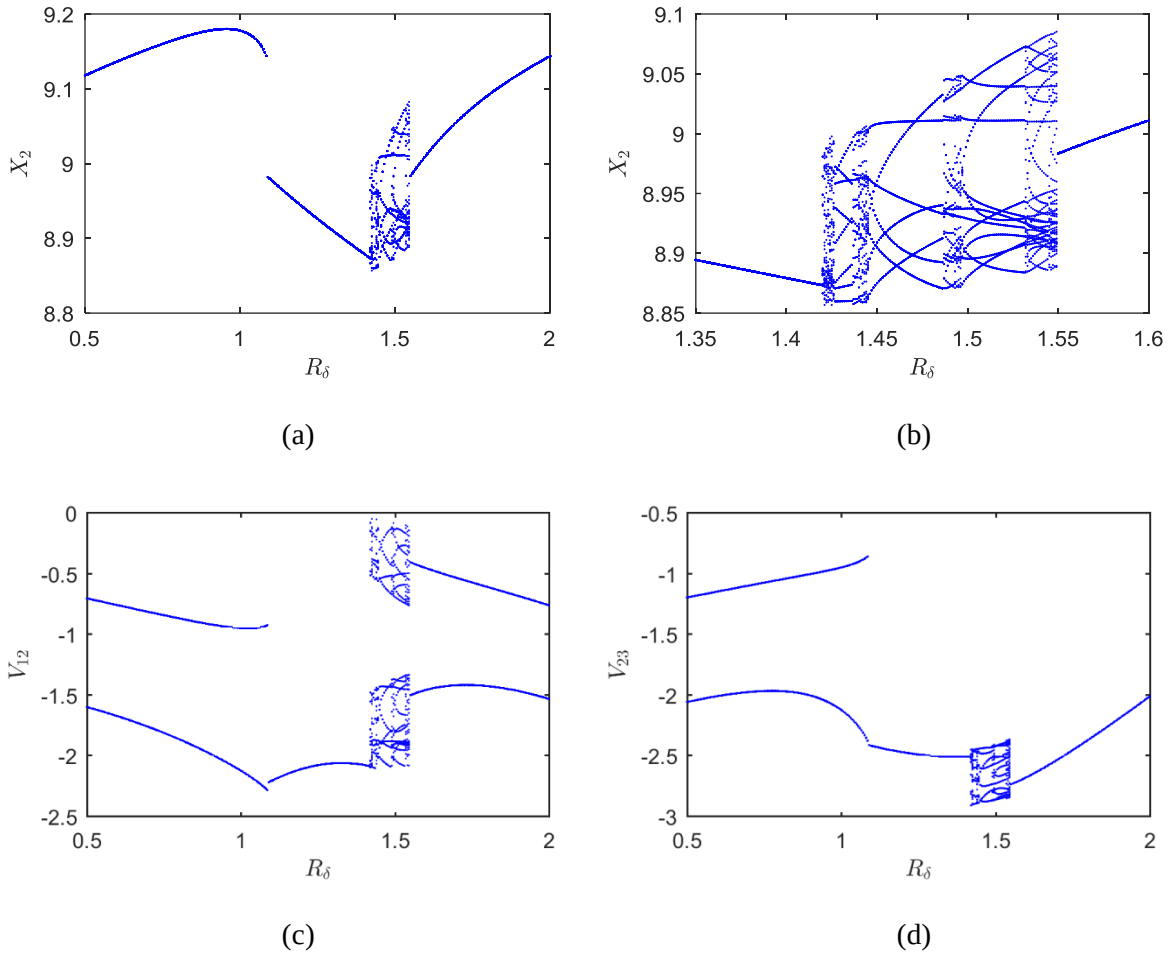

Figure 4.7 Bifurcation diagrams of (a) X_2 versus R_δ and (b) its local enlargement, and the bifurcation diagrams of V_{12} and V_{23} versus R_δ, i.e. (c) and (d), respectively.

From the bifurcation diagrams of X_2, i.e. Figure 4.7(a) and (b), it could be seen that the system undertakes complicated dynamic variation with the change of R_δ. The corresponding bifurcation diagrams of the just-before-impact velocities, i.e. Figure 4.7(c) and (d), show the relevant impact situations. It is clear that there exists a jump at which the vibration amplitude drops suddenly and the number of impacts that happen in one motion period or one forcing cycle decreases from two to one as R_δ passes through the jump point from left to right. The corresponding time history and phase plot of D_1 at the jump point and the point just after the jump are given in Figure 4.8 to show the details of the impact and vibration characteristics.

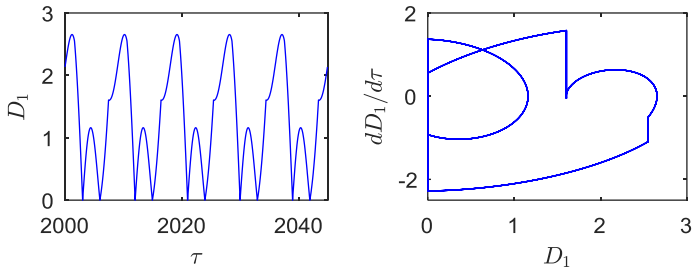

(a)

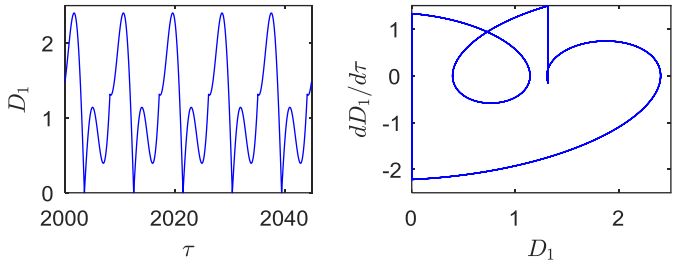

(b)

Figure 4.8 Time histories (left) and phase plot (right) of D_1 for (a) $R_\delta = 1.085$ and (b) $R_\delta = 1.090$.

Grazing bifurcation occurs at $R_\delta = 1.419$ and it is obvious in Figure 4.7 (b) that the dynamics of the system becomes much more complicated due to grazing bifurcation. The time history and phase plot of both D_1 and D_2 are given in Figure 4.9 to verify and show the details, and it is clear that grazing impact appears only between m_1 and m_2. Besides, the vibration responses are asymmetric owing to the asymmetric mass spacing.

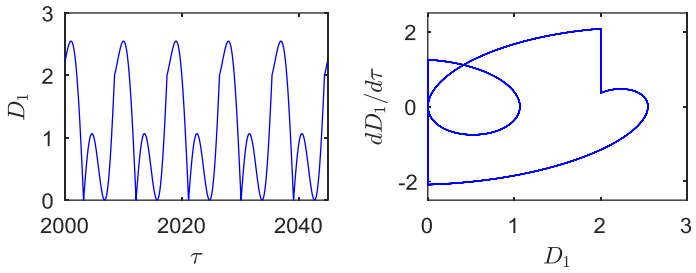

(a)

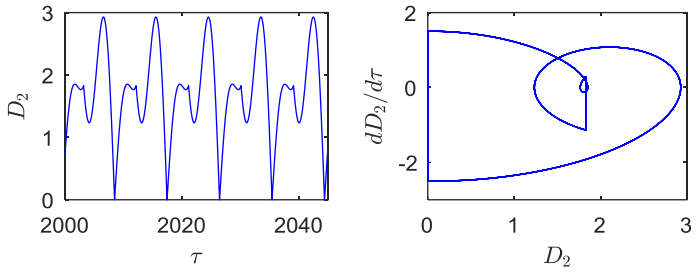

(b)

Figure 4.9 Time histories (left) and phase plots (right) of (a) D_1 and (b) D_2 for grazing impact at $R_\delta = 1.419$.

Since there occurs a period-doubling cascade with non-periodic windows in Figure 4.7(b), and all periodic, period-doubling and non-periodic motions appear with the variation of R_δ, a comparison of the electrical output among different motion characteristics is convenient. The PSD (power spectral density) and Poincaré section of X_2, a time history of current, the average harvested power versus the number of excitation periods are shown in Figure 4.10 for different types of response. The average power output for these different responses are shown in Figure 4.11. It is concluded that high-order periodic motion has lower average power output relative to simple periodic motion. It appears that power decreases as the order of the periodicity increases. However, none of them seem to generate more than a few micro-watts of power.

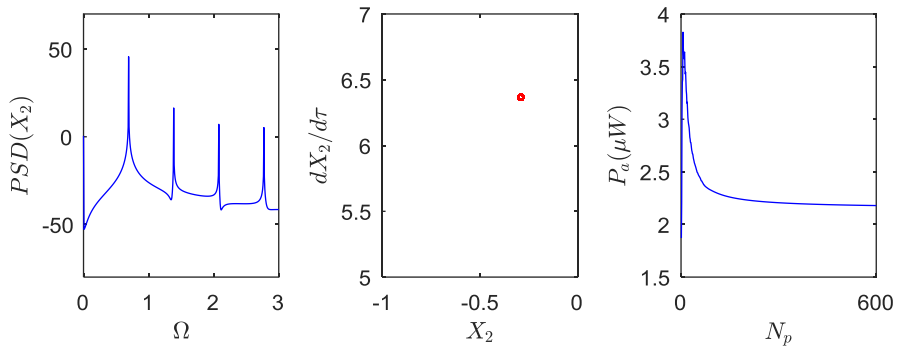

(a)

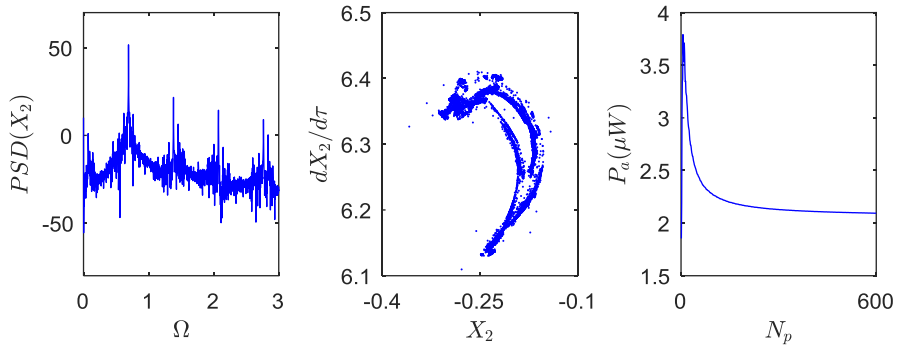

(b)

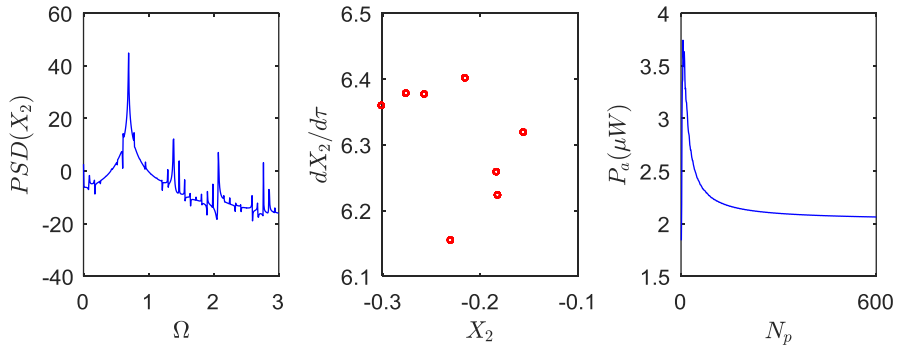

(c)

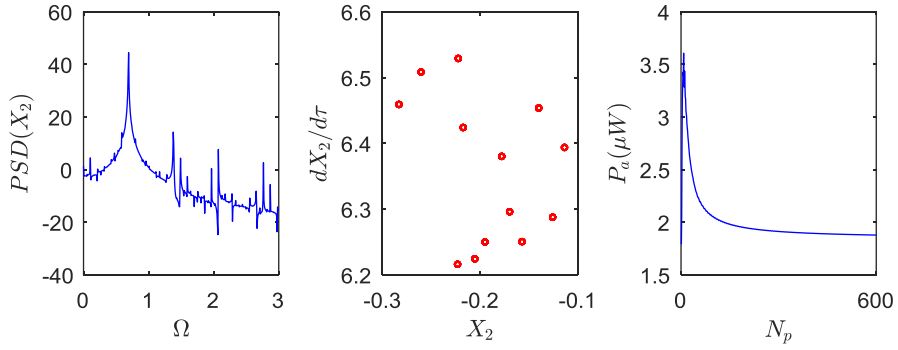

(d)

Figure 4.10 The PSD and Poincaré section of X_2, time history of current and average power (from left to right) for (a) $R_\delta = 1.415$ (periodic motion), (b) $R_\delta = 1.423$ (chaotic motion), (c) $R_\delta = 1.430$ (period-8 motion) and (d) $R_\delta = 1.512$ (period-13 motion).

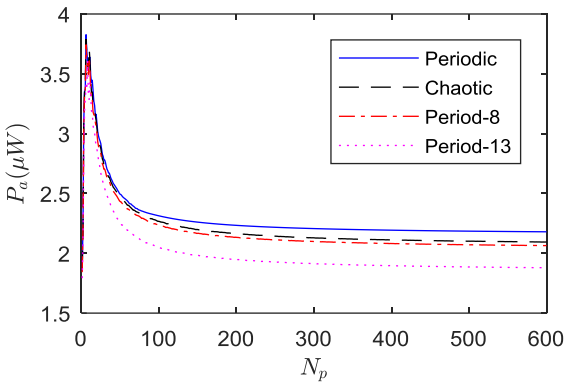

Figure 4.11 The comparison of P_a between different types of motions.

4.4.2.2. Symmetric Mass Spacing

In the consideration of symmetric mass spacing, the structural parameters (i.e., mass, stiffness, damping, mass spacing) are also all assumed symmetric. Consequently, the dynamic response of the system is mostly symmetric, though symmetry-breaking [213] of the dynamic response can exist.

In the modelling of the non-dimensional system, the mass spacing, δ_1, is used as a normalization parameter (i.e., the non-dimensional displacements are $X_i = \frac{x_i}{\delta_1}$ $(i = 1, 2, 3)$). Therefore, for a given dimensional displacement, a smaller mass spacing would result in a larger non-dimensional displacement. To circumvent this dependence, the bifurcation diagram in Figure 4.12 is shown in terms of δX_2 versus δ rather than X_2 versus δ. Here, the excitation frequency is held fixed at $\Omega = 0.75$. The diagram shows that vibration amplitude tends to grow with an increase in mass spacing and that the response can be complicated at smaller mass spacing. It is noted that there exists Hopf bifurcation, which might be of great importance in some dynamic systems, such as in railway vehicle systems, where Hopf bifurcation can lead to unstable motions, such as hunting [214].

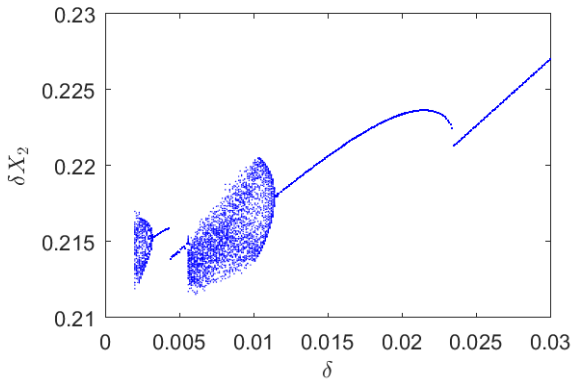

Figure 4.12 The bifurcation diagram of δX_2 versus the symmetric mass spacing δ.

4.4.3. The Effect of Mass Ratio

While the size of the mass spacing mostly affects the location at which the masses come into contact, the mass ratio can influence the way the masses interact with each other. If the mass ratio equals one, i.e., $R_{\mathrm{m}} = \frac{m_2}{m_1} = \frac{m_2}{m_3} = 1$, all three masses are equal, there is no impact among them after the system reaches its steady state (all other parameters, i.e., the mass spacing, the stiffness and the dampings, are assumed to be symmetric as well). This is due to the absolute symmetry of the structural parameters.

4.4.3.1. Mass Ratio's Effect on the Number of Impacts

To observe the dynamic response and electric output at mass ratios other than one, the time histories of D_1 and the generated current I and the diagram of the average power P_{a} are shown in Figure 4.13 for different mass ratios. It is observed that the number of impacts between m_1 and m_2 in one excitation period increases from one to three as the mass ratio R_{m} increases. This results in an increase in electrical output (note that impacts between m_2 and m_3 show the same effect).

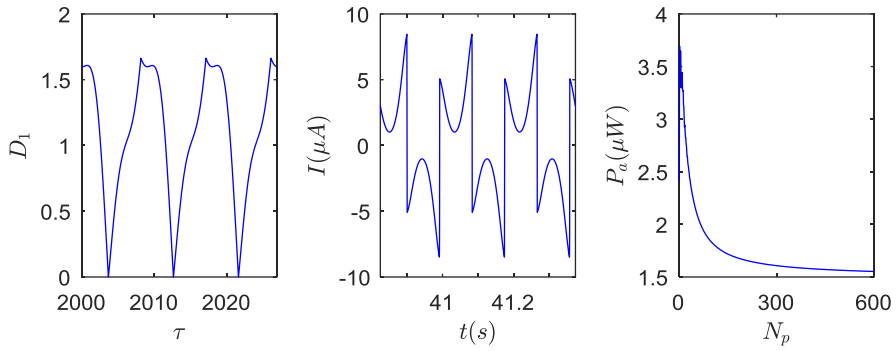

(a)

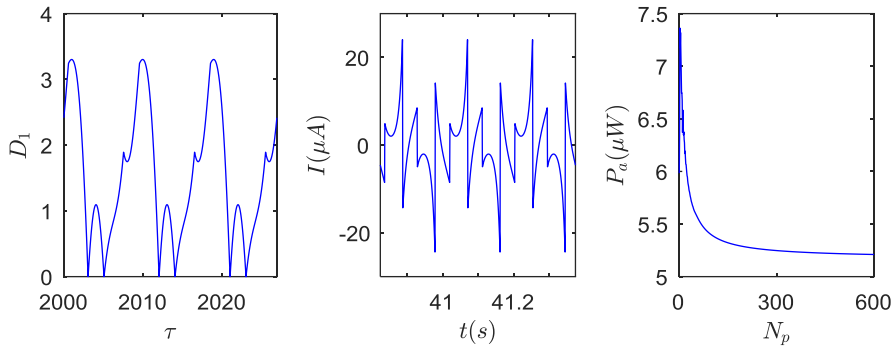

(b)

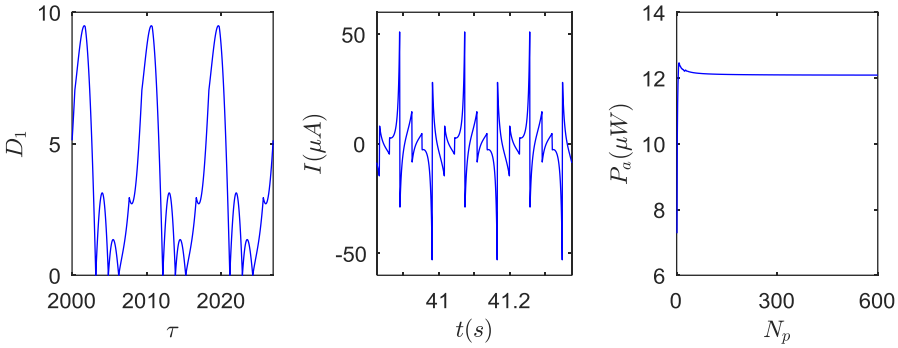

(c)

Figure 4.13 Time histories of D_1 and I and the diagram of average power P_{a} against the number of excitation periods N_{p} (from left to right) of (a) $R_{\mathrm{m}} = 1.2$, (b) $R_{\mathrm{m}} = 1.6$ and (c) $R_{\mathrm{m}} = 2.5$.

4.4.3.2. Optimal Mass Ratio

The bifurcation diagram of X_2 versus R_{m} when $\Omega = 0.72$ is shown in Figure 4.14(a), while Figure 4.14(b) shows the corresponding 'bifurcation diagram of V_{12} against R_{m}'. It can be seen that there is an optimal mass ratio at which the impact velocities reach a maximum at each impact. In Figure 4.14(b), the number of the countable dots at each R_{m} represents the

number of impacts that happen in one excitation period for periodic motions, for instance, there are three impacts between m_1 and m_2 in one forcing cycle of the periodic motion at $R_{\mathrm{m}} = 4$, while the number of the 'line segments' at each R_{m} (of the values approximately between $R_{\mathrm{m}} = 3.06$ and $R_{\mathrm{m}} = 3.64$) corresponds to the number of impacts that happen in one excitation period for non-periodic motions, for example, three impacts happen between m_1 and m_2 at the non-periodic motion of $R_{\mathrm{m}} = 3.5$. Because of higher impact velocity corresponds to higher electrical output, hence, there exists an optimal R_{m} at which it has the best electrical output performance. Figure 4.15 shows the average power outputs of three different mass ratios from Figure 4.14 for comparison and verification. It is clear that the average power output reaches the maximum at around $R_{\mathrm{m}} = 3.5$. The parameters used are the same as previous except for $\delta_1 = \delta_2 = 20$ mm and $m_1 = m_3 = 50 \times 10^{-3}$ kg.

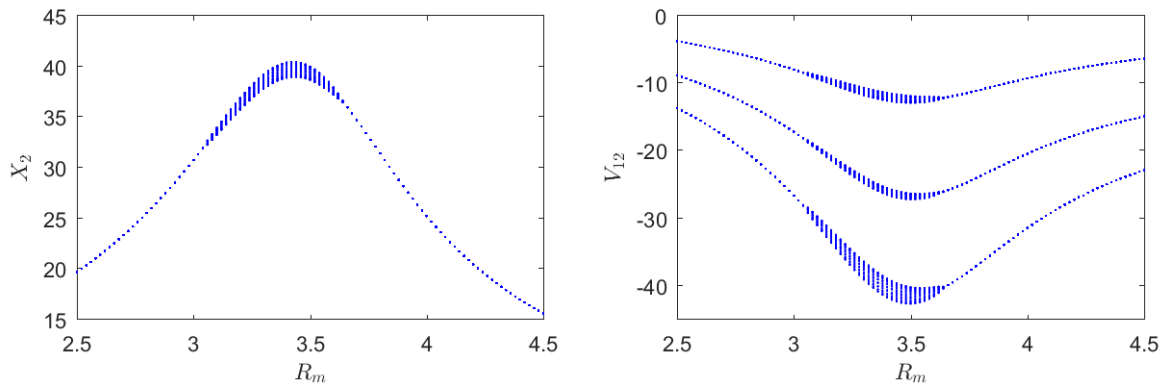

(a) (b)

Figure 4.14 Bifurcation diagrams of (a) X_2 and (b) V_{12}, respectively, versus R_{m} of $\Omega = 0.72$.

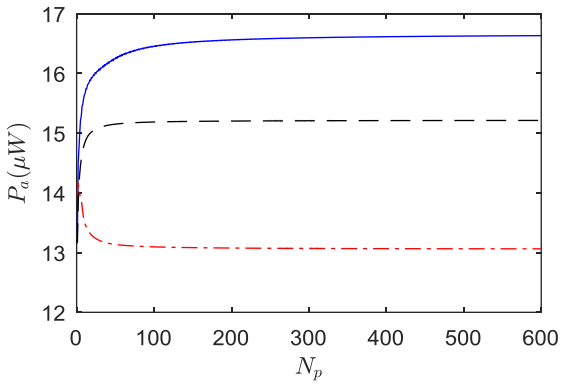

Figure 4.15 Average power outputs of three different mass ratios at $\Omega = 0.72$ (blue solid line represents $R_{\mathrm{m}} = 3.5$, black dashed line $R_{\mathrm{m}} = 3.0$, and red dash-dot line $R_{\mathrm{m}} = 2.5$).

Here, the optimal mass ratios, R_{mo}, of the frequencies between $\Omega = 0.55$ and $\Omega = 0.95$ are obtained and shown in Figure 4.16, and it is clear that the optimal mass ratio decreases with the increase of excitation frequency.

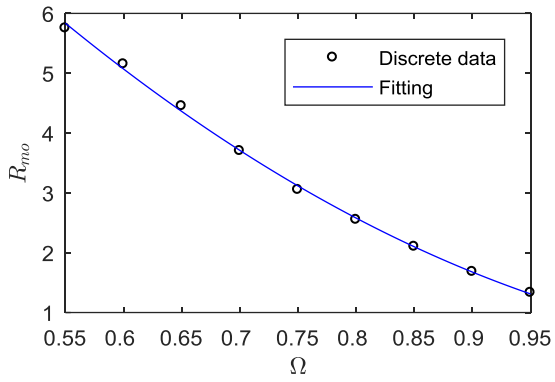

Figure 4.16 The variation of R_{mo} against Ω.

However, there would be no impact owing to the absolute symmetry of structural parameters as R_{mo} gradually approaches one. The bifurcation diagrams of X_2 and V_{12} of two higher excitation frequencies, $\Omega = 1.30$ and $\Omega = 2.00$, are calculated and given in Figure 4.17 as examples to show the variation of impact velocity at higher excitation frequencies. It can be observed that the magnitude of impact velocity would gradually approach a stable value as the mass ratio grows bigger, which means there is not an obvious optimal ratio for higher excitation frequencies.

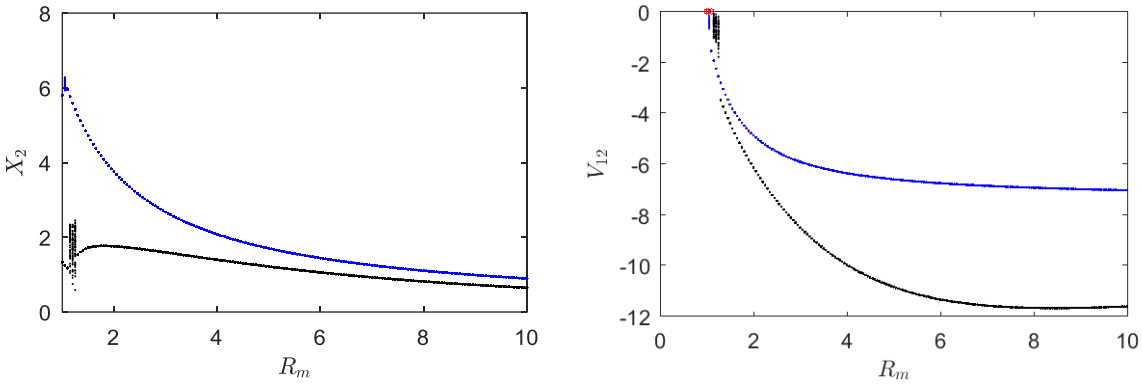

(a) (b)

Figure 4.17 Bifurcation diagrams of (a) X_2 and (b) V_{12} for $\Omega = 1.30$ (in blue) and $\Omega = 2.00$ (in black) (For interpretation of the references to colour in this figure, the reader is referred to the web version of this thesis).

For lower excitation frequencies, the response of the system can become quite complicated with the variation of mass ratio. The bifurcation diagram of X_2 versus R_m for $\Omega = 0.30$ and its local enlargement are given in Figure 4.18 as an example, and there appears a period-doubling cascade with non-periodic windows in Figure 4.18(b). Figure 4.19 shows the Poincaré sections of the non-periodic motion of $\Omega = 0.30$ and $R_\mathrm{m} = 4.21$ from Figure 4.18(b).

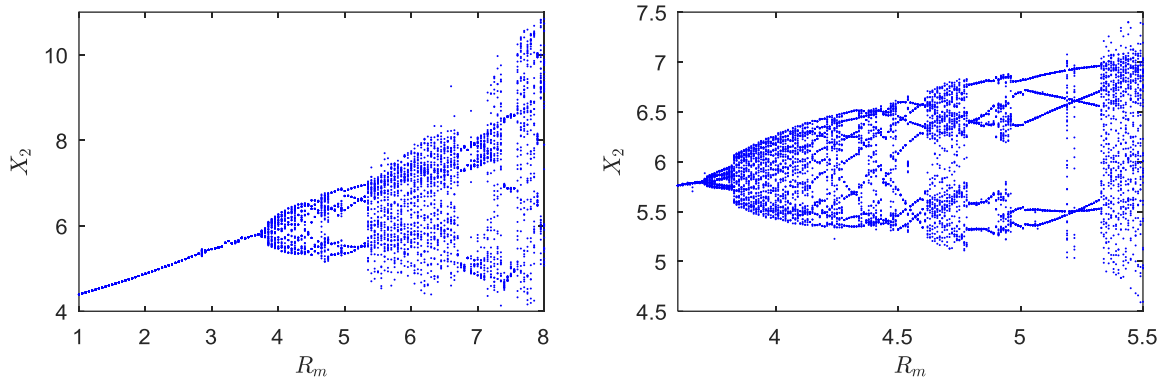

(a) (b)

Figure 4.18 Bifurcation diagram of X_2 versus R_m for (a) $\Omega = 0.30$ and (b) its local enlargement.

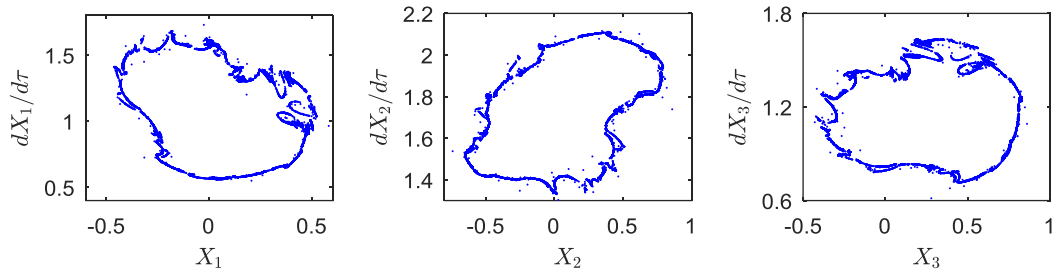

(a) (b) (c)

Figure 4.19 Poincaré sections of (a) X_1, (b) X_2 and (c) X_3 of a non-periodic motion at $\Omega = 0.30$, $R_\mathrm{m} = 4.21$.

4.4.4. Utilization of Chatter

Chatter has been a challenge for machining processes including turning, milling and drilling. It can cause problems like poor surface finish, excessive noise, breakage of machine tools, decreased tool life, and low productivity [215, 216]. Chatter is characterized by many consecutive impacts and might therefore be exploited in triboelectric energy harvesting from vibro-impact systems. In the study of a multi-degree-of-freedom vibro-impact system, Wagg

[217, 218] discussed the chattering and sticking behaviour which appeared at low forcing frequencies, and showed that a variety of non-smooth events could possibly occur. Here, a numerical simulation is conducted to determine whether chatter can appear in the present system at low forcing frequencies.

The bifurcation diagram of X_2 versus Ω, which includes a chatter range, is shown in Figure 4.20. The parameters used are $m_1 = 50 \times 10^{-3}$ kg, $R_{\mathrm{m}} = 3$ and $\delta = 5$ mm. To observe the details of the chatter range as well as the resonant range, local views are shown in Figure 4.21(a) and (b), respectively, while Figure 4.21(c) and (d) give the relevant 'bifurcation diagrams of V_{12}', in which the number of the dots at each Ω represents the number of impacts that happen in one excitation period, and the y-values of the dots represent the relative impact velocities. It is clear that there are plenty of consecutive impacts when chatter takes place while only three impacts exist at the excitation frequencies around resonance. Besides, chatter does not appear around a resonance but at some lower frequencies. Resonance, as usual, can have the strongest vibration and impact, but its high vibration amplitude would results in large separation distances between plates, which might not be beneficial to triboelectric energy harvesting. Therefore, there is the possibility of using chatter to harvest more energy than can be harvested by operating at resonance.

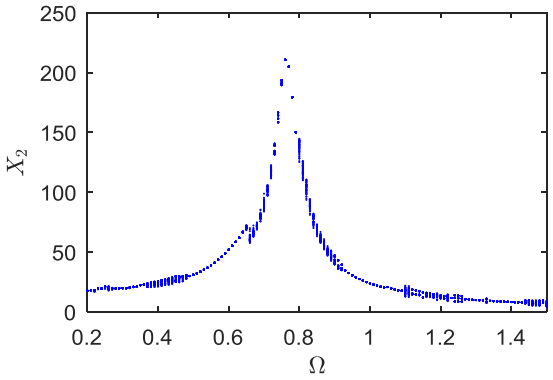

Figure 4.20 Bifurcation diagram of X_2 versus Ω with a chatter range.

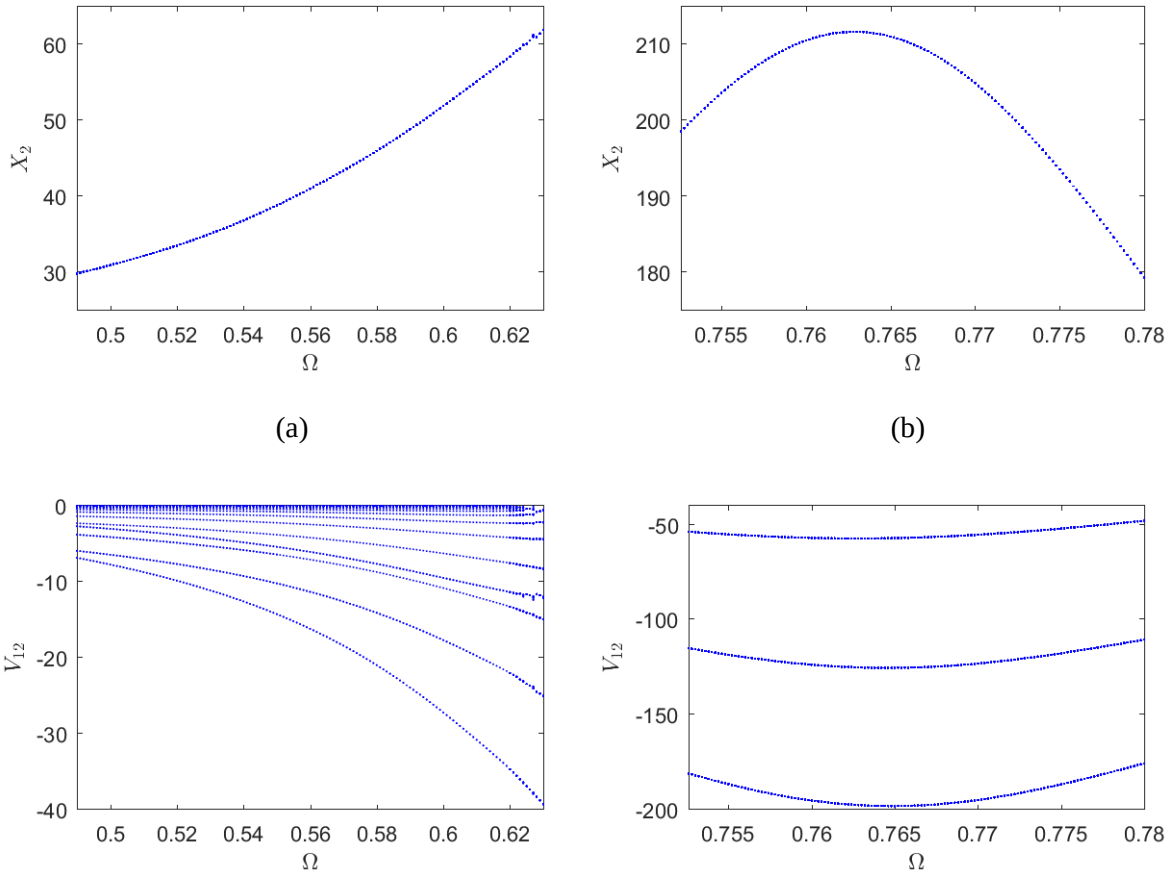

Figure 4.21 The local enlargements of Figure 4.18 for (a) chatter range and (b) resonant range, and their corresponding bifurcation diagrams of V_{12}, i.e. (c) and (d), respectively.

To see the details of the vibration and impact both around chatter frequency and resonant frequency, two excitation frequencies, $\Omega = 0.600$ and $\Omega = 0.76$, are chosen as the examples. The corresponding time history and phase plot of D_1 at these two excitation frequencies are shown in Figure 4.22 and Figure 4.23.

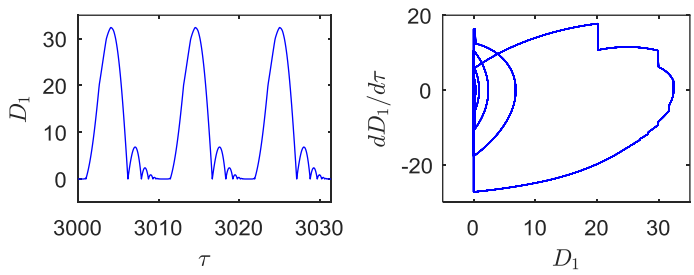

Figure 4.22 Time history and phase plot of D_1, i.e. (a) and (b), respectively, for $\Omega = 0.600$.

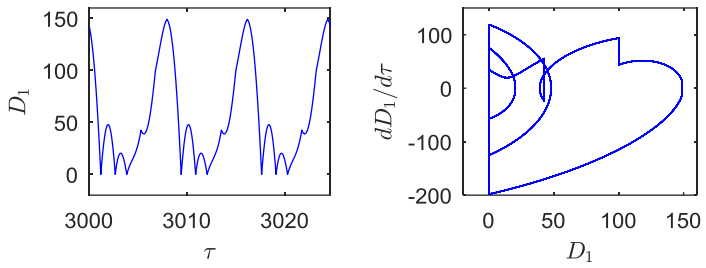

(a) (b)

Figure 4.23 Time history and phase plot of D_1, i.e. (a) and (b), respectively, for $\Omega = 0.765$.

It can be seen, from Figure 4.22(b), that the middle mass m_2 encounters chatter on both sides. Hence, there are many impact events. However, only six impacts in total would occur in the resonant case in Figure 4.23. On the other hand, most of the impacts in chatter are quite small compared with those at resonance. Therefore, to determine which one is superior in terms of harvesting energy, the average power output both around chatter zone and resonant zone are given in Figure 4.24 to compare the capability of efficient energy harvesting, in which it is clear that chatter frequencies perform much better than resonant frequencies in producing higher electrical output. Besides, since the chatter zone appears in a relatively lower frequency range compared with the resonant zone under the present parameters, it will be quite beneficial to harvesting energy from low-frequency ambient vibrations.

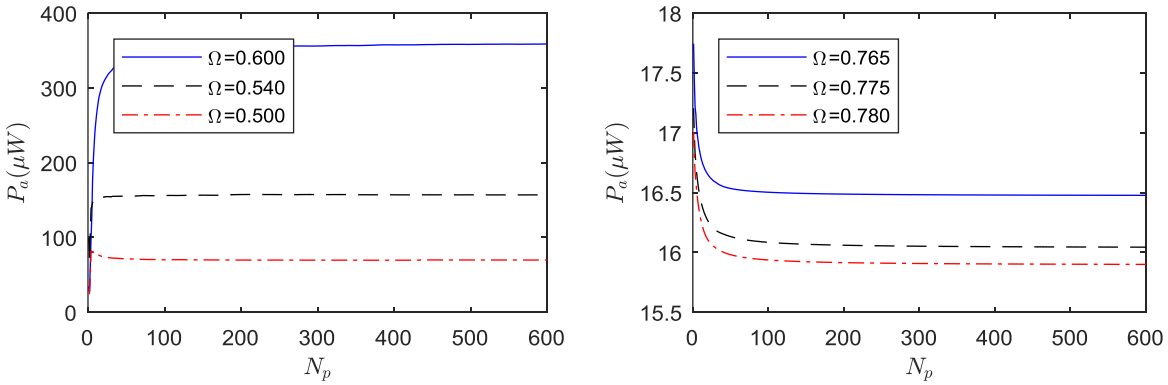

(a) (b)

Figure 4.24 The average power output both at around (a) chatter zone and (b) resonant zone.

To consider the details of both chatter and resonance cases and understand why forcing the system in the chatter regime results in such relatively high power output, some more detailed results of $\Omega = 0.600$ and $\Omega = 0.765$ are shown in Figure 4.25 and Figure 4.26. The non-

dimensional time and dimensional time in these figures correspond to each other. It can be seen that the equivalent capacitance gets bigger when $(D_1 + D_2)$ becomes smaller, and the peaks of the equivalent capacitance correspond to the peaks of current. Although the non-chatter case has higher equivalent voltage, i.e., at $\Omega = 0.765$, the equivalent capacitance in the chatter case is much bigger, actually two orders of magnitude bigger, than that of the non-chatter case. The relationship between the equivalent capacitance and the generated current indicates that the equivalent capacitance's variation seems to play a bigger role than that of the equivalent voltage. Besides, from Figure 4.25(a) and (b), it can be observed that the two chatter events, respectively, between m_1 and m_2, and m_2 and m_3 appear just one after the other, which means that the middle mass m_2 gets into chatter motion with one of the side masses, i.e., m_1 or m_3, firstly and then gets into chatter motion with the other one. More specifically, the relative motion between the middle mass m_2 and one of the side masses firstly undergoes chattering until they split apart from sticking, just after which the other side mass impacts the middle mass (Figure 4.25(d), (e)) pushing it into an additional impact with the mass from which it just split. After this, the original side mass flies away, while the newcomer (the other side mass) begins chattering with the middle mass. This is similar to the motion of a Newton's cradle. Interestingly, it seems that the small impact events during chatter are not directly responsible for the spikes of the electric output. Rather, it is the chatter-induced sticking motion that provides a chance for these three masses to come into impact nearly at the same time. When this occurs, the capacitance between the top and bottom electrodes spikes up because of the great decrease of the separation distance between them (the capacitance between two electrodes is inversely proportional to the separation distance in between, see Eq. (4.12)).

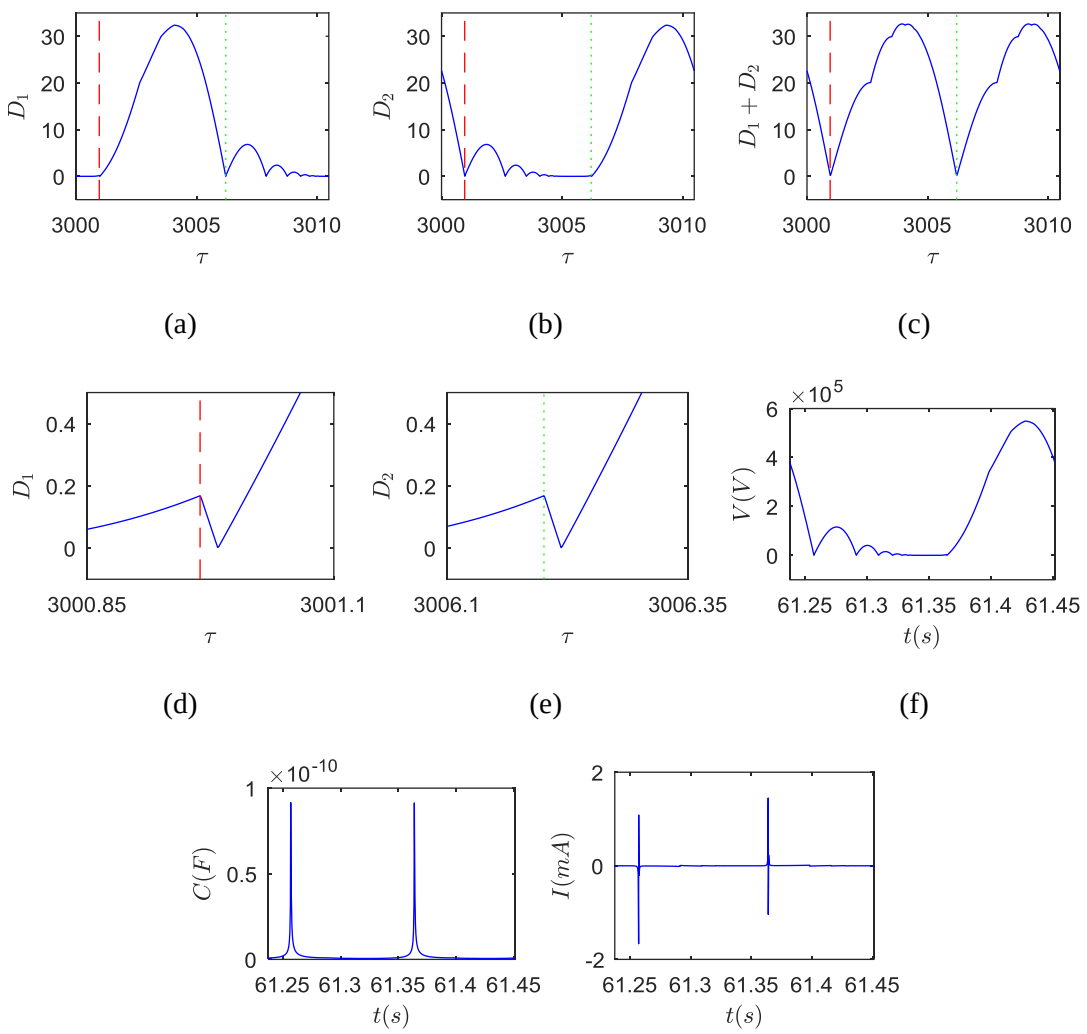

Figure 4.25 Time histories of (a) D_1, (b) D_2, (c) $D_1 + D_2$ and the corresponding local views (d) and (e), and (f) and (g), respectively, the equivalent voltage V and capacitance C, and (h) the generated current in one excitation period when $\Omega = 0.600$ (red dashed lines and green dotted lines in (a), (b), (c), (d), and (e) are reference lines).

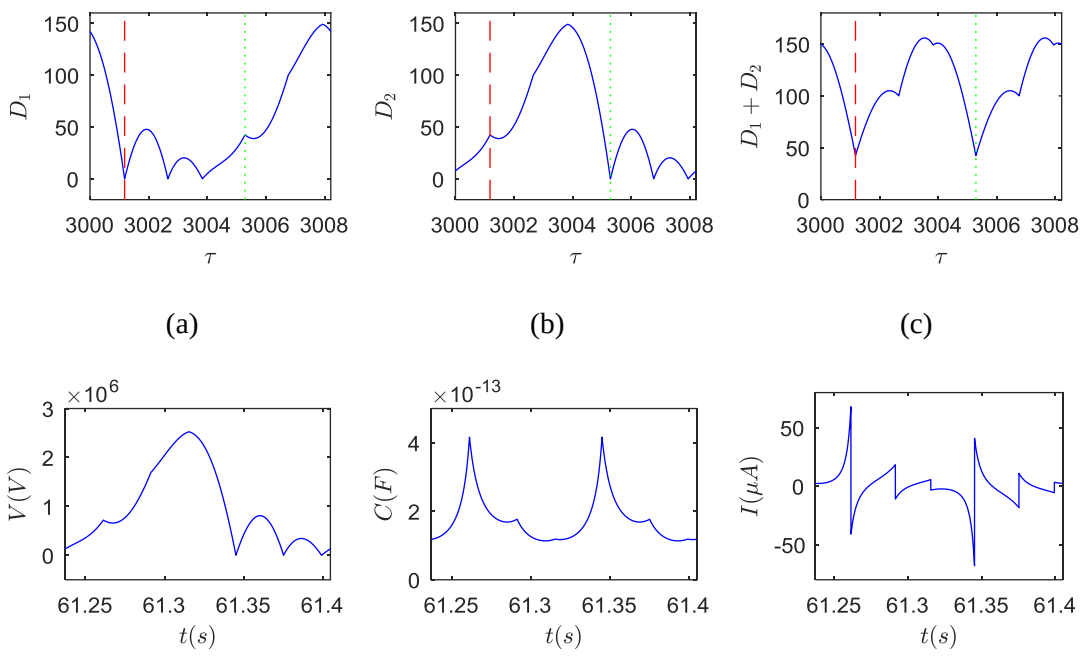

Figure 4.26 Time histories of (a) D_1, (b) D_2, (c) $D_1 + D_2$, and (d) and (e), respectively, the equivalent voltage V and capacitance C, and (f) the generated current in one excitation period when $\Omega = 0.765$ (red dashed lines and green dotted lines in (a), (b), and (c) are reference lines).

4.5. Conclusions

The dynamic model of a three-degree-of-freedom vibro-impact oscillator is developed. In this system, every mass can impact its neighbour(s), which produces very complicated vibro-impact motions. Then the theoretical model of the oscillator-based triboelectric energy harvester is constructed, and the equivalent circuit model is developed in Simulink to simulate the corresponding electrical output. Both the nonlinear dynamics of the vibro-impact system and the electrical output performance of the harvester are investigated, and the conclusions are drawn as follows:

(1) Different mass distributions could lead to very distinct impact characteristics. Among those four possible configurations, i.e., two symmetric configurations: $m_1 = m_3 < m_2$ and $m_1 = m_3 > m_2$, and two asymmetric configurations: $m_1 > m_2 > m_3$ and $m_1 < m_2 < m_3$, symmetric cases tend to be more beneficial to energy harvesting than asymmetric cases, and the first symmetric configuration has better harvesting performance than the second.

(2) The initial mass spacing between the three masses affect the displacement conditions of impact directly, thus grazing bifurcation or impact is likely to appear, which could influence the dynamics of the system and the electrical output deeply. Besides, it has been found that period-doubling motion could somewhat reduce the electrical output, and the higher the order of the periodicity, the more the reduction.

(3) The mass ratio determines how the masses impact and interact with each other. The number of impacts in one excitation period increases with the growth of the mass ratio, which then leads to the improvement of electrical output. There may also exist an optimal mass ratio at which the electrical output reaches the maximum, and it decreases with the increase of excitation frequency.

(4) The electrical output increases greatly when chatter and sticking occur in motion. Resonance, as usual, can have the highest vibration amplitudes and impact velocities, but this can be detrimental to electrical output and thus the maximal electric output does not appear at around resonance, which is different from other types of vibration-based energy harvesters, such as piezoelectric energy harvesters and electromagnetic energy harvesters, both of which usually have the highest electrical output at resonance. In addition, the appearance of chatter and sticking in the low excitation frequency range can help harvest energy from low-frequency ambient vibration, which should be leveraged in the design of future systems.

Chapter 5

Triboelectric Energy Harvesting from the Vibro-Impact of Three Cantilevered Beams

5.1. Introduction

To improve the understanding of the working mechanisms and advance the modelling methods of TEHs of freestanding triboelectric-layer mode, a new TEH of this unique mode based on the vibro-impact of three cantilevered beams is studied both numerically and experimentally in this chapter. For the aforementioned research gaps and issues in Chapter 2, a velocity-dependent coefficient of restitution law can be important to a more accurate prediction of the relationship between impact and restitution. In this chapter, relevant experiments of identifying the relationship between the just-before-impact velocity and the corresponding value of coefficient of restitution is conducted, and the identified relationship is used in the following numerical simulation. In addition to the more advanced modelling of impact, two modelling methods of the mechanical vibration of a cantilever beam with a tip mass, differing in whether the eccentricity of the tip mass is considered, are presented. The theoretical model or the V-Q-x relationship governing the electrical system is established instead of using the circuit simulator developed in Chapter 4, and the corresponding ordinary differential equation (ODE) is found to be stiff. Two schemes, which are based on the TR (the trapezoidal rule) and TR-BDF2 (the composite of the trapezoidal rule and the second order backward differentiation formula) methods, are proposed to solve the non-smooth mechanical system and the stiff electrical system. Experimental investigations of the effects of electrostatic force and air damping between cantilever tips are carried out. Numerical results are validated via experiments to verify the proposed methods.

The outline of the rest of this chapter is as follows: Section 5.2 presents the mechanical modelling of the vibro-impact system. Two different modelling methods are presented first and then the modelling of the impact between the beam tips is shown. The electrical

modelling of proposed TEH is then presented in Section 5.3. In Section 5.4, the methods to solve the non-smooth dynamical system and the stiff ODE modelling electrical output are described, and two candidate numerical solution schemes are proposed. Section 5.5 shows the measurement of the coefficient of restitution, and the relationship between the just-before-impact velocity and the coefficient of restitution is revealed experimentally. Section 5.6 experimentally investigates the effect of the electrostatic force and the air damping between cantilever tips to determine whether they are important to the theoretical model. Section 5.7 provides the experimental study of the potential for a frequency shifting phenomenon in the TEH. The numerical analysis and experimental validation of the system responses are given in Section 5.8. Section 5.9 presents the conclusions of this study.

This chapter is based on the following paper published by the author of this thesis and his supervisors:

Y. Fu, H. Ouyang, R.B. Davis, Triboelectric energy harvesting from the vibro-impact of three cantilevered beams, Mechanical Systems and Signal Processing 121 (2019) 509-531.

5.2. Mechanical Modelling of the Three Cantilever Beam Vibro-Impact System

5.2.1. Vibration of a Cantilever Beam with a Tip Mass at Its Free End

A clamped-free Euler-Bernoulli beam with a tip mass, m, at its free end is shown on the left hand side of Figure 5.1. The transverse displacement of the beam at any point y and time t can be represented by $w(y,t)$. In the absence of base excitation, the equation of motion of the undamped free vibration of the Euler-Bernoulli beam may be written as [219]

$$EI\frac{\partial^4 w(y,t)}{\partial y^4}+\rho A_{\mathrm{c}}\frac{\partial^2 w(y,t)}{\partial t^2}=0 \tag{5.1}$$

where E is the Young's modulus and I the moment of inertia of the beam's cross section; ρ is the beam's mass density and A_{c} the area of cross section.

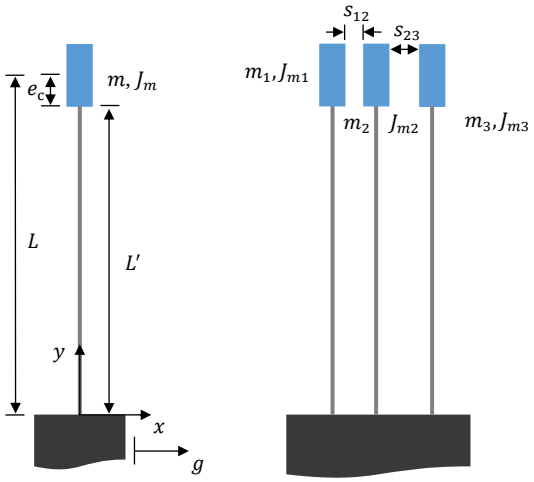

Figure 5.1 A clamped-free Euler-Bernoulli beam with a tip mass (left) and the three-cantilever-beam vibro-impact system (right).

When the structure is subject to base excitation, the absolute transverse motion of the cantilever beam at any point y and time t can be written as the following form according to Timoshenko et al. [220].

$$w(y,t) = w_{\mathrm{b}}(y,t) + w_{\mathrm{rel}}(y,t) \tag{5.2}$$

where $w_{\mathrm{rel}}(y,t)$ is the beam's transverse displacement relative to its clamped end, and $w_{\mathrm{b}}(y,t)$ is the base excitation and is given by

$$w_{\mathrm{b}}(y,t) = \delta_1(y)g(t) + \delta_2(y)h(t) \tag{5.3}$$

where $\delta_1(y)$ and $\delta_2(y)$ are the displacement influence functions for the transverse and rotational base motions, i.e., $g(t)$ and $h(t)$, respectively, and for the cantilevered beam case, $\delta_1(y) = 1$ and $\delta_2(y) = y$ [220, 221]. Substituting Eqs. (5.2) and (5.3) into Eq. (5.1) and considering the inertial force and moment applied to the cantilever tip by the tip mass m and tip moment of inertia J_m yield [222]

$$\begin{aligned} EI\frac{\partial^4 w_{\mathrm{rel}}(y,t)}{\partial y^4} + \rho A_{\mathrm{c}}\frac{\partial^2 w_{\mathrm{rel}}(y,t)}{\partial t^2} &= -[\rho A_{\mathrm{c}} + m\delta(y-L)]\frac{\partial^2 w_{\mathrm{b}}(y,t)}{\partial t^2} \\ &+ J_m\frac{\partial^3 w_{\mathrm{b}}(y,t)}{\partial t^2 \partial y}\frac{\mathrm{d}\delta(y-L)}{\mathrm{d}y} \end{aligned} \tag{5.4}$$

where $\delta(\,)$ is the Dirac delta function. Eq. (5.4) represents the forced vibration equation for the relative vibratory motion of the structure, which has the following boundary conditions.

$$w_{\mathrm{rel}}(0,t) = 0 \tag{5.5}$$

$$\left[\frac{\partial w_{\mathrm{rel}}(y,t)}{\partial y}\right]_{y=0} \tag{5.6}$$

$$\left[EI\frac{\partial^2 w_{\mathrm{rel}}(y,t)}{\partial y^2} + J_m\frac{\partial^3 w_{\mathrm{rel}}(y,t)}{\partial t^2 \partial y}\right]_{y=L} = 0 \tag{5.7}$$

$$\left[EI\frac{\partial^3 w_{\mathrm{rel}}(y,t)}{\partial y^3} - m\frac{\partial^2 w_{\mathrm{rel}}(y,t)}{\partial t^2}\right]_{y=L} = 0 \tag{5.8}$$

The solution of Eq. (5.4), i.e., the relative transverse displacement $w_{\mathrm{rel}}(y,t)$, may be written in the form

$$w_{\mathrm{rel}}(y,t) = \sum_{r=1}^{\infty} q_r(t)\phi_r(y) \tag{5.9}$$

where $q_r(t)$ are the temporal modal coordinates, $\phi_r(y)$ are the associated spatial functions or the mode-shape functions with the following form

$$\phi_r(y) = C_r\left\{\left[\cos\left(\frac{\beta_r}{L}y\right) - \cosh\left(\frac{\beta_r}{L}y\right)\right] + \sigma_r\left[\sin\left(\frac{\beta_r}{L}y\right) - \sinh\left(\frac{\beta_r}{L}y\right)\right]\right\} \tag{5.10}$$

where coefficients σ_r and eigenvalues β_r can be determined from the associated eigensystem, modal amplitude constants C_r can be obtained from the orthonormality conditions. (The corresponding formulas are not given here since they are similar to Eqs. (13), (14), and (16) in Ref. [222].)

The undamped natural frequency of the r-th mode is given by

$$\omega_r = \beta_r^2\sqrt{\frac{EI}{\rho A_{\mathrm{c}} L^4}} \tag{5.11}$$

Considering the first mode only, applying Galerkin projection, including dissipation, involving the transverse and harmonic base excitation only, and applying the orthonormality conditions, Eq. (5.4) is transformed into the second order ODE of a single-degree-of-freedom system as

$$\ddot{q}_1 + 2\zeta\omega_1\dot{q}_1 + \omega_1^2 q_1 = \alpha_r \ddot{g} \tag{5.12}$$

where ζ is the damping ratio which is determined by experiments and the over-dot denotes a derivative with respect to time t, $\ddot{g}$ is the second derivative of the transverse base excitation, and

$$\alpha_r = -\rho A_\mathrm{c} \int_0^L \phi_1 \mathrm{d}y - m\phi_1(L) \tag{5.13}$$

The above formulation is based on the assumption that the centre of tip mass coincides with its attachment point, i.e., a lumped mass is attached at the free end of a cantilever beam of length L. Another method is modelling the attachment of the tip mass with an eccentricity e_c, as shown in Figure 5.1, which is theoretically closer to reality when the tip mass is relatively big. In this study, the length ratio of tip mass to cantilever beam (L') is $\frac{e_\mathrm{c}}{L'} = \frac{2}{7}$ and the thickness ratio of tip mass to cantilever beam $\frac{t_m}{t_b}$ is even bigger because the thickness of the beam (spring steel) t_b equals 0.3 mm and the thickness of tip mass (aluminium and/or copper) is not less than 2 mm. Therefore, the second method is also worth exploring.

Under the consideration of eccentricity and using Eqs. (5.1) to (5.3) and only involving the transverse base motion, one can get the equation of motion as follows

$$\begin{aligned} EI\frac{\partial^4 w_\mathrm{rel}(y,t)}{\partial y^4} + \rho A_\mathrm{c}\frac{\partial^2 w_\mathrm{rel}(y,t)}{\partial t^2} \\ = -\left[\rho A_\mathrm{c} + m\delta(y-L') - me_\mathrm{c}\frac{\mathrm{d}\delta(y-L')}{\mathrm{d}y}\right]\frac{\mathrm{d}^2 w_\mathrm{b}(t)}{\mathrm{d}t^2} \end{aligned} \tag{5.14}$$

which has the same boundary conditions at the clamped end described by Eqs. (5.5) and (5.6) as well as the following boundary conditions at the free end

$$\left[EI\frac{\partial^2 w_\mathrm{rel}(y,t)}{\partial y^2} + me_\mathrm{c}\frac{\partial^2 w_\mathrm{rel}(y,t)}{\partial t^2} + (J_m + me_\mathrm{c}^2)\frac{\partial^3 w_\mathrm{rel}(y,t)}{\partial t^2 \partial y}\right]_{y=L'} = 0 \tag{5.15}$$

$$\left[EI\frac{\partial^3 w_\mathrm{rel}(y,t)}{\partial y^3} - m\frac{\partial^2 w_\mathrm{rel}(y,t)}{\partial t^2} - me_\mathrm{c}\frac{\partial^3 w_\mathrm{rel}(y,t)}{\partial t^2 \partial y}\right]_{y=L'} = 0 \tag{5.16}$$

By applying the method of separation of variables, one can express the solutions of Eq. (5.14) in the same forms as Eqs. (5.9) and (5.10) with L being replaced by L'. The eigenvalue β_r is similar to Eq. (18) in Ref. [223] and thus will not be given here. σ_r is determined by

$$\sigma_r = \frac{B_2}{B_1} \tag{5.17}$$

where B_1 and B_2 are defined as

$$B_1 = -(1 + D_2)\cos(\beta_r) + (D_2 - 1)\cosh(\beta_r) + D_1(\sin(\beta_r) + \sinh(\beta_r))$$

$$B_2 = D_1(\cosh(\beta_r) - \cos(\beta_r)) - (1 + D_2)\sin(\beta_r) + (D_2 - 1)\sinh(\beta_r)$$

$$D_1 = \frac{m\beta_r^3}{\rho A_c L'^3}\left(\frac{J_m}{m} + e_c^2\right)$$

$$D_2 = \frac{m\beta_e^2 e_c}{\rho A_c L'^2}$$

The modal amplitude constants C_r can be evaluated from the orthonormality condition as follows

$$\begin{aligned}\int_0^{L'} \phi_r(y)\rho A_c \phi_s(y)\mathrm{d}y + \phi_r(L')m\phi_s(L') + me_c\phi_r(L')\frac{\mathrm{d}\phi_s(L')}{\mathrm{d}y} \\ + me_c\frac{\mathrm{d}\phi_r(L')}{\mathrm{d}y}\phi_s(L') + \frac{\mathrm{d}\phi_r(L')}{\mathrm{d}y}(J_m + me_c^2)\frac{\mathrm{d}\phi_s(L')}{\mathrm{d}y} = \delta_{rs}\end{aligned} \tag{5.18}$$

where $\phi_s(y)$ represents an arbitrary mode-shape function, δ_{rs} is the Kronecker delta (equals 1 for $r = s$ and 0 for $r \neq s$). After the application of the same process as the first method, one can get the same equation as Eqs. (5.12) and (5.13) except that α_r has been changed into

$$\alpha_r = -\rho A_c \int_0^{L'} \phi_1 \mathrm{d}y - m\phi_1(L') - me_c\frac{\mathrm{d}\phi_1(L')}{\mathrm{d}y} \tag{5.19}$$

The results of the two methods will be compared in the following study and the superior one will be employed.

5.2.2. Modelling of the Impact Between Tip Masses

For the three cantilever beam vibro-impact system, any two adjacent tip masses can impact. The separation distances between m_1 and m_2 and between m_2 and m_3 are represented by d_{12} and d_{23}, respectively, and are given, in the first method, as

$$d_{12} = s_{12} - (q_2\phi_2(L) - q_1\phi_1(L)) \tag{5.20}$$

$$d_{23} = s_{23} - (q_3\phi_3(L) - q_2\phi_2(L)) \tag{5.21}$$

It is noted that q_i and ϕ_i $(i = 1, 2, 3)$ are, respectively, the temporal coordinates and spatial functions of the first modes of cantilever beams 1 to 3; s_{12} and s_{23} are the initial separation distances between m_1 and m_2 and between m_2 and m_3, respectively.

In the second method, considering the rigid body displacement owing to the slope at the free end and using the small-angle approximation, i.e., $\frac{\mathrm{d}w_{\mathrm{rel}}(L',t)}{\mathrm{d}y} = \sin(\theta) \approx \theta \approx \tan(\theta)$, the separation distances can be expressed as

$$d_{12} = s_{12} - \left[\left(q_2\phi_2(L') + e_{\mathrm{c}}q_2\frac{\mathrm{d}\phi_2(L')}{\mathrm{d}y}\right) - \left(q_1\phi_1(L') + e_{\mathrm{c}}q_1\frac{\mathrm{d}\phi_1(L')}{\mathrm{d}y}\right)\right] \tag{5.22}$$

$$d_{23} = s_{23} - \left[\left(q_3\phi_3(L') + e_{\mathrm{c}}q_3\frac{\mathrm{d}\phi_3(L')}{\mathrm{d}y}\right) - \left(q_2\phi_2(L') + e_{\mathrm{c}}q_2\frac{\mathrm{d}\phi_2(L')}{\mathrm{d}y}\right)\right] \tag{5.23}$$

When the system is away from any impact, i.e., $d_{12} > 0$ and $d_{23} > 0$, its equations of motion are of the form

$$\ddot{q}_i + 2\zeta_i\omega_i\dot{q}_i + \omega_i^2 q_i = \alpha_{ri}\ddot{g}, (i = 1, 2, 3) \tag{5.24}$$

where ζ_i and ω_i are the damping ratio and first undamped natural frequencies of each single beam-mass system, and the damping ratios are measured via the free decay tests. If $d_{12} = 0$ and/or $d_{23} = 0$, there may exist impact(s). Furthermore, if the contact between any two masses occurs at non-zero relative velocity, i.e., $v_{12} = \dot{q}_2\phi_2(L) - \dot{q}_1\phi_1(L) \neq 0$ and/or $v_{23} = \dot{q}_3\phi_3(L) - \dot{q}_2\phi_2(L) \neq 0$, one can get the just-after-impact velocities by using the conservation of momentum and Newton's law of restitution

$$v_{p+} = \frac{m_p - \mu m_q}{m_p + m_q}v_{p-} + \frac{m_q(1+\mu)}{m_p + m_q}v_{q-} \tag{5.25}$$

$$v_{q+} = \frac{m_p(1+\mu)}{m_p + m_q}v_{p-} + \frac{m_q - \mu m_p}{m_p + m_q}v_{q-} \tag{5.26}$$

where μ is the coefficient of restitution; $v_p = \dot{q}_p\phi_p(L)$ and $v_q = \dot{q}_q\phi_q(L)$ ($p = 1, q = 2$ or $p = 2, q = 3$) are the velocities of two impacting masses, and the subscript '-' represents the state just before impact while '+' represents the state just after impact. Note that the second method will have the same expressions for velocities by replacing L with L' and assuming

that the mass centre of the tip mass has the same linear velocity as its attachment point. If impact takes place between m_1 and m_2, then $m_p = m_{e1}, m_q = m_{e2}$. If it occurs between m_2 and m_3, then $m_p = m_{e2}, m_q = m_{e3}$. If m_1 and m_2 are stuck together and go into impact with m_3, then $m_p = m_{e1} + m_{e2}, m_q = m_{e3}$. Finally, if m_1 impacts with m_2 and m_3 joined together, then $m_p = m_{e1}, m_q = m_{e2} + m_{e3}$, where m_{ei} $(i = 1, 2, 3)$ represent the equivalent mass of each single beam-mass system and have the form of $m_{ei} = m_i + \frac{33}{140}\rho A_c L$ (all three cantilever beams are of the same material and dimensions).

Sticking motion can happen between any two adjacent tip masses, during which contact force is necessary to maintain the dynamic equilibrium and prevent interpenetration. Let N_{pq} be the contact force, which can be derived from the equilibrium of forces (the specific expressions will not be given here, please refer to the method used in Chapter 4 if necessary), then the sticking conditions between any two adjacent masses are $d_{pq} = 0$, $v_p = v_q$ and $N_{pq} > 0$.

5.3. Electrical Modelling of the Triboelectric Energy Harvester Based on the Above System

The electrical model of the present TEH is established to simulate and assess its output. The model is based on a freestanding mode triboelectric generator [94, 210]. The middle tip mass, m_2, can be regarded as a freestanding metal layer, which works only as a charge inductor, and the left and the right tip masses, m_1 and m_3, work as the two electrodes. Two PTFE films (assumed massless) attached to the two side tip masses, respectively, act as the dielectrics. It is noted that all tip masses could be made of aluminium and copper blocks, but the contact is always between the aluminium block (which also works as electrodes) and the PTFE film.

The contact-separation mode triboelectric harvester works through a combination of contact electrification and electrostatic induction [94]. The charge transfer process of the presented triboelectric energy harvester is the same as that depicted in Figure 4.2.

The equivalent capacitance and the open-circuit voltage of the presented triboelectric energy harvester are given as [210]

$$C_e = \frac{\varepsilon_0 S}{d_0 + D} \tag{5.27}$$

$$V_{\mathrm{oc}} = \frac{2\sigma d_{23}}{\varepsilon_0} \tag{5.28}$$

where ε_0 is the vacuum permittivity, S is the area of contact, D is the separation distance between the left and the right electrodes and is assumed as $D = d_{12} + d_{23}$, d_0 is the effective dielectric thickness and $d_0 = \frac{d_1}{\varepsilon_{\mathrm{r1}}} + \frac{d_2}{\varepsilon_{\mathrm{r2}}}$, where d_1 and d_2 are the thickness of the left and the right dielectrics, respectively, and $\varepsilon_{\mathrm{r}i}$ $(i = 1, 2)$ are the relative permittivity of the corresponding materials, and σ is the tribo-charge surface density.

The electricity generation equation of the harvester can be of the form [94, 210]

$$V = -\frac{1}{C_{\mathrm{e}}} Q + V_{\mathrm{oc}} \tag{5.29}$$

where Q is the amount of charge transferred between electrodes, V is the voltage across the resistor R (as shown in Figure 5.2) and can be calculated by Ohm's law as $V = RI = R\frac{\mathrm{d}Q}{\mathrm{d}t}$. By substituting Eqs. (5.27) and (5.28) into Eq. (5.29), one can get the differential equation

$$R\frac{\mathrm{d}Q}{\mathrm{d}t} + \frac{d_0 + D}{\varepsilon_0 S} Q - \frac{2\sigma d_{23}}{\varepsilon_0} = 0 \tag{5.30}$$

With the assumption that there is no charge transfer at the beginning, i.e., $Q(0) = 0$, one can solve the differential equation and calculate the transferred charge and voltage across the load from

$$Q(t) = [\int_0^t \frac{2\sigma d_{23}(\tau_2)}{R\varepsilon_0} \mathrm{e}^{\int_0^{\tau_2} \frac{d_0 + D(\tau_1)}{R\varepsilon_0 S} \mathrm{d}\tau_1} \, \mathrm{d}\tau_2] \mathrm{e}^{-\int_0^t \frac{d_0 + D(\tau)}{R\varepsilon_0 S} \mathrm{d}\tau} \tag{5.31}$$

$$V(t) = \frac{2\sigma d_{23}(t)}{\varepsilon_0} - \frac{d_0 + D(t)}{\varepsilon_0 S} \mathrm{e}^{-\int_0^t \frac{d_0 + D(\tau)}{R\varepsilon_0 S} \mathrm{d}\tau} \int_0^t \frac{2\sigma d_{23}(\tau_2)}{R\varepsilon_0} \mathrm{e}^{\int_0^{\tau_2} \frac{d_0 + D(\tau_1)}{R\varepsilon_0 S} \mathrm{d}\tau_1} \, \mathrm{d}\tau_2 \tag{5.32}$$

For the non-smooth system under this study, it is very difficult or impossible to obtain analytical solutions, and thus Eq. (5.30) is numerically solved together with the non-smooth dynamical system. Furthermore, to avoid the error that might be caused from differentiating the unevenly spaced data (which is common for the solution of a non-smooth system), Eq. (5.29) is used to obtain the voltage output.

5.4. Methods to Solve the Non-Smooth Dynamical System and Its Response Dependent Stiff ODE of Electrical Output

The non-smooth mechanical system presented above can be solved by several explicit methods, such as the fourth-order Runge-Kutta method (RK4). However, the ordinary differential equation of electrical output, i.e., Eq. (5.30), is likely to be stiff because the order of magnitude of ε_0 is of -12 and load R can vary in a wide range. Implicit methods, such as the Backward Euler, Trapezoidal (TR), second-order Backward Differentiation Formula (BDF2) and the combination of the last two, i.e., the TR-BDF2 method, are often used to solve stiff ODEs. It is intended to use an implicit method to solve the non-smooth dynamical system as well as the response dependent stiff ODE of the electrical output.

5.4.1. The TR-BDF2 Method

The TR-BDF2 method [224] is a single step method of second-order accuracy that it is popular in circuit and semiconductor simulations. It has been shown to be optimal in a class of practical one-step methods [225], and some variants [225, 226] based on it have been developed. However, the authors are not aware of any applications of the TR or TR-BDF2 method in solving a non-smooth dynamical system. Therefore, this study includes a brief description of its application to a non-smooth system.

The TR-BDF2 method consists of two sub steps, namely a trapezoidal step from t_n to $t_{n+\gamma}$ and a second-order backward difference step from $t_{n+\gamma}$ to t_{n+1}, where $t_{n+\gamma} = t_n + \gamma\Delta t_n$, $\gamma \in (0,1)$ and $t_{n+1} = t_n + \Delta t_n$, and Δt_n is the whole time step. Therefore, in any one step of the integration of $\frac{\mathrm{d}q}{\mathrm{d}t} = h(q)$, one can firstly advance the solution from t_n to $t_{n+\gamma}$ as

$$q_{n+\gamma} - \gamma\frac{\Delta t_n}{2}h_{n+\gamma} = q_n + \gamma\frac{\Delta t_n}{2}h_n \tag{5.33}$$

Then, in the second sub step, one can advance the solution from $t_{n+\gamma}$ to t_{n+1} as

$$q_{n+1} - \frac{1-\gamma}{2-\gamma}\Delta t_n h_{n+1} = \frac{1}{\gamma(2-\gamma)}q_{n+\gamma} - \frac{(1-\gamma)^2}{\gamma(2-\gamma)}q_n \tag{5.34}$$

A special choice of γ is $\gamma = 2 - \sqrt{2}$ which can offer the least truncation error [224], the same Jacobian matrix for both sub-steps (when the Newton-Raphson method is applied to solve the implicit difference equations), and the largest linearized stability region [227].

The derivation of the corresponding difference equations is shown in Appendix A.

5.4.2. Two Different Schemes

5.4.2.1. Scheme 1: TR Method

By applying the TR rule only (to the steps with or without impact events), the algorithm can be quite straightforward because the TR method is a one-step method. It should be noted that the state vector just after the impact, i.e., $\mathbf{Z}_+ = [z_{1+}, z_{2+}, z_{3+}, z_{4+}, z_{5+}, z_{6+}, z_{7+}]$ (see Appendix A), should be used to further advance the system, where the subscript '+' of $\mathbf{Z}_+$ represents the state just after an impact, and the subscript '-' will be used to indicate the state just before an impact.

5.4.2.2. Scheme 2: Composite of TR and TR-BDF2 Methods

For a step without impact, scheme 2 uses the TR-BDF2 method to split the step into two sub-steps and applies the TR rule to the first sub-step and the BDF2 rule to the second. For a step with an impact or multiple impacts, the scheme employs only the TR rule for the whole step, which is the same as Scheme 1. For a case of one impact event, scheme 2 is depicted in Figure 5.2, where $\alpha \in (0, 1)$ and BDF2 rule (solid arrows) needs the state vectors of two sub steps since it is a two-step method. A conclusion might be that the BDF2 rule cannot be used just after an impact event, because the state vector is non-smooth in displacements and is discontinuous in velocities, and the TR rule seems to have to be used just after an impact event, which may be interesting for further mathematical study.

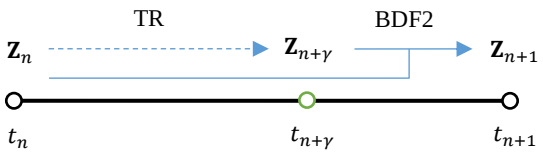

(a) One step without impact

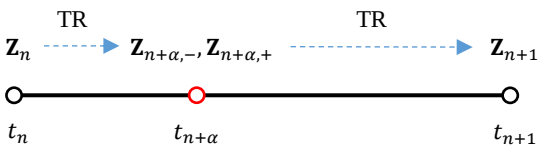

(b) One step with an impact

Figure 5.2 Depiction of scheme 2.

5.5. The Measurement of the Impact-Velocity-Dependent Coefficient of Restitution

In most research of a vibro-impact system, Newton's law of restitution is adopted to model the relationship between the just-before- and just-after- impact velocities as [228, 229]

$$V_+ = -\mu V_- \tag{5.35}$$

where V_- and V_+ are the relative approaching and separating velocities between two objects just before impact and just after impact, respectively; μ is the coefficient of restitution, which is often assumed as a constant in numerical simulations, and it is rare to find work involving the measurement of coefficient of restitution in the study of vibro-impact systems. However, the relationship between the just-before- and just-after- impact velocities is often much more complicated than a linear model could possibly represent [230, 231]. The differences or errors due to a misrepresentation might be magnified when it comes to nonlinear systems. To get a more accurate relationship, an experiment is performed.

5.5.1. The Experimental Setup of the Measurement of Coefficient of Restitution

The experimental setup is shown in Figure 5.3, in which two square aluminium blocks ($20 \times 20 \times 1.2$ mm^3 at the top and $20 \times 20 \times 3$ mm^3 at the bottom) are glued onto both sides of the tip of each cantilever (made from spring steel), and a PTFE film is attached onto the outside (relative to the aluminium-cantilever interface) of each aluminium block. The other end of the beam is clamped in the fixture. Another aluminium block ($42 \times 20 \times 1.2$ mm^3) is stuck onto the fixture right under the tip block. Therefore, the contact or impact will occur between the tip block's PTFE film and the fixed aluminium block, which is consistent with the contact situation in the presented triboelectric energy harvester. A Laser Doppler Vibrometer (LDV, Polytec PSV-500) was used to measure the velocity response of the central point of the upper tip block, and the sampling rate used in experiments was 50 kHz. The cantilever tip was lifted and released repeatedly by hand to generate different impact velocities. It should be noted that there was initially a very small gap between the tip block and the fixed block, so the results are assumed to be applicable to cases where the gaps between the blocks are small.

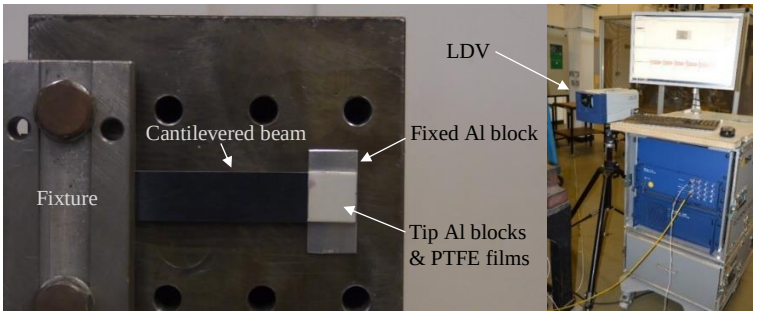

(a) The picture of the experimental setup

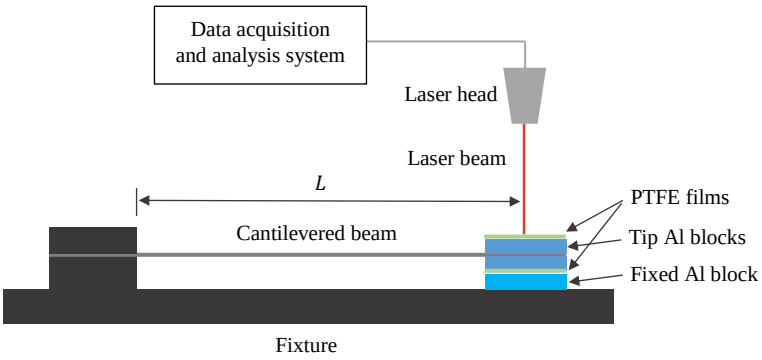

(b) The configuration of the experimental setup

Figure 5.3 The experimental setup of the measurement of coefficient of restitution.

5.5.2. Velocity Responses of the Tip

The cantilever tip was lifted and released at various initial deflections to produce different impact velocities, and a sufficient number of tests were carried out to get a more accurate value of the coefficient of restitution. An example of the time history of the tip's velocity, i.e., V, is shown in Figure 5.4. Note that there is some noise appearing away from the impact pulses and is thus not a concern.

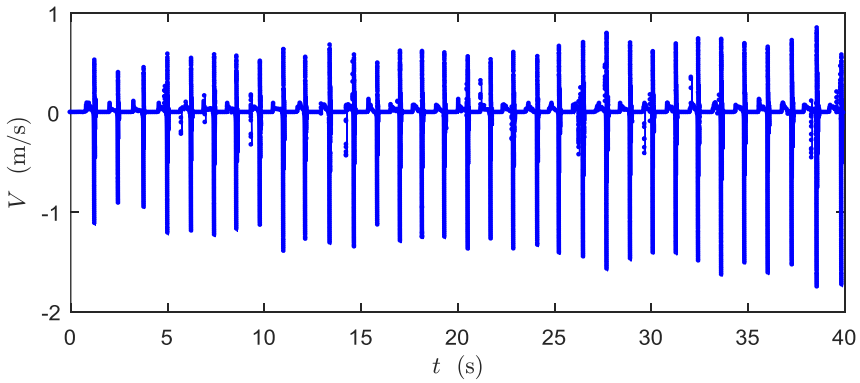

Figure 5.4 An example of the time history of the cantilever tip's velocity.

Three local views of low-, medium-, and high-velocity impacts are shown in Figure 5.5 to reveal the impact characteristics and also to illustrate the picking of the points of just-before- and just-after-impacts. It can be seen that the impact duration, i.e., $\Delta_t = t(V_+) - t(V_-)$, decreases with the increase of impact velocity.

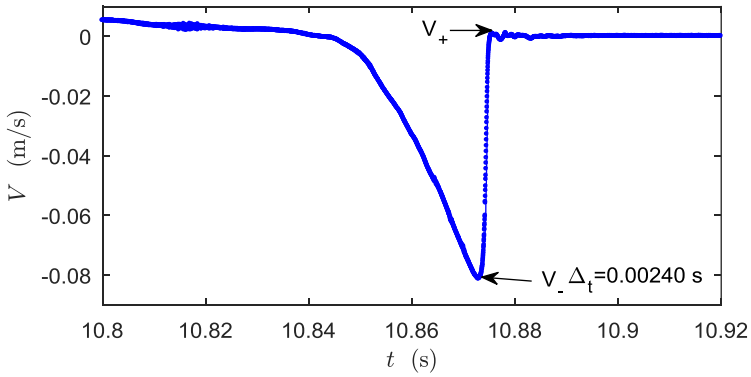

(a) Low-velocity impact

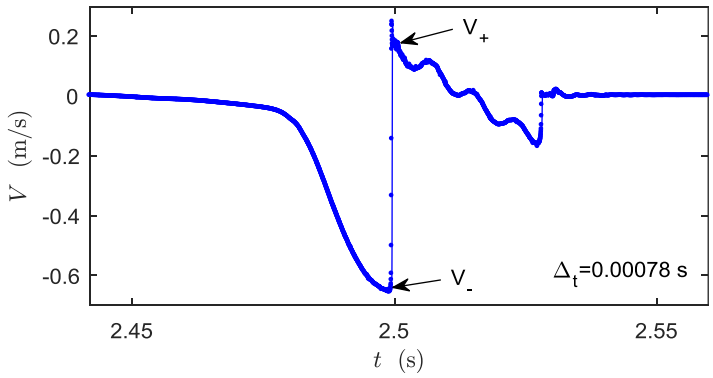

(b) Medium-velocity impact

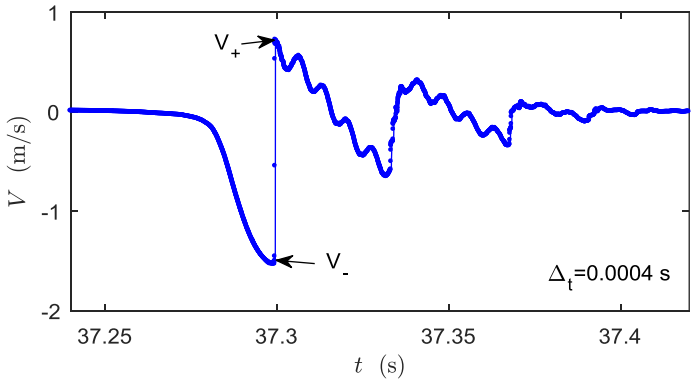

(c) High-velocity impact

Figure 5.5 Velocity responses of the tip in (a) low-, (b) medium-, and (c) high-velocity impacts.

5.5.3. Experimental Data and Curve Fitting

The obtained just-before- and just-after-impact velocities and the derived coefficient of restitution are shown in black dots in Figure 5.6 in both 3D and 2D figures. It is obvious that there exists a relationship among V_-, V_+ and μ. The piecewise quadratic fitting [232] is applied (see Appendix B for details), and the relationship between V_- and μ is of our main concern.

The fitted curve of the relationship between the just-before-impact velocity V_- and the coefficient of restitution μ is shown as the blue curves in Figure 5.6. The surface in Figure 5.6(a) is $\mu = \left|\frac{V_+}{V_-}\right| \left(z = \left|\frac{y}{x}\right|\right)$, and both the data points (V_-, V_+, μ) and the fitted curve are on the surface. Figure 5.6(a) also shows the true spread of data points and the fitting result. The data are well fit, and the V_--μ relationship is quite clear. It can be seen that the coefficient of restitution follows a roughly sigmoidal curve with increasing values of V_-. The fitted relationship between the just-before-impact velocity and the coefficient of restitution will be used in numerical simulations to identify the velocity just after an impact. It is noted that, for impact velocities above or below the tested range, the maximal or the minimal value of the coefficient of restitution of the fitting result in Figure 5.6(b) will be adopted in numerical simulations.

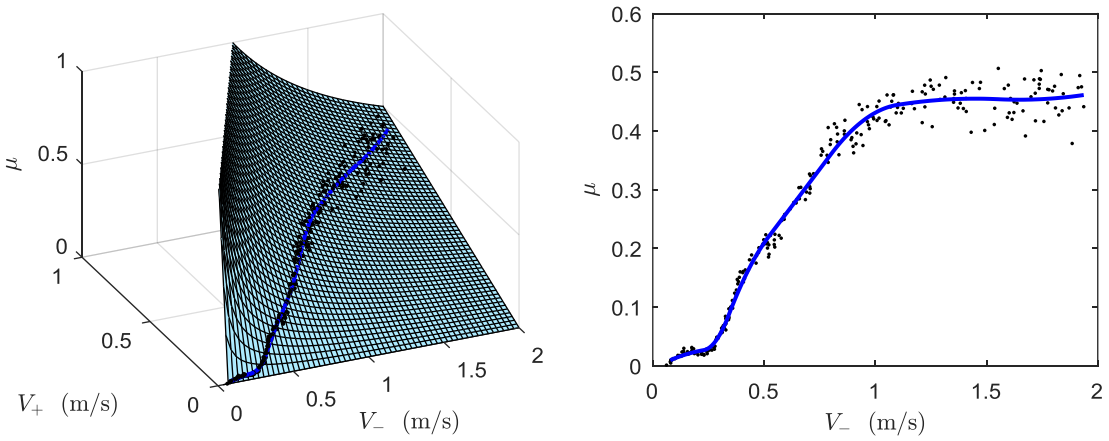

(a) (b)

Figure 5.6 Experimental data and curve fitting in (a) 3D space of V_--V_+-μ and (b) 2D plane of V_--μ.

5.6. Experimental Investigation of Electrostatic Force and Air Damping Between Tips

Since the two side dielectrics and the middle freestanding layer are oppositely charged, there exist the electrostatic forces between m_1 and m_2 and between m_2 and m_3. These forces may be given by the following expressions

$$F_{\mathrm{e1}} = \frac{\varepsilon_{\mathrm{r}}\varepsilon_0 S V_{12}^2}{2d_{12}^2} \tag{5.36}$$

$$F_{\mathrm{e2}} = \frac{\varepsilon_{\mathrm{r}}\varepsilon_0 S V_{23}^2}{2d_{23}^2} \tag{5.37}$$

where ε_{r} is the relative permittivity of PTFE, S the area of contact, V_{12} and V_{23} are the voltage differences between m_1 and m_2 and between m_2 and m_3, respectively. The electrostatic forces might affect the stiffness and damping of the system. Additionally, there exists viscous air damping between any two contacting or separating tips.

To find out whether the electrostatic force and the air damping can influence the dynamic behaviour, a simple contact-mode triboelectric energy harvester is set up as shown in Figure 5.7. A cantilever beam (identical to the one used in the measurement of coefficient of restitution) with a tip mass ($20 \times 20 \times 2\ \mathrm{mm}^3$, aluminium) attached with PTFE dielectric film is placed under base excitation. A much thicker metal beam (assumed to be rigid compared with the spring steel beam) works as a fixed frame, and the two sides of its tip are attached with an aluminium block ($20 \times 20 \times 2\ \mathrm{mm}^3$) and an acrylic block ($20 \times 20 \times 2\ \mathrm{mm}^3$). No impact between the two tips occurred in the test. This is necessary to ensure that the impacts do not obscure the measurements of the electrostatic force effects. The tip displacement of the flexible cantilever beam was measured by a laser displacement sensor (LK-G402, sensitivity of $0.1\ \mathrm{V/mm}$). An accelerometer (PCB 354C03, sensitivity of $10.19\ \mathrm{mV/ms^{-2}}$) was used to monitor the vibration of the shaker table (APS 113). The shaker was supplied a harmonic base motion of amplitude A and frequency f.

Three cases were studied experimentally. To assess the effects of air damping between the tips, case 1 (a single flexible cantilever) is compared with case 2 (single flexible cantilever vibrating near an electrically inert fixed beam, i.e., the flexible tip faces the acrylic fixed block). Case 3 involves a single flexible cantilever vibrating near an electrically active fixed

beam, i.e., the flexible tip faces the aluminium fixed block). To evaluate the effects of electrostatic force, case 2 is compared with case 3. Note that only case 3 can generate electricity and thus electrostatic force between tips. The initial separation gaps in cases 2 and 3 were carefully set to be close or equal.

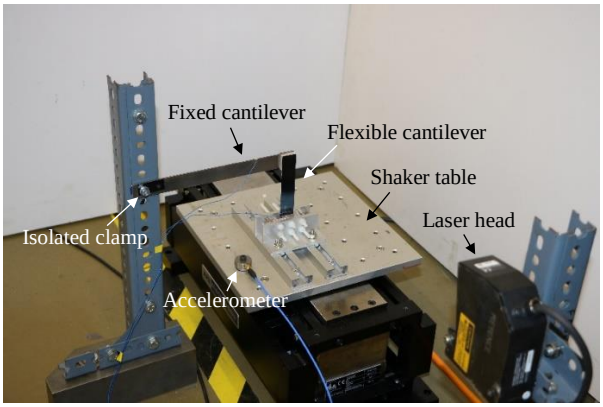

(a) Overall setup

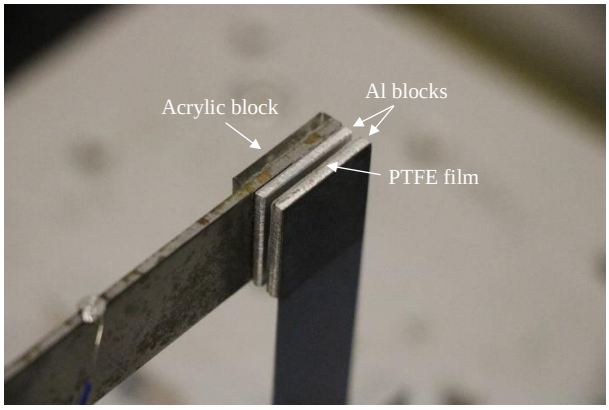

(b) Zoomed-in view of tips

Figure 5.7 The simple contact-mode triboelectric energy harvester model for exploring the effects of electrostatic force and air damping between cantilever tips.

The time histories of the displacement of the flexible tip under different excitation frequencies are shown in Figure 5.8, in which the results of cases 1 to 3 are shown in blue dash-dot, black dot, and red lines, respectively. By comparing cases 2 and 3 with case 1 in terms of the amplitude of vibration, it can be concluded that the effect of viscous air damping between tips appears only when the flexible tip gets close to the fixed tip, and the amplitude reduction is not obvious. While the comparison between cases 2 and 3 suggests that the effect of electrical damping caused by the electrostatic force between tips seems to be negligible as well.

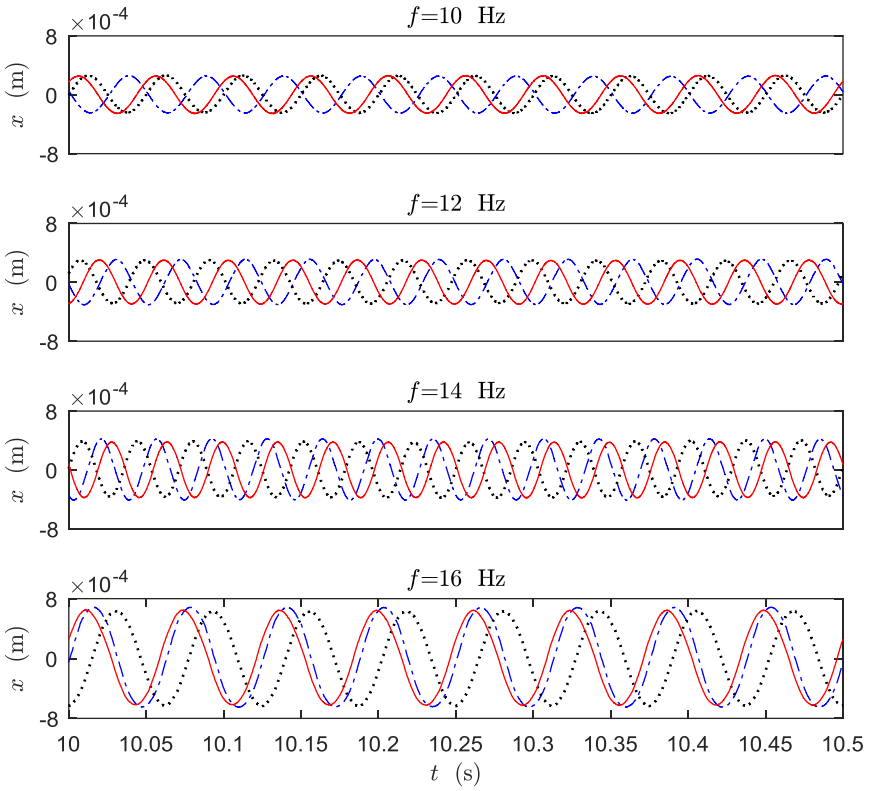

Figure 5.8 Time histories of the displacement of the flexible tip under different excitation frequencies and setups: case 1 (in blue dash-dot), case 2 (in black dot), and case 3 (in red); other parameters are excitation amplitude $A = 0.1$ mm, initial separation distances between tips in cases 2 and 3, i.e., $d_{\mathrm{tt}} = 0.80$ mm, and the load resistance $R = 88$ MΩ.

The power spectral densities (PSD) of the three cases under the excitation frequency of 16 Hz are shown in Figure 5.9, from which it can be seen that the dominant frequency components are the same for these three cases. Therefore, the electrostatic force and air damping between cantilever tips are not necessary to be considered in the modelling work. Without the electrostatic force, the mechanical system and electrical system are uncoupled, but the latter is still dependent on the solutions of the former. Note that the dominant frequency components appear a little bit away from 16 Hz and its multiples, which is assumed being caused by less perfect control of the excitation output of the shaker table.

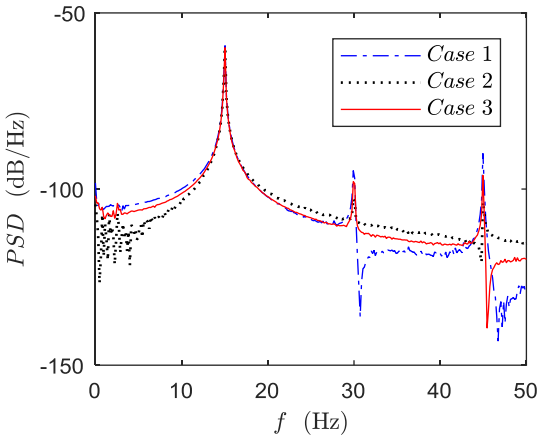

Figure 5.9 PSD response of beam tip for the three cases with an excitation frequency of 16 Hz.

5.7. Experimental Exploration of Load Resistance Effect on the Potential Shifting

In piezoelectric energy harvesting, the resistive shunt damping effect can result in both an upward frequency shift and vibration attenuation [16]. Here, the existence of the load resistance effect in the experimental TEH is studied.

The effect is studied using the experimental setup shown in Figure 5.10. Three identical cantilever beams are vertically clamped onto the shaker table (APS 113). Aluminium and copper blocks are attached at the tips of the three cantilever beams ($89.8 \times 20 \times 0.3\ \mathrm{mm}^3$). In addition, PTFE films ($20 \times 20 \times 0.1\ \mathrm{mm}^3$) are glued onto the two outside tip masses. Impact or contact occurs between the middle aluminium block and the PTFE films on the side blocks. The two side cantilever beams also function as electrodes. The BK Precision 4052 function generator and the APS 125 power amplifier were used to power the shaker table to apply excitation. One accelerometer (PCB 354C03, sensitivity of $10.19\ \mathrm{mV/ms^{-2}}$) was fixed onto the shaker table to monitor the excitation applied. Two laser displacement sensors, KEYENCE LK-G500 on the left and LK-G402 on the right (both sensitivities are $0.1\ \mathrm{V/mm}$), were used to measure the displacements of the left and middle tip masses (m_1 and m_2), respectively. The analogue outputs of the sensors and the electrical output of the harvester were processed by the NI-9234 data acquisition module (DAQ) and LabVIEW 2013. It is noted that the NI-9234 module is meant for vibration tests and has a relatively low input impedance (305 kΩ in differential mode), and thus it cannot be directly used in electric tests when the unit under test is of higher output impedance. However, triboelectric energy

harvesters often have high output impedances. One way to get around this problem is shown in Figure 5.11, in which a voltage follower or a buffer is used to isolate the high output impedance of the harvester and keep the voltage across the load resistance R the same as that across R_{o} or the output voltage V_{out}.

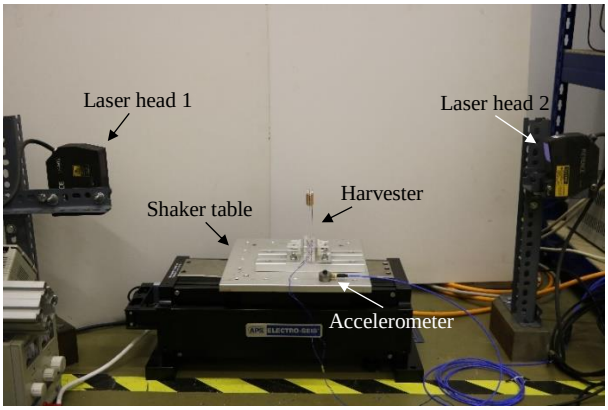

(a) Overall experimental setup

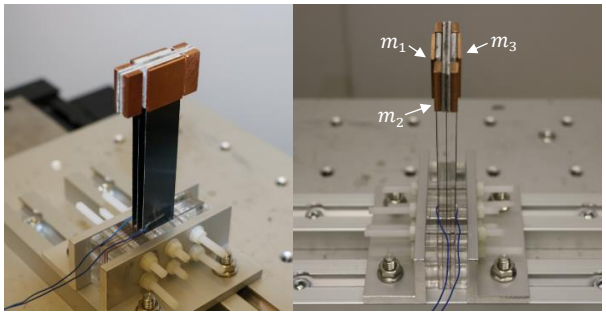

(b) Front and side views of the harvester

Figure 5.2 Experimental setup of the vibro-impact TEH using three cantilevered beams.

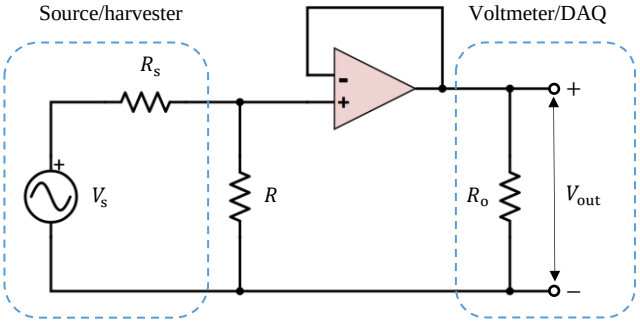

Figure 5.3 The voltage follower in the circuit between the harvester and the DAQ.

By varying the load resistance R, the corresponding frequency responses of w_{rel1} and w_{rel2} and the voltage outputs, i.e., the mean peak-to-peak voltage V_{ppm} and the root mean square

voltage V_{rms}, are obtained and shown in Figure 5.12 (a possible shift trend of the frequency response in a piezoelectric energy harvesting is denoted by the black dotted arrows in Figure 5.12(a) for reference). It can be seen that the load resistance variation does not result in either a frequency shift or vibration attenuation in the current TEH. This is assumed to be a result of the weak electrostatic effect between the beam tips. In piezoelectric energy harvesters, on the other hand, the piezoelectric effect under the change of the voltage across the piezo patch can result in the stiffness change of the piezo patch, which then induces the stiffness variation of the structure. The electrostatic effect, which is theoretically capable of doing the similar thing as well, seems to be too weak to cause any obvious change of the stiffness or damping of the current system. Since the load resistance will be different in various applications, the fact that the resonance peak does not shift with resistance may be advantageous. Note the voltage output increases with the increase of load resistance, which is a common phenomenon. For a clear depiction of frequency shifting in piezoelectric energy harvesters, interested readers are referred to Figures 3.16 and 3.18(b) in Ref. [16].

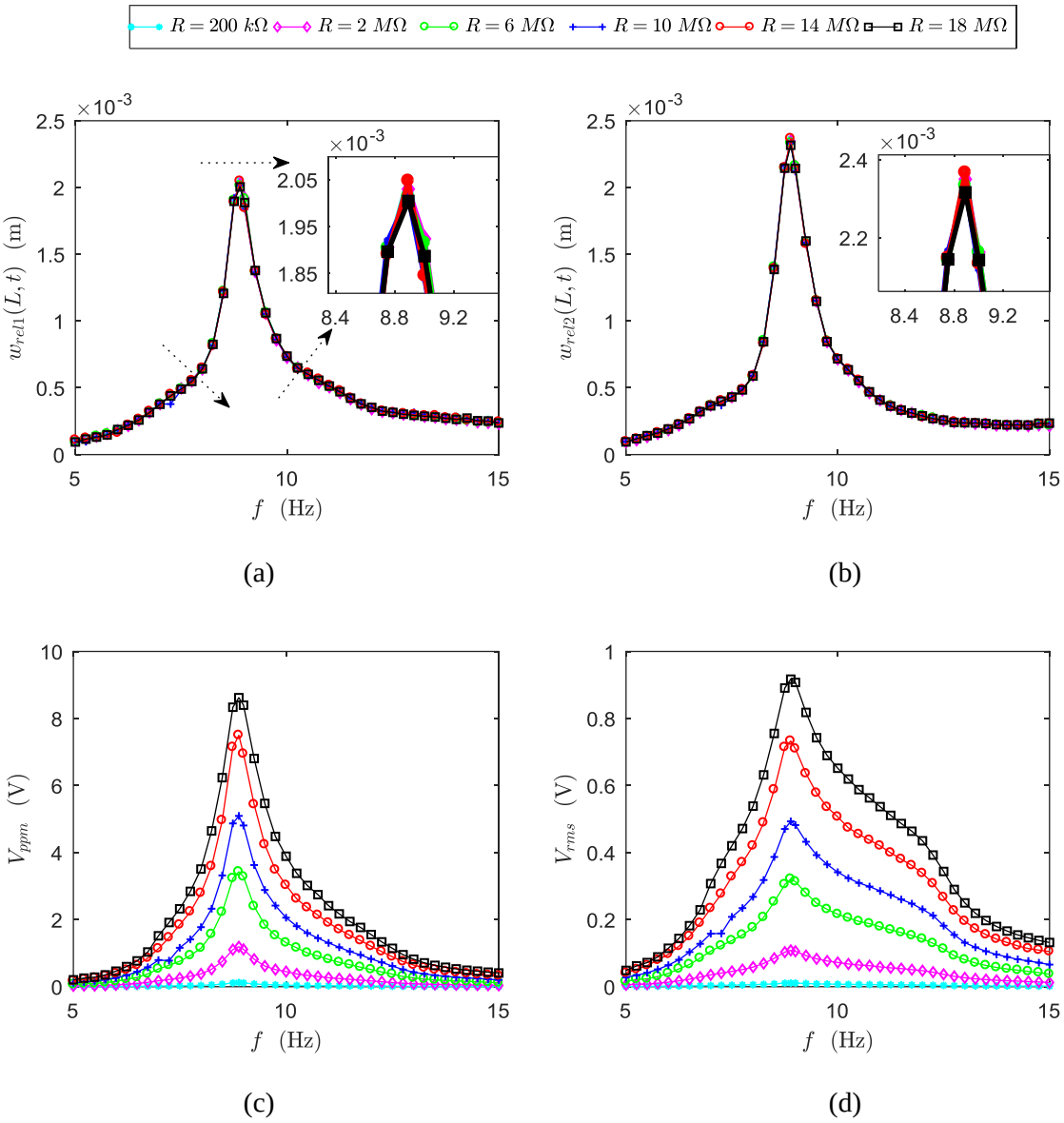

Figure 5.4 Frequency responses of (a) w_{rel1}, (b) w_{rel2}, (c) the mean peak-to-peak voltage output V_{ppm}, and (d) the root mean square voltage output V_{rms}; Other parameters are $A = 0.16$ mm, $m_1 = m_3 = 10.3$ g, $m_2 = 25$ g, $s_{12} = 0.25$ mm and $s_{23} = 0.45$ mm (The subfigures in (a) and (b) are the local views of the peaks).

5.8. Numerical and Experimental Comparisons and Validations of the System Responses

5.8.1. Comparisons and Validations of the Two Modelling Methods of the Mechanical Vibration

Two different methods are used to model the vibration of the system in Section 5.1, and the difference is that the eccentricity of the tip mass is considered in model 2. The frequency responses of w_{rel1} and w_{rel2} computed (using the RK4 method) from the two modelling methods are shown in Figure 5.13 and compared with the experimental results. The experimental setup is the same as shown in Figure 5.10, and the parameters used are given in Table 1 if not otherwise specified. The two modelling methods produce very similar results, both of which are in a good correlation with the experimental results considering the complexity of the vibro-impact system being studied. Model 1 seems to perform slightly better at/around the resonance peak. Therefore, model 1 will be adopted in the following study.

Table 5.1 Parameters used in simulation and experiment.

Parameter	Value
Length of the cantilever in model 1, L	79.8 mm
Length of the cantilever in model 2, L'	69.8 mm
Thickness of the cantilever, t_{b}	0.3 mm
Width of the cantilever, b	20 mm
Eccentricity of the tip mass in model 2, e_{c}	10 mm
Density of the cantilever, ρ	7900 kg/m^3
Young's modulus of the cantilever, E	193 GPa
Damping ratio of the cantilever, ζ	0.0026
Area of contact, S	20×20 mm^2
Thickness of the dielectric, d_1, d_2	0.1 mm
Relative permittivity of the dielectric, $\varepsilon_{\mathrm{r1}}$, $\varepsilon_{\mathrm{r2}}$	2.0

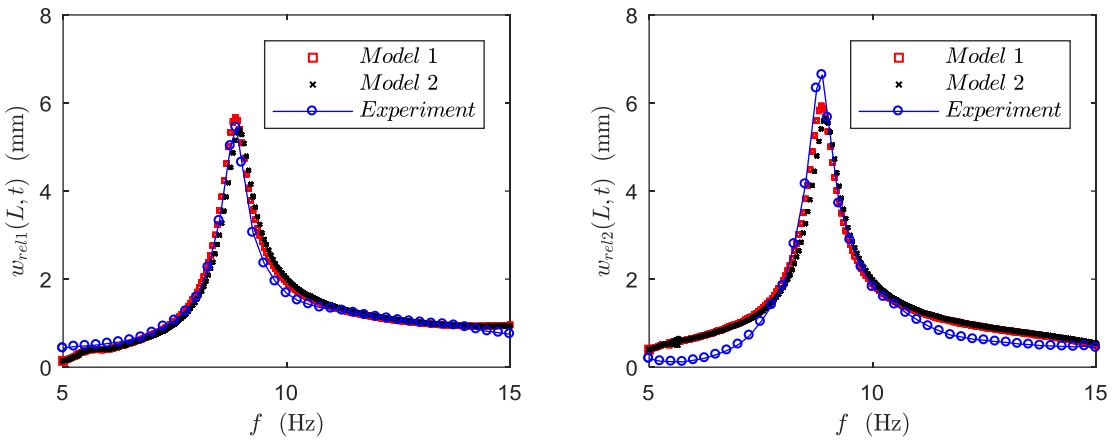

(a) (b)

Figure 5.5 Frequency responses of (a) w_{rel1} and (b) w_{rel2} from the numerical simulation and the experiment; $A = 0.4$ mm, $m_1 = m_3 = 10.3$ g, $m_2 = 25$ g, $J_{m1} = J_{m3} = 3.58 \times 10^{-7}$ kg m^2, $J_{m2} = 9.51 \times 10^{-7}$ kg m^2, $s_{12} = 0.26$ mm, and $s_{23} = 0.52$ mm.

5.8.2. Comparisons and Validations of Different Numerical Methods

The ODEs of the non-smooth dynamical system are not stiff and thus can be solved using any explicit methods, such as RK4 which is of higher order accuracy than the TR and TR-BDF2 methods. However, RK4 cannot solve the stiff ODE of electrical output, i.e., Eq. (5.31), correctly (the solution may be divergent) or efficiently (a very small time step is required). The two schemes proposed in Section 5.4.2 are compared with one another, with the RK4 and with the experimental results to determine the best algorithm for solving the whole system (the non-smooth structural system and the stiff electrical system).

The frequency responses of w_{rel1} and w_{rel2} computed from the RK4 method, scheme 1, and scheme 2 are shown in Figure 5.14 in comparison with the experimental results. It is clear that the solutions are very close to each other. Both of the schemes solve the non-smooth dynamical system as well as the RK4 method does, and they are all in a good agreement with the experimental results.

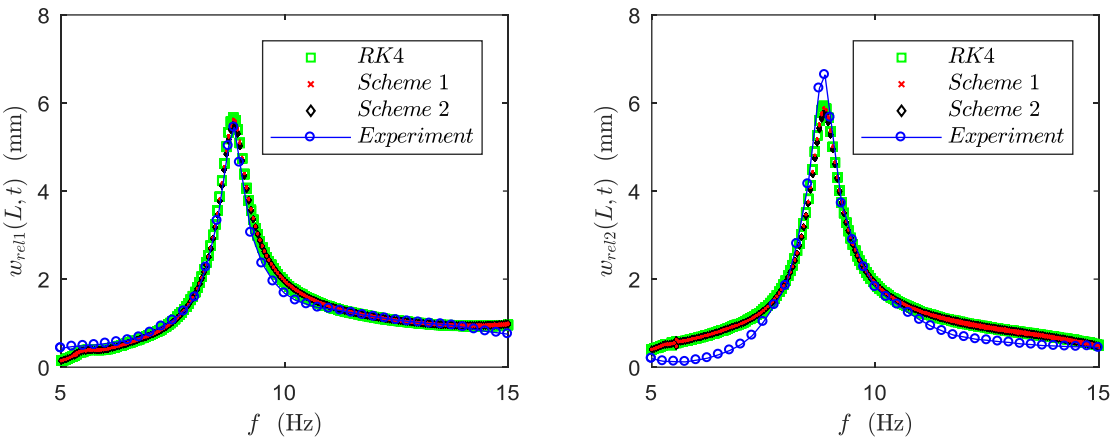

(a) (b)

Figure 5.6 Comparisons of the frequency responses of (a) $w_{\mathrm{rel1}}(L,t)$ and (b) $w_{\mathrm{rel2}}(L,t)$ computed from the RK4 method, scheme 1, and scheme 2, respectively; $A = 0.4$ mm, $m_1 = m_3 = 10.3$ g, $J_{m1} = J_{m3} = 3.58 \times 10^{-7}$ kg m^2, $J_{m2} = 9.51 \times 10^{-7}$ kg m^2, $m_2 = 25.0$ g, $s_{12} = 0.26$ mm, $s_{23} = 0.52$ mm.

To compare between the two schemes in solving the stiff ODE of electrical output, the frequency responses of the root mean square voltage, i.e., V_{rms}, of the two schemes and the experiment are shown in Figure 5.15, from which good agreement can be observed. It is noted that the root mean square voltage V_{rms} from the simulation is computed by using evenly spaced data points from its time history even though the time history itself is calculated using different size time steps due to the non-smooth characteristics. Any potential errors arising from the use of evenly spaced time steps in the RMS calculation can be reduced by using smaller time steps and more samples. Besides, the least squares and the bisection methods are used in comparing the numerical solutions with the experimental results to identify the value of the tribo-charge surface density. To show more details, the steady state time histories of the voltage output obtained from both the experiment and the simulation at $f = 8.75$ Hz (around the peak vibration) are given in Figure 5.16 for comparison. It can be seen that the overall agreement between the experiment and simulation is good. The results of the two schemes mainly differ around the impact events. The local view shown on the right of Figure 5.16(b) illustrates the oscillations of the solutions just after an impact event. Apparently, scheme 2 is more stable or less oscillatory than scheme 1. Therefore, scheme 2 is to be employed in solving a non-smooth system-based triboelectric energy harvesting system.

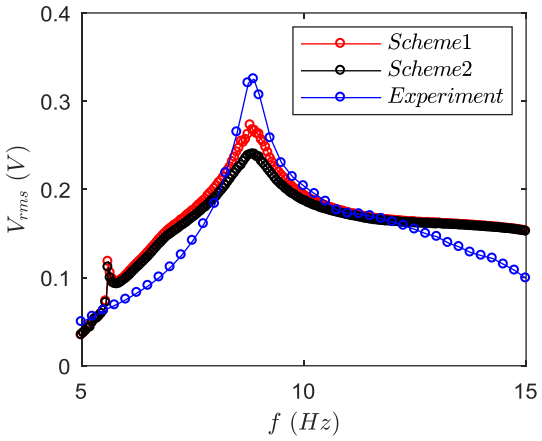

Figure 5.7 Comparisons of the frequency responses of V_{rms} between the two schemes and the experiment; the parameters are the same as Figure 5.14, and an estimated tribo-charge surface density of $\sigma = 5.72\ \mu\mathrm{C/m^2}$ and a load resistance of $R = 1\ \mathrm{M\Omega}$ are used).

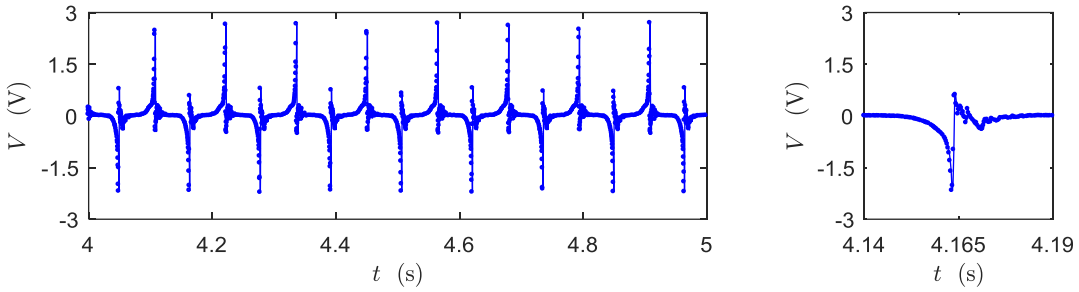

(a)

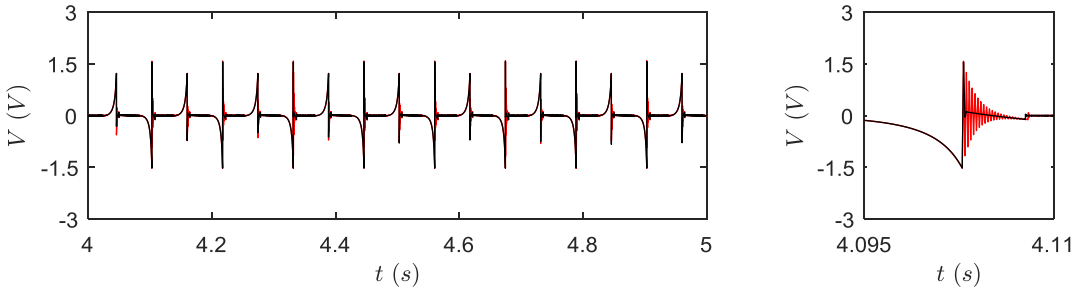

(b)

Figure 5.8 Comparisons of the steady state time histories of the voltage output (left) obtained from (a) the experiment (in blue) and (b) the simulation (scheme 1 in red and scheme 2 in black) at $f = 8.75$ Hz and their local views (right).

5.8.3. The Effect of Tip Mass Ratio

The tip mass ratio is defined as the ratio of the middle tip mass to the side tip mass, i.e., $R_{\mathrm{m}} = \frac{m_2}{m_1} = \frac{m_2}{m_3}$. The experimental and numerical frequency responses of $w_{\mathrm{rel1}}(L,t)$ and V_{rms} of four different tip mass ratios are given in Figure 5.17. Good agreement between experimental and numerical results is found, especially for vibration responses. It can be seen that the small tip mass ratio $R_{\mathrm{m}} = 2.43$ has much stronger peak vibration which, however, does not induce obvious electrical output difference compared with $R_{\mathrm{m}} = 2.94$. Bigger tip mass ratios have better electricity generation performance at relatively high frequencies and have a wider bandwidth over which its performance is superior to smaller tip mass ratios. Besides, the much smaller peak vibration amplitude of the harvester at relatively larger mass ratios can be an advantage in real applications.

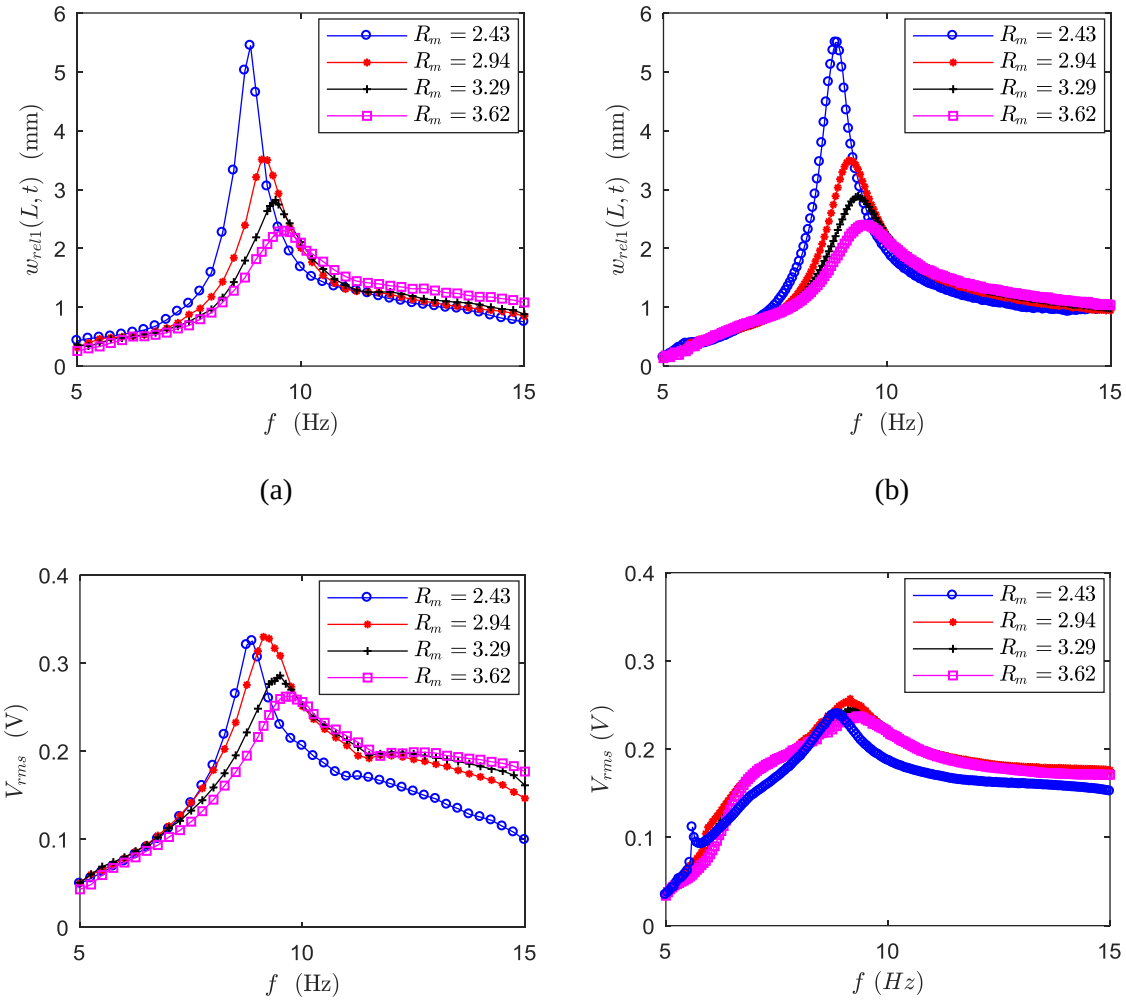

Figure 5.9 Experimental (left column, (a) and (c)) and numerical (right column, (b) and (d)) frequency responses of $w_{\mathrm{rel1}}(L,t)$ (first row, (a) and (b)) and V_{rms} (second row, (c) and (d)) at different tip mass ratios; $m_2 = 25.0$ g, $J_{m2} = 9.51 \times 10^{-7}$ kg m^2, $A = 0.4$ mm, $s_{12} = 0.26$ mm, $s_{23} = 0.52$ mm, and $R = 1$ MΩ; mass moments of inertia and estimated tribo-charge surface densities are $J_{m1} = J_{m3} = 3.58 \times 10^{-7}$ kg m^2 and $\sigma = 5.72$ μC/m^2 at $R_{\mathrm{m}} = 2.43$, $J_{m1} = J_{m3} = 2.92 \times 10^{-7}$ kg m^2 and $\sigma = 5.75$ μC/m^2 at $R_{\mathrm{m}} = 2.94$, $J_{m1} = J_{m3} = 2.88 \times 10^{-7}$ kg m^2 and $\sigma = 5.38$ μC/m^2 at $R_{\mathrm{m}} = 3.29$, and $J_{m1} = J_{m3} = 2.51 \times 10^{-7}$ kg m^2 and $\sigma = 4.98$ μC/m^2 at $R_{\mathrm{m}} = 3.62$.

5.8.4. The Effect of Excitation Amplitude

The experimental and numerical frequency responses of $w_{\mathrm{rel1}}(L,t)$ and V_{rms} under different excitation levels are shown in Figure 5.18. Obviously, both the vibration amplitude and the electrical output increase along with the rise of the excitation level, and the increase seems to be linear. The graph of the estimated tribo-charge surface density σ against the excitation

amplitude A is given in Figure 5.19, and a quadratic polynomial can give a relatively good fitting for the discrete data points, which then indicates a quadratic relationship between the tribo-charge surface density and the excitation amplitude in the excitation range being studied.

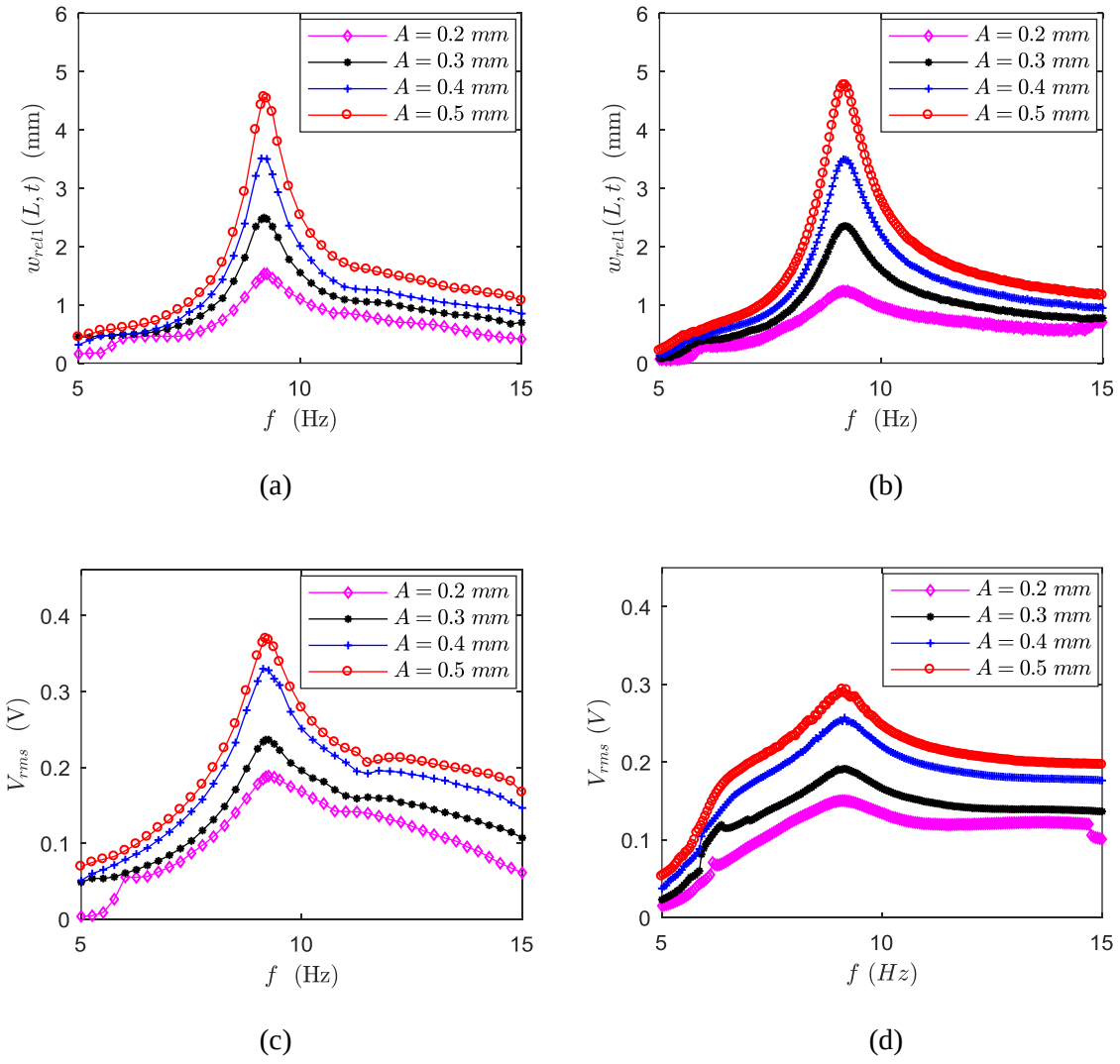

Figure 5.10 Experimental (left column, (a) and (c)) and numerical (right column, (b) and (d)) frequency responses of $w_{\mathrm{rel1}}(L,t)$ (first row, (a) and (b)) and V_{rms} (second row, (c) and (d)) at different excitation levels; $m_2 = 25.0$ g, $R_{\mathrm{m}} = 2.94$, $J_{m1} = J_{m3} = 2.92 \times 10^{-7}$ kg m^2, $J_{m2} = 9.51 \times 10^{-7}$ kg m^2, $s_{12} = 0.26$ mm, $s_{23} = 0.52$ mm, and $R = 1$ MΩ; estimated tribo-charge surface densities are $\sigma = 4.56$ μC/m^2 at $A = 0.2$ mm, $\sigma = 4.75$ μC/m^2 at $A = 0.3$ mm, $\sigma = 5.75$ μC/m^2 at $A = 0.4$ mm, and $\sigma = 6.09$ μC/m^2 at $A = 0.5$ mm.

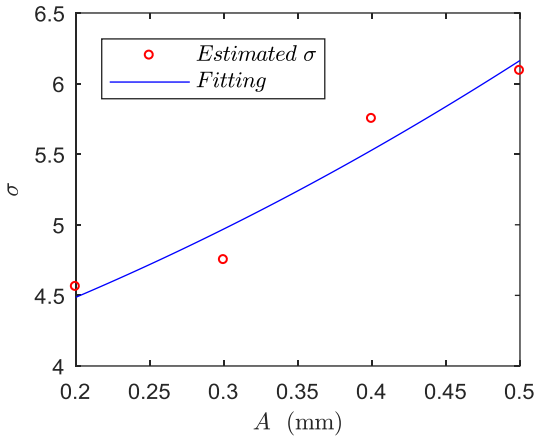

Figure 5.19 Relationship between the tribo-charge surface density σ and the excitation amplitude A; the quadratic polynomial used in fitting is $\sigma(A) = 3.75A^2 + 2.965A + 3.743$ (with 95% confidence bounds).

To demonstrate the harvester's charging performance at high excitation levels, a capacitor charging experiment is carried out. The diagram of the circuit used in this experiment is shown in Figure 5.20(a), in which a full-bridge diode rectifier is employed to convert the alternating current (AC) to the direct current (DC) and a voltmeter is used to monitor the charging process. A 10-μF and 50-V capacitor is used with an excitation of $f = 9.185$ Hz and $A = 0.5$ mm. The charging result is shown in Figure 5.20(b). It can be seen that the capacitor is charged up to 160 mV in about 1 min. Considering the small size of the harvester and the low level of excitation, its performance is satisfying. Since a main purpose of this study is to develop the methods to study the non-smooth triboelectric energy harvesters from the perspective of structural dynamics, the triboelectric materials used in experiments are not micro- or nano- textured on contact surfaces (such as nano-etched triboelectric materials). Because nano-etched triboelectric materials are more efficient than those without nano-etching [93], the performance of the proposed harvester would be much higher had nanomaterials been used.

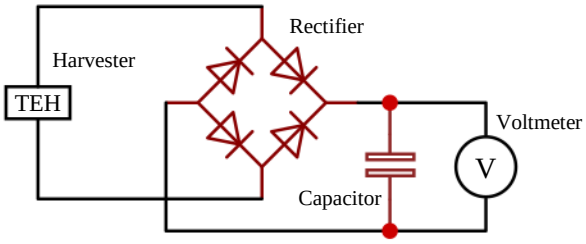

(a)

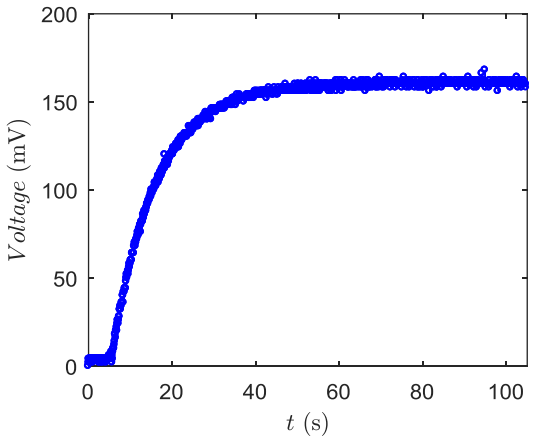

(b)

Figure 5.11 Charging capacitor; (a) the circuit diagram of the experiment and (b) the charging time history; a 10-μF and 50-V capacitor was used in the experiment.

5.9. Conclusions

This chapter presents theoretical modelling, numerical simulation and experimental validation of a new triboelectric energy harvester in the form of a three-cantilever-beam vibro-impact system. Two modelling methods of the mechanical vibration of the three-cantilever-beam vibro-impact system are presented, and an experimentally identified relationship between the just-before-impact velocity and the velocity-dependent coefficient of restitution is used in the modelling of the impact. The electrical modelling of the contact freestanding mode triboelectric energy harvester is then presented. This ordinary differential equation (ODE) modelling the electrical output of the triboelectric energy harvester is found to be stiff. The TR-BDF2 (the combination of the trapezoidal rule and the second-order backward differentiation formula) as an implicit numerical integration method is introduced

and two schemes are shown to successfully solve the non-smooth dynamical system and the response-dependent stiff ODE of the electrical output. This is the first application of a TR-BDF2 scheme to a non-smooth system. Experimental investigations of the electrostatic force and air damping between cantilever tips, the load resistance effect on the potential frequency shifting phenomenon, and the mass ratio and excitation amplitude effects on electricity generation performance are then conducted. Good agreement between experimental and numerical results is found, especially for vibration responses, and the first mechanical model, which does not involve the eccentricity of the tip mass, performs better than the second one in comparison with the experimental results. The main conclusions are drawn as follows.

(1) Both the electrostatic force and air damping between cantilever tips can be neglected, which further results in a theoretical simplification due to the uncoupling between the mechanical and electrical systems.

(2) The triboelectric energy harvester under this study does not have the frequency shifting phenomenon commonly seen in piezoelectric energy harvesting, and the reason seems to be the weak electrostatic effect between the tip masses. The non-shifting resonance peak of the harvester can be an advantage relative to piezoelectric energy harvesters.

(3) Two numerical schemes are implemented to solve the stiff electrical system. The second of these schemes solves for the electrical output more accurately around non-smooth events. This indicates that the second scheme may be useful in the modelling of other triboelectric energy harvesting systems, such as the in-plane sliding mode triboelectric energy harvesters where friction-induced vibration is involved. The non-smooth mechanical system outputs from both numerical schemes match those obtained with a fourth-order Runge-Kutta method.

(4) A smaller tip mass ratio does not generate much higher electricity despite inducing much stronger vibration. A larger ratio performs better at relatively high frequencies and has a wider bandwidth over which its electricity generation performance is superior.

(5) Both the vibration amplitude and the electrical output linearly increase with increasing excitation level, and the relationship between the tribo-charge surface density and the excitation amplitude is found to be quadratic after curve fitting.

Chapter 6

Nonlinear Structural Dynamics of a Triboelectric Energy Harvester in Sliding Mode with Multistability

6.1. Introduction

The relationship between friction and triboelectrification is more interesting in sliding mode TEHs. However, different combinations of triboelectric materials have different values of coefficients (static and kinetic) of friction which can also be affected by material surface morphologies. Thus, to draw a general conclusion of this relationship from the study of certain combinations of triboelectric materials may not be feasible. Besides, friction and triboelectrification seem to have a mutual interaction, which makes the relevant study more difficult but interesting. Nevertheless, investigating such a relationship from the prospects of materials is beyond the scope of this research. Instead, the effect of friction on the output performance of the sliding mode TEH proposed in this chapter is studied via structural dynamics. In addition, magnetic multistability is incorporated in the harvester in order to achieve broadband energy harvesting, and some interesting topics that have been raised, such as the categorization of different types of multistability of a non-conservative system and the effect of initial conditions on the dynamics of the system, are discussed.

The outline for the rest of this chapter is as follows: Section 6.2 introduces the design of the harvester and describes its working mechanism. Section 6.3 presents the mechanical modelling of the vibration of a cantilever beam when its tip is subject to both magnetic and frictional forces. The electrical modelling of the harvester's output is given in Section 6.4. The method used to solve the non-smooth mechanical mechanical system and the stiff electrical system is the same as the method that has been used in Chapter 5 and a brief description is given in Section 6.5.1. Section 6.5.2 analyses the effect of the electrostatic force. Coupled and uncoupled electromechanical models are compared. The influence of the non-conservative force (the friction force) on the multistability of the system is investigated

in Section 6.5.3. Section 6.5.4 makes the comparison among three types of stability of the system via discrete numerical frequency sweeps. Section 6.5.5 presents a study investigating the effect of the excitation level on the system response. The influence of the friction is discussed in Section 6.5.6. Afterwards, the basins of attraction are analysed in Section 6.5.7. The conclusions of this study are drawn in Section 6.6.

This chapter is based on the following paper submitted by the author of this thesis and his supervisors:

Y. Fu, H. Ouyang, R.B. Davis, Nonlinear structural dynamics of a new sliding mode triboelectric energy harvester with multistability, Nonlinear Dynamics, under review.

6.2. Design

The configuration of the proposed sliding-mode triboelectric energy harvester is shown in Figure 6.1(a). All the components are integrated onto a base which receives a sinusoidal excitation. A cantilever beam is clamped onto the base and its free end is attached with a slider in which a cylindrical magnet is embedded. Additionally, two identical magnets are fixed to the base and symmetrically located to attract the oscillating magnet. As shown in Figure 6.1(b), the slider has a circular contact area and slides over two specially made patches. The slider is attached with an electrode (known as the top electrode) and a dielectric (such as PTFE). The base is composed by an electrically active patch (EAP, aluminium) and an electrically inert patch (EIP, PTEG). The circular electrically active area works as the bottom electrode and has the same circular area as the top electrode. Both the top and bottom electrodes are wired into an outside circuit to form a loop (not shown in Figure 6.1). Under the base excitation, the slider can oscillate, and its motion will be affected by the magnetic field.

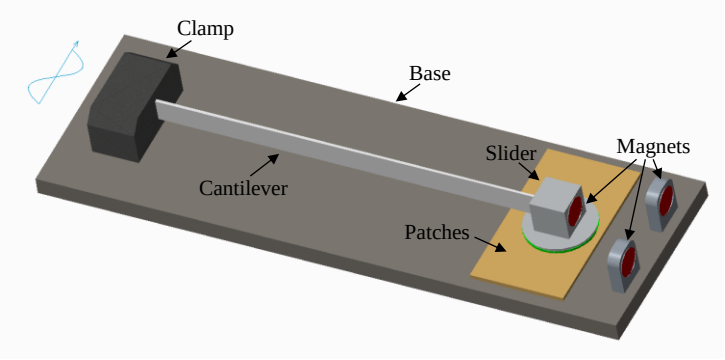

(a)

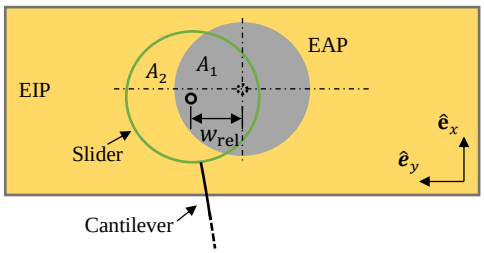

(b)

Figure 6.1 Configurations of (a) the sliding-mode triboelectric energy harvester and (b) the slider on patches.

During sliding, triboelectrification only happens in the contact area between the slider and the electrically active patch (EAP). The charge transfer process [107] of the TEH is depicted in Figure 6.2, where a resistor denoted by *R* is wired with the harvester and the current in the circuit is represented by *I* (note that the electrically inert patch (EIP) is not shown in Figure 6.2). When the top dielectric fully overlaps the bottom electrode (the EAP), charge transfer occurs at the contact area owing to the triboelectric effect, and the aluminium loses electrons while the PTFE gains electrons. The charge transfer process at this stage will result in net positive charges on the EAP and equivalent net negative charges on the dielectric, as shown in Figure 6.2(a). As the slider slides out of the EAP, an electric potential difference between the two electrodes is established simultaneously, which drives the electrons in the top electrode to flow to the bottom electrode. The electron flow induces an instantaneous current that flows in an opposite direction as shown in Figure 6.2(b). When the slider fully slides outside the EAP, the electrons will be balanced between the top dielectric and top electrode, as shown in Figure 6.2(c). Once the slider starts sliding back, as illustrated in Figure 6.2(d), the balance gets broken and the current will flow from the top electrode to the bottom

electrode until the slider fully overlaps the EAP again. Thereafter, the process is repeated as slider oscillates.

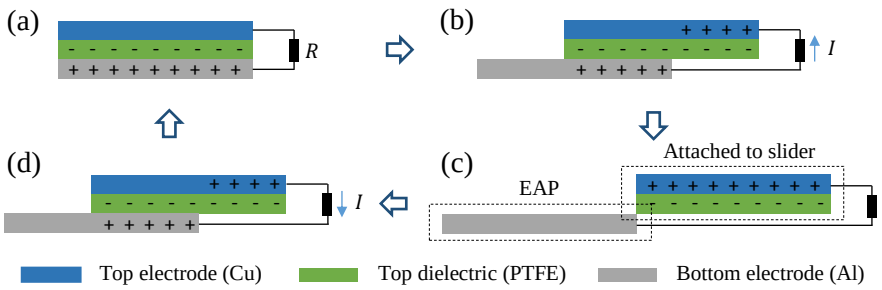

Figure 6.2 The charge transfer process [107] of the presented sliding-mode triboelectric energy harvester.

Note that although the configuration is similar to some bistable piezoelectric energy harvesters [169], the energy harvesting mechanism is completely new and the system is no longer smooth due to the involvement of friction between the slider and the patches. Nevertheless, the presented triboelectric energy harvester can be combined with a bistable piezoelectric energy harvester to form a hybrid energy harvester, in which case the harvesting performance may be enhanced.

6.3. Modelling of the Mechanical System

The equations modelling the mechanical system can be derived using the Lagrange-d'Alembert principle which is an extended Hamilton's principle in the presence of external forces, such as friction force. The corresponding variational equation is

$$\int_{t_1}^{t_2} [\delta(T-U)+\delta W]\,\mathrm{d}t = 0 \tag{6.1}$$

where T and U are the kinetic and the potential energies and T consists of two parts, i.e., the kinetic energies of the beam and the slider, and U comprises of the potential energies of the beam and the magnetic field, W is the work done by the external force, i.e., the friction force F_f, and $W = \int_0^{L_\mathrm{b}} F_\mathrm{f}\delta(x-L_\mathrm{b})\,w_\mathrm{rel}(x,t)\mathrm{d}x$ where L_b is the length of the cantilever beam, $\delta(x-L_\mathrm{b})$ is the Dirac's delta function and $w_\mathrm{rel}(x,t)$ is the transverse displacement relative to the base, δ represents an infinitesimal variation, and t_1 and t_2 are the start and the end times.

The kinetic energy of the cantilever beam can be given as

$$T_{\mathrm{b}} = \frac{1}{2}\int_0^{L_{\mathrm{b}}} \rho_{\mathrm{b}} A_{\mathrm{b}} \left[\frac{\partial w_{\mathrm{rel}}(x,t)}{\partial t} + \frac{\mathrm{d}g(t)}{\mathrm{d}t}\right]^2 \mathrm{d}x \tag{6.2}$$

where ρ_{b} and A_{b} are the cantilever beam's density and cross sectional area, and $g(t)$ is the base displacement.

The kinetic energy of the slider is

$$T_{\mathrm{s}} = \frac{1}{2} m_{\mathrm{s}} \left[\frac{\partial w_{\mathrm{rel}}(x,t)}{\partial t} + \frac{\mathrm{d}g(t)}{\mathrm{d}t}\right]^2_{x=L_{\mathrm{b}}} + \frac{1}{2} J_{\mathrm{s}} \left[\frac{\partial^2 w_{\mathrm{rel}}(x,t)}{\partial x \partial t}\right]^2_{x=L_{\mathrm{b}}} \tag{6.3}$$

where m_{s} and J_{s} are the mass and the second moment of inertia of the slider, where the latter is considered negligible for the small tip mass used in this harvester.

The elastic potential energy of the cantilever beam is

$$U_{\mathrm{b}} = \frac{1}{2}\int_0^{L_{\mathrm{b}}} EI \left[\frac{\partial^2 w_{\mathrm{rel}}(x,t)}{\partial x^2}\right]^2 \mathrm{d}x \tag{6.4}$$

where E is the Young's modulus of the beam and I is the second moment of area of the beam's cross section.

The relative locations of the magnets are shown in Figure 6.3. Magnetic dipoles are used to represent them.

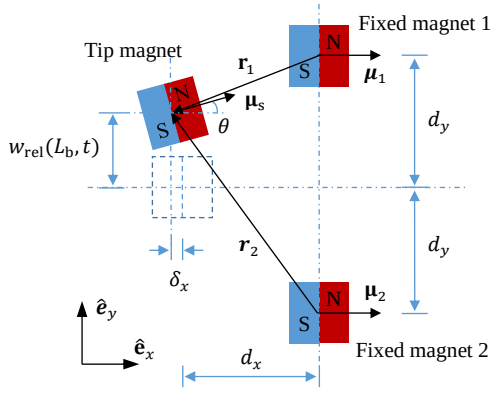

Figure 6.3 Relative locations of the magnets.

The elastic potential energy provided by the magnetic field is given as

$$U_{\mathrm{m}} = -\sum_{i=1}^{n} \mathbf{B}_i \cdot \boldsymbol{\mu}_{\mathrm{s}} \tag{6.5}$$

where n is the number of fixed magnets (two in this case), $\mathbf{B}_i$ is the magnetic field generated by the i-th fixed magnet at the location of the tip magnet (in the slider), $\boldsymbol{\mu}_{\mathrm{s}}$ is the magnetic moment vector of the tip magnet and is expressed as

$$\boldsymbol{\mu}_{\mathrm{s}} = M_{\mathrm{s}} V_{\mathrm{s}} \cos\theta \, \hat{\mathbf{e}}_x + M_{\mathrm{s}} V_{\mathrm{s}} \sin\theta \, \hat{\mathbf{e}}_y \tag{6.6}$$

where M_{s} is the magnitude of the magnetization of the magnet at the cantilever tip and can be estimated using the residual flux density B_{r} as $M_{\mathrm{s}} = B_{\mathrm{r}}/\mu_0$, where μ_0 is the vacuum permeability; V_{s} is the magnet's volume, θ is the slope of the beam at the tip, $\hat{\mathbf{e}}_x$ and $\hat{\mathbf{e}}_y$ are the unit vectors along the x- and the y- axis, respectively.

Similarly, the magnetic moment vectors for the fixed magnets are given as

$$\boldsymbol{\mu}_i = M_i V_i \, \hat{\mathbf{e}}_x \tag{6.7}$$

where M_i and V_i are the magnitude of the magnetization and the volume of the i-th fixed magnet, respectively.

The separation vectors from the positions of the fixed magnets to that of the tip magnet are expressed as

$$\begin{aligned} \mathbf{r}_1 &= -(d_x + \delta_x) \, \hat{\mathbf{e}}_x + \left[w_{\mathrm{rel}}(L_{\mathrm{b}}, t) - d_y \right] \hat{\mathbf{e}}_y \\ \mathbf{r}_2 &= -(d_x + \delta_x) \, \hat{\mathbf{e}}_x + \left[w_{\mathrm{rel}}(L_{\mathrm{b}}, t) + d_y \right] \hat{\mathbf{e}}_y \end{aligned} \tag{6.8}$$

where δ_x is the longitudinal displacement of the tip and it can be derived as

$$\delta_x = \frac{1}{2} \int_0^{L_{\mathrm{b}}} \left[\frac{\partial w_{\mathrm{rel}}(x,t)}{\partial x} \right]^2 \mathrm{d}x \tag{6.9}$$

Then, the magnetic field generated by the i-th fixed magnet upon the tip magnet is of the form

$$\mathbf{B}_i = -\frac{\mu_0}{4\pi} \nabla \frac{\boldsymbol{\mu}_i \cdot \mathbf{r}_i}{\|\mathbf{r}_i\|_2^3} \tag{6.10}$$

where $\|\cdot\|_2$ denotes the Euclidean norm and ∇ represents the gradient operator.

Assuming the cantilever beam is a uniform Euler-Bernoulli beam and supposing the first mode is dominant, the transverse displacement of the beam can be written in the form

$$w_{\mathrm{rel}}(x,t) = \phi(x)q(t) \tag{6.11}$$

where $q(t)$ is the temporal modal coordinate, $\phi(x)$ is the mode shape function

$$\phi(x) = C\left\{\left[\cos\left(\frac{\beta}{L_{\mathrm{b}}}x\right) - \cosh\left(\frac{\beta}{L_{\mathrm{b}}}x\right)\right] + \sigma\left[\sin\left(\frac{\beta}{L_{\mathrm{b}}}x\right) - \sinh\left(\frac{\beta}{L_{\mathrm{b}}}x\right)\right]\right\} \tag{6.12}$$

where σ and β are determined from the associated eigensystem, C can be derived from the corresponding orthonormality conditions (the corresponding formulas are not given here).

Substituting Eq. (6.11) into Eqs. (6.2) to (6.5), one can get the expressions of kinetic energies of the beam and the slider and potential energies of the beam and the magnetic field in the form of the modal coordinate and mode shape function as

$$T_{\mathrm{b}} = \frac{1}{2}\int_0^{L_{\mathrm{b}}} \rho_{\mathrm{b}} A_{\mathrm{b}}(\dot{q}^2\phi^2 + \dot{g}^2 + 2\dot{q}\phi\dot{g})\,\mathrm{d}x$$

$$T_{\mathrm{s}} = \frac{1}{2}m_{\mathrm{s}}[\dot{q}^2\phi^2(L_{\mathrm{b}}) + \dot{g}^2 + 2\dot{q}\phi(L_{\mathrm{b}})\dot{g}] + \frac{1}{2}J_{\mathrm{s}}\dot{q}^2[\phi']^2_{x=L_{\mathrm{b}}}$$

$$U_{\mathrm{b}} = \frac{1}{2}\int_0^{L_{\mathrm{b}}} EIq^2(\phi'')^2\,\mathrm{d}x \tag{6.13}$$

$$U_{\mathrm{m}} = \sum_{i=1}^{n}\frac{\mu_0 M_i V_i M_{\mathrm{s}} V_{\mathrm{s}}}{4\pi}\left\{\frac{\cos\theta}{r_i^3} - \frac{3}{r_i^5}[(d_x + q^2\delta_{\mathrm{c}})^2\cos\theta - (d_x + q^2\delta_{\mathrm{c}})\left[q\phi(L_{\mathrm{b}}) + (-1)^i d_y\right]\sin\theta\right\}$$

where the over-dot and the prime denote a derivative with respect to time, t, and location, x, respectively, r_i are the Euclidean norms of vectors $\mathbf{r}_i$, and $\cos\theta$ and $\sin\theta$ can be obtained through geometrical approximation. These terms are given by

$$r_i = \left[(d_x + q^2\delta_{\mathrm{c}})^2 + \left[q\phi(L_{\mathrm{b}}) + (-1)^i d_y\right]^2\right]^{1/2}$$

$$\delta_{\mathrm{c}} = \frac{1}{2}\int_0^{L_{\mathrm{b}}} (\phi')^2\,\mathrm{d}x$$

$$\cos\theta = 1 - \frac{1}{2}q^2[\phi']^2_{x=L_\mathrm{b}}$$

$$\sin\theta = q[\phi']_{x=L_\mathrm{b}}$$

The Lagrangian of the mechanical system is expressed as

$$L = T_\mathrm{b} + T_\mathrm{s} - U_\mathrm{b} - U_\mathrm{m} \tag{6.14}$$

Based on the Lagrange-d'Alembert principle, which is equivalent to the Euler-Lagrange equations with external forces, the governing equation of the mechanical system can be obtained as

$$\frac{\mathrm{d}}{\mathrm{d}t}\left(\frac{\partial L}{\partial \dot{q}}\right) - \frac{\partial L}{\partial q} = F_\mathrm{f}\phi(L_\mathrm{b}) \tag{6.15}$$

where F_f is the kinetic friction force exerting on the slider and will be detailed in the following section.

Incorporating Eqs. (6.11), (6.13) and (6.14) into Eq. (6.15) and applying the orthonormality conditions and including damping yield

$$\ddot{q} + 2\zeta\omega\dot{q} + \omega^2 q + F_\mathrm{m} = \alpha\ddot{g} + F_\mathrm{f}\phi(L_\mathrm{b}) \tag{6.16}$$

where ζ is the damping ratio, ω is the undamped natural frequency of the first mode of the beam without the tip mass, $\ddot{g} = \hat{A}\sin\varphi(t)$ is the base excitation, where $\hat{A}$ is the acceleration amplitude and $\dot{\varphi}(t)/2\pi = f(t)$ is the excitation frequency (in Hz), and F_m is the magnetic force exerted by the magnetic field at the tip. The expression for F_m and those of α and ω are given as

$$F_\mathrm{m} = \frac{\partial U_\mathrm{m}}{\partial q}$$

$$\alpha = -\rho_\mathrm{b}A_\mathrm{b}\int_0^{L_\mathrm{b}} \phi \,\mathrm{d}x - m_\mathrm{s}\phi(L_\mathrm{b})$$

$$\omega = \beta^2\sqrt{\frac{EI}{\rho_\mathrm{b}A_\mathrm{b}L_\mathrm{b}^4}}$$

Owing to the rotation of the cantilever tip mass, a circular contact area between the slider and the patches is more convenient for modelling the charge transfer process and calculating the friction force in between. As shown in Figure 6.1(b), w_{rel} is the displacement of the slider, A_1 and A_2 are the contact areas between the slider and the EAP, and between the slider and the EIP, respectively. The slider has the same circular area as the EAP, and its radius is r and hence $A_1 + A_2 = \pi r^2$.

According to Coulomb's law of friction, the kinetic friction force on the slider can be given as

$$F_{\mathrm{f}} = -(\mu_{\mathrm{k1}} A_1 + \mu_{\mathrm{k2}} A_2) \frac{N}{S} \mathrm{sgn}(\dot{q}\phi(L_{\mathrm{b}})) \tag{6.17}$$

where μ_{k1} and μ_{k2} are the kinetic coefficients of friction between the slider and the EAP and between the slider and the EIP, respectively; $\mathrm{sgn}(\cdot)$ is the signum function, S is the total contact area, and N is the normal force are expressed as

$$N = C_{\mathrm{r}} m_{\mathrm{s}} \mathrm{g}$$

$$S = \pi r^2$$

$$A_1 = \begin{cases} 2r^2 \cos^{-1}\left(\dfrac{|q\phi(L_{\mathrm{b}})|}{2r}\right) - \dfrac{1}{2}|q\phi(L_{\mathrm{b}})|\sqrt{4r^2 - [q\phi(L_{\mathrm{b}})]^2}, & |q\phi(L_{\mathrm{b}})| < 2r \\ 0, & |q\phi(L_{\mathrm{b}})| \geq 2r \end{cases}$$

$$A_2 = \begin{cases} S - A_1, & |q\phi(L_{\mathrm{b}})| < 2r \\ S, & |q\phi(L_{\mathrm{b}})| \geq 2r \end{cases}$$

where $C_{\mathrm{r}} \in [0 \quad 1]$ is the contact force ratio describing the contact situation between the slider and patches and g is the gravitational acceleration.

Without loss of generality, stick-slip may happen between the slider and the patches during oscillation. During sticking, the beam-slider system is in a dynamically balanced state and the slider has no motion relative to the moving base. The static friction force between the slider and the patches is given by

$$f_{\mathrm{s}} = -\left[EIq[\phi''']_{x=L_{\mathrm{b}}} - \frac{F_{\mathrm{m}}}{\phi(L_{\mathrm{b}})} - (m_{\mathrm{s}} + m_{\mathrm{e}})\ddot{g}\right] \tag{6.18}$$

where m_{e} is the equivalent mass of the cantilever beam and can be expressed as $m_{\mathrm{e}} = \frac{33}{140}\rho_{\mathrm{b}}A_{\mathrm{b}}L_{\mathrm{b}}$.

The maximal static friction force is as follows

$$f_{\max} = \begin{cases} (\mu_{\mathrm{s1}}A_1 + \mu_{\mathrm{s2}}A_2)\dfrac{N}{S}, & |q\phi(L_{\mathrm{b}})| < 2r \\ \mu_{\mathrm{s2}}N, & |q\phi(L_{\mathrm{b}})| \geq 2r \end{cases} \tag{6.19}$$

where μ_{s1} and μ_{s2} are the static coefficients of friction between the slider and the EAP and between the slider and the EIP, respectively.

The conditions for sticking are then

$$\begin{aligned} \dot{q}\phi(L_{\mathrm{b}}) &= 0 \\ |f_{\mathrm{s}}| &\leq f_{\max} \end{aligned} \tag{6.20}$$

6.4. Modelling of the Electrical System

According to Ref. [107], during slipping and when $|w_{\mathrm{rel}}(L_{\mathrm{b}}, t)| < 2r$, the equivalent capacitance, i.e., C_{e}, and the open-circuit voltage, i.e., V_{oc}, for the presented triboelectric energy harvester can be derived as

$$C_{\mathrm{e}} = \frac{\varepsilon_0\varepsilon_{\mathrm{r}}A_1}{t_{\mathrm{d}}} \tag{6.21}$$

$$V_{\mathrm{oc}} = \frac{\sigma A_2 t_{\mathrm{d}}}{\varepsilon_0\varepsilon_{\mathrm{r}}A_1} \tag{6.22}$$

where ε_0 and ε_{r} are the vacuum permittivity and the relative permittivity of the top dielectric (PTFE), respectively, t_{d} is the thickness of the top dielectric, and σ is the tribo-charge surface density.

The relationship between the voltage across a resistor R in an outer circuit, i.e., V, and the amount of transferred charges between electrodes, i.e., Q, of the harvester can be given by [94, 107]

$$V = -\frac{1}{C_{\mathrm{e}}}Q + V_{\mathrm{oc}} \tag{6.23}$$

Applying Ohm's law, i.e., $V = RI = R\frac{\mathrm{d}Q}{\mathrm{d}t}$, and substituting Eqs. (6.21) and (6.22) into Eq. (6.23) yield the differential equation

$$R\frac{\mathrm{d}Q}{\mathrm{d}t} + \frac{t_\mathrm{d}}{\varepsilon_0\varepsilon_\mathrm{r}A_1}Q - \frac{\sigma A_2 t_\mathrm{d}}{\varepsilon_0\varepsilon_\mathrm{r}A_1} = 0 \tag{6.24}$$

However, a singularity will occur in Eq. (6.24) when the top electrode (attached to the slider) fully slides out of the bottom one (the EAP), i.e., the denominators of the coefficients of the second and the third terms become zero when $w_\mathrm{rel}(L_\mathrm{b}, t) \geq 2r$, and it will result in a zero equivalent capacitance and an infinitely large open-circuit voltage. Nevertheless, the transferred charges between the electrodes will saturate when the top electrode fully slides out of the bottom one [102, 107], and the open-circuit voltage V_oc has been measured to be finite in experiment when the two electrodes fully slide out of each other [102]. To avoid this singularity, it is assumed that the top electrode will not fully slide out of the bottom electrode during oscillation. This will be monitored during the numerical simulations.

When sticking, the transferred charges between electrodes can be given by

$$\begin{aligned} Q &= Q(q = q_\mathrm{s}) = \text{const.} \\ \frac{\mathrm{d}Q}{\mathrm{d}t_\mathrm{s}} &= 0 \end{aligned} \tag{6.25}$$

where q_s is the temporal modal coordinate when sticking motion starts to take place and t_s is the corresponding time instant.

6.5. Numerical Simulation

6.5.1. Numerical Scheme

The ordinary differential equation (ODE) of the electrical output, i.e., Eq. (6.24), can be stiff, and owing to the non-smoothness of the mechanical system, i.e., the sign change of the friction force and the stick-slip motion, the TR-BDF2 method can only be directly applied to steps without any non-smooth events. As the numerical scheme proposed in Chapter 5, for a time step containing non-smooth events, only the trapezoidal rule or the TR method is used for the whole step. The derivation of the corresponding difference equations is given in Appendix C.

The values of the main parameters used in simulation are given in Table 6.1.

Table 6.1 The values of the main parameters used in simulation.

Parameter	Value
Tip mass (slider), m	12.9 g
Cantilever dimension, $L_{\mathrm{b}} \times A_{\mathrm{b}}$	$200 \times 10 \times 1$ mm^3
Cantilever density, ρ_{b}	7800 kg $\cdot$ m^{-3}
Young's modulus of cantilever, E	210 GPa
Damping ratio, ζ	0.0035
Radius of EAP	20 mm
Static friction coefficient of EAP, μ_{s1}	0.35
Kinetic friction coefficient of EAP, μ_{k1}	0.25
Static friction coefficient of EIP, μ_{s2}	0.30
Kinetic friction coefficient of EIP, μ_{k2}	0.20
Thickness of the PTFE layer, t_{d}	0.1 mm
Tribo-charge surface density, σ	6 μC $\cdot$ m^{-2}
Relative permittivity of PTFE, ε_{r}	2.0
Resistance in circuit, R	20 MΩ
Residual flux density of magnet, B_{r}	1.45 T
Volume of single magnet, V_i	$\pi \times 5^2 \times 5$ mm^3

6.5.2. Effect of the Electrostatic Force

Theoretically, there exists an attractive electrostatic force between the slider and the EAP because the dielectric on the slider, i.e., the PTFE film, and the EAP (Al) are oppositely charged. The electrostatic force can be expressed as

$$F_{\mathrm{e}} = \frac{\varepsilon_0 \varepsilon_{\mathrm{r}} A_1 V_{\mathrm{c}}^2}{2 t_{\mathrm{d}}^2} \tag{6.26}$$

And the voltage across a capacitor, i.e., V_{c}, can be given by

$$V_{\mathrm{c}} = \frac{Q}{C_{\mathrm{e}}} \tag{6.27}$$

Substituting Eqs. (6.21) and (6.27) into Eq. (6.26), the electrostatic force can be rewritten as

$$F_{\mathrm{e}} = \frac{Q^2}{2 \varepsilon_0 \varepsilon_{\mathrm{r}} A_1} \tag{6.28}$$

Since the harvester is of the sliding mode, the electrostatic force will act as part of the normal force exerted on the slider, and the new normal force is then

$$N = C_{\mathrm{r}}(m_{\mathrm{s}} \mathrm{g} + F_{\mathrm{e}}) \tag{6.29}$$

The electrostatic force, therefore, may affect the system's behaviour through its contribution to the possible increase of friction force, which is thus worth investigating. It is noted that the mechanical system described by Eq. (6.16) and the electrical system modelled by Eq. (6.24) are coupled when the electrostatic force is considered, in which case, the Jacobian matrix should be updated accordingly, and the new matrix elements are given in the appendix.

To simplify the comparison, the two fixed magnets are removed and the slider no longer experiences the magnetic force. The comparison of the tip displacements and the RMS voltage outputs under discrete numerical frequency sweeps (from 5 Hz to 15 Hz with a step of 0.05 Hz) with and without the consideration of the electrostatic force (EF), is shown in Figure 6.4. If the EF is adequately big, the model that includes the EF should produce a smaller amplitude response relative to the model without the EF because of the increase in the friction force caused by the EF. However, it can be seen in Figure 6.4 that both the mechanical and electrical responses are almost identical in the two cases. Therefore, it can be concluded that the electrostatic force between the two electrodes (or between the slider and

the EAP) for this TEH can be neglected and the EF will not be modelled in the subsequent results. Nevertheless, the feedback of the EF into the electromechanical system may be taken into consideration in some miniaturized/MEMS-based electrostatic transducers, such as in Ref. [233].

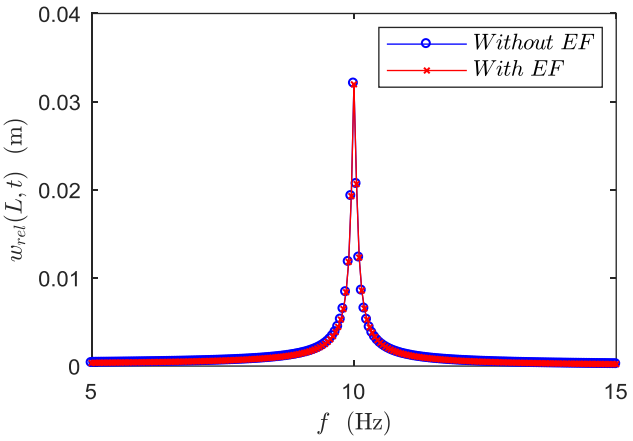

(a)

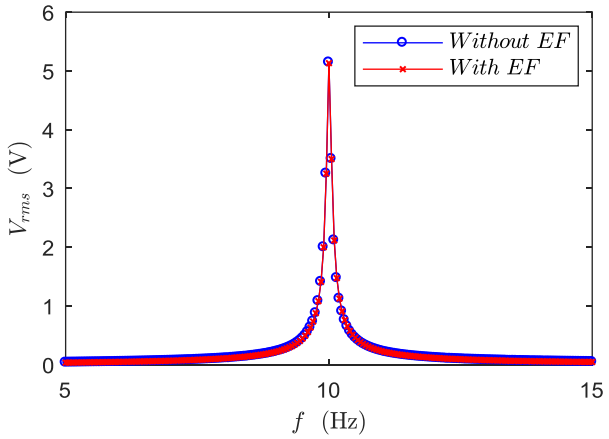

(b)

Figure 6.4 Comparisons of (a) the tip displacements and (b) the RMS voltage outputs of the cases with and without the electrostatic force (EF) under discrete numerical frequency sweeps when $\hat{A} = 0.10\text{g}$ and $C_\text{r} = 0.1$.

6.5.3. Analysis of Multistability

At first, friction is not considered. The total potential energy of the system, U, consists of two parts: the strain energy of the cantilever beam, U_b, and the magnetic potential energy, U_m. The variation of the strain energy of the cantilever beam only depends on the deflection of the beam. The magnetic potential energy, however, not only is related to the distance

between the magnets but also the alignment of the magnets within the field. Therefore, the horizontal and vertical distances between magnets, i.e., d_x and d_y, can notably affect the total potential energy, and thus the behaviour of the system.

When the horizontal distance is fixed at $d_x = 17$ mm, the variation of the total potential energy with the vertical distance and the tip displacement is shown in Figure 6.5(a), and the corresponding projections on the U-w_{rel} plane are given in Figure 6.5(b). It can be seen that the system is monostable when the two fixed magnets are close (i.e., d_y is small). In this case, the two fixed magnets act as one stronger magnet. As the two fixed magnets are placed farther away from each other, the system exhibits monostability, bistability, and weak tristability.

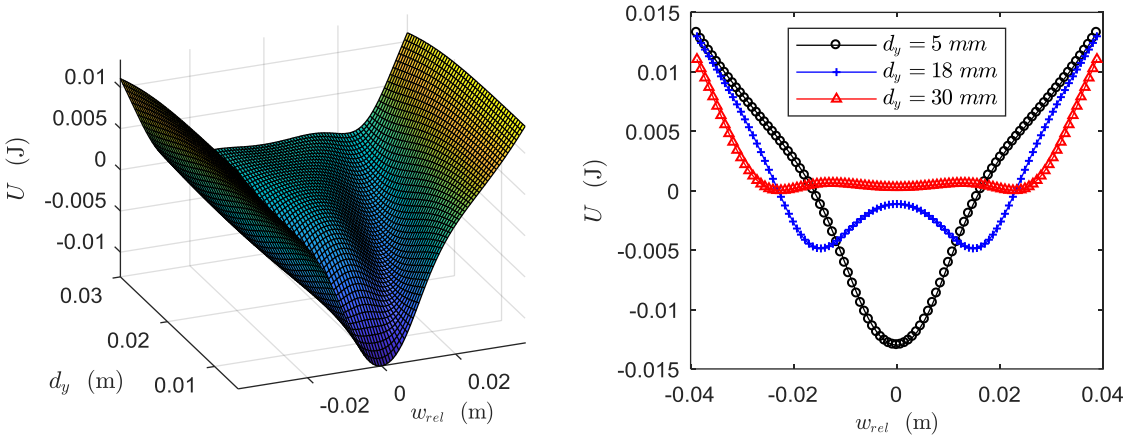

(a) (b)

Figure 6.5 The variation of the total potential energy (U) with the vertical distance (d_y) and the tip displacement (w_{rel}); (a) 3D surface plot and (b) its projections on the U-w_{rel} plane.

The system has different stabilities at different combinations of d_x and d_y, and the possible scenarios are shown in Figure 6.6 on the parametric plane of d_x-d_y which is divided into three areas according to their stabilities. Therefore, the multistability of the friction-free (conservative) system can be determined analytically through the potential energy function, i.e., the sum of U_{b} and U_{m} in Eq. (6.13). Apparently, there is no potential energy function for a non-conservative force or system. Thus, the multistability of the system with the presence of friction can no longer be revealed by Eq. (6.13). However, it is interesting to see how those three areas will evolve on the parametric plane with the involvement of friction, and

such a study of the effect of non-conservative forces on the multistability of a system is rare in the open literature.

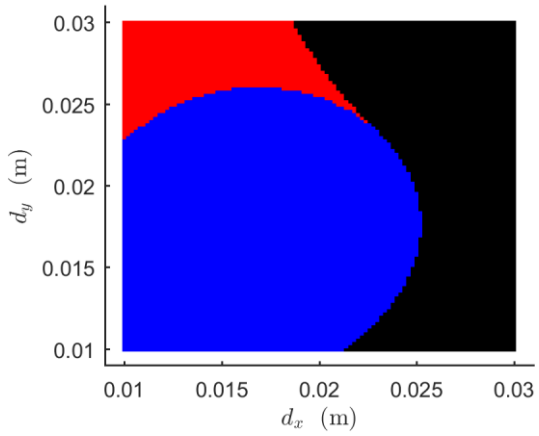

Figure 6.6 The system stability shown on the d_x-d_y plane; black parametric area indicates monostability, blue indicates bistability, and red indicates tristability (For interpretation of the references to colours in this figure, readers are referred to the web version of this thesis).

Using numerical simulations, the system involving friction at each combination of d_x and d_y (a grid of 101×101 is used) is integrated at different excitation frequencies with different initial conditions. The algorithm used for the categorization of different types of stability is shown in a flowchart in Figure D.1 in Appendix D. Even though the multistability of the system is not dependent on the level of the external excitation, a proper selection of the excitation frequency and amplitude can improve the efficiency of the categorization. This is because in multistable systems, large excitations can easily result in interwell oscillations and small excitations will mostly lead to intrawell oscillations. In practice, this means that more tip displacement time history samples (or more sets of initial conditions) are needed to confidently determine the type of the multistability at a given combination of d_x and d_y.

In simulation, the excitation amplitude $\hat{A}$ is fixed at 0.15g, and two excitation frequencies, 3 Hz and 13 Hz, are used. Generally, it is easier for an oscillator to settle down into a well if the initial displacement is within the potential well (assuming the initial velocity is zero). Therefore, fifteen samples of the initial tip displacement linearly spaced between -0.025 m and -0.001 m are used with each of the two excitation frequencies (initial velocities and transferred charge are zero). The categorized results with three different contact force ratios are shown in Figure 6.7. It can be seen that the categorization scheme performs quite well, and the performance at boundaries can be enhanced by using more sets of initial conditions

and/or excitation frequencies. In comparison with Figure 6.6, the bistable and tristable areas have shrunk while the monostable area has enlarged. These differences between Figure 6.6 and Figure 6.7 seem to require only a small amount of friction to materialize. With the increase of the contact force ratio or the friction force, there is no obvious change of the areas of various stabilities.

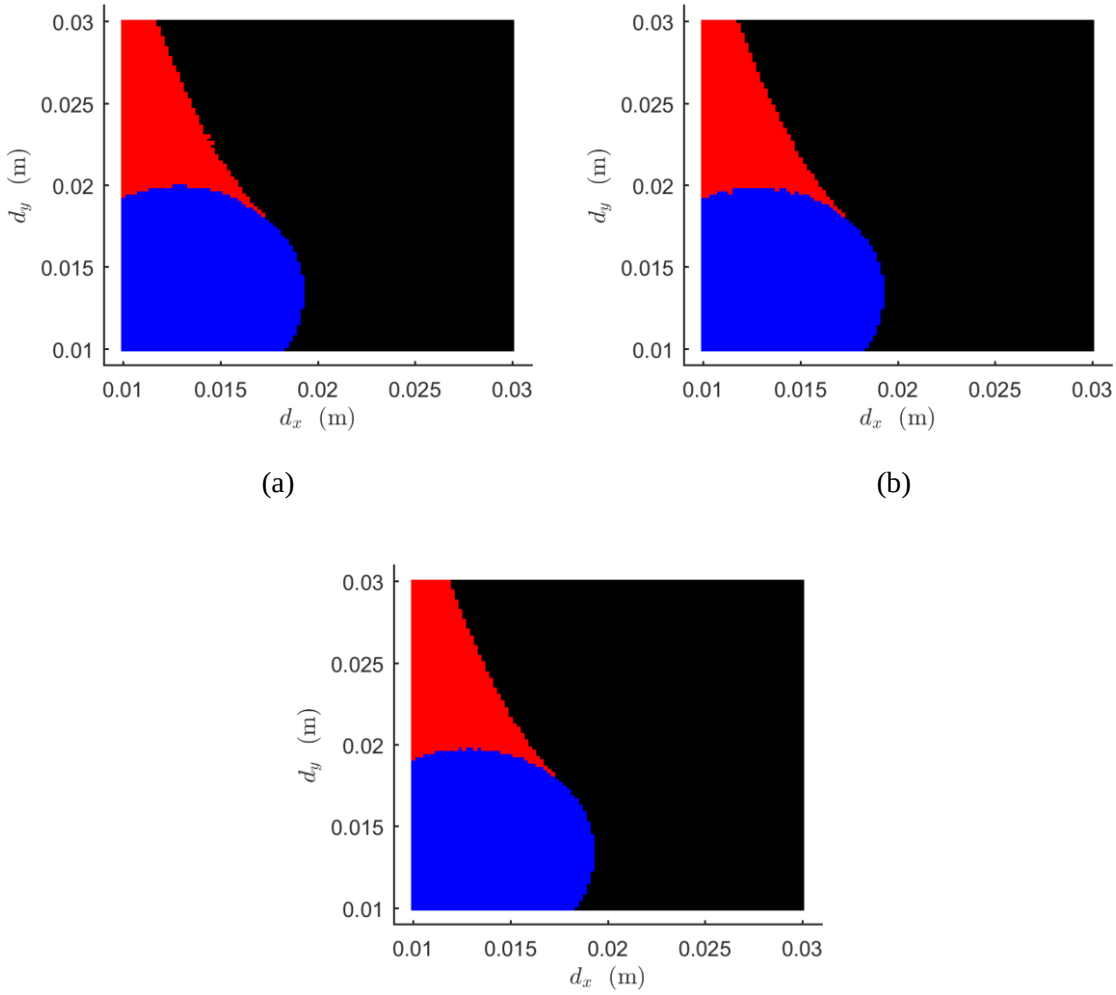

(a) (b)

(c)

Figure 6.7 Numerically categorized different types of stability on the parametric plane of d_x and d_y; (a) for $C_r = 0.001$, (b) for $C_r = 0.1$, and (c) for $C_r = 0.5$ (For interpretation of the references to colours in this figure, readers are referred to the web version of this thesis).

6.5.4. Comparison Between Various Types of Stability

The dynamics of the system can be highly dependent on the magnetic field. The magnetic field is mostly influenced by the relative locations between the magnets, i.e., d_x and d_y. As

shown in the last section, the relative locations of magnets result in different types of stability. Besides, the system is non-smooth owing to the presence of friction. Thus, the steady state of the system can be dependent on the initial conditions [171], and various dynamic regimes can theoretically coexist, though only one of them can practically appear under certain conditions. Moreover, broad harvesting frequency span and large vibration amplitude are often beneficial to vibration energy harvesting. Therefore, discrete numerical frequency sweeps can be used to study the coexisting regimes (mainly the coexistence of intrawell and interwell oscillations) and compare between various types of stability.

To generate the discrete numerical frequency sweeps, fifty pairs of initial conditions $\mathbf{w}_0 = (w_{\mathrm{rel}}(L,0), \dot{w}_{\mathrm{rel}}(L,0), 0)$ are randomly selected from the set

$$\left\{\left(w_{\mathrm{rel}}(L,0), \dot{w}_{\mathrm{rel}}(L,0)\right): w_{\mathrm{rel}}(L,0) \in [-0.025 \quad 0.025],\ \ \dot{w}_{\mathrm{rel}}(L,0) \in [-1.5 \quad 1.5]\right\}$$

where both $w_{\mathrm{rel}}(L,0)$ and $\dot{w}_{\mathrm{rel}}(L,0)$ follow uniform distributions. The tip displacement $w_{\mathrm{rel}}(L,t)$ with these initial conditions under the discrete numerical frequency sweeps are shown in Figure 6.8. The maximal and minimal vibration amplitudes in steady states at each excitation frequency are marked and connected through vertical line in this figure (blue circles for interwell oscillations and red asterisk for intrawell oscillations except the results of the monostable system shown in Figure 6.8(a)), and the response of the latest instant at one frequency is used as the initial conditions for the integration of the system under the next frequency. Obviously, there are no coexisting behaviours in the monostable system. However, intrawell and interwell oscillations can coexist in the bistable system. The situation is similar in the tristable system. The bistable system has the broadest frequency span over which the oscillation is at high amplitude. Therefore, bistability is superior to both monostability and tristability in terms of broadband energy harvesting.

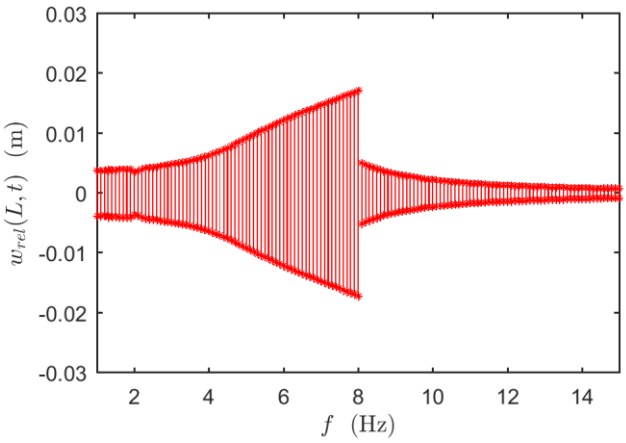

(a)

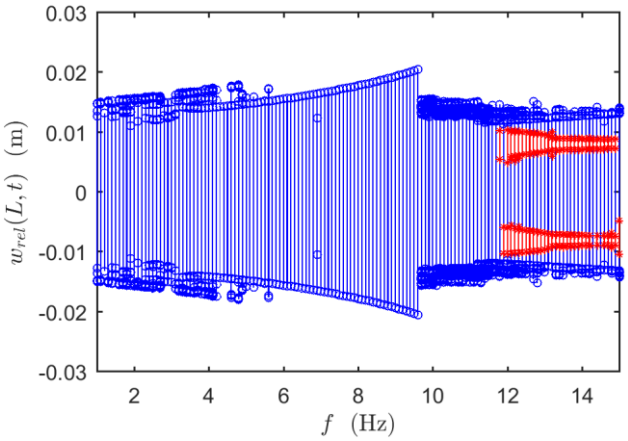

(b)

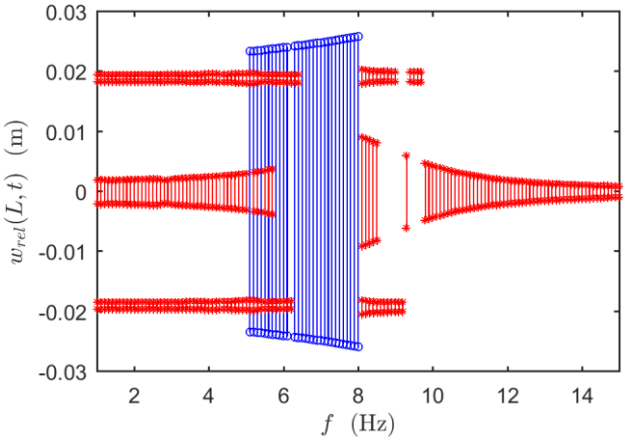

(c)

Figure 6.8 Tip vibration amplitudes under discrete numerical frequency sweeps of (a) monostable system with $d_x = 0.019$ m and $d_y = 0.020$ m, (b) bistable system with $d_x = 0.017$ m and $d_y = 0.018$ m and (c) tristable system with $d_x = 0.013$ m and $d_y = 0.025$ m; $\hat{A} = 0.50$g and $C_\mathrm{r} = 0.1$.

It is clear that there exist sudden jumps of the tip displacement in Figure 6.8 in all the three kinds of systems. For a better explanation, the tip vibration amplitudes under the single forward (blue circles) and backward (red asterisks) frequency sweeps of the monostable system are shown in Figure 6.9. It can be seen that there exist hysteresis and stiffness-hardening, which are believed to be caused by the magnetic force.

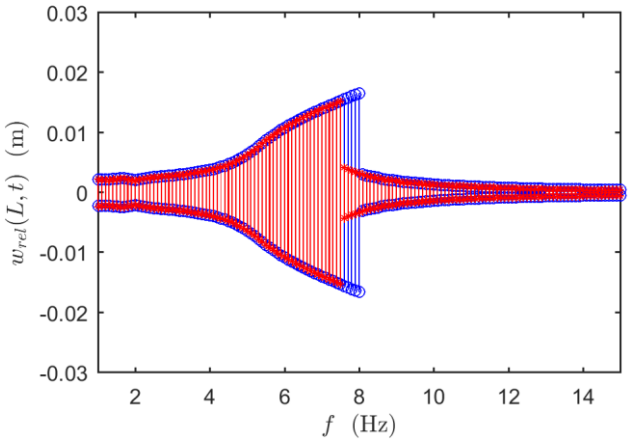

Figure 6.9 Tip vibration amplitudes under forward (blue circles) and backward (red asterisks) discrete numerical frequency sweeps; $d_x = 0.019$ m $d_y = 0.020$ m, $\hat{A} = 0.30$g, $C_\mathrm{r} = 0.1$ and $w_0 = (0.001,0,0)$ for both sweeps.

6.5.5. The Effect of the Excitation Level

In multistable systems, the excitation level often plays an important role in exciting high-energy orbit oscillations, especially when it comes to high and wide potential barriers between wells. The tip vibration amplitudes under discrete numerical frequency sweeps of the bistable system at different excitation levels are shown in Figure 6.10. In combination with Figure 6.8(b), it can be observed that the frequency bandwidths at which interwell oscillations occur, shrinks considerably with the decrease in the excitation level. For reduction of excitation level from 0.5g to 0.3g, there still exists a considerable frequency span over which the system performs interwell oscillations, though intrawell oscillations completely become dominant at high frequencies. A further decrease to 0.1g results in a significant reduction of the frequency span for interwell oscillations, and a much smaller excitation level ceases to excite any interwell oscillations, see Figure 6.10(c).

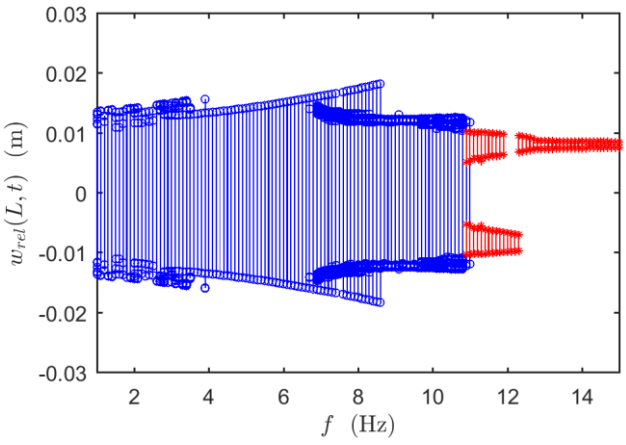

(a)

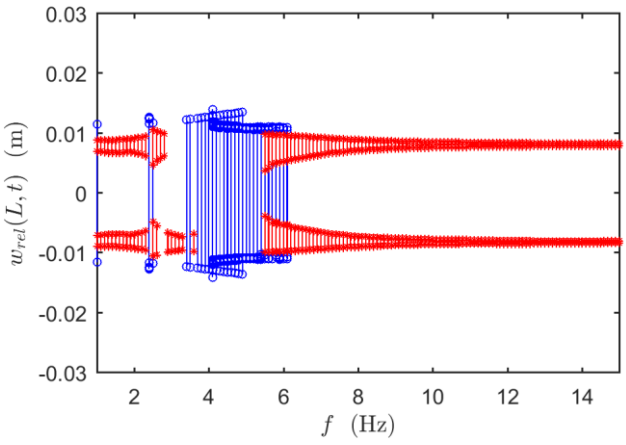

(b)

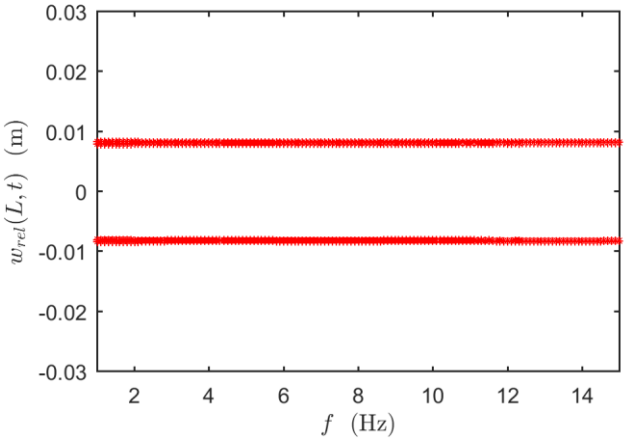

(c)

Figure 6.10 Tip vibration amplitudes under discrete numerical frequency sweeps of the bistable system at (a) $\hat{A} = 0.30$g, (b) $\hat{A} = 0.10$g, and (c) $\hat{A} = 0.01$g; $d_x = 0.017$ m, $d_y = 0.018$ m, $C_\mathrm{r} = 0.1$.

6.5.6. The Effect of the Friction

Triboelectrification is largely influenced by friction and can be enhanced through repeated rubbing [234]. Thus friction is essential in sliding-mode TEHs. On the other hand, friction is well-known for dissipating energy by means of generating waves, atomic motions, and heat [235], and hence friction is also a limitation with regards to maximal energy harvesting. Therefore, the relationship between friction and energy harvesting (or electrical output) becomes even more complicated in TEHs and a study investigating this relationship is still missing. The mechanism by which friction affects triboelectrification is beyond the scope of this research. Nevertheless, it is intended to study the effect of friction on the performance of the current TEH by investigating its influence on the system dynamics.

There are various combinations of triboelectric materials and each combination has its own values of coefficients of friction (both static and kinetic). Besides, the contact between the slider and the patches (and thus the friction) can be affected by the tilt of the tip slider and the assembly of the harvester. The tip vibration amplitudes under discrete numerical frequency sweeps of the bistable system with different values of contact force ratio are shown in Figure 6.11, and by combining with Figure 6.10(a), it can be seen that the distribution of the intrawell oscillation spreads from high frequencies down to relatively low frequencies with the increase of the contact force ratio. In addition, the jump frequency (due to the hardening effect) shifts towards lower frequencies. In comparison, low frequencies are unlikely to result in intrawell oscillations. Since the base excitation amplitude is fixed in terms of the applied acceleration, the resultant base displacement is inversely proportional to the forcing frequency square. Thus, the displacement response tends to be small at high frequencies.

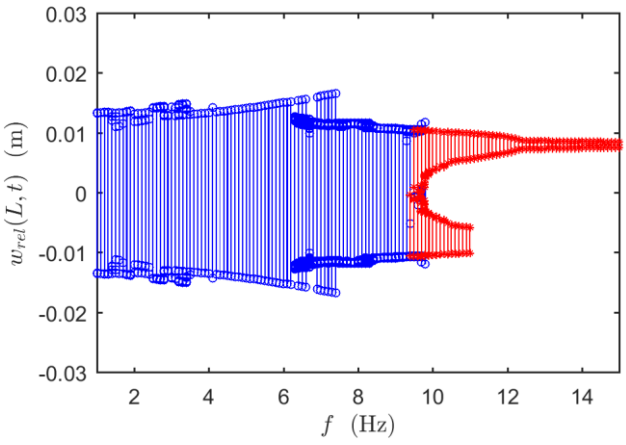

(a)

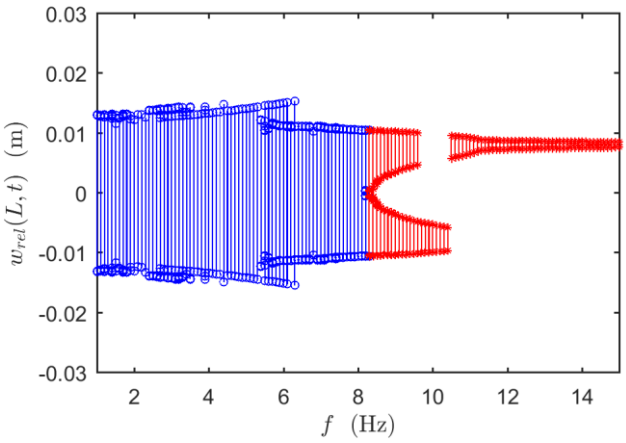

(b)

Figure 6.11 Tip vibration amplitudes under discrete numerical frequency sweeps of the bistable system under different contact force ratios, (a) $C_{\mathrm{r}} = 0.3$ and (b) $C_{\mathrm{r}} = 0.5$; $\hat{A} = 0.30\mathrm{g}$; $d_x = 0.017$ m, $d_y = 0.018$ m.

6.5.7. Basins of Attraction

Since the dynamics of the system can be sensitively dependent on the initial conditions, basins of attraction are computed to investigate the eventual dynamic behaviour of the system given a set of initial conditions.

The initial conditions $\mathbf{w}_0 = (w_{\mathrm{rel}}(L,0), \dot{w}_{\mathrm{rel}}(L,0), 0)$ are taken from the phase plane below using a grid of 250×250.

$$\left\{\left(w_{\mathrm{rel}}(L,0), \dot{w}_{\mathrm{rel}}(L,0)\right): w_{\mathrm{rel}}(L,0) \in [-0.025 \quad 0.025],\ \ \dot{w}_{\mathrm{rel}}(L,0) \in [-1.5 \quad 1.5]\right\}$$

The steady-state of the system at each sampling point is categorized according to the attractor onto which the system eventually settles down. The attractors are categorized into period-1 intrawell oscillations (shown in red), non-periodic or high-periodicity intrawell oscillations (in black), period-1 interwell oscillations (in blue), and non-periodic or high-periodicity interwell oscillations (in green).

The generated basins of attraction of the bistable system under the excitation of $\hat{A} = 0.3$g and $\hat{A} = 0.5$g at two different excitation frequencies are shown in Figure 6.12. It can be seen that the increase of the excitation level has profound effects on the evolution of the basins of attraction. At $f = 8$ Hz, the spiral basins both for the period-1 interwell oscillations and the non-periodic or high-periodicity interwell oscillations become scattered with the increase of the excitation level, and the basin of the former becomes dominant, see Figure 6.12(a). At $f = 13$ Hz, the weak spiral structure at $\hat{A} = 0.3$g disappears due to the rise of the excitation level to $\hat{A} = 0.5$g, and the basins of the non-periodic or high-periodicity intrawell oscillations and the period-1 interwell oscillations seem to intermingle in the off-centre area at $\hat{A} = 0.5$g. Additionally, it has been found that the system undergoes purely interwell oscillations at lower frequencies (such as at $f = 2$ Hz) even for smaller excitation levels. The corresponding basins of attraction are purely green and are not presented here.

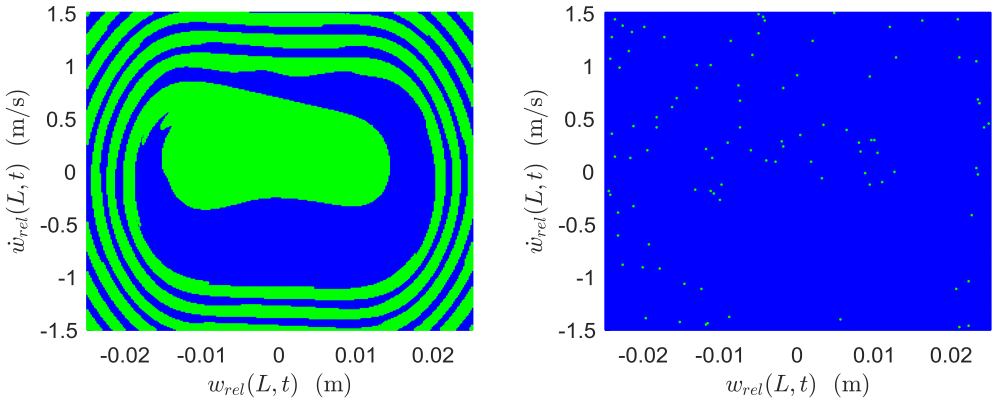

(a)

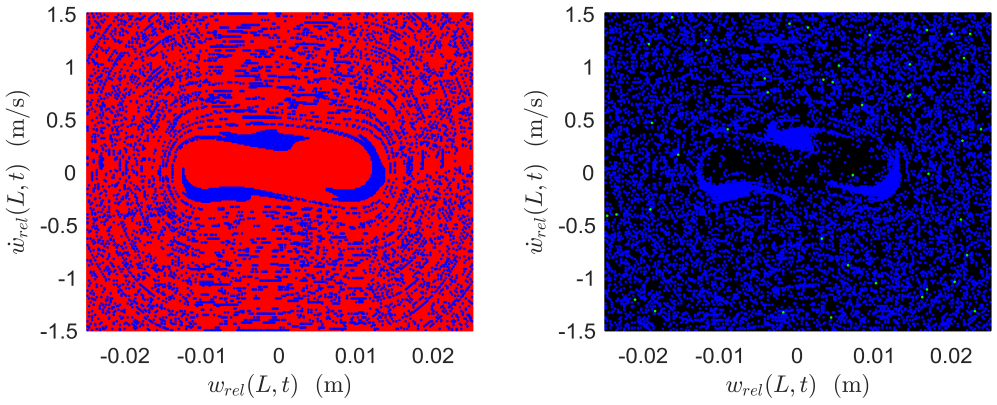

(b)

Figure 6.12 Basins of attraction of the bistable system under the excitation of $\hat{A} = 0.30$g (left column) and $\hat{A} = 0.50$g (right column) at (a) $f = 8$ Hz and (b) $f = 13$ Hz; $d_x = 0.017$ m, $d_y = 0.018$ m, $C_\mathrm{r} = 0.1$ (For interpretation of the references to colours in this figure, readers are referred to the web version of this thesis).

Similarly, the basins of attraction of the tristable system under the excitation of $\hat{A} = 0.3$g and $\hat{A} = 0.5$g at these two excitation frequencies are obtained and shown in Figure 6.13. Interesting structures appear at $f = 8$ Hz, see Figure 6.13(a). Basins of non-periodic or high-periodicity intrawell oscillations arise around the two side stable equilibria while the basin of period-1 intrawell oscillations emerges in the middle and has a fractal boundary. In addition, the tail of the spiral basin of the period-1 interwell oscillation is separated by an intermingled spiral basin of the period-1 and non-periodic or high-periodicity intrawell oscillations, and the increase of the excitation level thickens the tail of the basin of the period-1 interwell oscillation. At the relatively higher frequency of $f = 13$ Hz, the system merely performs intrawell oscillations at a relatively low excitation level, and basins of interwell oscillations

start to emerge in a fractal structure with the increase of the excitation level, see Figure 6.13(b). The tristable system only performs intrawell oscillations at low frequencies (such as at $f = 2$ Hz) even when the excitation level is increased (the corresponding basins of attraction are not given here), and relative to the bistable system, the tristable system always settles down onto attractors of intrawell oscillations at low frequencies, which is not beneficial for energy harvesting.

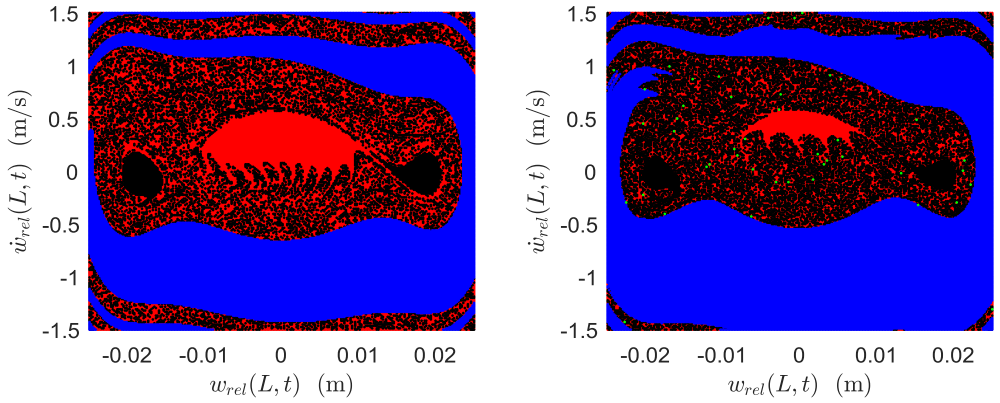

(a)

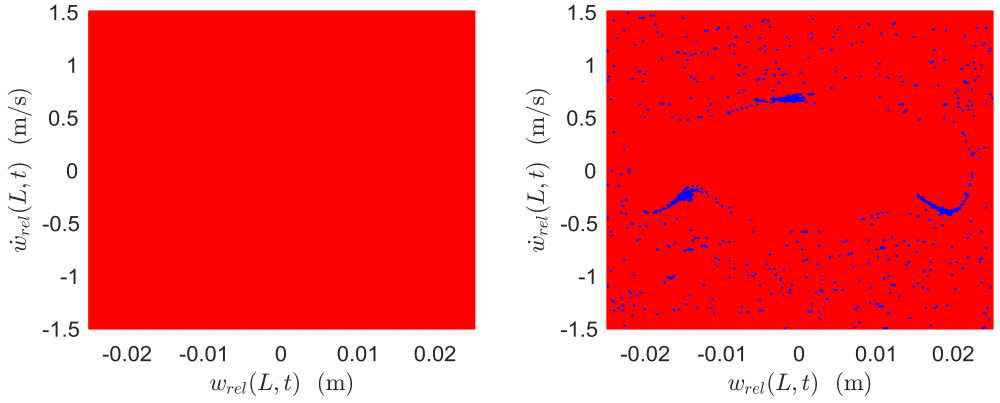

(b)

Figure 6.13 Basins of attraction of the tristable system under the excitation of $\hat{A} = 0.30$g (left column) and $\hat{A} = 0.50$g (right column) at (a) $f = 8$ Hz and (b) $f = 13$ Hz; $d_x = 0.013$ m, $d_y = 0.025$ m, $C_\mathrm{r} = 0.1$ (For interpretation of the references to colours in this figure, readers are referred to the web version of this thesis).

6.6. Conclusions

This Chapter presents the investigation of a new TEH which works in a sliding mode and involves three kinds of stabilities. The design concept is first introduced. The modelling of the mechanical vibration of a cantilever beam with a tip mass subjected to both magnetic and frictional forces under base excitation is then presented. The modelling of the electrical dynamics of the sliding mode TEH based on the established mechanical system is presented accordingly. Detailed numerical simulations are carried out. This work includes the first studies of both the sliding mode TEH and magnetic multistability in TEHs from the perspectives of structural dynamics. The main conclusions are drawn as follows:

(1) The comparison between the coupled and uncoupled electromechanical models (with and without the consideration of the electrostatic force between the electrodes, respectively) suggests that the electrostatic force can be ignored, which makes the uncoupled model preferable in the dynamical analysis.

(2) The effect of the non-conservative force (the friction force) on the multistability of the system is investigated. It is found that the distribution of the multistability on the d_x-d_y (two distances describing the relative locations of two magnets fixed to the base in relation to one magnet embedded in the slider) parametric plane changes when friction is involved, and the proportions of occurrence of the bistability and tristability decrease while that of the monostability increases.

(3) Among the three types of stability, bistability is found to provide the broadest frequency band over which the system oscillates on high-energy orbits or in interwell oscillations. Additionally, the stiffness-hardening effect caused by the magnetic force appears in systems of all three kinds of stabilities.

(4) The base excitation level plays an important role in bistable or multistable system for broadband energy harvesting. Low excitation levels will not enable the systems to cross the energy barriers between the potential wells and achieve interwell motions. In addition, the increase of friction will transfer intrawell oscillations from high frequencies down to low frequencies and shrink the frequency band over which energy harvesting is effective.

(5) The study of the basins of attraction reveals that at low frequencies the bistable system can undergo purely interwell oscillations while the tristable system will undergo intrawell

oscillations. Intermingled basins can appear in both bistable and tristable systems. An increase of the excitation level can break the basins into discrete pieces and/or points.

Chapter 7

Effects of Electrical Properties on Vibrations via Electromechanical Coupling in Triboelectric Energy Harvesting

7.1. Introduction

A few reports on the investigation of the effects of electrical properties on the vibrations of harvesters due to the electromechanical coupling can be found. It has been shown that the resistive shunt damping can affect the vibrational characteristics (resonance frequency and amplitude) of piezoelectric energy harvesters owing to electromechanical coupling [16, 236]. On the other hand, harvesters can be tuned to increase the output power using a generalized electrical load because of the electromechanical coupling effect [237], and similar work has been done for an electromagnetic energy harvester [238]. However, a comprehensive study of the effects of electrical properties on mechanical behaviours of TEHs is still missing.

In Chapter 5, the effect of the load resistance on the vibration of the TEH prototyped was experimentally investigated and no obvious influence was observed. Besides, in Chapter 6, the necessity of involving the electrostatic force in the modelling of the multistable sliding mode TEH was discussed and it turned out that the electrostatic force was negligible. However, these studies were based on the models or TEHs that had small tribo-charge surface densities (around 6 $\mu C/m^2$) and relatively large volumes or dimensions. For TEHs having bigger tribo-charge surface densities and/or smaller volumes, the resultant effects might be more significant. In addition, the environment, such as the temperature, humidity and adsorption, can affect the triboelectrification and further the tribo-charge surface density [239]. Different combinations of triboelectric materials also result in different tribo-charge surface densities. Hence, it is interesting to find out how the variation of the tribo-charge surface density can affect the mechanical behaviours of TEHs of two most common working

modes: vertical contact-separation and lateral sliding modes. Another electrical property that is worth investigating is the load resistance, since it can be used to electrically tune the harvesters and different values of it are usually used in practice. Therefore, in this chapter, the effects of both the tribo-charge surface density and the load resistance on the vibrations of TEHs of two most common working modes will be investigated. Note that an optimal load resistance is often used in practice and thus the change of load resistance may affect the output performance. However, tuning the harvester to let it work at resonance frequency when the ambient excitation frequency changes can help improve the harvesting performance. Therefore, there may exist a trade-off problem which is worth investigating but is beyond the scope of this research and thus will not be covered.

The outline of the rest of this chapter is organised as follows: Section 7.2 first presents the modelling of a sliding mode TEH and then shows the effects of tribo-charge surface density and load resistance on vibrations of the presented TEH. In Section 7.3, the modelling of a vertical contact-separation mode TEH is first established, and then the effects of the same electrical properties on vibrations of the proposed TEH are studied. The last section, i.e., Section 7.4, draws the main conclusions of this study.

This chapter is based on the following paper submitted by the author of this thesis and his supervisors:

Y. Fu, H. Ouyang, R.B. Davis, Effects of electrical properties on vibrations via electromechanical coupling in triboelectric energy harvesting, Journal of Physics D: Applied Physics, under review.

7.2. Effects of Electrical Properties on Vibrations of a Sliding Mode TEH

7.2.1. Modelling of the System

The configuration of the sliding mode TEH presented in this chapter for studying the effects of electrical properties on vibrations is shown in Figure 7.1, and it is simialr to the multistable sliding mode TEH shown in Figure 6.1 in Chapter 6 with all three magnets removed and the dimensions miniaturized and the tip mass reduced. Since the electromechanical coupling from the electrical system to the mechanical system can be weak and the volume and weight of the harvester can affect the influence caused by electrical properties on the mechanical

system, a miniaturized harvester is used. The new values of parameters used are given in Table 7.1 and other parameters not given in Table 7.1 can be found in Table 6.1.

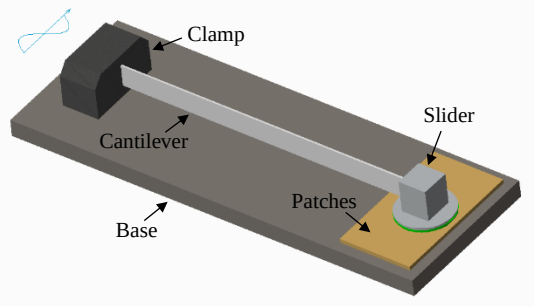

Figure 7.1 The configuration of the sliding mode TEH.

Table 7.1 The values of the main parameters used in simulation.

Parameter	Value
Tip mass (slider), m	2 g
Cantilever dimension, $L_b \times A_b$	$150 \times 10 \times 0.5$ mm^3
Thickness of the PTFE layer, t_d	0.05 mm

The governing equations of the electrical system are the same as Eqs. (6.24) and (6.25), and those of the mechanical system can be obtained by removing the magnetic force term, i.e., the F_m, in Eqs. (6.16) and (6.18). The numerical scheme proposed in Chapter 5 is used in simulation. The effects of charge density and load resistance on vibrations are investigated and shown in the following sections.

7.2.2. Effects of Charge Density on Vibrations

The frequency responses of the amplitude of the cantilever tip displacement under different tribo-charge surface densities at $R = 1$ MΩ and $\hat{A} = 0.25$g are shown in Figure 7.2(a), and the corresponding frequency responses of the RMS voltage are given in Figure 7.2(b). It can be seen that the increase of the tribo-charge surface density reduces the vibration amplitude and shifts the peak towards left a little, because a larger tribo-charge surface density means a stronger electric field and a bigger electrostatic attractive force which seems to confine the

vibration greatly when the tribo-charge surface density is large enough. The resultant effect on vibrations is quite similar to that of the structural damping. Since tribo-charge surface density is a key factor that affects the electrical output, by comparing Figure 7.2(a) and (b), it can be seen that large tribo-charge surface densities can result in much higher electrical output than bigger vibration amplitudes.

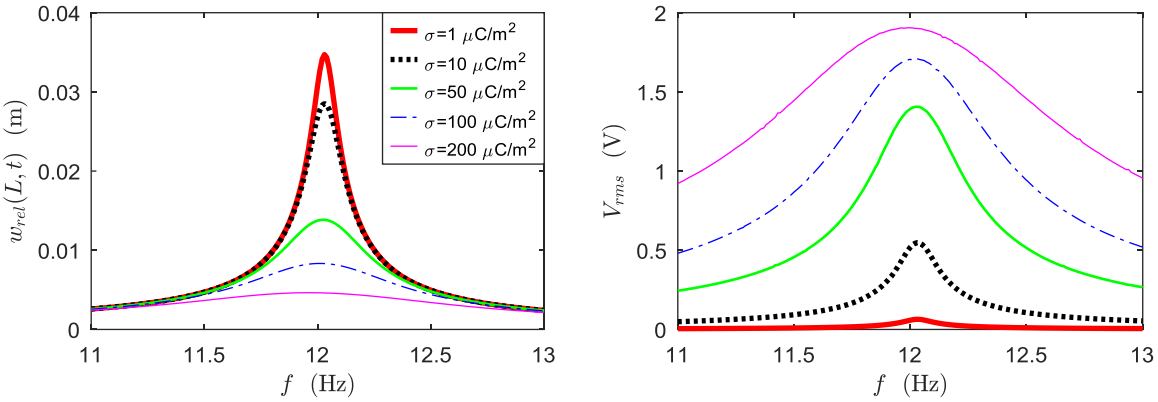

(a) (b)

Figure 7.2 Frequency responses of (a) the cantilever tip displacement and (b) the RMS voltage under different tribo-charge surface densities at $R = 1\text{M}\Omega$ and $\hat{A} = 0.25\text{g}$.

7.2.3. Effects of Load Resistance on Vibrations

For a relatively small tribo-charge surface density of $\sigma = 5\ \mu\text{C/m}^2$, the frequency responses of the amplitude of the cantilever tip displacement under different load resistances are obtained and given in Figure 7.3(a) while a local enlargement of the peaks is shown in Figure 7.3(b). Overall, the effect of load resistance on the vibration is not obvious. Only around the resonance peak do the vibration amplitudes decrease with increasing resistance, and the resonance frequency first shifts to the left slightly and then seems to undergo a very tiny shift to the right. Nevertheless, it can be concluded that the resistive shunt damping effect is not noticeable at small tribo-charge surface densities.

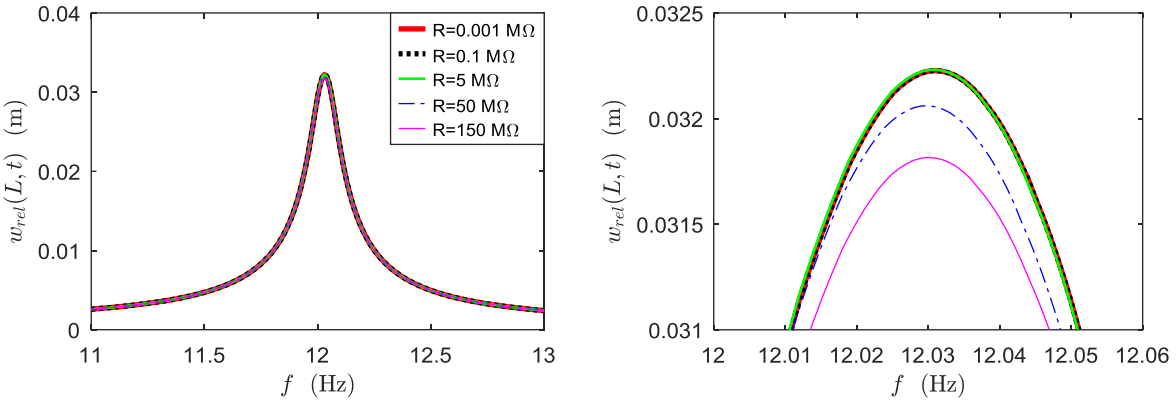

Figure 7.3 Frequency responses of (a) the amplitude of the cantilever tip displacement under different resistances at $\sigma = 5\ \mu C/m^2$ and $\hat{A} = 0.25g$ and (b) its local enlargement around the peaks.

The corresponding results under a large tribo-charge surface density of $\sigma = 200\ \mu C/m^2$ are presented in Figure 7.4, in which the restitive shunt damping phenomeon can be observed. With the increase of the load resistance, the peak is first shifted towards left and its amplitude decreased slightly, and then the peak is shifted backwards (towards right) with further increase of the resistance and the amplitude is further decreased, which is different from the variation caused by the resitive shunt damping effect in piezoelectric energy harvestings [16, 236], in which the peak amplitude can increase up to almost the same level as the initial state after certain decrease but a frequency shifting will remain when the system experiences a monotonous increase of the load resistance.

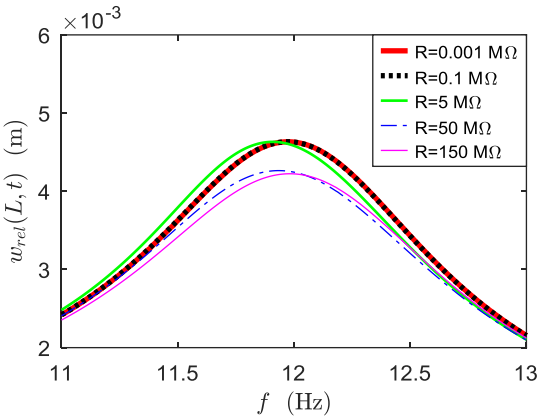

Figure 7.4 Frequency responses of the amplitude of the cantilever tip displacement under different load resistances at $\sigma = 200\ \mu C/m^2$ and $\hat{A} = 0.25g$.

To get a clearer view of the variation of the peaks, the resonance frequencies, i.e., f_{r}, and the corresponding amplitudes of the tip displacement, i.e., w_{r}, are drawn against the load resistance, and the obtained relationships are shown in Figure 7.5. It can be seen that the resistive shunt damping results in an interesting spiral curve in the 3D space of R-f_{r}-w_{r} in Figure 7.5(a). With the increase of the resistance, the resonance frequency first experiences a drop and then an increase and it can increase beyond the value at the initial state (which is of a very small resistance), as shown in Figure 7.5(b). While the resonance amplitude first undergoes an increase and then a gradual drop and seems stabilized at a certain level eventually, as shown in Figure 7.5(c).

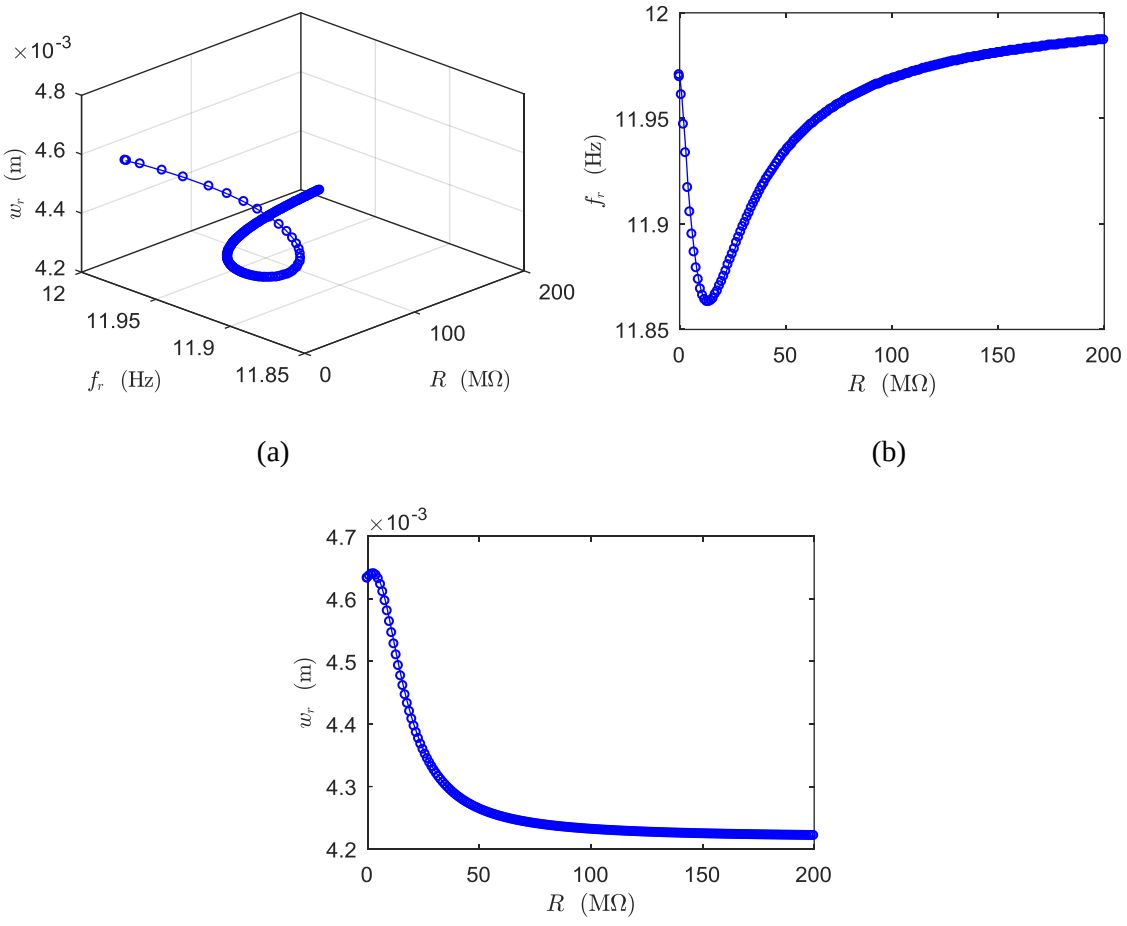

Figure 7.5 The relationships among load resistance, resonance frequency and amplitude: (a) a 3D plot, (b) load resistance against resonance frequency, and (c) load resistance against resonance amplitude; $\sigma = 200\ \mu\mathrm{C/m^2}$, $\hat{A} = 0.25\mathrm{g}$.

7.3. Effects of Electrical Properties on Vibrations of a Vertical Contact-Separation Mode TEH

7.3.1. Modelling of the System

7.3.1.1. Modelling of the Mechanical System

The configuration of a typical vertical contact-separation mode TEH is shown in Figure 7.6, where m is the mass, k is the stiffness, d_0 is the initial separation gap between the top electrode and the bottom dielectric, c is the damping and can be given as $c = 2\zeta\sqrt{km}$, where ζ is the damping ratio. The whole system is under sinusoidal base excitation.

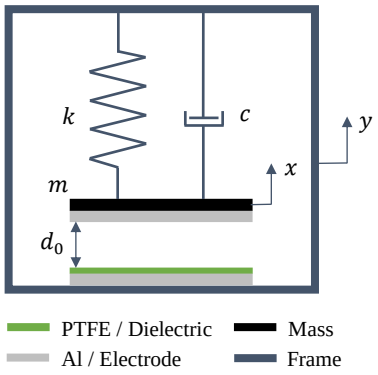

Figure 7.6 The configuration of the vertical contact-separation mode TEH.

The equation of motion of the mechanical system away from any two consecutive impacts can be given by

$$m\ddot{x} + c(\dot{x} - \dot{y}) + k(x - y) - F_{\mathrm{e}} = 0 \tag{7.1}$$

where $y = A\sin(\omega t)$and $\omega = 2\pi f$, F_{e} is the electrostatic attractive force, and the over-dot denotes a derivative over time t. The separation distance between the top electrode and the bottom dielectric is expressed as

$$d = d_0 + (x - y) \tag{7.2}$$

At impact, the relationship below can be established using Newton's law of restitution.

$$(\dot{x}_+ - \dot{y}) = -\mu(\dot{x}_- - \dot{y}) \tag{7.3}$$

where $\dot{x}_-$ is the velocity just before impact, $\dot{x}_+$ is the velocity just after impact, and μ is the coefficient of restitution which can be velocity-dependent, and the relationship between the

just-before-impact velocity and the value of coefficient of restitution experimentally identified in Chapter 5 (shown in Figure 5.7) is employed in simulation.

Stick may happen between the mass (or the top electrode) and the base (or the bottom dielectric). During stick, the mass has the same velocity and acceleration as the base, the separation distance d equals zero, and a contact force exists between them and is given in the following form. Note that charge transfer ceases during stick but the electrostatic force is not zero.

$$N = m\ddot{y} - kd_0 - F_{\mathrm{e}} \tag{7.4}$$

7.3.1.2. Modelling of the Electrical System

It has been found that a parasitic capacitor, which mainly comes from the structural interconnection and the external signal cables [240] and are in parallel with the harvester and the load, may be involved to alter the electrical model, especially when using high-value resistors [241].

According to Ref. [106, 241], the differential equation that governs the electrical system can be described by

$$\dot{Q} = \frac{1}{\left(1 + \frac{C_{\mathrm{p}}}{C_{\mathrm{e}}}\right)}\left(\frac{V_{\mathrm{oc}}}{R} - Q\left(\frac{1}{RC_{\mathrm{e}}} - \frac{C_{\mathrm{p}}}{C_{\mathrm{e}}^2}\dot{C}_{\mathrm{e}}\right)\right) \tag{7.5}$$

where Q is the amount of transferred charges between electrodes, R is the load resistance in circuit, C_{p} is the parasitic capacitance, and C_{e} and V_{oc} are the equivalent capacitance and the open-circuit voltage, respectively, and their expressions are [94, 106]

$$C_{\mathrm{e}} = \frac{\varepsilon_0 S}{t_{\mathrm{d}}/\varepsilon_{\mathrm{r}} + d} \tag{7.6}$$

$$V_{\mathrm{oc}} = \frac{\sigma d}{\varepsilon_0} \tag{7.7}$$

where S is the circular area of each electrode, ε_0 and ε_{r} are the vacuum permittivity and the relative permittivity of the bottom PTFE dielectric, t_{d} is the thickness of the dielectric, and σ is the tribo-charge surface density.

The total capacitance and potential energy of the capacitive system can be obtained as [242]

$$C(t) = C_{\mathrm{e}} + C_{\mathrm{p}} \tag{7.8}$$

$$U_{\mathrm{e}} = \frac{Q^2}{2C(t)} \tag{7.9}$$

Thus, the amount of the electrostatic force is given as

$$F_{\mathrm{e}} = -\frac{\mathrm{d}U_{\mathrm{e}}}{\mathrm{d}x_{\mathrm{r}}} = -\frac{\varepsilon_0 S Q^2}{2\left[\varepsilon_0 S + C_{\mathrm{p}}(t_{\mathrm{d}}/\varepsilon_{\mathrm{r}} + d)\right]^2} \tag{7.10}$$

where x_{r} is the displacement of the mass relative to the frame and $x_{\mathrm{r}} = x - y$.

7.3.2. Effects of Charge Density on Vibrations

The same numerical scheme is used here. The main parameters used in simulation are given in Table 7.2. The thickness of the dielectric layer or the PTFE layer is identical to that of the sliding mode TEH presented in Section 7.1.

Table 7.2 The values of the main parameters used in simulation

Parameter	Value
Mass, m	20 g
Damping ratio, ζ	0.005
Stiffness, k	240 N/m
Area, S	4 cm^2
Initial gap, d_0	3 mm
Parasitic capacitance, C_{p}	1 pF

The frequency responses of the amplitude of the separation distance under different tribo-charge surface densities at low and high load resistances of 1 MΩ and 100 MΩ at an excitation amplitude of $\hat{A} = 0.30$g, where $\hat{A} = A\omega^2$, are shown in Figure 7.7. As tribo-charge surface density is increased, it can be seen that the vibration amplitude is reduced and the resonance band is shifted towards the left. Further, the resonance band becomes wider,

especially in the high load resistance case as shown in Figure 7.7(b). This is because a larger tribo-charge surface density induces a larger electrostatic attractive force which, in turn, confines the oscillation of the mass to a relatively smaller range close to the bottom dielectric layer. Since the electrostatic attractive force can cause stiffness softening, i.e., the total displacement-related force is $f_{\mathrm{d}} = k(x-y) - F_{\mathrm{e}}$ so that the equivalent "spring" force is $\frac{\partial f_{\mathrm{d}}}{\partial x} = k - \frac{C_{\mathrm{p}}\varepsilon_0 SQ^2}{[\varepsilon_0 S + C_{\mathrm{p}}(t_{\mathrm{d}}/\varepsilon_{\mathrm{r}} + d)]^3} < k$, it results in a lower stiffness and thus shifts the resonance band towards the left.

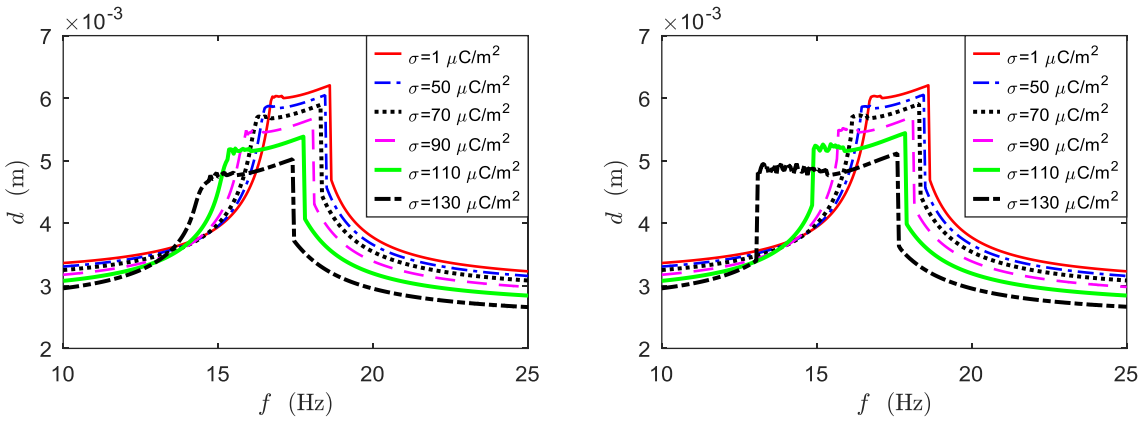

Figure 7.7 Frequency responses of the separation distance under different tribo-charge surface densities at (a) $R = 1$ MΩ and (b) $R = 100$ MΩ and $\hat{A} = 0.30$g.

Additionally, at larger tribo-charge surface densities and higher resistances, the mass (i.e., the top electrode) can get into contact with the bottom dielectric layer at smaller excitation frequencies. This is due to the increase of the electrostatic attractive force. The corresponding time histories of d at $f = 13.05$ Hz (blue dash-dot line) and $f = 13.10$ Hz (red solid line) are shown in Figure 7.8(a), while those at $f = 17.60$ Hz (red solid line) and $f = 17.65$ Hz (blue dash-dot line) are shown in Figure 7.8(b). It can be seen that the mass suddenly begins impacting with the bottom dielectric after just a small increase of excitation frequency from $f = 13.05$ Hz to $f = 13.10$ Hz, though there is a relatively long free-flight state between two consecutive impact events. At $f = 17.60$ Hz, the impacts are more frequent and intense, but disappear altogether when the frequency is increased to 17.65 Hz.

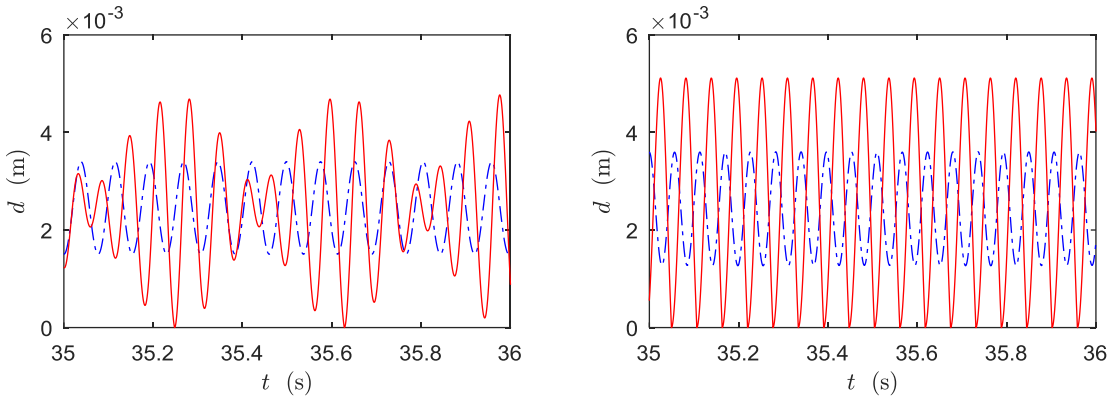

(a) (b)

Figure 7.8 Time histories of the separation distance d at (a) $f = 13.05$ Hz (blue dash-dot line) and $f = 13.10$ Hz (red solid line) and (b) $f = 17.60$ Hz (red solid line) and $f = 17.65$ Hz (blue dash-dot line); $\sigma = 130\ \mu\text{C/m}^2$, $R = 100\ \text{M}\Omega$, $\hat{A} = 0.30\text{g}$.

Returning attention to Figure 7.7, there exist some ripples on the left part of the resonance band. These ripples indicate non-periodic vibrations at the corresponding frequencies. This is because in generating the frequency response, the maximal vibration amplitude of the steady-state response over a hundred excitation periods is taken at each excitation frequency. Thus, the response curve fluctuates at frequencies where non-periodic vibrations are present. To give a clearer view, a bifurcation diagram of the system at $\sigma = 130\ \mu\text{C/m}^2$ and $R = 100\ \text{M}\Omega$ is shown in Figure 7.9. It can be seen that the system is in periodic motion before the mass experiences vibro-impact motion. With the increase of the excitation frequency, impact occurs and the system response becomes non-periodic, and grazing bifurcation might happen in this process. However, the system will eventually return to stable periodic motion with the increase of the excitation frequency.

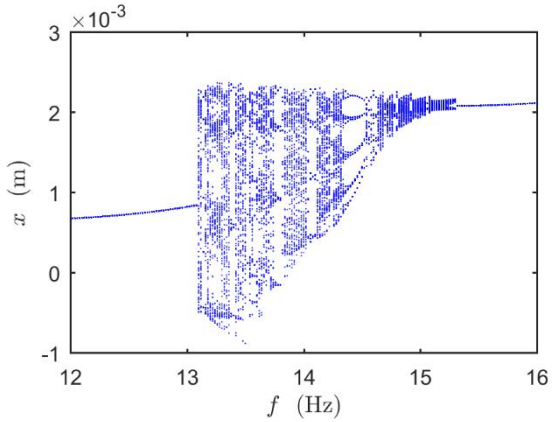

Figure 7.9 Bifurcation diagram of the amplitude of the displacement of the mass when $\sigma = 130\ \mu\text{C/m}^2$, $R = 100\ \text{M}\Omega$ and $\hat{A} = 0.30\text{g}$.

7.3.3. Effects of Load Resistance on Vibrations

For different load resistances, the corresponding frequency response of the separation distance are shown in Figure 7.10(a) and (b) for tribo-charge surface densities of $\sigma = 1\ \mu\text{C/m}^2$ and $\sigma = 100\ \mu\text{C/m}^2$. In Figure 7.10(a), the variation of the load resistance does not have an obvious effect on the frequency responses when the tribo-charge surface density is small. However, the influence can be observed at a larger tribo-charge surface density, as shown in Figure 7.10(b) and (c). The resonance band becomes slightly wider with the increase of the load resistance.

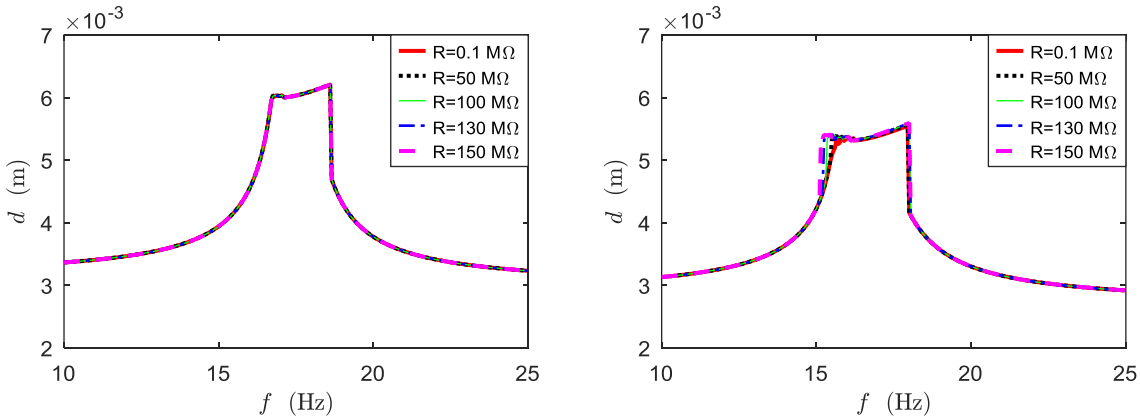

(a) (b)

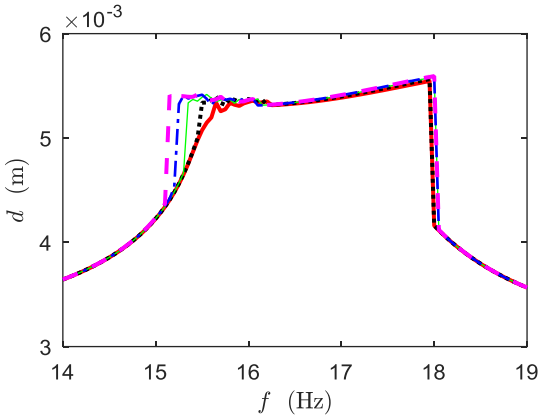

(c)

Figure 7.10 Frequency responses of the amplitude of the separation distance under different load resistances at (a) $\sigma = 1$ μC/m^2, (b) $\sigma = 100$ μC/m^2, and (c) a local view of (b); $\hat{A} = 0.30$g.

7.4. Conclusions

The effects of electrical properties on the vibrations of TEHs of both vertical contact-separation and lateral sliding modes are investigated in this chapter and are shown in two separate parts. In the first part, the model used for the sliding mode TEH is the same as that presented in Chapter 6 but with magnets removed and dimensions reduced. The effects of the tribo-charge surface density and the load resistance on vibrations are studied separately. In the second part, the modelling of a vertical contact-separation mode TEH, which is based on a single-degree-of-freedom vibro-impact oscillator, is first established, and then the effects of the same electrical properties on vibrations are investigated. This brief study intends to fill an existing research gap by analysing the effects of electrical properties on mechanical vibration

due to “reverse electromechanical coupling”, i.e., the coupling from the electrical system to the mechanical system. The main conclusions are as follows:

For the lateral sliding mode TEH, the increase of the tribo-charge surface density has an effect that is similar to mechanical damping, i.e., increasing tribo-charge surface density attenuates the vibration amplitudes and shifts the resonance peaks towards slightly lower frequencies. At large tribo-charge surface densities, the increase of the load resistance results in an interesting resistive shunt damping phenomenon involving both vibration amplitude attenuation and resonance frequency shifting, which is quite different from what appears in piezoelectric energy harvesters.

For the vertical contact-separation mode TEH, the increase of the tribo-charge surface density leads to both obvious vibration amplitude attenuation and resonance frequency shifting at both low and high load resistances, and it also results in a wider resonance band and complex oscillations. While the increase of the load resistance has only a minor influence at large tribo-charge surface densities, it tends to widen the resonance band slightly.

These studies and findings further reveal the electromechanical coupling mechanisms in TEHs and shed some light on tuning the electrical properties of the devices.

Chapter 8

Conclusions and Outlooks

8.1. Conclusions

This thesis presents the study of triboelectric energy harvesters (TEHs) of different working modes mainly from the perspectives of structural dynamics. Since TEHs are usually non-smooth systems owing to the nature of their working mechanisms, for example, the vertical contact-separation mode TEH is dependent on vibro-impact motions while the lateral sliding mode TEH involves friction and potential friction-induced vibrations, the modelling and investigation of the relevant non-smooth systems are paid much attention in this thesis. Due to the electromechanical coupling, the dynamics of the non-smooth mechanical systems shapes the output of the coupled electrical systems, which allows the analysis and optimization of the performance of TEHs from the prospects of structural dynamics and becomes the foundation on which most of the investigations in this thesis are based. In addition to the studies based on the "direct electromechanical coupling", the effects of the electrical properties on the behaviours of the mechanical systems in TEHs are researched based on the "reverse electromechanical coupling" which is achieved by the electrostatic force resultant from the opposite charges induced. This part of study reveals the electromechanical coupling mechanisms and sheds some light on tuning the harvester from the electrical aspects.

Studies are carried out mainly through theoretical modelling and numerical simulation, and experimental investigations and validations are conducted for some of the research topics. Major contributions to knowledge are listed below as bullet points with reference to the published papers covering them, and they also correspond to the research gaps and issues identified in Chapter 2.

- A theoretical model describing the mechanical vibration of a typical contact freestanding triboelectric-layer mode TEH is established, and a circuit simulator is

developed in Simulink [243]. The combination of them allows the analyses of the vibro-impact dynamics and its influence on the harvesting performance.

- Two key parameters related to the masses, i.e., the ratio and initial spacing between them, of the contact freestanding triboelectric-layer mode TEH are studied and shown to result in distinct vibro-impact dynamics. And under certain values of these parameters, chatter and sticking occur and are shown to be able to outperform resonance in terms of efficient energy harvesting [243].

- A relationship between the just-before-impact velocity and the velocity-dependent coefficient of restitution for the impact between PTFE and aluminium is experimentally identified [244]. This relationship can be used to model the impact in TEHs which are based on vibro-impact and adopt the same combination of materials.

- A more advanced theoretical model incorporating both the mechanical and electrical systems of a contact freestanding triboelectric-layer mode TEH is established and validated by experiments [244]. This modelling work facilitates further research to be conducted on this unique mode TEHs.

- A numerical scheme, which is based on the TR-BDF2 (Trapezoidal Rule and Backward Difference Formula of second order) method, is proposed to integrate the non-smooth mechanical system and the stiff electrical system and is verified by experiments [244]. This numerical scheme is also applicable to other TEHs.

- A theoretical model, which involves friction and magnetic multistability, of a sliding mode TEH is established. Broadband energy harvesting is achieved by the involvement of bistability. Simulations revealing the effects of friction and initial conditions are conducted.

- A numerical algorithm is developed to categorize different types of multistability of a non-conservative multistable system. The influence of the non-conservative force or the friction force on the variation of the multistability of the system is revealed.

- The effects of the electrical properties, including the tribo-charge surface density and the load resistance, on the behaviours of the mechanical systems in TEHs of two most common working modes, i.e., vertical contact-separation mode and lateral sliding mode, are revealed owing to the "reverse electromechanical coupling" via electrostatic force.

8.2. Outlooks and Discussion

8.2.1. Friction in Triboelectric Energy Harvesting

How does the friction between two triboelectric materials affect their triboelectrification, especially in lateral sliding mode TEHs, is still not much unveiled, which will be an interdisciplinary research and will require the knowledge of physics and material science. Too slight friction may affect the strength of triboelectrification while too heavy friction will definitely reduce the durability of triboelectric materials in the first place, but it is interesting to find out whether there exists a range within which the triboelectrification will be strengthened with the increase of friction.

On the other hand, friction may be affected by triboelectrification, and the coefficients of friction or the normal force may be changed with the variation of the strength of triboelectrification or the electrostatic attractive force. The corresponding research will mainly be experimental as well.

In addition, material surface modification in nano- or micro-scale has been shown to be able to enhance the triboelectric charge density [245]. However, whether the material surface modification will influence the characteristics of friction, such as the static and kinetic coefficients of friction, is still unknown. Relevant studies can be carried out by testing the coefficients of friction between triboelectric materials with different modification scales and patterns.

Finally, the choice or development of friction laws can be an interesting topic. Friction and triboelectrification may be coupled through an advanced friction law tailored for the study of the sliding mode TEHs. In that case, the mutual influence to each side will be incorporated into the theoretical models.

8.2.2. Triboelectric Energy Harvesting from Random Vibrations

In engineering practice, many excitations exhibit randomly fluctuating characteristics rather than simple harmonic forms, such as the vibration of bridges, though deterministic harmonic excitations, as an idealised excitation form, have been adopted in many studies and in various fields. Studies of energy harvestings from the combined harmonic and stochastic vibrations or pure stochastic vibrations have drawn much attention in both PEHs and EEHs. However, the investigation of TEHs from the perspectives of structural dynamics is still at an early stage, the research work presented in this thesis, therefore, has adopted deterministic harmonic excitations.

In addition to the commonly used numerical techniques, such as the Monte Carlo simulation, in the study of randomly excited systems, the theoretical methods seen in the literature include stochastic averaging [246], equivalent linearization [247], multiple scale method [248], etc. However, these theoretical methods are developed based on smooth dynamical systems and cannot be directly applied to non-smooth systems. Nevertheless, some particular techniques, which can transform the non-smooth models into smooth ones [249], have been developed to facilitate the application of those theoretical methods. These techniques include the power-law phenomenological modelling, the Zhuravlev and Ivanov non-smooth coordinate transformations, the Hertzian contact law, etc. The applicability and accuracy of non-smooth coordinate transformations depend on the extent of impact loss, and large impact loss often results in poor approximations. Other techniques mentioned above usually need the experimental estimations of certain parameters and may only stand under some particular assumptions. Therefore, the study of TEHs under stochastic excitations using the available theoretical methods can be complex and challenging, especially when it comes to multi-degree-of-freedom nonlinear TEHs. Besides, using the numerical techniques to study TEHs under stochastic excitations can be complicated and time-consuming as well, considering the large-scale computation involved in the simulation of a TEH consisting of a non-smooth mechanical system and a stiff electrical system. Nevertheless, relevant studies can always be carried out from the experimental aspects.

8.2.3. Power Management and Optimization

Despite the progress that has been made on nonlinear vibration energy harvesting, a notable knowledge gap still exists in integrating nonlinear energy harvesters with effective nonlinear

rectifying and power management circuits for practical applications [250]. In comparison, using energy harvesters as the sources is quite different from using batteries [251]. First, energy harvesters have limits on the maximum rate at which the energy can be used. Second, the output performance of an energy harvester is highly dependent on the characteristics of the input excitation and can vary in a nondeterministic way. While a deterministic metric, such as the residual battery, can only be used to characterize the energy availability when a battery is used as the source, an appropriate characterization may be necessary when an energy harvester works as the source. Finally, in practical applications, different energy harvesting nodes can have distinct harvesting opportunity. Therefore, these three issues make the power management and optimization for energy-harvesting nodes even more challenging, but interesting topics are also covered and can be carried out from the perspectives of electronics.

Appendix A

The Application of the TR-BDF2 Method in Chapter 4

To employ the TR-BDF2 method to integrate the system of equations which includes the non-smooth dynamical equations of vibration and the stiff ODE of electrical output, the second order ODEs of equations of motion, i.e., Eq. (5.24), need to be transferred into first order ODEs.

Let $z_1 = q_1$, $z_2 = \dot{q}_1$, $z_3 = q_2$, $z_4 = \dot{q}_2$, $z_5 = q_3$, $z_6 = \dot{q}_3$, $z_7 = Q$, the system of first order ODEs are then

$$\begin{aligned}
\dot{z}_1 &= z_2 \\
\dot{z}_2 &= \alpha_{r1}\ddot{g} - 2\zeta_1\omega_1 z_2 - \omega_1^2 z_1 \\
\dot{z}_3 &= z_4 \\
\dot{z}_4 &= \alpha_{r2}\ddot{g} - 2\zeta_2\omega_2 z_4 - \omega_2^2 z_3 \\
\dot{z}_5 &= z_6 \\
\dot{z}_6 &= \alpha_{r3}\ddot{g} - 2\zeta_3\omega_3 z_6 - \omega_3^2 z_5 \\
\dot{z}_7 &= \frac{2\sigma}{\varepsilon_0 R}[s_{23} - (z_5\phi_3(L) - z_3\phi_2(L))] \\
&\quad - \frac{z_7}{\varepsilon_0 SR}[d_0 + s_{12} + s_{23} + z_1\phi_1(L) - z_5\phi_3(L)]
\end{aligned} \tag{A.1}$$

By applying the TR rule to the first sub step, one can get the implicit difference equations as follows

$$z_{1,n+\gamma} - \gamma\frac{\Delta t_n}{2} z_{2,n+\gamma} = z_{1,n} + \gamma\frac{\Delta t_n}{2} z_{2,n}$$

$$z_{2,n+\gamma} - \gamma\frac{\Delta t_n}{2}\left(\alpha_{r1}\ddot{g}_{n+\gamma} - 2\zeta_1\omega_1 z_{2,n+\gamma} - \omega_1^2 z_{1,n+\gamma}\right) =$$

$$z_{2,n} + \gamma\frac{\Delta t_n}{2}\left(\alpha_{r1}\ddot{g}_n - 2\zeta_1\omega_1 z_{2,n} - \omega_1^2 z_{1,n}\right)$$

$$z_{3,n+\gamma} - \gamma\frac{\Delta t_n}{2} z_{4,n+\gamma} = z_{3,n} + \gamma\frac{\Delta t_n}{2} z_{4,n}$$

$$z_{4,n+\gamma} - \gamma\frac{\Delta t_n}{2}\left(\alpha_{r2}\ddot{g}_{n+\gamma} - 2\zeta_2\omega_2 z_{4,n+\gamma} - \omega_2^2 z_{3,n+\gamma}\right) =$$

$$z_{4,n} + \gamma\frac{\Delta t_n}{2}\left(\alpha_{r2}\ddot{g}_n - 2\zeta_2\omega_2 z_{4,n} - \omega_2^2 z_{3,n}\right) \tag{A.2}$$

$$z_{5,n+\gamma} - \gamma\frac{\Delta t_n}{2} z_{6,n+\gamma} = z_{5,n} + \gamma\frac{\Delta t_n}{2} z_{6,n}$$

$$z_{6,n+\gamma} - \gamma\frac{\Delta t_n}{2}\left(\alpha_{r3}\ddot{g}_{n+\gamma} - 2\zeta_3\omega_3 z_{6,n+\gamma} - \omega_3^2 z_{5,n+\gamma}\right) =$$

$$z_{6,n} + \gamma\frac{\Delta t_n}{2}\left(\alpha_{r3}\ddot{g}_n - 2\zeta_3\omega_3 z_{6,n} - \omega_3^2 z_{5,n}\right)$$

$$z_{7,n+\gamma} - \gamma\frac{\Delta t_n}{2} u_{7,n+\gamma} = z_{7,n} + \gamma\frac{\Delta t_n}{2} u_{7,n}$$

where $u_{7,n+\gamma}$ is as follows and $u_{7,n}$ can be obtained by replacing the subscript $n+\gamma$ of the state variables in the last equation of Eq. (A.2) by n.

$$\begin{aligned} u_{7,n+\gamma} = {} & \frac{2\sigma}{\varepsilon_0 R}\left[s_{23} - \left(z_{5,n+\gamma}\phi_3(L) - z_{3,n+\gamma}\phi_2(L)\right)\right] \\ & - \frac{z_{7,n+\gamma}}{\varepsilon_0 SR}\left[d_0 + s_{12} + s_{23} + z_{1,n+\gamma}\phi_1(L) - z_{5,n+\gamma}\phi_3(L)\right] \end{aligned} \tag{A.3}$$

To use the Newton-Raphson method to solve these implicit difference equations for new state variables, i.e., $z_{i,n+\gamma}$ $(i = 1, 2, \cdots, 7)$, the Jacobian matrix is first obtained as

$$\mathbf{J} = \begin{bmatrix} \mathbf{H}_1 & \mathbf{H}_0 & \mathbf{H}_0 & \mathbf{H}_0 \\ \mathbf{H}_0 & \mathbf{H}_2 & \mathbf{H}_0 & \mathbf{H}_0 \\ \mathbf{H}_0 & \mathbf{H}_0 & \mathbf{H}_3 & \mathbf{H}_0 \\ \mathbf{H}_4 & \mathbf{H}_5 & \mathbf{H}_6 & \mathbf{H}_7 \end{bmatrix} \tag{A.4}$$

where the component matrices are

$$\mathbf{H}_i = \begin{bmatrix} 1 & -\gamma\frac{\Delta t_n}{2} \\ \gamma\frac{\Delta t_n}{2}\omega_i^2 & 1+\gamma\Delta t_n\zeta_i\omega_i \end{bmatrix}, i = 1,2,3$$

$$\mathbf{H}_0 = \begin{bmatrix} 0 & 0 \\ 0 & 0 \end{bmatrix}, \mathbf{H}_4 = \begin{bmatrix} \gamma\frac{\Delta t_n}{2}\frac{\phi_1(L)}{\varepsilon_0 SR}z_{7,n+\gamma} & 0 \end{bmatrix},$$

$$\mathbf{H}_5 = \begin{bmatrix} -\gamma\frac{\Delta t_n}{2}\frac{2\sigma}{\varepsilon_0 R}\phi_2(L) & 0 \end{bmatrix}, \mathbf{H}_6 = \begin{bmatrix} \gamma\frac{\Delta t_n\phi_3(L)}{2}\left(\frac{2\sigma}{\varepsilon_0 R} - \frac{z_{7,n+\gamma}}{\varepsilon_0 SR}\right) & 0 \end{bmatrix}$$

$$\mathbf{H}_7 = \left[1+\gamma\frac{\Delta t_n}{2}\frac{1}{\varepsilon_0 SR}\left[d_0 + s_{12} + s_{23} + z_{1,n+\gamma}\phi_1(L) - z_{5,n+\gamma}\phi_3(L)\right]\right]$$

After the TR step, the BDF2 rule is applied to the second sub step, one can then get the following implicit difference equations

$$z_{1,n+1} - \frac{1-\gamma}{2-\gamma}\Delta t_n z_{2,n+1} = \frac{1}{\gamma(2-\gamma)}z_{1,n+\gamma} - \frac{(1-\gamma)^2}{\gamma(2-\gamma)}z_{1,n}$$

$$z_{2,n+1} - \frac{1-\gamma}{2-\gamma}\Delta t_n\left(\alpha_{r1}\ddot{g}_{n+1} - 2\zeta_1\omega_1 z_{2,n+1} - \omega_1^2 z_{1,n+1}\right) =$$

$$\frac{1}{\gamma(2-\gamma)}z_{2,n+\gamma} - \frac{(1-\gamma)^2}{\gamma(2-\gamma)}z_{2,n}$$

$$z_{3,n+1} - \frac{1-\gamma}{2-\gamma}\Delta t_n z_{4,n+1} = \frac{1}{\gamma(2-\gamma)}z_{3,n+\gamma} - \frac{(1-\gamma)^2}{\gamma(2-\gamma)}z_{3,n}$$

$$z_{4,n+1} - \frac{1-\gamma}{2-\gamma}\Delta t_n\left(\alpha_{r2}\ddot{g}_{n+1} - 2\zeta_2\omega_2 z_{4,n+1} - \omega_2^2 z_{3,n+1}\right) = \quad \text{(A.5)}$$

$$\frac{1}{\gamma(2-\gamma)}z_{4,n+\gamma} - \frac{(1-\gamma)^2}{\gamma(2-\gamma)}z_{4,n}$$

$$z_{5,n+1} - \frac{1-\gamma}{2-\gamma}\Delta t_n z_{6,n+1} = \frac{1}{\gamma(2-\gamma)}z_{5,n+\gamma} - \frac{(1-\gamma)^2}{\gamma(2-\gamma)}z_{5,n}$$

$$z_{6,n+1} - \frac{1-\gamma}{2-\gamma}\Delta t_n\left(\alpha_{r3}\ddot{g}_{n+1} - 2\zeta_3\omega_3 z_{6,n+1} - \omega_3^2 z_{5,n+1}\right) =$$

$$\frac{1}{\gamma(2-\gamma)}z_{6,n+\gamma} - \frac{(1-\gamma)^2}{\gamma(2-\gamma)}z_{6,n}$$

$$z_{7,n+1} - \frac{1-\gamma}{2-\gamma}\Delta t_n \left\{ \frac{2\sigma}{\varepsilon_0 R}\left[s_{23} - \left(z_{5,n+1}\phi_3(L) - z_{3,n+1}\phi_2(L) \right) \right] \right.$$
$$\left. - \frac{z_{7,n+1}}{\varepsilon_0 SR}\left[d_0 + s_{12} + s_{23} + z_{1,n+1}\phi_1(L) - z_{5,n+1}\phi_3(L) \right] \right\}$$
$$= \frac{1}{\gamma(2-\gamma)} z_{7,n+\gamma} - \frac{(1-\gamma)^2}{\gamma(2-\gamma)} z_{7,n}$$

The Jacobian matrix of Eq. (A.5) is the same as Eq. (A.4) if the special value of γ, i.e., $\gamma = 2 - \sqrt{2}$, is chosen [226]. Otherwise, their Jacobian matrix can be obtained by replacing the $\frac{\gamma}{2}$ of each matrix element of Eq. (A.4) by $\frac{1-\gamma}{2-\gamma}$.

Appendix B

Piecewise Quadratic Fitting in Chapter 4

To use the piecewise quadratic fitting, the experimental data points are first broken into seven sets with eight breakpoints. Then, each data set or segment is fitted using the quadratic polynomial. The breakpoints are

$$\mathbf{V}_{-} = [V_{-1}, V_{-2}, V_{-3}, V_{-4}, V_{-5}, V_{-6}, V_{-7}, V_{-8}]$$
$$\mathbf{V}_{-} = [0.06169, 0.22920, 0.34040, 0.52020, 0.79970, 1.10000, 1.55300, 1.93700] \tag{B.1}$$

And the piecewise polynomial coefficients are calculated and shown as follows

$$\mathbf{P} = \begin{bmatrix} \mathbf{P}_1 \\ \mathbf{P}_2 \\ \mathbf{P}_3 \\ \mathbf{P}_4 \\ \mathbf{P}_5 \\ \mathbf{P}_6 \\ \mathbf{P}_7 \end{bmatrix} = \begin{bmatrix} -0.31911 & 0.17235 & 0.00684 \\ 4.17132 & 0.06544 & 0.02676 \\ -1.37635 & 0.99314 & 0.08561 \\ 0.01063 & 0.49821 & 0.21969 \\ -0.73922 & 0.50415 & 0.35977 \\ -0.08613 & 0.06018 & 0.44450 \\ 0.09539 & -0.01786 & 0.45408 \end{bmatrix} \tag{B.2}$$

in which $\mathbf{P}_i$ ($i = 1, 2, \ldots, 7$) are the corresponding row vectors in Eq. (B.2).

Therefore, one can have the piecewise quadratic polynomial

$$\mu = \mathbf{P}_i \mathbf{V}_i \tag{B.3}$$

where $\mathbf{V}_i^{\mathrm{T}} = [(V - V_{-i})^2, (V - V_{-i}), 1]$, and

$$\mathbf{P}_i = \begin{cases} \mathbf{P}_1, & V_{-1} \le V < V_{-2} \\ \mathbf{P}_2, & V_{-2} \le V < V_{-3} \\ \mathbf{P}_3, & V_{-3} \le V < V_{-4} \\ \mathbf{P}_4, & V_{-4} \le V < V_{-5} \\ \mathbf{P}_5, & V_{-5} \le V < V_{-6} \\ \mathbf{P}_6, & V_{-6} \le V < V_{-7} \\ \mathbf{P}_7, & V_{-7} \le V < V_{-8} \end{cases}$$

Appendix C

The Application of the TR-BDF2 Method in Chapter 5

To use the TR-BDF2 method, the second order ODE of the equation of motion, i.e., Eq. (6.16), is turned into the first order ODE. Let $z_1 = q$, $z_2 = \dot{q}$, and $z_3 = Q$. If there is no sticking motion, the governing equations of the whole system can be given as

$$\dot{z}_1 = z_2$$

$$\begin{aligned}\dot{z}_2 = {} & \alpha\ddot{g} + s_1[(\mu_{k1} - \mu_{k2})A_1(z_1) + \mu_{k2}S]\frac{N}{S}\phi(L_\mathrm{b}) - 2\zeta\omega z_2 - \omega^2 z_1 \\ & - \sum_{i=1}^{n}\frac{\mu_0 M_i V_i M_\mathrm{s} V_\mathrm{s}}{4\pi}\left[\frac{G_1(z_1)}{r_i^6(z_1)} - \frac{3G_2(z_1)}{r_i^{10}(z_1)}\right]\end{aligned} \tag{C.1}$$

$$\dot{z}_3 = \frac{\sigma t_\mathrm{d}[S - A_1(z_1)] - t_\mathrm{d} z_3}{\varepsilon_0 \varepsilon_\mathrm{r} A_1(z_1) R}$$

where

$$A_1(z_1) = 2r^2\cos^{-1}\left(\frac{s_2 z_1\phi(L_\mathrm{b})}{2r}\right) - \frac{1}{2}s_2 z_1\phi(L_\mathrm{b})\sqrt{4r^2 - [z_1\phi(L_\mathrm{b})]^2}$$

$$G_1(z_1) = -r_i^3(z_1)z_1[\phi']_{x=L_\mathrm{b}}^2 - 3r_i^2(z_1)\frac{\mathrm{d}r_i(z_1)}{\mathrm{d}z_1}\cos\theta$$

$$\begin{aligned}G_2(z_1) = {} & r_i^5(z_1)\{-z_1[\phi']_{x=L_\mathrm{b}}^2(d_x + z_1^2\delta_\mathrm{c})^2 + 4\delta_\mathrm{c} z_1(d_x + z_1^2\delta_\mathrm{c})\cos\theta \\ & - [d_x\phi(L_\mathrm{b}) + 3\delta_\mathrm{c} z_1^2\phi(L_\mathrm{b}) + 2(-1)^i d_y\delta_\mathrm{c} z_1]\sin\theta \\ & - (d_x + z_1^2\delta_\mathrm{c})[z_1\phi(L_\mathrm{b}) + (-1)^i d_y][\phi']_{x=L_\mathrm{b}}\} \\ & - 5r_i^4(z_1)\{(d_x + z_1^2\delta_\mathrm{c})^2\cos\theta \\ & - (d_x + z_1^2\delta_\mathrm{c})[z_1\phi(L_\mathrm{b}) + (-1)^i d_y]\sin\theta\}\frac{\mathrm{d}r_i(z_1)}{\mathrm{d}z_1}\end{aligned}$$

$$\frac{\mathrm{d}r_i(z_1)}{\mathrm{d}z_1} = r_i^{-1}(z_1)[2\delta_\mathrm{c} z_1(d_x + z_1^2\delta_\mathrm{c}) + [z_1\phi(L_\mathrm{b}) + (-1)^i d_y]\phi(L_\mathrm{b})]$$

in which the expressions of $r_i(z_1)$, $\sin\theta$ and $\cos\theta$ can be obtained by replacing the qs in the equations given in the context with z_1, and the values of s_1 and s_2 are given as

$$s_1 = \begin{cases} -1, & \dot{z}_1\phi(L_\mathrm{b}) > 0 \\ 1, & \dot{z}_1\phi(L_\mathrm{b}) < 0 \end{cases}$$

$$s_2 = \begin{cases} 1, & z_1\phi(L_\mathrm{b}) > 0 \\ -1, & z_1\phi(L_\mathrm{b}) < 0 \end{cases}$$

By applying the TR rule to the first sub step, one can get the implicit difference equations as follows

$$z_{1,n+\gamma} - \gamma\frac{\Delta t_n}{2} z_{2,n+\gamma} = z_{1,n} + \gamma\frac{\Delta t_n}{2} z_{2,n}$$

$$\begin{aligned} z_{2,n+\gamma} - \gamma\frac{\Delta t_n}{2}\Bigg\{ & \alpha\ddot{g}_{n+\gamma} + s_1\left[(\mu_{k1}-\mu_{k2})A_1\left(z_{1,n+\gamma}\right) + \mu_{k2}S\right]\frac{N}{S}\phi(L_\mathrm{b}) - 2\zeta\omega z_{2,n+\gamma} \\ & - \omega^2 z_{1,n+\gamma} - \sum_{i=1}^{n}\frac{\mu_0 M_i V_i M_\mathrm{s} V_\mathrm{s}}{4\pi}\left[\frac{G_1\left(z_{1,n+\gamma}\right)}{r_i^6\left(z_{1,n+\gamma}\right)} - \frac{3G_2\left(z_{1,n+\gamma}\right)}{r_i^{10}\left(z_{1,n+\gamma}\right)}\right]\Bigg\} \\ = z_{2,n} + \gamma\frac{\Delta t_n}{2}\Bigg\{ & \alpha\ddot{g}_n + s_1\left[(\mu_{k1}-\mu_{k2})A_1\left(z_{1,n}\right) + \mu_{k2}S\right]\frac{N}{S}\phi(L_\mathrm{b}) - 2\zeta\omega z_{2,n} \\ & - \omega^2 z_{1,n} - \sum_{i=1}^{n}\frac{\mu_0 M_i V_i M_\mathrm{s} V_\mathrm{s}}{4\pi}\left[\frac{G_1\left(z_{1,n}\right)}{r_i^6\left(z_{1,n}\right)} - \frac{3G_2\left(z_{1,n}\right)}{r_i^{10}\left(z_{1,n}\right)}\right]\Bigg\} \end{aligned} \tag{C.2}$$

$$z_{3,n+\gamma} - \gamma\frac{\Delta t_n}{2}\frac{\sigma t_\mathrm{d}\left[S - A_1\left(z_{1,n+\gamma}\right)\right] - t_\mathrm{d} z_{3,n+\gamma}}{\varepsilon_0\varepsilon_\mathrm{r}A_1\left(z_{1,n+\gamma}\right)R} = z_{3,n} + \gamma\frac{\Delta t_n}{2}\frac{\sigma t_\mathrm{d}\left[S - A_1\left(z_{1,n}\right)\right] - t_\mathrm{d} z_{3,n}}{\varepsilon_0\varepsilon_\mathrm{r}A_1\left(z_{1,n}\right)R}$$

To use the Newton-Raphson method to solve these implicit difference equations for the state variables at the intermediate time instant, i.e., $z_{i,n+\gamma}$ $(i = 1, 2, 3)$, the Jacobian matrix is first obtained as

$$\mathbf{J} = \begin{bmatrix} \mathbf{H}_1 \\ \mathbf{H}_2 \\ \mathbf{H}_3 \end{bmatrix} \tag{C.3}$$

where the component matrices are

$$\mathbf{H}_1 = \begin{bmatrix} 1 & -\gamma\dfrac{\Delta t_n}{2} & 0 \end{bmatrix}$$

$$\mathbf{H}_2 = [\mathrm{H}_{21} \quad 1+\gamma\Delta t_n\zeta\omega \quad 0]$$

$$\mathbf{H}_3 = \begin{bmatrix} \mathrm{H}_{31} & 0 & 1+\dfrac{\gamma\Delta t_n t_\mathrm{d}}{2\varepsilon_0\varepsilon_\mathrm{r}A_1\left(z_{1,n+\gamma}\right)R} \end{bmatrix}$$

in which

$$\mathrm{H}_{21} = -\frac{\gamma\Delta t_n s_1(\mu_{k1}-\mu_{k2})N\phi(L_\mathrm{b})}{2S}\frac{\partial A_1\left(z_{1,n+\gamma}\right)}{\partial z_{1,n+\gamma}} + \gamma\omega^2\frac{\Delta t_n}{2} + \sum_{i=1}^{n}\frac{\gamma\Delta t_n\mu_0 M_i V_i M_\mathrm{s} V_\mathrm{s}}{8\pi}\frac{\partial}{\partial z_{1,n+\gamma}}\left(\frac{G_1\left(z_{1,n+\gamma}\right)}{r_i^6\left(z_{1,n+\gamma}\right)} - \frac{3G_2\left(z_{1,n+\gamma}\right)}{r_i^{10}\left(z_{1,n+\gamma}\right)}\right)$$

$$\mathrm{H}_{31} = -\gamma\frac{\Delta t_n}{2}\frac{\partial}{\partial z_{1,n+\gamma}}\left(\frac{\sigma t_\mathrm{d}\left[S - A_1\left(z_{1,n+\gamma}\right)\right] - t_\mathrm{d}z_{3,n+\gamma}}{\varepsilon_0\varepsilon_\mathrm{r}A_1\left(z_{1,n+\gamma}\right)R}\right)$$

By using Eq. (5.34), one can obtain the difference equations for the BDF2 sub step (the derived equations are not detailed here). The Jacobian matrix of the difference equations of the BDF2 sub step is same with that of the TR sub step if $\gamma = 2-\sqrt{2}$.

When the electrostatic force is involved, matrix $\mathbf{H}_2$ ($\mathbf{H}_2 = [\mathbf{H}_2(1) \quad \mathbf{H}_2(2) \quad \mathbf{H}_2(3)]$) should be updated, and the updated elements are

$$\mathbf{H}_2(1) = \mathrm{H}_{21} + \frac{\gamma\Delta t_n s_1\mu_{k2}z_{3,n+\gamma}^2 C_\mathrm{r}\phi(L_\mathrm{b})}{4\varepsilon_0\varepsilon_\mathrm{r}A_1^2}\frac{\partial A_1\left(z_{1,n+\gamma}\right)}{\partial z_{1,n+\gamma}}$$

$$\mathbf{H}_2(3) = -\frac{\gamma\Delta t_n s_1 z_{3,n+\gamma}C_\mathrm{r}\phi(L_\mathrm{b})}{2\varepsilon_0\varepsilon_\mathrm{r}}\left(\frac{\mu_{k1}-\mu_{k2}}{S} + \frac{\mu_{k2}}{A_1}\right) \tag{C.4}$$

Appendix D

The Algorithm for the Categorization in Chapter 6

The algorithm used for the categorization of different types of stability in Chapter 6 is shown in a flowchart in Figure D.1, where **f** is the excitation frequency array, $\mathbf{w_{rel}}(L, 0)$ the initial tip displacement array, t_s the time within steady state, and $\boldsymbol{w}_{\mathbf{mean}}(h)$ the mean of $\boldsymbol{w}_{\mathbf{max2}}(h)$ and $\boldsymbol{w}_{\mathbf{min2}}(h)$.

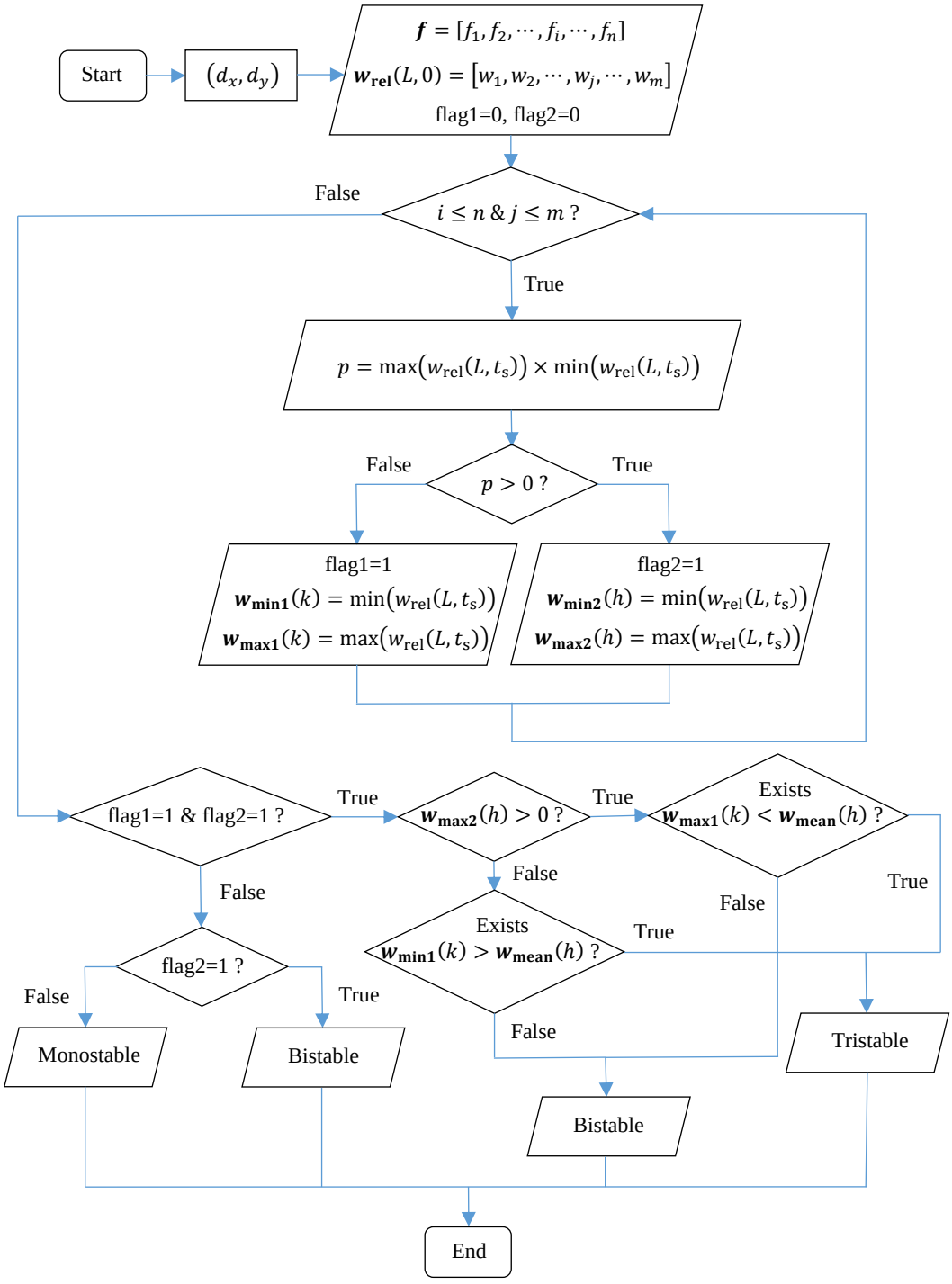

Figure D.1 Flowchart of the algorithm used for the categorization of different types of stability.

Appendix E

List of Publications

Accepted Journal Papers

- Y. Fu, H. Ouyang, R.B. Davis, Nonlinear dynamics and triboelectric energy harvesting from a three-degree-of-freedom vibro-impact oscillator, Nonlinear Dynamics 92 (2018) 1985-2004.

- Y. Fu, H. Ouyang, R.B. Davis, Triboelectric energy harvesting from the vibro-impact of three cantilevered beams, Mechanical Systems and Signal Processing 121 (2019) 509-531.

Papers Under Review

- Y. Fu, H. Ouyang, R.B. Davis, Nonlinear structural dynamics of a new sliding mode triboelectric energy harvester with multistability, Nonlinear Dynamics, under review.

- Y. Fu, H. Ouyang, R.B. Davis, Effects of electrical properties on vibrations via electromechanical coupling in triboelectric energy harvesting, Journal of Physics D: Applied Physics, under review.

References

[1] L. Atzori, A. Iera, G. Morabito, The internet of things: A survey, Computer Networks, 54 (2010) 2787-2805.

[2] D. Evans, The internet of things: How the next evolution of the internet is changing everything, CISCO White Paper, 1 (2011) 1-11.

[3] H. Lasi, P. Fettke, H.-G. Kemper, T. Feld, M. Hoffmann, Industry 4.0, Business & Information Systems Engineering, 6 (2014) 239-242.

[4] A. Caragliu, C. Del Bo, P. Nijkamp, Smart cities in Europe, Journal of Urban Technology, 18 (2011) 65-82.

[5] R. Min, M. Bhardwaj, S.-H. Cho, E. Shih, A. Sinha, A. Wang, A. Chandrakasan, Low-power wireless sensor networks, VLSI Design 2001. Fourteenth International Conference on VLSI Design, IEEE, 2001, pp. 205-210.

[6] J. Polastre, R. Szewczyk, D. Culler, Telos: enabling ultra-low power wireless research, Proceedings of the 4th International Symposium on Information Processing in Sensor Networks, IEEE Press, 2005, pp. 48.

[7] J.A. Martos-Sitcha, J. Sosa, D. Ramos-Valido, F.J. Bravo, C. Carmona-Duarte, H.L. Gomes, J.À. Calduch-Giner, E. Cabruja, A. Vega, M.Á. Ferrer, Ultra-low power sensor devices for monitoring physical activity and respiratory frequency in farmed fish, Frontiers in Physiology, 10 (2019).

[8] L.J. Currano, S. Bauman, W. Churaman, M. Peckerar, J. Wienke, S. Kim, M. Yu, B. Balachandran, Latching ultra-low power MEMS shock sensors for acceleration monitoring, Sensors and Actuators A: Physical, 147 (2008) 490-497.

[9] Z.L. Wang, J. Chen, L. Lin, Progress in triboelectric nanogenerators as a new energy technology and self-powered sensors, Energy & Environmental Science, 8 (2015) 2250-2282.

[10] Z.L. Wang, Self-powered nanotech, Scientific American, 298 (2008) 82-87.

[11] J. Yang, J. Chen, Y. Liu, W. Yang, Y. Su, Z.L. Wang, Triboelectrification-based organic film nanogenerator for acoustic energy harvesting and self-powered active acoustic sensing, ACS Nano, 8 (2014) 2649-2657.

[12] A. Sultana, M.M. Alam, T.R. Middya, D. Mandal, A pyroelectric generator as a self-powered temperature sensor for sustainable thermal energy harvesting from waste heat and human body heat, Applied Energy, 221 (2018) 299-307.

[13] M. Safaei, R.M. Meneghini, S.R. Anton, Force detection, center of pressure tracking, and energy harvesting from a piezoelectric knee implant, Smart Materials and Structures, 27 (2018) 13.

[14] B. Jaffe, Piezoelectric ceramics, Elsevier, 2012.

[15] G.J. Snyder, E.S. Toberer, Complex thermoelectric materials, materials for sustainable energy: a collection of peer-reviewed research and review articles from Nature Publishing Group, World Scientific, 2011, pp. 101-110.

[16] A. Erturk, D.J. Inman, Piezoelectric energy harvesting, John Wiley & Sons, 2011.

[17] V. Annapureddy, H. Palneedi, G.-T. Hwang, M. Peddigari, D.-Y. Jeong, W.-H. Yoon, K.-H. Kim, J. Ryu, Magnetic energy harvesting with magnetoelectrics: an emerging technology for self-powered autonomous systems, Sustainable Energy & Fuels, 1 (2017) 2039-2052.

[18] S. Naifar, S. Bradai, C. Viehweger, O. Kanoun, Survey of electromagnetic and magnetoelectric vibration energy harvesters for low frequency excitation, Measurement, 106 (2017) 251-263.

[19] D. Spreemann, Y. Manoli, Electromagnetic vibration energy harvesting devices: Architectures, design, modeling and optimization, Springer Science & Business Media, 2012.

[20] C.B. Williams, R.B. Yates, Analysis of a micro-electric generator for microsystems, Sensors and Actuators A: Physical, 52 (1996) 8-11.

[21] C.B. Williams, R.B. Yates, Analysis of a micro-electric generator for microsystems, Proceedings of the International Solid-State Sensors and Actuators Conference - TRANSDUCERS '95, 1995, pp. 369-372.

[22] M.T. Penella, M. Gasulla, A review of commercial energy harvesters for autonomous sensors, 2007 IEEE Instrumentation & Measurement Technology Conference IMTC 2007, 2007, pp. 1-5.

[23] H. Toshiyoshi, S. Ju, H. Honma, C.H. Ji, H. Fujita, MEMS vibrational energy harvesters, Science and Technology of Advanced Materials, 20 (2019) 124-143.

[24] A.R.M. Foisal, C. Hong, G.S. Chung, Multi-frequency electromagnetic energy harvester using a magnetic spring cantilever, Sensors and Actuators A-Physical, 182 (2012) 106-113.

[25] B. Alavikia, T.S. Almoneef, O.M. Ramahi, Wideband resonator arrays for electromagnetic energy harvesting and wireless power transfer, Applied Physics Letters, 107 (2015) 5.

[26] M.P.S. dos Santos, J.A.F. Ferreira, J.A.O. Simoes, R. Pascoal, J. Torrao, X.Z. Xue, E.P. Furlani, Magnetic levitation-based electromagnetic energy harvesting: a semi-analytical non-linear model for energy transduction, Scientific Reports, 6 (2016) 9.

[27] F.M. Foong, C.K. Thein, B.L. Ooi, D. Yurchenko, Increased power output of an electromagnetic vibration energy harvester through anti-phase resonance, Mechanical Systems and Signal Processing, 116 (2019) 129-145.

[28] H.L. Dai, A. Abdelkefi, U. Javed, L. Wang, Modeling and performance of electromagnetic energy harvesting from galloping oscillations, Smart Materials and Structures, 24 (2015) 11.

[29] M. Belhaq, M. Hamdi, Energy harvesting from quasi-periodic vibrations, Nonlinear Dynamics, 86 (2016) 2193-2205.

[30] P.V. Malaji, S.F. Ali, Magneto-mechanically coupled electromagnetic harvesters for broadband energy harvesting, Applied Physics Letters, 111 (2017) 083901.

[31] K. Pancharoen, D. Zhu, S.P. Beeby, Temperature dependence of a magnetically levitated electromagnetic vibration energy harvester, Sensors and Actuators A: Physical, 256 (2017) 1-11.

[32] P.L. Green, K. Worden, K. Atallah, N.D. Sims, The benefits of Duffing-type nonlinearities and electrical optimisation of a mono-stable energy harvester under white Gaussian excitations, Journal of Sound and Vibration, 331 (2012) 4504-4517.

[33] S. Palagummi, F.G. Yuan, An optimal design of a mono-stable vertical diamagnetic levitation based electromagnetic vibration energy harvester, Journal of Sound and Vibration, 342 (2015) 330-345.

[34] K. Fan, M. Cai, H. Liu, Y. Zhang, Capturing energy from ultra-low frequency vibrations and human motion through a monostable electromagnetic energy harvester, Energy, 169 (2019) 356-368.

[35] J. Cannarella, J. Selvaggi, S. Salon, J. Tichy, D.A. Borca-Tasciuc, Coupling factor between the magnetic and mechanical energy domains in electromagnetic power harvesting applications, IEEE Transactions on Magnetics, 47 (2011) 2076-2080.

[36] C.N. Loong, C.-C. Chang, E.G. Dimitrakopoulos, Circuit nonlinearity effect on the performance of an electromagnetic energy harvester-structure system, Engineering Structures, 173 (2018) 449-459.

[37] H. Zhang, L.R. Corr, T. Ma, Effects of electrical loads containing non-resistive components on electromagnetic vibration energy harvester performance, Mechanical Systems and Signal Processing, 101 (2018) 55-66.

[38] A. Bibo, R. Masana, A. King, G. Li, M.F. Daqaq, Electromagnetic ferrofluid-based energy harvester, Physics Letters A, 376 (2012) 2163-2166.

[39] Y. Kim, Induced voltage characteristics of back-iron effect for electromagnetic energy harvester using magnetic fluid, IEEE Transactions on Applied Superconductivity, 28 (2018) 1-4.

[40] K.Q. Fan, Y.W. Zhang, H.Y. Liu, M.L. Cai, Q.X. Tan, A nonlinear two-degree-of-freedom electromagnetic energy harvester for ultra-low frequency vibrations and human body motions, Renewable Energy, 138 (2019) 292-302.

[41] Y. Pan, T. Lin, F. Qian, C. Liu, J. Yu, J.Y. Zuo, L. Zuo, Modeling and field-test of a compact electromagnetic energy harvester for railroad transportation, Applied Energy, 247 (2019) 309-321.

[42] M. Iqbal, F.U. Khan, Hybrid vibration and wind energy harvesting using combined piezoelectric and electromagnetic conversion for bridge health monitoring applications, Energy Conversion and Management, 172 (2018) 611-618.

[43] N.V. Satpute, S.N. Satpute, L.M. Jugulkar, Hybrid electromagnetic shock absorber for energy harvesting in a vehicle suspension, Proceedings of the Institution of Mechanical Engineers Part C-Journal of Mechanical Engineering Science, 231 (2017) 1500-1517.

[44] A. Cammarano, S. Neild, S. Burrow, D. Wagg, D. Inman, Optimum resistive loads for vibration-based electromagnetic energy harvesters with a stiffening nonlinearity, Journal of Intelligent Material Systems and Structures, 25 (2014) 1757-1770.

[45] S. Chiacchiari, F. Romeo, D.M. McFarland, L.A. Bergman, A.F. Vakakis, Vibration energy harvesting from impulsive excitations via a bistable nonlinear attachment-experimental study, Mechanical Systems and Signal Processing, 125 (2019) 185-201.

[46] F. Khan, F. Sassani, B. Stoeber, Nonlinear behaviour of membrane type electromagnetic energy harvester under harmonic and random vibrations, Microsystem Technologies, 20 (2014) 1323-1335.

[47] D.A. Wang, C.Y. Chiu, H.T. Pham, Electromagnetic energy harvesting from vibrations induced by Karman vortex street, Mechatronics, 22 (2012) 746-756.

[48] J. Park, G. Morgenthal, K. Kim, S.D. Kwon, K.H. Law, Power evaluation of flutter-based electromagnetic energy harvesters using computational fluid dynamics simulations, Journal of Intelligent Material Systems and Structures, 25 (2014) 1800-1812.

[49] G. Caruso, G. Chirianni, G. Vairo, Energy harvesting from wind-induced bridge vibrations via electromagnetic transduction, Engineering Structures, 115 (2016) 118-128.

[50] H.J. Jung, I.H. Kim, S.J. Jang, An energy harvesting system using the wind-induced vibration of a stay cable for powering a wireless sensor node, Smart Materials & Structures, 20 (2011) 9.

[51] B. Padasdao, E. Shahhaidar, C. Stickley, O. Boric-Lubecke, Electromagnetic biosensing of respiratory rate, IEEE Sensors Journal, 13 (2013) 4204-4211.

[52] B.S. Joyce, J. Farmer, D.J. Inman, Electromagnetic energy harvester for monitoring wind turbine blades, Wind Energy, 17 (2014) 869-876.

[53] S.J. Guo, L. Xu, Y.L. Liu, X.X. Guo, L. Zuo, Modeling and experiments of a hydraulic electromagnetic energy-harvesting shock absorber, IEEE-ASME Transactions on Mechatronics, 22 (2017) 2684-2694.

[54] G.M. Karageorgos, C. Manopoulos, A. Kiourti, A. Karagiannis, S. Tsangaris, K.S. Nikita, An approach for self-powered cardiovascular monitoring based on electromagnetic induction, IEEE Sensors Journal, 18 (2018) 83-93.

[55] A. Afsharfard, Application of nonlinear magnetic vibro-impact vibration suppressor and energy harvester, Mechanical Systems and Signal Processing, 98 (2018) 371-381.

[56] H.A. Sodano, D.J. Inman, G. Park, A review of power harvesting from vibration using piezoelectric materials, Shock and Vibration Digest, 36 (2004) 197-206.

[57] N.W. Hagood, A. von Flotow, Damping of structural vibrations with piezoelectric materials and passive electrical networks, Journal of Sound and Vibration, 146 (1991) 243-268.

[58] E. Dimitriadis, C. Fuller, C. Rogers, Piezoelectric actuators for distributed vibration excitation of thin plates, Journal of Vibration and Acoustics, 113 (1991) 100-107.

[59] H.J. Pahk, D.S. Lee, J.H. Park, Ultra precision positioning system for servo motor–piezo actuator using the dual servo loop and digital filter implementation, International Journal of Machine Tools and Manufacture, 41 (2001) 51-63.

[60] H. Fu, G. Chen, N. Bai, Electrode coverage optimization for piezoelectric energy harvesting from tip excitation, Sensors, 18 (2018) 804.

[61] Y. Kuang, M. Zhu, Design study of a mechanically plucked piezoelectric energy harvester using validated finite element modelling, Sensors and Actuators A: Physical, 263 (2017) 510-520.

[62] M. Pozzi, M. Zhu, Plucked piezoelectric bimorphs for energy harvesting, Advances in Energy Harvesting Methods, Springer, 2013, pp. 119-140.

[63] H.L. Fu, E.M. Yeatman, Effective piezoelectric energy harvesting using beam plucking and a synchronized switch harvesting circuit, Smart Materials and Structures, 27 (2018) 13.

[64] R. Dauksevicius, A. Kleiva, V. Grigaliunas, Analysis of magnetic plucking dynamics in a frequency up-converting piezoelectric energy harvester, Smart Materials and Structures, 27 (2018) 19.

[65] B. Kathpalia, D. Tan, I. Stern, A. Erturk, An experimentally validated model for geometrically nonlinear plucking-based frequency up-conversion in energy harvesting, Smart Materials and Structures, 27 (2018) 9.

[66] P. Firoozy, S.E. Khadem, S.M. Pourkiaee, Power enhancement of broadband piezoelectric energy harvesting using a proof mass and nonlinearities in curvature and inertia, International Journal of Mechanical Sciences, 133 (2017) 227-239.

[67] A. Garg, S.K. Dwivedy, Nonlinear dynamics of parametrically excited piezoelectric energy harvester with 1:3 internal resonance, International Journal of Non-Linear Mechanics, 111 (2019) 82-94.

[68] W. Yang, S. Towfighian, A parametric resonator with low threshold excitation for vibration energy harvesting, Journal of Sound and Vibration, 446 (2019) 129-143.

[69] S.C. Stanton, A. Erturk, B.P. Mann, D.J. Inman, Nonlinear piezoelectricity in electroelastic energy harvesters: modeling and experimental identification, Journal of Applied Physics, 108 (2010) 9.

[70] A. Abdelkefi, A.H. Nayfeh, M.R. Hajj, Effects of nonlinear piezoelectric coupling on energy harvesters under direct excitation, Nonlinear Dynamics, 67 (2012) 1221-1232.

[71] H. Zhang, L.R. Corr, T. Ma, Effects of electrical loads containing non-resistive components on piezoelectric energy harvesting, Mechanical Systems and Signal Processing, 111 (2018) 210-221.

[72] A. Morel, A. Badel, R. Grezaud, P. Gasnier, G. Despesse, G. Pillonnet, Resistive and reactive loads' influences on highly coupled piezoelectric generators for wideband vibrations energy harvesting, Journal of Intelligent Material Systems and Structures, 30 (2019) 386-399.

[73] S. Nabavi, L.H. Zhang, Design and optimization of piezoelectric MEMS vibration energy harvesters based on genetic algorithm, IEEE Sensors Journal, 17 (2017) 7372-7382.

[74] V.R. Franco, P.S. Varoto, Parameter uncertainties in the design and optimization of cantilever piezoelectric energy harvesters, Mechanical Systems and Signal Processing, 93 (2017) 593-609.

[75] D. Gedeon, S.J. Rupitsch, Finite element based system simulation for piezoelectric vibration energy harvesting devices, Journal of Intelligent Material Systems and Structures, 29 (2018) 1333-1347.

[76] X.Y. Li, D. Upadrashta, K.P. Yu, Y.W. Yang, Analytical modeling and validation of multi-mode piezoelectric energy harvester, Mechanical Systems and Signal Processing, 124 (2019) 613-631.

[77] A. Bibo, M.F. Daqaq, Energy harvesting under combined aerodynamic and base excitations, Journal of Sound and Vibration, 332 (2013) 5086-5102.

[78] J.D. Hobeck, D.J. Inman, A distributed parameter electromechanical and statistical model for energy harvesting from turbulence-induced vibration, Smart Materials and Structures, 23 (2014) 15.

[79] M.Y. Zakaria, M.Y. Al-Haik, M.R. Hajj, Experimental analysis of energy harvesting from self-induced flutter of a composite beam, Applied Physics Letters, 107 (2015) 023901.

[80] Y.S. Cha, W.J. Chae, H. Kim, H. Walcott, S.D. Peterson, M. Porfiri, Energy harvesting from a piezoelectric biomimetic fish tail, Renewable Energy, 86 (2016) 449-458.

[81] M. Demori, M. Ferrari, A. Bonzanini, P. Poesio, V. Ferrari, Autonomous sensors powered by energy harvesting from Von Karman vortices in airflow, Sensors, 17 (2017) 15.

[82] G. Quaranta, F. Trentadue, C. Maruccio, G.C. Marano, Analysis of piezoelectric energy harvester under modulated and filtered white Gaussian noise, Mechanical Systems and Signal Processing, 104 (2018) 134-144.

[83] H. Wang, M.Q. Mao, Y. Liu, H.B. Qin, M. Zhang, W. Zhao, Impact energy harvesting system using mechanical vibration frequency stabilizer, Smart Materials and Structures, 28 (2019) 10.

[84] Y. Amini, M. Heshmati, P. Fatehi, S.E. Habibi, Piezoelectric energy harvesting from vibrations of a beam subjected to multi-moving loads, Applied Mathematical Modelling, 49 (2017) 1-16.

[85] C.G. Cooley, T. Chai, Energy harvesting from the vibrations of rotating systems, Journal of Vibration and Acoustics-Transactions of the Asme, 140 (2018) 11.

[86] C.G. Cooley, T.Q. Tran, T. Chai, Comparison of viscous and structural damping models for piezoelectric vibration energy harvesters, Mechanical Systems and Signal Processing, 110 (2018) 130-138.

[87] H. Mutsuda, Y. Tanaka, Y. Doi, Y. Moriyama, Application of a flexible device coating with piezoelectric paint for harvesting wave energy, Ocean Engineering, 172 (2019) 170-182.

[88] X. Chou, J. Zhu, S. Qian, X. Niu, J. Qian, X. Hou, J. Mu, W. Geng, J. Cho, J. He, All-in-one filler-elastomer-based high-performance stretchable piezoelectric nanogenerator for kinetic energy harvesting and self-powered motion monitoring, Nano Energy, 53 (2018) 550-558.

[89] A.T. Eshghi, S. Lee, M.K. Sadoughi, C. Hu, Y.C. Kim, J.H. Seo, Design optimization under uncertainty and speed variability for a piezoelectric energy harvester powering a tire pressure monitoring sensor, Smart Materials and Structures, 26 (2017) 18.

[90] K.B. Kim, J.Y. Cho, H. Jabbar, J.H. Ahn, S.D. Hong, S.B. Woo, T.H. Sung, Optimized composite piezoelectric energy harvesting floor tile for smart home energy management, Energy Conversion and Management, 171 (2018) 31-37.

[91] Y.H. Shin, I. Jung, M.S. Noh, J.H. Kim, J.Y. Choi, S. Kim, C.Y. Kang, Piezoelectric polymer-based roadway energy harvesting via displacement amplification module, Applied Energy, 216 (2018) 741-750.

[92] F.-R. Fan, Z.-Q. Tian, Z.L. Wang, Flexible triboelectric generator, Nano Energy, 1 (2012) 328-334.

[93] C. Jin, D.S. Kia, M. Jones, S. Towfighian, On the contact behavior of micro-/nano-structured interface used in vertical-contact-mode triboelectric nanogenerators, Nano Energy, 27 (2016) 68-77.

[94] Z.L. Wang, L. Lin, J. Chen, S. Niu, Y. Zi, Triboelectric nanogenerators, Springer, 2016.

[95] Z. Saadatnia, S.G. Mosanenzadeh, E. Esmailzadeh, H.E. Naguib, A high performance triboelectric nanogenerator using porous Polyimide aerogel film, Scientific Reports, 9 (2019) 1370.

[96] N. Cui, J. Liu, L. Gu, S. Bai, X. Chen, Y. Qin, Wearable triboelectric generator for powering the portable electronic devices, Acs Applied Materials & Interfaces, 7 (2015) 18225-18230.

[97] X. Wang, S. Niu, Y. Yin, F. Yi, Z. You, Z.L. Wang, Triboelectric nanogenerator based on fully enclosed rolling spherical structure for harvesting low‐frequency water wave energy, Advanced Energy Materials, 5 (2015) 1501467.

[98] Z.L. Wang, New wave power, Nature, 542 (2017) 159-160.

[99] J. Chen, J. Yang, H. Guo, Z. Li, L. Zheng, Y. Su, Z. Wen, X. Fan, Z.L. Wang, Automatic mode transition enabled robust triboelectric nanogenerators, ACS Nano, 9 (2015) 12334-12343.

[100] S.A. Shankaregowda, C.B. Nanjegowda, X.-L. Cheng, M.-Y. Shi, Z.-F. Liu, H.-X. Zhang, A flexible and transparent graphene-based triboelectric nanogenerator, IEEE Transactions on Nanotechnology, 15 (2016) 435-441.

[101] J. Chun, B.U. Ye, J.W. Lee, D. Choi, C.-Y. Kang, S.-W. Kim, Z.L. Wang, J.M. Baik, Boosted output performance of triboelectric nanogenerator via electric double layer effect, Nature Communications, 7 (2016) 12985.

[102] S. Wang, L. Lin, Y. Xie, Q. Jing, S. Niu, Z.L. Wang, Sliding-triboelectric nanogenerators based on in-plane charge-separation mechanism, Nano Letters, 13 (2013) 2226-2233.

[103] J. Yang, J. Chen, Y. Yang, H.L. Zhang, W.Q. Yang, P. Bai, Y.J. Su, Z.L. Wang, Broadband vibrational energy harvesting based on a triboelectric nanogenerator, Advanced Energy Materials, 4 (2014) 9.

[104] W. Du, X. Han, L. Lin, M. Chen, X. Li, C. Pan, Z.L. Wang, A three dimensional multi‐layered sliding triboelectric nanogenerator, Advanced Energy Materials, 4 (2014) 1301592.

[105] L. Lin, Y. Xie, S. Niu, S. Wang, P.-K. Yang, Z.L. Wang, Robust triboelectric nanogenerator based on rolling electrification and electrostatic induction at an instantaneous energy conversion efficiency of~ 55%, ACS Nano, 9 (2015) 922-930.

[106] S. Niu, S. Wang, L. Lin, Y. Liu, Y.S. Zhou, Y. Hu, Z.L. Wang, Theoretical study of contact-mode triboelectric nanogenerators as an effective power source, Energy & Environmental Science, 6 (2013) 3576-3583.

[107] S. Niu, Y. Liu, S. Wang, L. Lin, Y.S. Zhou, Y. Hu, Z.L. Wang, Theory of sliding‐mode triboelectric nanogenerators, Advanced Materials, 25 (2013) 6184-6193.

[108] S. Niu, Z.L. Wang, Theoretical systems of triboelectric nanogenerators, Nano Energy, 14 (2015) 161-192.

[109] S. Niu, Y.S. Zhou, S. Wang, Y. Liu, L. Lin, Y. Bando, Z.L. Wang, Simulation method for optimizing the performance of an integrated triboelectric nanogenerator energy harvesting system, Nano Energy, 8 (2014) 150-156.

[110] S. Niu, Y. Liu, Y.S. Zhou, S. Wang, L. Lin, Z.L. Wang, Optimization of triboelectric nanogenerator charging systems for efficient energy harvesting and storage, IEEE Transactions on Electron Devices, 62 (2014) 641-647.

[111] B. Yang, W. Zeng, Z.H. Peng, S.R. Liu, K. Chen, X.M. Tao, A fully verified theoretical analysis of contact-mode triboelectric nanogenerators as a wearable power source, Advanced Energy Materials, 6 (2016) 8.

[112] Y. Su, J. Chen, Z. Wu, Y. Jiang, Low temperature dependence of triboelectric effect for energy harvesting and self-powered active sensing, Applied Physics Letters, 106 (2015) 013114.

[113] R.I.G. Dharmasena, J.H. Deane, S.R.P. Silva, Nature of power generation and output optimization criteria for triboelectric nanogenerators, Advanced Energy Materials, 8 (2018) 1802190.

[114] H.-W. Park, N.D. Huynh, W. Kim, C. Lee, Y. Nam, S. Lee, K.-B. Chung, D. Choi, Electron blocking layer-based interfacial design for highly-enhanced triboelectric nanogenerators, Nano Energy, 50 (2018) 9-15.

[115] A. Nafari, H. Sodano, Surface morphology effects in a vibration based triboelectric energy harvester, Smart Materials and Structures, 27 (2017) 015029.

[116] S. Wang, L. Lin, Z.L. Wang, Nanoscale triboelectric-effect-enabled energy conversion for sustainably powering portable electronics, Nano Letters, 12 (2012) 6339-6346.

[117] L. Dhakar, H. Liu, F. Tay, C. Lee, A wideband triboelectric energy harvester, Journal of Physics: Conference Series, IOP Publishing, 2013, pp. 012128.

[118] L. Helseth, X. Guo, Triboelectric motion sensor combined with electromagnetic induction energy harvester, Sensors and Actuators A: Physical, 246 (2016) 66-72.

[119] A. Ibrahim, A. Ramini, S. Towfighian, Experimental and theoretical investigation of an impact vibration harvester with triboelectric transduction, Journal of Sound and Vibration, 416 (2018) 111-124.

[120] A. Ibrahim, M. Jain, E. Salman, R. Willing, S. Towfighian, A smart knee implant using triboelectric energy harvesters, Smart Materials and Structures, (2018).

[121] Z. Wen, J. Chen, M.H. Yeh, H.Y. Guo, Z.L. Li, X. Fan, T.J. Zhang, L.P. Zhu, Z.L. Wang, Blow-driven triboelectric nanogenerator as an active alcohol breath analyzer, Nano Energy, 16 (2015) 38-46.

[122] M.H. Yeh, H.Y. Guo, L. Lin, Z. Wen, Z.L. Li, C.G. Hu, Z.L. Wang, Rolling friction enhanced free-standing triboelectric nanogenerators and their applications in self-powered electrochemical recovery systems, Advanced Functional Materials, 26 (2016) 1054-1062.

[123] A.I. Uddin, P.S. Kumar, K. Hassan, H.C. Kim, Enhanced sensing performance of bimetallic Al/Ag-CNF network and porous PDMS-based triboelectric acetylene gas sensors in a high humidity atmosphere, Sensors and Actuators B: Chemical, 258 (2018) 857-869.

[124] R.A. Ibrahim, Vibro-impact dynamics. modeling, mapping and applications, Springer, 2009.

[125] A.C.J. Luo, Y. Guo, Vibro-impact Dynamics, 1st ed., Wiley.

[126] V.I. Babitskiĭ, N. Birkett, Theory of vibro-impact systems and applications, English ed. / translated by N. Birkett. ed., Springer, 2013.

[127] R.A. Ibrahim, Recent advances in vibro-impact dynamics and collision of ocean vessels, Journal of Sound & Vibration, 333 (2014) 5900-5916.

[128] Q.-J. Cao, M. Wiercigroch, E. Pavlovskaia, S.-P. Yang, Bifurcations and the penetrating rate analysis of a model for percussive drilling, Acta Mechanica Sinica, (2010) 467.

[129] R. DesRoches, M. Delemont, Seismic retrofit of simply supported bridges using shape memory alloys, Engineering Structures, 24 (2002) 325-332.

[130] E. Sitnikova, E. Pavlovskaia, J. Ing, M. Wiercigroch, Suppressing nonlinear resonances in an impact oscillator using SMAs, Smart Materials and Structures, 21 (2012) 075028.

[131] G. Luo, J. Yu, J. Xie, Codimension two bifurcation and chaos of a vibro-impact forming machine associated with 1: 2 resonance case, Acta Mechanica Sinica, 22 (2006) 185-198.

[132] H. Zhang, Y. Zhang, G. Luo, Basins of coexisting multi-dimensional tori in a vibro-impact system, Nonlinear Dynamics, 79 (2015) 2177-2185.

[133] E. Bureau, F. Schilder, M. Elmegård, I.F. Santos, J.J. Thomsen, J. Starke, Experimental bifurcation analysis of an impact oscillator—determining stability, Journal of Sound and Vibration, 333 (2014) 5464-5474.

[134] M. Elmegård, B. Krauskopf, H. Osinga, J. Starke, J.J. Thomsen, Bifurcation analysis of a smoothed model of a forced impacting beam and comparison with an experiment, Nonlinear Dynamics, 77 (2014) 951-966.

[135] K. Czolczynski, B. Blazejczyk-Okolewska, T. Kapitaniak, Impact force generator: self-synchronization and regularity of motion, Chaos, Solitons & Fractals, 11 (2000) 2505-2510.

[136] D. Huang, W. Xu, D. Liu, Q. Han, Multi-valued responses of a nonlinear vibro-impact system excited by random narrow-band noise, Journal of Vibration and Control, 22 (2016) 2907-2920.

[137] Z. Huang, Z. Liu, W. Zhu, Stationary response of multi-degree-of-freedom vibro-impact systems under white noise excitations, Journal of Sound and Vibration, 275 (2004) 223-240.

[138] M.P. Soares dos Santos, J.A.F. Ferreira, J.A.O. Simões, R. Pascoal, J. Torrão, X. Xue, E.P. Furlani, Magnetic levitation-based electromagnetic energy harvesting: a semi-analytical non-linear model for energy transduction, Scientific Reports, 6 (2016) 18579.

[139] A. Haroun, I. Yamada, S. Warisawa, Study of electromagnetic vibration energy harvesting with free/impact motion for low frequency operation, Journal of Sound and Vibration, 349 (2015) 389-402.

[140] B. Edwards, P.A. Hu, K.C. Aw, Validation of a hybrid electromagnetic–piezoelectric vibration energy harvester, Smart Materials and Structures, 25 (2016) 055019.

[141] N.S. Yuksek, M. Almasri, Z.C. Feng, Broadband electromagnetic power harvester from vibrations via frequency conversion by impact oscillations, Applied Physics Letters, 105 (2014).

[142] B. Edwards, K.C. Aw, A.P. Hu, Mechanical frequency up-conversion for sub-resonance, low-frequency vibration harvesting, Journal of Intelligent Material Systems and Structures, 27 (2016) 2145-2159.

[143] Ö. Zorlu, H. Külah, A MEMS-based energy harvester for generating energy from non-resonant environmental vibrations, Sensors and Actuators A: Physical, 202 (2013) 124-134.

[144] Z. Ö, E.T. Topal, H. Kulah, A vibration-based electromagnetic energy harvester using mechanical frequency up-conversion method, IEEE Sensors Journal, 11 (2011) 481-488.

[145] P. Podder, A. Amann, S. Roy, Combined effect of bistability and mechanical impact on the performance of a nonlinear electromagnetic vibration energy harvester, IEEE-ASME Transactions on Mechatronics, 21 (2016) 727-739.

[146] Z. Lin, Y. Zhang, Dynamics of a mechanical frequency up-converted device for wave energy harvesting, Journal of Sound and Vibration, 367 (2016) 170-184.

[147] C. Wang, Q. Zhang, W. Wang, Low-frequency wideband vibration energy harvesting by using frequency up-conversion and quin-stable nonlinearity, Journal of Sound and Vibration, 399 (2017) 169-181.

[148] E. Dechant, F. Fedulov, D.V. Chashin, L.Y. Fetisov, Y.K. Fetisov, M. Shamonin, Low-frequency, broadband vibration energy harvester using coupled oscillators and frequency up-conversion by mechanical stoppers, Smart Materials and Structures, 26 (2017) 065021.

[149] M.A. Halim, J.Y. Park, Piezoceramic based wideband energy harvester using impact-enhanced dynamic magnifier for low frequency vibration, Ceramics International, 41 (2015) S702-S707.

[150] R. Ai, L.L.S. Monteiro, P.C.C. Monteiro, P. Pacheco, M.A. Savi, Piezoelectric vibration-based energy harvesting enhancement exploiting nonsmoothness, Actuators, 8 (2019) 15.

[151] Y.P. Wu, A. Badel, F. Formosa, W.Q. Liu, A. Agbossou, Nonlinear vibration energy harvesting device integrating mechanical stoppers used as synchronous mechanical switches, Journal of Intelligent Material Systems and Structures, 25 (2014) 1658-1663.

[152] J. Rastegar, C. Pereira, H.-L. Nguyen, Piezoelectric-based power sources for harvesting energy from platforms with low-frequency vibration, Smart Structures and Materials 2006: Industrial and Commercial Applications of Smart Structures Technologies, International Society for Optics and Photonics, 2006, pp. 617101.

[153] H. Li, C. Tian, Z.D. Deng, Energy harvesting from low frequency applications using piezoelectric materials, Applied Physics Reviews, 1 (2014) 041301.

[154] R. Dauksevicius, R. Gaidys, V. Ostasevicius, R. Lockhart, A.V. Quintero, N. de Rooij, D. Briand, Nonlinear piezoelectric vibration energy harvester with frequency-tuned impacting resonators for improving broadband performance at low frequencies, Smart Materials and Structures, 28 (2019) 21.

[155] K. Vijayan, M.I. Friswell, H.H. Khodaparast, S. Adhikari, Non-linear energy harvesting from coupled impacting beams, International Journal of Mechanical Sciences, 96-97 (2015) 101-109.

[156] W. Li, N.E. Wierschem, X. Li, T. Yang, On the energy transfer mechanism of the single-sided vibro-impact nonlinear energy sink, Journal of Sound and Vibration, 437 (2018) 166-179.

[157] D. Liu, J.L. Li, Y. Meng, Probabilistic response analysis for a class of nonlinear vibro-impact oscillator with bilateral constraints under colored noise excitation, Chaos Solitons & Fractals, 122 (2019) 179-188.

[158] D.A. Jacobs, K.J. Waldron, Modeling inelastic vollisions with the Hunt-Crossley model using the energetic coefficient of restitution, Journal of Computational and Nonlinear Dynamics, 10 (2015) 10.

[159] X.L. Fu, W.H. Liao, Nondimensional model and parametric studies of impact piezoelectric energy harvesting with dissipation, Journal of Sound and Vibration, 429 (2018) 78-95.

[160] J. Chen, G. Zhu, W.Q. Yang, Q.S. Jing, P. Bai, Y. Yang, T.C. Hou, Z.L. Wang, Harmonic-resonator-based triboelectric nanogenerator as a sustainable power source and a self-powered active vibration sensor, Advanced Materials, 25 (2013) 6094-6099.

[161] G. Liu, W. Xu, X. Xia, H. Shi, C. Hu, Newton's cradle motion-like triboelectric nanogenerator to enhance energy recycle efficiency by utilizing elastic deformation, Journal of Materials Chemistry A, 3 (2015) 21133-21139.

[162] W. Yang, J. Chen, G. Zhu, X. Wen, P. Bai, Y. Su, Y. Lin, Z. Wang, Harvesting vibration energy by a triple-cantilever based triboelectric nanogenerator, Nano Research, 6 (2013) 880-886.

[163] S. Wang, S. Niu, J. Yang, L. Lin, Z.L. Wang, Quantitative measurements of vibration amplitude using a contact-mode freestanding triboelectric nanogenerator, ACS Nano, 8 (2014) 12004-12013.

[164] X.N. Wen, W.Q. Yang, Q.S. Jing, Z.L. Wang, Harvesting broadband kinetic impact energy from mechanical triggering/vibration and water waves, ACS Nano, 8 (2014) 7405-7412.

[165] D. Nelson, A. Ibrahim, S. Towfighian, A tunable triboelectric wideband energy harvester, Journal of Intelligent Material Systems and Structures, 30 (2019) 1745-1756.

[166] S.C. Stanton, C.C. McGehee, B.P. Mann, Nonlinear dynamics for broadband energy harvesting: investigation of a bistable piezoelectric inertial generator, Physica D: Nonlinear Phenomena, 239 (2010) 640-653.

[167] R.L. Harne, K. Wang, A review of the recent research on vibration energy harvesting via bistable systems, Smart Materials and Structures, 22 (2013) 023001.

[168] M.D. Shrimali, A. Prasad, R. Ramaswamy, U. Feudel, The nature of attractor basins in multistable systems, International Journal of Bifurcation and Chaos, 18 (2008) 1675-1688.

[169] A. Erturk, D.J. Inman, Broadband piezoelectric power generation on high-energy orbits of the bistable Duffing oscillator with electromechanical coupling, Journal of Sound and Vibration, 330 (2011) 2339-2353.

[170] R. Masana, M.F. Daqaq, Energy harvesting in the super-harmonic frequency region of a twin-well oscillator, Journal of Applied Physics, 111 (2012) 044501.

[171] H. Fang, K. Wang, Piezoelectric vibration-driven locomotion systems–exploiting resonance and bistable dynamics, Journal of Sound and Vibration, 391 (2017) 153-169.

[172] A. Erturk, J. Hoffmann, D.J. Inman, A piezomagnetoelastic structure for broadband vibration energy harvesting, Applied Physics Letters, 94 (2009) 254102.

[173] C. Lan, W. Qin, Enhancing ability of harvesting energy from random vibration by decreasing the potential barrier of bistable harvester, Mechanical Systems and Signal Processing, 85 (2017) 71-81.

[174] J. Cao, S. Zhou, D.J. Inman, Y. Chen, Chaos in the fractionally damped broadband piezoelectric energy generator, Nonlinear Dynamics, 80 (2015) 1705-1719.

[175] G. Pennisi, B. Mann, N. Naclerio, C. Stephan, G. Michon, Design and experimental study of a nonlinear energy sink coupled to an electromagnetic energy harvester, Journal of Sound and Vibration, 437 (2018) 340-357.

[176] H. Vocca, I. Neri, F. Travasso, L. Gammaitoni, Kinetic energy harvesting with bistable oscillators, Applied Energy, 97 (2012) 771-776.

[177] D. Nelson, A. Ibrahim, S. Towfighian, Dynamics of a threshold shock sensor: combining bi-stability and triboelectricity, Sensors and Actuators A: Physical, 285 (2019) 666-675.

[178] R. Naseer, H. Dai, A. Abdelkefi, L. Wang, Piezomagnetoelastic energy harvesting from vortex-induced vibrations using monostable characteristics, Applied Energy, 203 (2017) 142-153.

[179] D.N. Betts, H.A. Kim, C.R. Bowen, D. Inman, Optimal configurations of bistable piezo-composites for energy harvesting, Applied Physics Letters, 100 (2012) 114104.

[180] F. Cottone, P. Basset, H. Vocca, L. Gammaitoni, T. Bourouina, Bistable electromagnetic generator based on buckled beams for vibration energy harvesting, Journal of Intelligent Material Systems and Structures, 25 (2014) 1484-1495.

[181] G. Pennisi, B.P. Mann, N. Naclerio, C. Stephan, G. Michon, Design and experimental study of a nonlinear energy sink coupled to an electromagnetic energy harvester, Journal of Sound and Vibration, 437 (2018) 340-357.

[182] G. Litak, M.I. Friswell, S. Adhikari, Regular and chaotic vibration in a piezoelectric energy harvester, Meccanica, 51 (2016) 1017-1025.

[183] Y.G. Leng, Y.J. Gao, D. Tan, S.B. Fan, Z.H. Lai, An elastic-support model for enhanced bistable piezoelectric energy harvesting from random vibrations, Journal of Applied Physics, 117 (2015) 12.

[184] G.Q. Wang, W.H. Liao, A bistable piezoelectric oscillator with an elastic magnifier for energy harvesting enhancement, Journal of Intelligent Material Systems and Structures, 28 (2017) 392-407.

[185] C.B. Lan, W.Y. Qin, Enhancing ability of harvesting energy from random vibration by decreasing the potential barrier of bistable harvester, Mechanical Systems and Signal Processing, 85 (2017) 71-81.

[186] C. Wang, Q.C. Zhang, W. Wang, J.J. Feng, A low-frequency, wideband quad-stable energy harvester using combined nonlinearity and frequency up-conversion by cantilever-surface contact, Mechanical Systems and Signal Processing, 112 (2018) 305-318.

[187] A.F. Arrieta, P. Hagedorn, A. Erturk, D.J. Inman, A piezoelectric bistable plate for nonlinear broadband energy harvesting, Applied Physics Letters, 97 (2010) 3.

[188] L. Van Blarigan, J. Moehlis, Dynamic analysis of a buckled asymmetric piezoelectric beam for energy harvesting, Chaos, 26 (2016) 7.

[189] R.L. Harne, K.W. Wang, On the fundamental and superharmonic effects in bistable energy harvesting, Journal of Intelligent Material Systems and Structures, 25 (2014) 937-950.

[190] A. Ibrahim, S. Towfighian, M.I. Younis, Dynamics of transition regime in bistable vibration energy harvesters, Journal of Vibration and Acoustics-Transactions of the Asme, 139 (2017) 15.

[191] S.C. Stanton, B.A. Owens, B.P. Mann, Harmonic balance analysis of the bistable piezoelectric inertial generator, Journal of Sound and Vibration, 331 (2012) 3617-3627.

[192] M.A. Karami, D.J. Inman, Equivalent damping and frequency change for linear and nonlinear hybrid vibrational energy harvesting systems, Journal of Sound and Vibration, 330 (2011) 5583-5597.

[193] S.C. Stanton, B.P. Mann, B.A. Owens, Melnikov theoretic methods for characterizing the dynamics of the bistable piezoelectric inertial generator in complex spectral environments, Physica D: Nonlinear Phenomena, 241 (2012) 711-720.

[194] M.F. Daqaq, R. Masana, A. Erturk, D.D. Quinn, On the role of nonlinearities in vibratory energy harvesting: a critical review and discussion, Applied Mechanics Reviews, 66 (2014) 040801.

[195] R.L. Harne, C.L. Zhang, B. Li, K.W. Wang, An analytical approach for predicting the energy capture and conversion by impulsively-excited bistable vibration energy harvesters, Journal of Sound and Vibration, 373 (2016) 205-222.

[196] C.L. Zhang, R.L. Harne, B. Li, K.W. Wang, Statistical quantification of DC power generated by bistable piezoelectric energy harvesters when driven by random excitations, Journal of Sound and Vibration, 442 (2019) 770-786.

[197] P.L. Green, K. Worden, N.D. Sims, On the identification and modelling of friction in a randomly excited energy harvester, Journal of Sound and Vibration, 332 (2013) 4696-4708.

[198] L.E. Helseth, Excitation of energy harvesters using stick-slip motion, Smart Materials and Structures, 23 (2014) 11.

[199] D. Wang, J. Mo, X. Wang, H. Ouyang, Z. Zhou, Experimental and numerical investigations of the piezoelectric energy harvesting via friction-induced vibration, Energy Conversion and Management, 171 (2018) 1134-1149.

[200] W. Liu, M. Han, X. Sun, B. Meng, X.-S. Zhang, H. Zhang, An unmovable single-layer triboloelectric generator driven by sliding friction, Nano Energy, 9 (2014) 401-407.

[201] W.Q. Zhang, D.F. Diao, K. Sun, X. Fan, P.F. Wang, Study on friction-electrification coupling in sliding-mode triboelectric nanogenerator, Nano Energy, 48 (2018) 456-463.

[202] M.K. Kim, M.S. Kim, S.E. Jo, Y.J. Kim, Triboelectric-thermoelectric hybrid nanogenerator for harvesting frictional energy, Smart Materials and Structures, 25 (2016) 8.

[203] P.H. Wang, L. Pan, J.Y. Wang, M.Y. Xu, G.Z. Dai, H.Y. Zou, K. Dong, Z.L. Wang, An ultra-low-friction triboelectric-electromagnetic hybrid nanogenerator for rotation energy harvesting and self-powered wind speed sensor, ACS Nano, 12 (2018) 9433-9440.

[204] L.B. Schein, G.P. Castle, D.J. Lacks, Triboelectrification, Wiley Encyclopedia of Electrical and Electronics Engineering, (1999) 1-14.

[205] J.D. Bittner, F. Hrach, S. Gasiorowski, L. Canellopoulus, H. Guicherd, Triboelectric belt separator for beneficiation of fine minerals, Procedia Engineering, 83 (2014) 122-129.

[206] I.I. Inculet, Electrostatics in industry, Journal of Electrostatics, 4 (1978) 175-192.

[207] K.A. Winters, B.C. Roberts, M. McGrath, The impact of triboelectrification on the ARES IX launch and considerations for other launch vehicles, 15th Conference on Aviation and Range Meteorological Society, Los Angeles, CA. P, 2011.

[208] S. Liu, T. Hua, X. Luo, N. Yi Lam, X.-m. Tao, L. Li, A novel approach to improving the quality of chitosan blended yarns using static theory, Textile research journal, 85 (2015) 1022-1034.

[209] J. Wang, L. Zhou, C. Zhang, Z.L. Wang, Small-scale energy harvesting from environment by triboelectric nanogenerators, Small-Scale Energy Harvesting, IntechOpen, 2019.

[210] S. Niu, Y. Liu, X. Chen, S. Wang, Y.S. Zhou, L. Lin, Y. Xie, Z.L. Wang, Theory of freestanding triboelectric-layer-based nanogenerators, Nano Energy, 12 (2015) 760-774.

[211] Z. Lin, J. Chen, J. Yang, Recent progress in triboelectric nanogenerators as a renewable and sustainable power source, Journal of Nanomaterials, 2016 (2016).

[212] D.J. Wagg, Multiple non-smooth events in multi-degree-of-freedom vibro-impact systems, Nonlinear Dynamics, 43 (2006) 137-148.

[213] Y. Yue, Bifurcations of the symmetric quasi-periodic motion and Lyapunov dimension of a vibro-impact system, Nonlinear Dynamics, 84 (2016) 1697-1713.

[214] D. Younesian, A. Jafari, R. Serajian, Effects of the bogie and body inertia on the nonlinear wheel-set hunting recognized by the hopf bifurcation theory, International Journal of Automotive Engineering, 1 (2011) 186-196.

[215] M. Siddhpura, R. Paurobally, A review of chatter vibration research in turning, International Journal of Machine Tools and Manufacture, 61 (2012) 27-47.

[216] S. Afazov, S. Ratchev, J. Segal, A. Popov, Chatter modelling in micro-milling by considering process nonlinearities, International Journal of Machine Tools and Manufacture, 56 (2012) 28-38.

[217] D.J. Wagg, Multiple non-smooth events in multi-degree-of-freedom vibro-impact systems, Nonlinear Dynamics, 43 (2006) 137-148.

[218] D.J. Wagg, S.R. Bishop, Dynamics of a two degree of freedom vibro-impact system with multiple motion limiting constraints, International Journal of Bifurcation and Chaos, 14 (2004) 119-140.

[219] L. Meirovitch, Fundamentals of vibrations, Waveland Press, 2010.

[220] S. Timoshenko, D. Young, W. Weaver, Vibration Problems in Engineering. John Willey and Sons, Inc., New York, (1974).

[221] A. Erturk, D.J. Inman, On mechanical modeling of cantilevered piezoelectric vibration energy harvesters, Journal of Intelligent Material Systems and Structures, 19 (2008) 1311-1325.

[222] A. Erturk, D.J. Inman, An experimentally validated bimorph cantilever model for piezoelectric energy harvesting from base excitations, Smart Materials and Structures, 18 (2009) 025009.

[223] D. Zhou, The vibrations of a cantilever beam carrying a heavy tip mass with elastic supports, Elsevier, 1997.

[224] R.E. Bank, W.M. Coughran, W. Fichtner, E.H. Grosse, D.J. Rose, R.K. Smith, Transient simulation of silicon devices and circuits, IEEE Transactions on Computer-Aided Design of Integrated Circuits and Systems, 4 (1985) 436-451.

[225] M. Hosea, L. Shampine, Analysis and implementation of TR-BDF2, Applied Numerical Mathematics, 20 (1996) 21-37.

[226] L. Bonaventura, A. Della Rocca, Unconditionally strong stability preserving extensions of the TR-BDF2 method, Journal of Scientific Computing, 70 (2017) 859-895.

[227] S. Dharmaraja, Y. Wang, G. Strang, Optimal stability for trapezoidal–backward difference split-steps, IMA journal of numerical analysis, 30 (2010) 141-148.

[228] Y. Zhang, G. Luo, Detecting unstable periodic orbits and unstable quasiperiodic orbits in vibro-impact systems, International Journal of Non-Linear Mechanics, 96 (2017) 12-21.

[229] J. Feng, Analysis of chaotic saddles in a nonlinear vibro-impact system, Communications in Nonlinear Science and Numerical Simulation, 48 (2017) 39-50.

[230] G. Weir, P. McGavin, The coefficient of restitution for the idealized impact of a spherical, nano-scale particle on a rigid plane, Proceedings of the Royal Society A: Mathematical, Physical and Engineering Sciences, 464 (2008) 1295-1307.

[231] R.L. Jackson, I. Green, D.B. Marghitu, Predicting the coefficient of restitution of impacting elastic-perfectly plastic spheres, Nonlinear Dynamics, 60 (2010) 217-229.

[232] S. Venkateshan, P. Swaminathan, Computational methods in engineering, Elsevier, 2013.

[233] D. Hoffmann, B. Folkmer, Y. Manoli, Fabrication, characterization and modelling of electrostatic micro-generators, Journal of Micromechanics and Microengineering, 19 (2009) 094001.

[234] A. Diaz, R. Felix-Navarro, A semi-quantitative tribo-electric series for polymeric materials: the influence of chemical structure and properties, Journal of Electrostatics, 62 (2004) 277-290.

[235] R.P. Feynman, R.B. Leighton, M. Sands, The feynman lectures on physics; vol. i, American Journal of Physics, 33 (1965) 750-752.

[236] A. Erturk, D.J. Inman, A distributed parameter electromechanical model for cantilevered piezoelectric energy harvesters, Journal of Vibration and Acoustics, 130 (2008) 041002.

[237] A. Cammarano, S. Burrow, D. Barton, A. Carrella, L. Clare, Tuning a resonant energy harvester using a generalized electrical load, Smart Materials and Structures, 19 (2010) 055003.

[238] P.D. Mitcheson, T.T. Toh, K.H. Wong, S.G. Burrow, A.S. Holmes, Tuning the resonant frequency and damping of an electromagnetic energy harvester using power electronics, IEEE Transactions on Circuits and Systems II: Express Briefs, 58 (2011) 792-796.

[239] V. Nguyen, R. Zhu, R. Yang, Environmental effects on nanogenerators, Nano Energy, 14 (2015) 49-61.

[240] K. Tao, S.W. Lye, J. Miao, L. Tang, X. Hu, Out-of-plane electret-based MEMS energy harvester with the combined nonlinear effect from electrostatic force and a mechanical elastic stopper, Journal of Micromechanics and Microengineering, 25 (2015) 104014.

[241] S. Boisseau, G. Despesse, T. Ricart, E. Defay, A. Sylvestre, Cantilever-based electret energy harvesters, Smart Materials and Structures, 20 (2011) 105013.

[242] S. Boisseau, G. Despesse, B.A. Seddik, Electrostatic conversion for vibration energy harvesting, Small-Scale Energy Harvesting, (2012) 1-39.

[243] Y. Fu, H. Ouyang, R.B. Davis, Nonlinear dynamics and triboelectric energy harvesting from a three-degree-of-freedom vibro-impact oscillator, Nonlinear Dynamics, 92 (2018) 1985-2004.

[244] Y. Fu, H. Ouyang, R.B. Davis, Triboelectric energy harvesting from the vibro-impact of three cantilevered beams, Mechanical Systems and Signal Processing, 121 (2019) 509-531.

[245] H.Y. Li, L. Su, S.Y. Kuang, C.F. Pan, G. Zhu, Z.L. Wang, Significant enhancement of triboelectric charge density by fluorinated surface modification in nanoscale for converting mechanical energy, Advanced Functional Materials, 25 (2015) 5691-5697.

[246] W.-A. Jiang, L.-Q. Chen, Stochastic averaging of energy harvesting systems, International Journal of Non-Linear Mechanics, 85 (2016) 174-187.

[247] W.-A. Jiang, L.-Q. Chen, An equivalent linearization technique for nonlinear piezoelectric energy harvesters under Gaussian white noise, Communications in Nonlinear Science and Numerical Simulation, 19 (2014) 2897-2904.

[248] R. Hai-wu, W. Xiang-dong, M. Guang, X. Wei, F. Tong, Response of nonlinear oscillator under narrow-band random excitation, Applied Mathematics and Mechanics, 24 (2003) 817-825.

[249] R.A. Ibrahim, Vibro-impact dynamics: modeling, mapping and applications, Springer Science & Business Media, 2009.

[250] W. Cai, R.L. Harne, Electrical power management and optimization with nonlinear energy harvesting structures, Journal of Intelligent Material Systems and Structures, 30 (2019) 213-227.

[251] A. Kansal, J. Hsu, S. Zahedi, M.B. Srivastava, Power management in energy harvesting sensor networks, ACM Transactions on Embedded Computing Systems (TECS), 6 (2007) 32.